Parson, L., Hawkins, J., Allan, J., et al., 1992
Proceedings of the Ocean Drilling Program, Initial Reports, Vol. 135

11. SITE 841[1]

Shipboard Scientific Party[2]

HOLE 841A

Date occupied: 30 January 1991

Date departed: 2 February 1991

Time on hole: 2 days, 29 min

Position: 23°20.746′S, 175°17.871′W

Bottom felt (rig floor; m, drill-pipe measurement): 4821.0

Distance between rig floor and sea level (m): 11.20

Water depth (drill-pipe measurement from sea level, m): 4809.8

Total depth (rig floor; m): 5007.60

Penetration (m): 186.60

Number of cores (including cores with no recovery): 21

Total length of cored section (m): 186.60

Total core recovered (m): 70.25

Core recovery (%): 37.7

Oldest sediment cored:
Depth (mbsf): 186.60
Nature: vitric siltstone and sandstone
Earliest age: late Miocene
Measured velocity (km/s): 1.877

HOLE 841B

Date occupied: 2 February 1991

Date departed: 10 February 1991

Time on hole: 10 days, 40 min

Position: 23°20.741′S, 175°17.872′W

Bottom felt (rig floor; m, drill-pipe measurement): 4821.0

Distance between rig floor and sea level (m): 11.20

Water depth (drill-pipe measurement from sea level, m): 4809.8

Total depth (rig floor; m): 5655.20

Penetration (m): 834.20

Number of cores (including cores with no recovery): 70

Total length of cored section (m): 664.4

Total core recovered (m): 185.38

Core recovery (%): 27.9

Oldest sediment cored:
Depth (mbsf): 834.20
Nature: rhyolite tuff/rhyolite breccia
Earliest age: late Eocene or older
Measured velocity (km/s): 3

Hard rock:
Depth (mbsf): 324.90
Nature: basalt/rhyolite
Measured velocity (km/s): 4.4–4.8

Basement:
Depth (mbsf): 605.00
Nature: rhyolite
Measured velocity (km/s): 4.5

HOLE 841C

Date occupied: 10 February 1991

Date departed: 14 February 1991

Time on hole: 5 days, 12 hr

Position: 23°20.720′S, 175°17.879′W

Bottom felt (rig floor; m, drill-pipe measurement): 4821.0

Distance between rig floor and sea level (m): 11.20

Water depth (drill-pipe measurement from sea level, m): 4809.8

Total depth (rig floor; m): 5596.0

Penetration (m): 775.0

Number of cores (including cores with no recovery): 0

Total length of cored section (m): 0

Total core recovered (m): 0

Principal results: Site 841 was planned to recover an estimated 500 m of sediment and to core 50 m into basement. The intent was to characterize both the sedimentary section and the basement. The hole was intended as a counterpart for comparison with forearc sites drilled in the Mariana and Bonin arc systems. In addition to petrologic studies of the rocks and sediments, it was intended to provide information about differential uplift and subsidence of the forearc. Other objectives included the acquisition of data for paleomagnetic measurements, physical properties, and fluid geochemistry. Drilling went faster than expected and the hole was extended to 834.2 mbsf. We had anticipated the possibility of drilling into serpentinite rocks but did not expect to drill into the remnants of a silicic volcanic arc. However, we did.

The core recovered at Site 841 (Fig. 1) gives an age record ranging from middle Pleistocene to late Eocene or older. A barren interval separates the middle Pleistocene from upper Miocene which may be due to dissolution because of deposition below the carbonate compensation depth (CCD). Sedimentation began in late Eocene to early Oligocene with the accumulation of carbonates in a shallow-water environment on an igneous substrate formed of low-K rhyolitic volcanic rocks. Carbonate sedimentation was disturbed by occasional influxes of volcanic debris from a nearby rhyolitic source. From the early Oligocene to early middle Miocene there was a hiatus in sedimentation followed by a phase of relative subsidence. This resulted in deposition of volcaniclastic conglomerates, sandstones, and siltstones mostly by gravity mass flows and turbidity currents. The sequence fines and thins upward but during the late Miocene a fresh influx of volcaniclastic conglomerates indicates rejuvenation of the volcanic source. Volcanic debris in the Miocene section ranges from basaltic to dacitic. Subsidence continued until, by the middle Pleistocene or possibly Pliocene age, Site 841 had subsided below the CCD. Epiclastic volcanic turbidites were reduced to very thin, rare intervals

[1] Parson, L., Hawkins, J., Allan, J., et al., 1992. *Proc. ODP, Init. Repts.,* 135: College Station, TX (Ocean Drilling Program).

[2] Shipboard Scientific Party is as given in the list of participants preceding the contents.

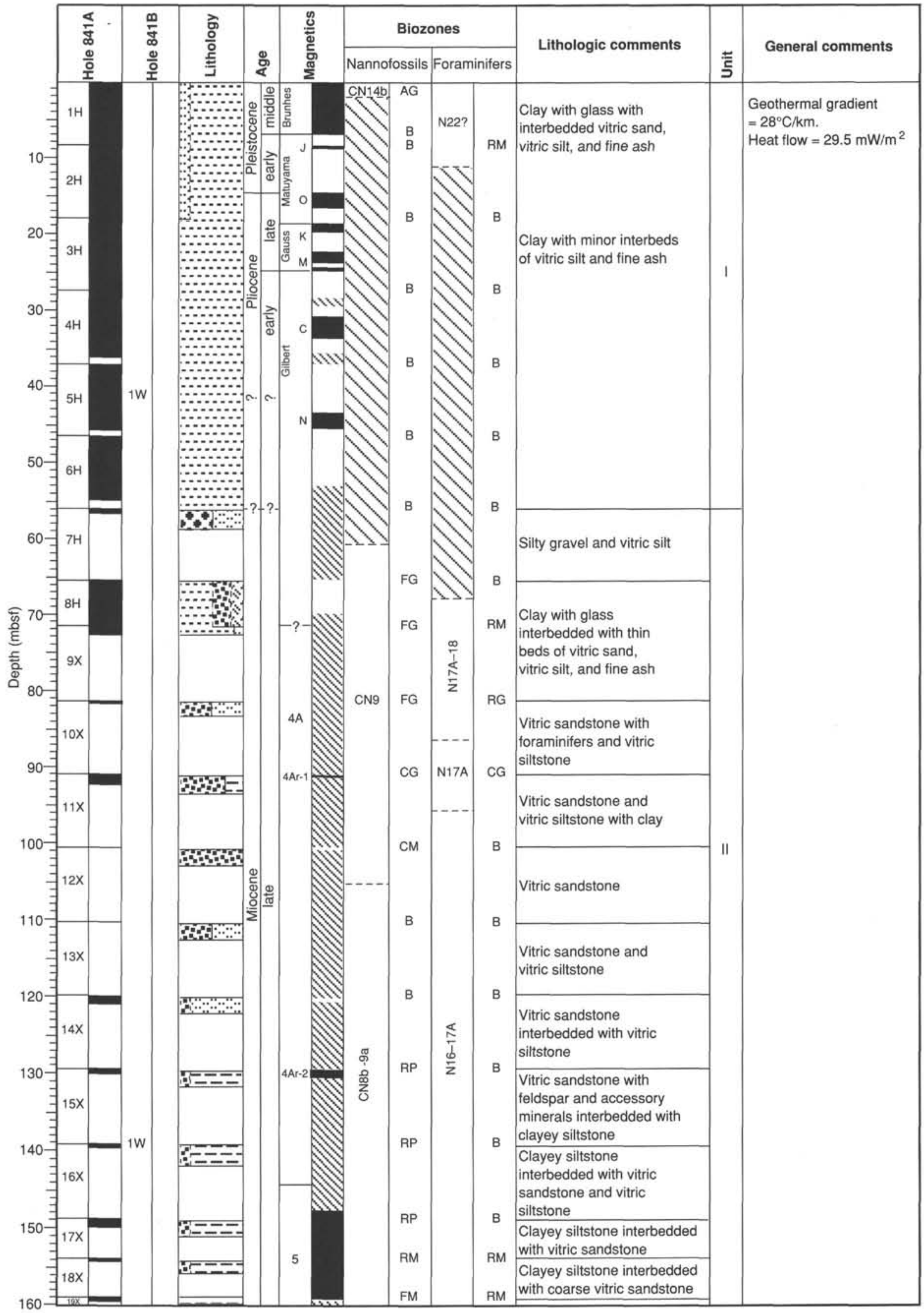

Figure 1. Site summary, Site 841. Abbreviations for abundance are as follows: A = abundant, C = common, F = few, R = rare, and B = barren. Those for preservation are as follows: G = good, M = moderate, and P = poor.

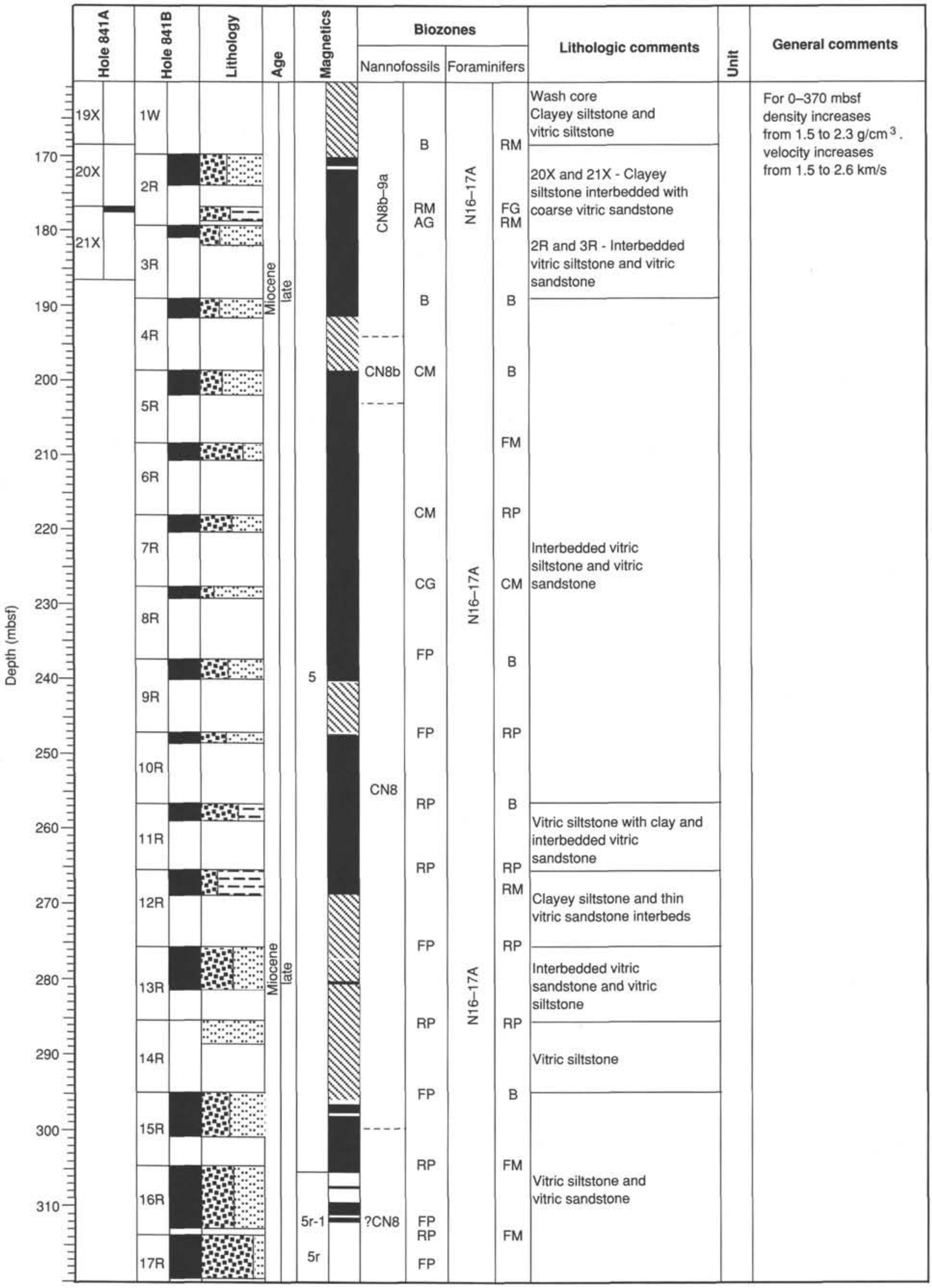

Figure 1 (continued).

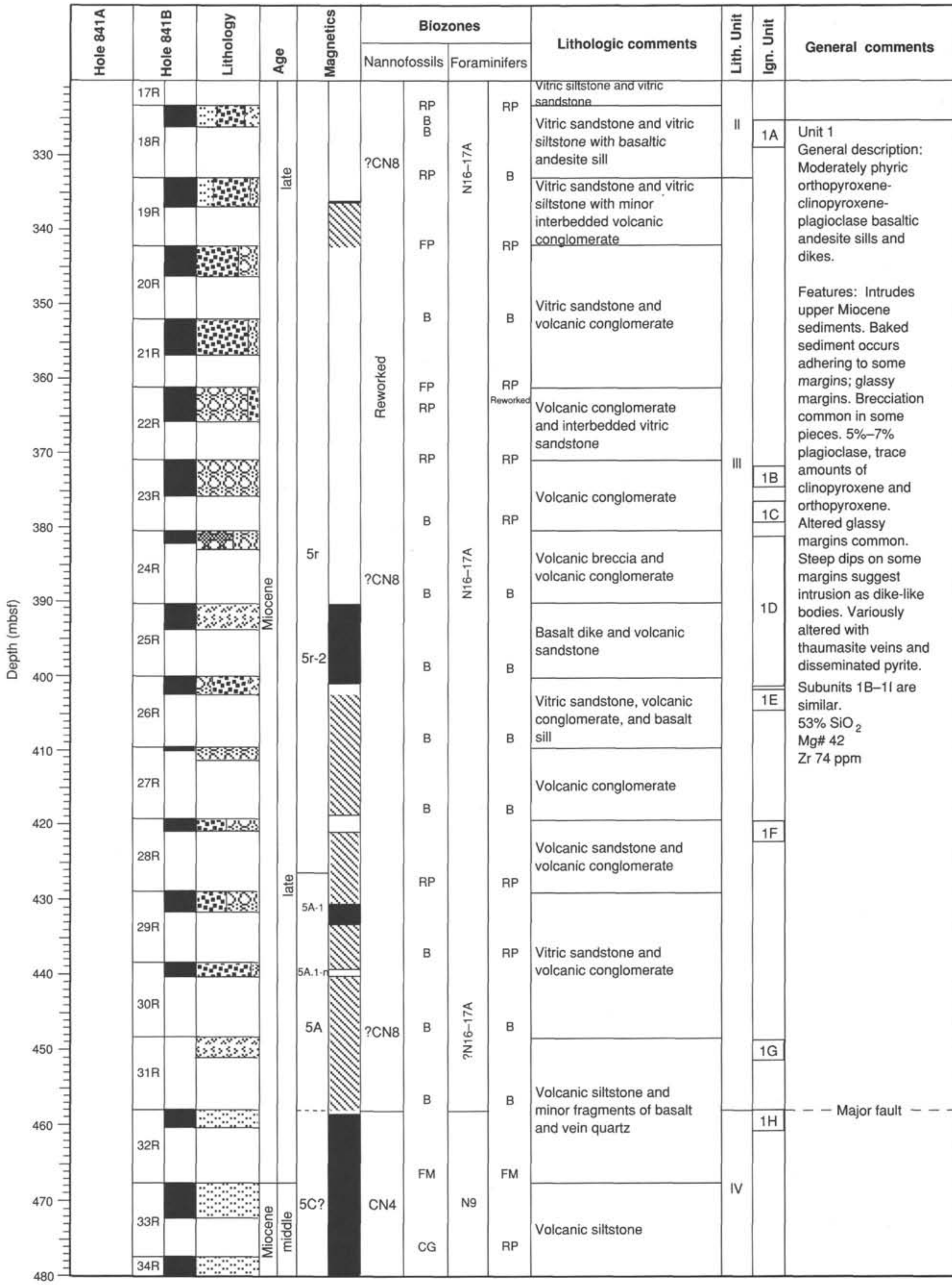

Figure 1 (continued).

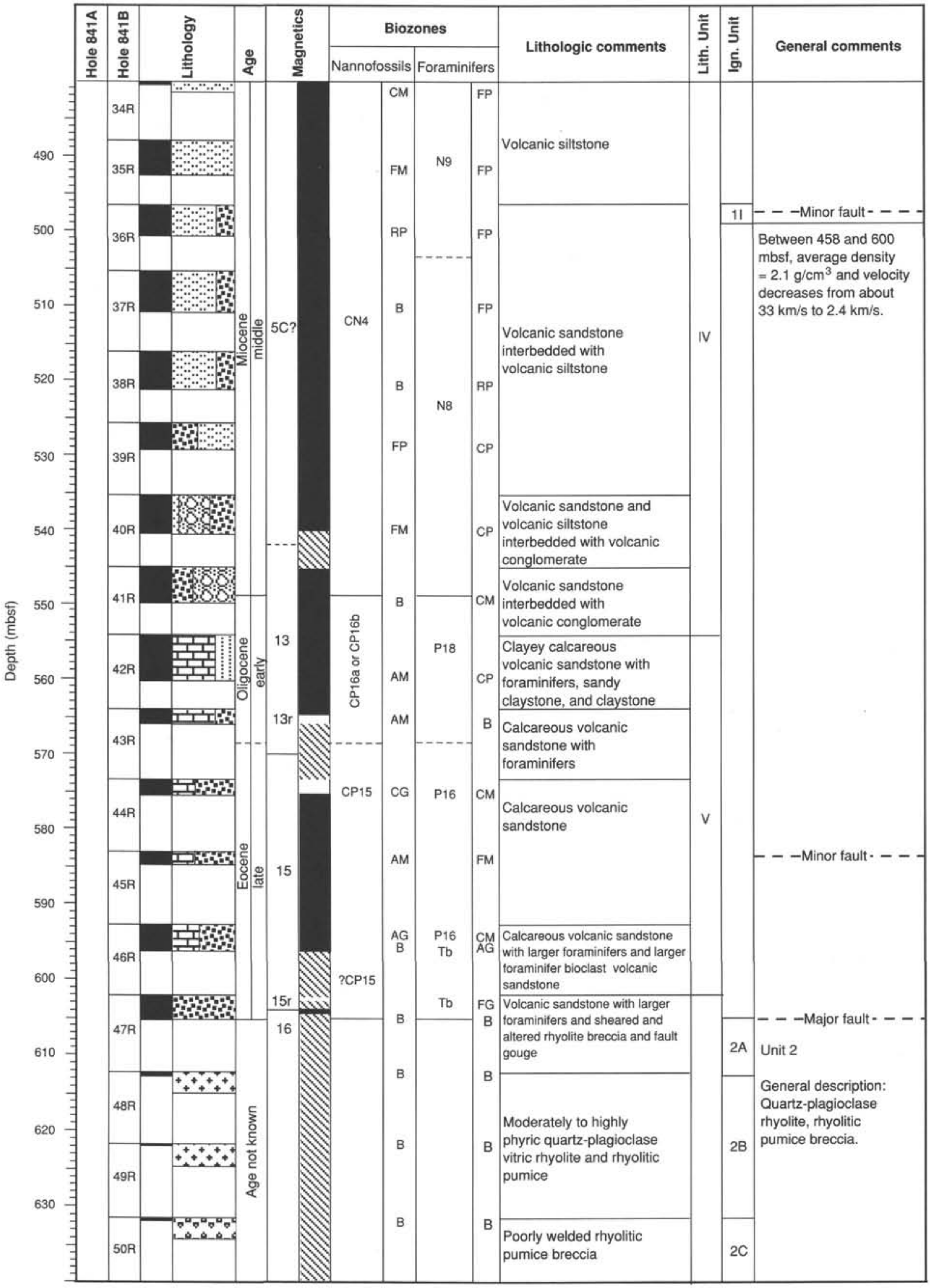

Figure 1 (continued).

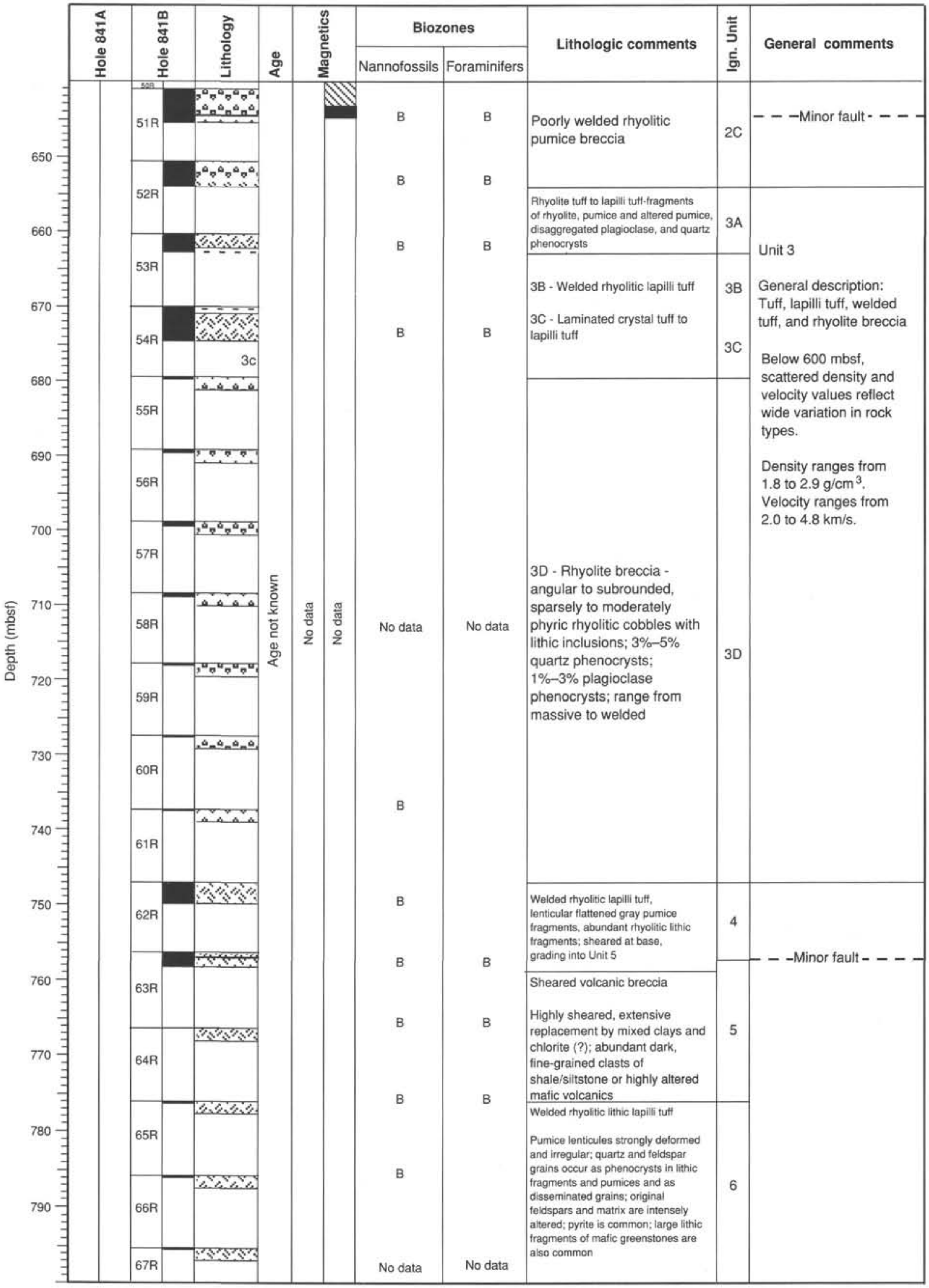

Figure 1 (continued).

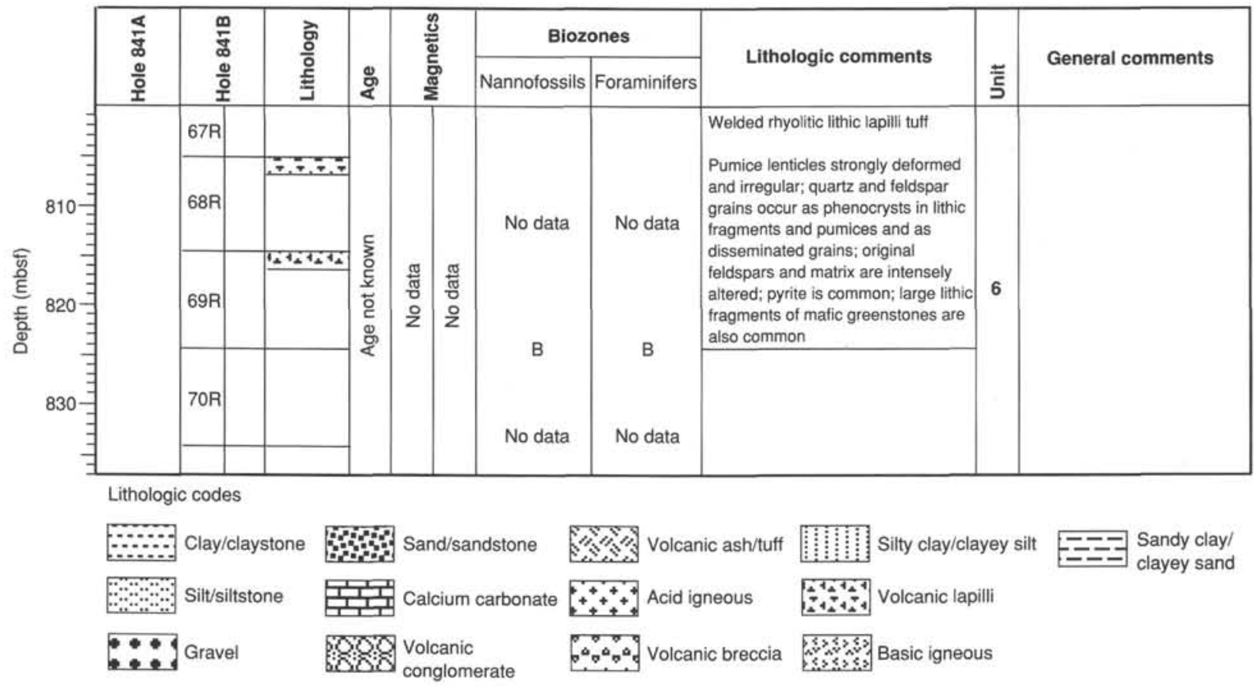

Figure 1 (continued).

within the pelagic clayey background sedimentation. Minor thin pyroclastic airfall deposits were also being deposited during the middle Pleistocene to present. Nannofossil oozes are present in minor amounts in the middle Pleistocene (to Pliocene?) sediments. The sedimentary accumulation rates vary widely with time and appear to be controlled largely by the input of volcaniclastic material. The interval from 604 to 549 mbsf, which includes an Eocene limestone with large foraminifers, accumulated at 14 mm/k.y. Both the biostratigraphic and paleomagnetic accumulation rate estimates give similar values. Between 549 and 458 mbsf (lower middle Miocene volcaniclastic sediments) the rate increases from 35 mm/k.y. in the lower part to 160 mm/k.y. in the upper part. The base of the upper Miocene to Pleistocene section (458 to 203 mbsf), an interval comprising volcanic sandstones and conglomerate, accumulated at 142 mm/k.y. The rate falls to 53 mm/k.y. between 203 and 60 mbsf and to 11 mm/k.y. above 60 mbsf.

Two major igneous rock sequences were recovered. There are nine separate small bodies (dikes, sills, or flows) of basaltic andesite and andesite in the upper Miocene to lower middle Miocene volcaniclastic series. These are dominantly plagioclase phyric with lesser amounts of orthopyroxene and clinopyroxene. The other major unit comprises a series of rhyolitic rocks including lapilli tuff, welded tuff, tuff breccias, and massive rhyolite. Visible amounts (0.5%–1%) of fine-grained disseminated pyrite are common in most of the samples. This high-silica, low-potassium (presumably island arc) volcanic complex, of pre-upper Eocene age, was totally unexpected. Similar rocks are rare in other intraoceanic island arcs, especially in their earliest stages of development. The closest known occurrence of similar rocks in a submarine oceanic area is on Lord Howe Rise, where Late Cretaceous rhyolitic flows and tuffs were found at Deep Sea Drilling Project (DSDP) Site 207. At this time there is nothing to suggest a geologic tie to that area other than their similar petrologic features and broadly similar ages. Broadly similar low-K rhyolite is also found in the Mariana Arc on Saipan.

Paleomagnetic studies of the advanced piston corer (APC) recovery from Hole 841A show that there is a relatively continuous sedimentary sequence from the Brunhes to the Gilbert Chron. The Brunhes Chron, Brunhes/Matuyama boundary, and Jaramillo Subchron all are clearly seen.

The porewater chemistry is extensively modified from standard seawater values, consisting of Ca- and Cl-rich brines below 200 mbsf. Large variations were noted in Ca, Mg, K, Na, and Cl concentrations in pore waters from the uppermost 200 m of sediments. These variations are abnormal for marine sediments and are probably caused by the combined effect of abundant volcanogenic material and high rates of sedimentation that have lead toward very low porewater diffusivity. Sulfate and phosphate decrease sharply and ammonia sharply increases downcore to 200 mbsf; these changes are likely to be related to decomposition of organic matter by sulfate-reducing bacteria. Si, Sr, and Mn substantially decrease in concentration with depth, changes which are probably controlled by diagenetic alteration of volcanogenic sediments.

The highest methane values recorded on Leg 135 were found in the lower part of Hole 841B but were only 15 ppm. Neither ethane nor propane was detected. The methane is associated only with the rhyolitic rocks at this level and it is possible that it could be derived from an unspecified nonbiological process.

BACKGROUND AND OBJECTIVES

Background

Location and Bathymetry

Site 841 is located on the upper trench slope, west of the axis of the Tonga Trench, in a water depth of 4810.0 m (Fig. 2). The site is 150 km east of the volcanic island of Ata and 235 km southeast from the uplifted coral platform of Tongatapu. Site 840, drilled on the crest of the Tonga platform in a water depth of 754.5 m, is 48 km to the west. The axis of the Tonga Trench lies about 40 km to the east of Site 841 and at this latitude reaches a depth of more than 10 km. Site 841 is situated on a minor up-arch in the topography of the upper trench slope on the south side of a small dome-like feature that is elongated in a north-south direction parallel to the slope. This small dome is one of several that disturbs an otherwise gently sloping surface that continues on down into the trench to a series of terrace-like features that characterize the inner (western) wall of the trench (Fig. 3A). Site selection was aided by several multichannel seismic lines (*S. P. Lee* L5-82-5P, Scholl et al., 1985) and numerous single-channel seismic reflection profile and echo sounder lines (*Charles Dar-*

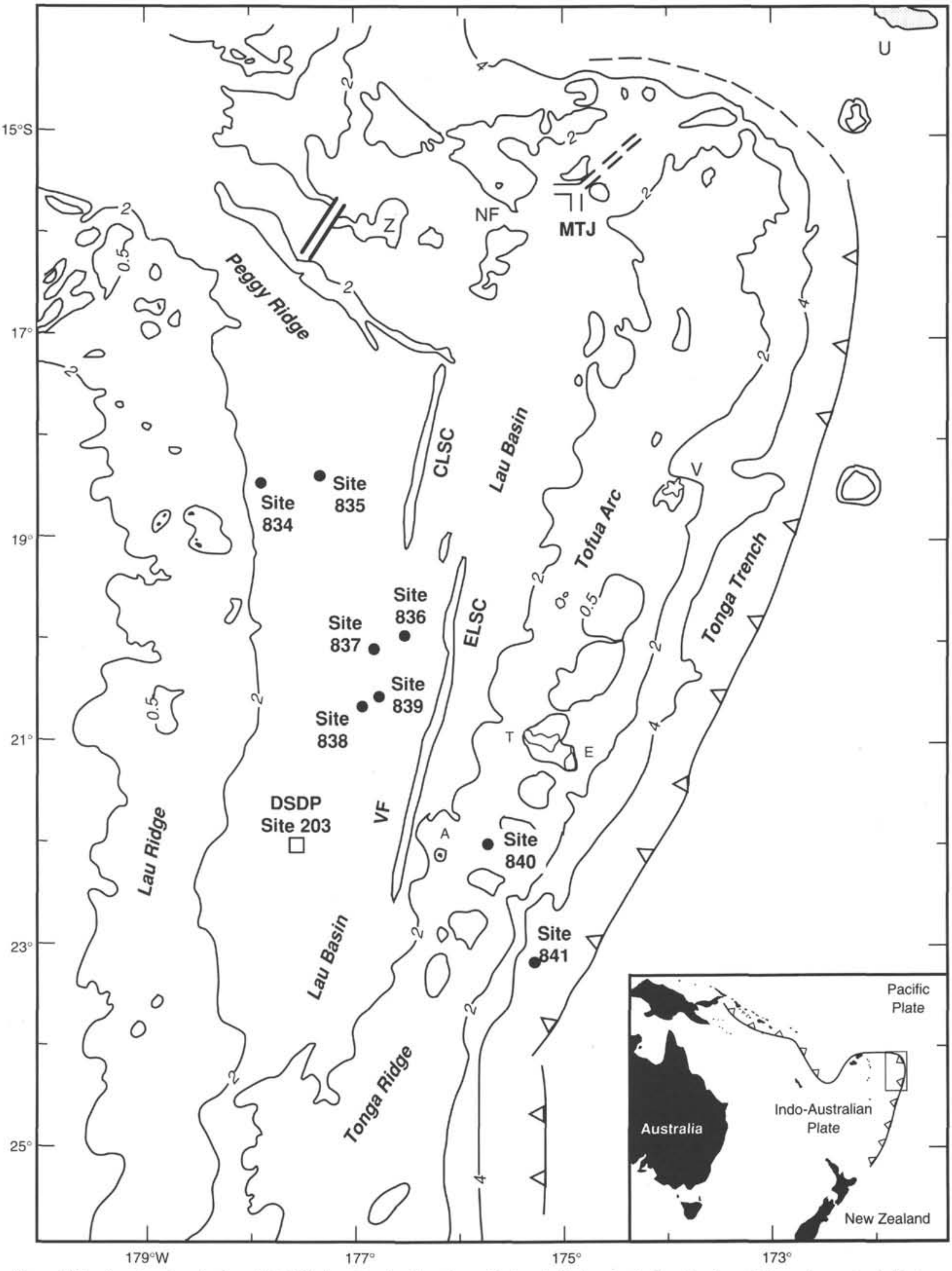

Figure 2. Regional setting for Leg 135 drill sites showing locations of other drill sites in the Lau Basin and the major geologic features of the Tonga Trench and Lau Basin system. Z = Zephyr Shoal; islands shown are T = Tongatapu, E = 'Eua, V = Vavau, NF = Niua Fo'ou, and U = Upolu. Locations of the Central Lau (CLSC) and Eastern Lau (ELSC) spreading centers, Valu Fa Ridge (VF), and Mangatolu Triple Junction (MTJ) are from von Stackelberg (1990), Parson et al. (1990), Hawkins et al. (1989), and Nilsson et al. (1989). DSDP Site 203 location is shown as an open square.

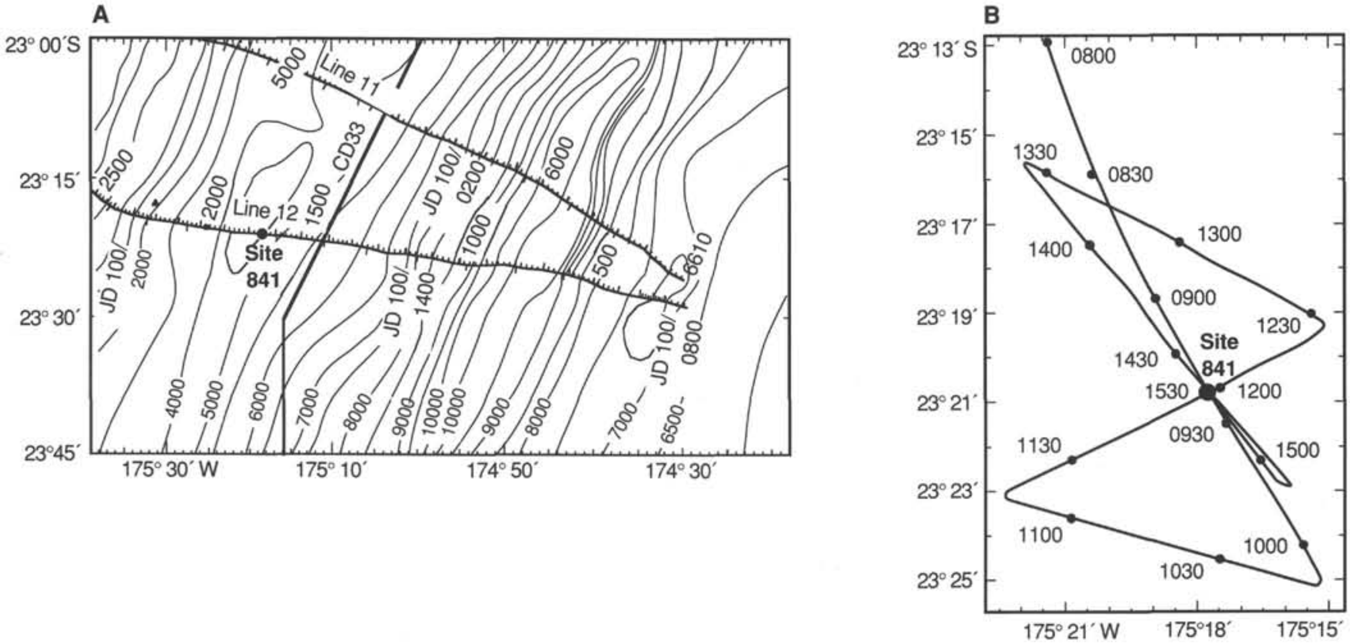

Figure 3. **A.** Track charts of the existing seismic profiles available for the area of Site 841, including USGS profiles collected by *S. P. Lee* in 1982 (Scholl et al., 1985), and those data acquired by *Charles Darwin* (CD33; Parson et al., 1989). Bathymetry for the area around the site is taken from Scholl and Vallier (1985). Contours in meters. **B.** Track chart of seismic reflection profiles collected by *JOIDES Resolution* during Leg 135.

win, CD33; Parson et al., 1989) shown in Figure 3A. GLORIA imagery was available for a part of the area in the vicinity of the site (L. Parson, unpubl. data, 1990). Seismic reflection profiles collected during the survey and approach lines to Site 841 by the *JOIDES Resolution* were useful in defining the shallower portion of the seismic section (Fig. 3B).

Seismic Stratigraphy

Multichannel seismic reflection data collected on the *S. P. Lee* across Site 841 is illustrated in Figure 4A, which is accompanied by a line-drawn interpretation in Figure 4B. This section has been reprocessed (including migration) and represents the best data available for the area. Our interpretation of the USGS multichannel line 12 is that a three-fold division of the seismic section can be made. For the purposes of this discussion, we have modified the designations for the forearc seismic units with an "F" prefix to avoid implication of correlation to seismic units already described for the backarc sites.

The uppermost section (Seismic Unit FA) comprises a total section of between 0.3 and 0.45 seconds two-way traveltime (s TWT), but includes and underlies a seafloor to near-seafloor seismic horizon up to 0.1 s TWT thick, dominated by a strong group of high-amplitude signals. The main portion of the sequence, however, is predominantly a transparent or very weakly laminated unit. Seismic Unit FB extends from around 0.3 s to as much as 0.6 s TWT below seafloor, and varies in its acoustic character from a semitransparent unit locally indistinguishable from the lower part of Seismic Unit FA, through laterally discontinuous groups of closely spaced planar laminar horizons. Single-channel seismic data recorded during Leg 135 clearly images the upper surface of Seismic Unit FB (Figs. 4C, 4D), often as "acoustic basement," and windows through this horizon into the underlying reflector sequences are not as obvious as on the multichannel data. Where Seismic Unit FB is not planar laminated or is unresolved, it is generally possible to identify a deeper horizon, which for the purposes of this discussion we shall refer to as acoustic basement and designate as Unit FC. This acoustic basement is observed only sporadically in the deeper parts of the section. The shallowest point in the section at which Unit FC is resolved is at Site 841, where it lies at approximately 0.55 s TWT below seafloor. On other multichannel seismic data close to Site 841, a discontinuous upper surface of Seismic Unit FC is identified at a variety of depths, locally as deep as 1.1 s TWT below seafloor. An illustration of the correlation of seismostratigraphic horizons with lithostratigraphic units is given in Figure 4E.

Overview of the Geology

Site 841 is located on the eastern edge of the Tonga Ridge in an area termed the southern Tonga platform by Herzer and Exon (1985). The Tonga Ridge is a high-standing block of crust that trends north-northeast–south-southwest and comprises two parallel belts of fundamentally different rocks. The eastern belt (Tonga platform) is formed of uplifted carbonate rocks with interbedded volcaniclastic material and, on the island of 'Eua, by uplifted pre–middle Eocene igneous basement that has been intruded by early Oligocene and early Miocene age dikes. Deformation of the Tonga platform has resulted in a complex arrangement of normal faults that give rise to a reticulated pattern with northwest trends, with north-trending blocks downdropped to the west. The western belt is formed by the active and inactive volcanoes, seamounts, and volcanic shoals of the Tofua Arc. These are largely basaltic or basaltic andesitic, but some shoals have erupted rhyolitic pumice in historic times. In planning the drill sites for the Tonga platform and the upper trench slope (Sites 840 and 841) it was assumed that much of the basement was crust detached from the Lau Ridge in the opening of the Lau Basin. It was also considered likely that remnants of the forearc to the Lau Ridge would be present and that the rocks exposed on the island of 'Eua might be representative of some of the older crust of the forearc region. Dredge collections from the Tonga Trench wall (e.g., Fisher and Engel, 1969; Bloomer and Fisher, 1987) had established that parts of the trench wall included all of the igneous units that are considered to constitute an ophiolite assemblage. Similar rocks have been collected from the walls of the Mariana Trench (e.g.,

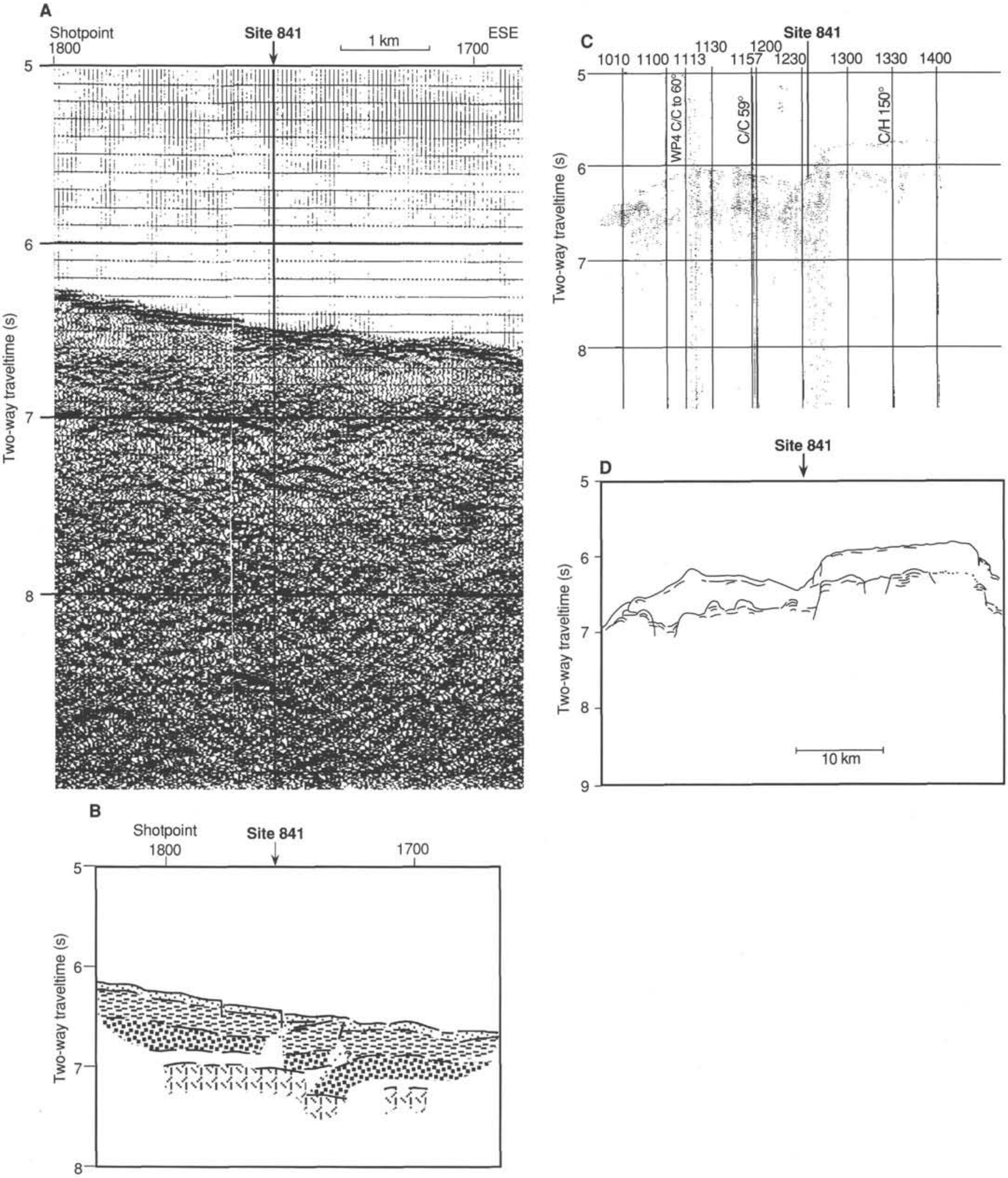

Figure 4. **A.** Part of processed multichannel seismic reflection profile L2-82-12, used to locate Site 841. **B.** Line drawing interpretation of multichannel profile in Figure 4A. Light and horizontal dashes correspond to Seismic Unit FA; dark stipple to Seismic Unit FB; and a dashed and vertical line combination ornament to Seismic Unit FC. **C.** Single-channel seismic reflection profile acquired by the *JOIDES Resolution*. **D.** Line drawing interpretation of Figure 4C. **E.** Multichannel seismic reflection profile recorded by the *S. P. Lee* (Scholl et al., 1985), with interpreted seismostratigraphic column. Seismic Units FA, FB, and FC are discussed in text.

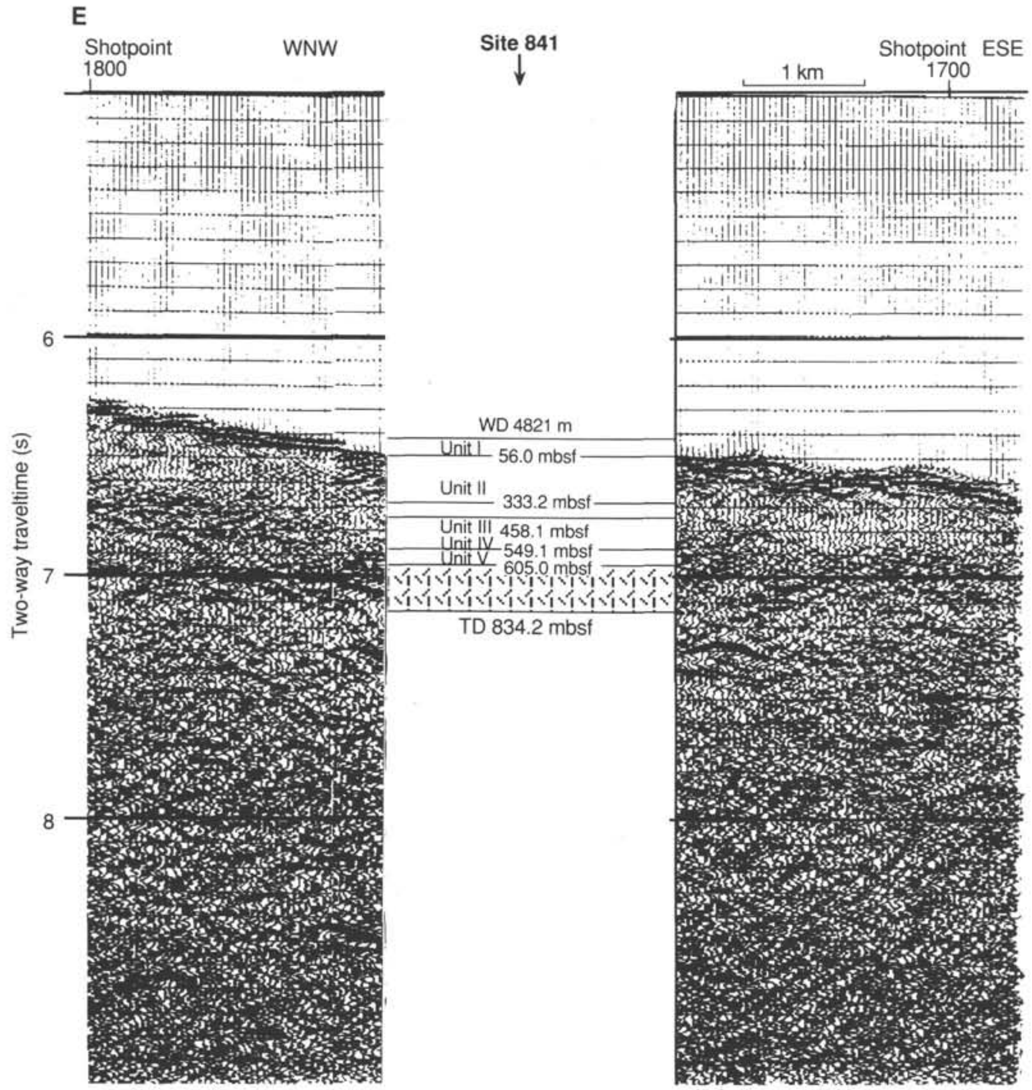

Figure 4 (continued).

Bloomer and Hawkins, 1983) and we considered that uplifted masses of these rocks might also constitute parts of the crust near the drill site. As mentioned above, the drill site was near a small dome-like feature on the upper trench slope. Similar dome-like features in the forearc of the Mariana Trench (Hawkins et al., 1979; Hussong and Fryer, 1985) have proven to be the seafloor expression of serpentinite diapirs. There is no indication, other than their shape and location, that the domes at the Tonga Trench have a similar origin, but serpentinite masses were also considered to be a likely material for the deep acoustic basement. Other low relief, dome-like features on the Tonga platform are considered to be the expression of buried reef buildup (Maung et al., 1981) or igneous intrusives (Alexander, 1985). This summary of rock types that we thought might be encountered at Site 841 covered many likely possibilities, but did not go far enough as the basement was quite different from anything anticipated.

Detailed summaries of the geology of the Tonga platform are given by Herzer and Exon (1985), Exon et al. (1985), Cawood (1985), Cunningham and Anscombe (1985), Packham (1985), and Tappin et al. (1991). Briefly, the geology of the Tonga platform may be summarized as follows. A pre–late Eocene basement, formed largely of arc tholeiitic series igneous rocks (Hoffmeister, 1932; Ewart and Bryan, 1972; Hawkins and Falvey, 1985) has been radiometrically dated as 46 Ma (Ewart et al., 1977) and 40–43 Ma (Duncan et al., 1985). These ages have been largely determined on clasts rather than *in-situ* rocks. The igneous rocks are overlain by upper–middle Eocene (to Oligocene?) platform limestone, further defined as a foraminiferal/algal wackestone-packstone with remains of echinoids, bryozoans, molluscs, and rare corals (Cunningham and Anscombe, 1985). The Oligocene age has been questioned and only upper–middle Eocene and upper Eocene limestones are considered to be present (G. Chaproniere, pers. comm., 1991). These limestones are, in turn, overlain by upper middle Miocene to lower Pliocene volcaniclastic turbidites. The contact is interpreted as a paraconformity or, locally, a fault (Tappin and Ballance, 1991). The volcaniclastic rocks are reworked deposits and the nature of the original protolith is obscured due to heavy alteration (Cunningham and Anscombe, 1985). The mineral constituents given in descriptions suggest that the protolith was of broadly andesitic to dacitic composition and a source from the Lau Ridge is likely but not proved. Pliocene to Quaternary coral and foraminiferal limestones overlie the volcaniclastic series without an apparent break on 'Eua but they onlap Eocene and Oligocene limestones both to the north and south.

Reworked volcanic detritus is present at the base of the limestones (lower Pliocene) but volcanic material is notably absent in the younger part of the limestone sequence. The interpretation of the geologic history of the area according to Herzer and Exon (1985) is as follows. The Tonga Ridge and Tonga Trench are considered to be parts of a convergent plate margin system that has been active at least since the Eocene. The Tonga Ridge has migrated eastward, relative to the Lau Ridge, since the Eocene as a consequence of lithosphere extension and formation of the Lau (backarc) Basin. During the Miocene, the southern Tonga platform accumulated a thick sequence of clastic rocks in a forearc basin lying to the east of a volcanic arc (presumably the Lau Ridge). The sedimentary filling thickened westward and accumulated to thicknesses on the order of 2000 m. Sedimentation was accompanied, or followed closely, by the emplacement of hypabyssal intrusives that form dikes or sills in the volcaniclastic series of Tongatapu. These intrusive bodies were radiometrically dated at 21.3 ± 0.4 Ma (early Miocene) and 13.9 ± 1 Ma (middle Miocene) and have intruded upper Eocene and older volcanic rocks. It is assumed that the intrusive rocks were feeders to the overlying Miocene volcanic rocks but the authors (Cunningham and Anscome, 1985) caution that the radiometric dates are minimum ages and may reflect alteration. The sedimentary and volcanic filling thinned to the east on to an outer ridge. During the late Miocene or early Pliocene, regional uplift formed large normal faults that strike nearly at right angles to the trend of the arc and developed an unconformity that separated Miocene from upper Pliocene sediments. During the late Pliocene or Quaternary, continued normal faulting caused (1) downdrop of blocks relatively to the west as the Lau Basin opened and (2) separation of blocks of the Tonga Ridge along faults at right angles to the trend of the arc. The latter, together with broad doming, has given rise to the segmented Tonga platform. Herzer and Exon (1985) proposed that the Miocene volcanic arc was split off from the active arc and carried *westward* as the Lau Basin opened beginning during the Pliocene. This contrasts with the models proposed by Karig (1970) and Hawkins et al. (1984) that visualized the Lau Ridge (remnant arc) as remaining fixed while the Tonga arc–trench system retreated eastward. The end result remains the same no matter what is the absolute direction of displacement of the trench and remnant arc. Both Hawkins et al. (1984) and Herzer and Exon (1985) proposed that the Tofua Arc was a young feature that has developed since the crustal extension and rifting that led to the development of the Lau Basin.

Tonga Trench

The Tonga Trench is a major tectonic feature in the southwestern Pacific basin (Raitt et al., 1955; Fisher, 1974) marking the zone of plate convergence that has been the most important control on the evolution of the Earth's crust in this area for at least 40 m.y. Oceanic crust presently being subducted into the trench is at least as old as Late Cretaceous (Vallier et al., 1985), but there is only meager evidence for accretion of seafloor rocks on the inner wall of the Tonga Trench. Nevertheless, there is good evidence for crustal erosion. Upper Cretaceous pelagic sediment was recovered from the bottom of the inner trench slope near the intersection of the Louisville seamount chain (Vallier et al., 1985). Fisher and Engel (1969) described a collection of mafic and ultramafic rocks from five dredge collections made at depths ranging from 7000 to 9400 m. The mafic rocks appear to be from the incoming Pacific Plate but are actually parts of a horst on the oceanic plate rather than material accreted to the trench wall. The landward slope of the trench includes harzburgite on its lower levels and andesite clasts on the upper levels. The composition of much of the forearc basement has been postulated to be part of an Eocene arc complex (Vallier et al., 1985; Bloomer and Fisher, 1985). The exposure of these rock types within 40 km of the trench axis, and the morphology of the trench, have been used to argue for subduction erosion along the Tonga Trench (Lonsdale, 1986; Bloomer and Fisher, 1985). If this were true, there should have been considerable crustal subsidence at Site 841 since the Eocene.

Lord Howe Rise and Norfolk Ridge

The Lord Howe Rise, located at approximately 163°E, and the Norfolk Ridge at 168°E are far removed from the Tonga arc–trench system but a brief review of their geologic history is useful as background material for Tonga Ridge Site 841. It has long been recognized that the area lying east of Australia and extending to the Tonga Trench has been the site of successive rifting and development of volcanic arcs and backarc basins (e.g., Karig, 1970; Burns and Andrews, 1973; and summary in Kroenke, 1984). Beginning during the Late Cretaceous, the eastern margin of Australia was rifted away and the rifted blocks were further segmented into the Lord Howe Rise and Norfolk Ridge (Burns and Andrews, 1973; Bentz, 1974). The New Caledonia Basin, separating the Lord Howe Rise and Norfolk Ridge, was formed by seafloor spreading before the late Paleocene and the opening of the Tasman Basin and Coral Sea continued until the early Eocene, displacing the Lord Howe Rise to the east from Australia. Although locally overlain by basalt, the Lord Howe Rise is likely to be a continental fragment. DSDP Site 207, drilled on the Lord Howe Rise, recovered rhyolitic lapilli tuffs, produced by explosive eruptions and vitrophyric low-K rhyolite flows that are autobrecciated in part. Both rock types formed in a subaerial or shallow-water subaqueous setting. The rhyolitic units were dated by K/Ar method and gave an age of 93.7 Ma ± 1.2 Ma. The rhyolite is overlain by Maestrichtian sandstone and silty claystone (van der Lingen, 1973).

Derivation of the Tonga and Lau ridges by the breaking up of a common parental ridge, first by the formation of the South Fiji Basin, and then by the Lau Basin, has been proposed by a number of workers and summarized by Kroenke (1984). It is postulated that this parental ridge in turn may have been derived from the Norfolk Ridge. The details of the geometry and trajectories of the successively formed splinters of the ancient Lord Howe Rise–Norfolk Ridge land mass, originally split off from the Australian continent, are unclear, and a detailed discussion is beyond the scope of this summary. It is likely that an arc system marked by the Three Kings Rise and Loyalty Islands may have been important as yet another intermediate stage that was active during the time of spreading in the South Fiji Basin. The South Fiji Basin opening may have overlapped some of the earliest history of the plate convergence and volcanism that led to the formation of the Lau Ridge.

In view of the complex history spanning 90 m.y. of formation of island arcs, crustal rifting, and unknown displacements of large blocks of continental and oceanic crust, it is obviously an unsupported speculation to attempt to correlate the Lord Howe Rise silicic rocks with petrologically similar rocks at Site 841. A major problem, apart from their separation in space, is an apparent age discrepancy of as much as 50 m.y. Dating of the Site 841 silicic rocks will be a first step in unraveling their place in the evolution of this part of the Pacific Basin.

Scientific Objectives

The principal objectives for Site 841 were to sample the 500–600 m of sediment and to drill into the acoustic basement. The original plan called for a 50-m hole into basement, but this was subsequently modified during the drilling operations to allow drilling as deep as 1000 mbsf if time permitted. The purpose was to determine the geology of the forearc and to interpret its history, which included an effort to (1) determine the minimum age of basement, (2) establish the petrology and biostratigraphy of the sedimentary series, (3) establish a tephrochronology for arc volcanism in the Tofua Arc, (4) sample pore water and measure fluid geochemistry of forearc rocks and sediments; and (5) look for evidence to document the uplift and subsidence history of the forearc. Specific objectives for the basement material were to (1) obtain a petrologic comparison with rocks from the Mariana and Bonin forearcs, (2) make paleomagnetic studies of the forearc basement, in an area away from the thermal effects of later arc volcanism, in order to constrain models predicting the rotation of the Tonga Arc, (3) ascertain the physical properties of forearc basement rocks, and (4) understand the volcanic history of the Tonga–Tofua Arc.

OPERATIONS

The 62-nautical-mile (nmi) transit from Site 840 to Site 841 began at 0124 Universal Time Coordinated (UTC) 30 January, and took 6.6 hr to complete at an average speed of 9.4 knots. Site 841 lies upslope and to the west of the trench-slope break on the forearc of the Tonga platform. The site was chosen as a complement to Site 840, in order to determine the temporal and compositional variation of volcanic sediments transported from the Tonga–Tofua Arc to the arc forearc, to sample the forearc deep basement, and to investigate the tectonic history of the Tonga forearc.

Site Approach and Site Survey

Site 841 is situated in a water depth of 4810 m at the edge of the trench-slope break, on the west slope of the Tonga Trench. It is located at approximately 23°20.7′S, 175°17.9′W, about 150 km east of the Tofua Arc volcanic island chain, 155 km southeast of Ata, and 55 km west of the axis of the Tonga Trench.

After slowing to deploy two 80-in.^{3} water guns, a single-channel 60-element Teledyne streamer, and a Geometrics 801 proton precession magnetometer, the ship completed a 7.5 hr, 44 nmi site geophysical survey (Fig. 3B). On the third crossing of the site, a beacon was dropped at 1443 UTC on 30 January 1991. The ship then made a Williamson turn to return to the site and recover underway geophysical gear. As the ship was positioning at the site to begin coring operations, the beacon signal was lost. A backup beacon was subsequently deployed at 1605 UTC on the same day, marking the site (Figs. 3B and 4C).

Drilling and Logging Summary

Our original plan was to drill two adjacent holes at Site 841, with the principal objectives of (1) coring the entire forearc sequence and (2) coring at least 50 m of the underlying "basement," the character of which was unknown. Hole 841A was planned to be an APC/XCB/MDCB hole with which we hoped to core through much of the estimated 600- to 800-m-thick sediments at the site. It was hoped that the motor-driven core barrel (MDCB) would allow sampling of any hard lithologies that might be encountered in this section. Hole 841B was planned to be an rotary core barrel (RCB) hole that continued coring the sediments and the underlying basement as time permitted before logging.

Hole 841A

Hole 841A was spudded in at 0100 UTC 31 January 1991 at a position of 23°20.746′S, 175°17.871′W. A mudline core established the seafloor depth as 4821.0 m below the driller's datum. Eight cores were taken with the APC, to a depth of 71.7 mbsf, with a recovery of 61.8 m (86.2%; Table 1). A nonmagnetic drill collar was used to minimize the drill string magnetic overprint on the cores, and the multishot tool provided orientation for Cores 135-841A-4H to 135-841A-8H. Temperature measurements were made at 27.5, 46.5, and 65.5 mbsf using the water sampler temperature probe (WSTP) tool. The last five APC cores were recovered using only partial strokes of the APC core barrel, due to the unusual hardness of the formation. The APC core barrel became stuck during retrieval of Core 135-841A-8H, producing 130,000 lb of overpull. As a result, the core barrel was drilled over by the bit to allow recovery, and APC coring was terminated. Thirteen continuous cores of sediments (71.7 to 186.6 mbsf) were taken in stable hole conditions with the extended core barrel (XCB), with poor recovery (8.45 m recovered, or 7.4% recovered). After recovering Core 135-841A-14X, it was discovered that the soft formation XCB bit had failed, requiring a switch to six-bladed, diamond-impregnated hard formation XCB bits. After recovering Core 135-841A-20X, it was discovered that one of our last two hard formation XCB bits had failed as well, requiring a change to the RCB after the cutting of one more core (Core 135-841A-21X).

Hole 841B

The ship was moved 20 m to the north, and Hole 841B was spudded at 1040 UTC 2 February 1991 at a position of 20°20.741′S, 175°17.872′W. A 9-7/8-in. RCB bottom-hole assembly was used. The seafloor was estimated to be at 4821.0 meters below rig floor (mbrf), and the hole was washed from 0.0–170.0 mbsf, recovering one wash core. Cores 135-841B-2R to 135-841B-70R were taken from 170.0–834.2 mbsf with the RCB, with 664.4 m cored and 181.4 m recovered (recovery of 27.3%). After the recovery of vitric siltstone in Core 135-841B-14R, the core barrel became plugged, causing the drill string water circulation pressure to increase substantially. After twice running the bit deplugger, core recovery was generally fair to good, but recovery in rhyolitic tuff, rhyolitic welded tuff, and rhyolitic lava below about 610 mbsf was often poor. Mud was circulated downhole to 700 mbsf every third or fourth core, and below that after every core, because of unstable hole conditions. At 834.2 mbsf, hole conditions became too bad to continue coring, and a large amount of mud was circulated before conditioning the hole for logging. While recovering Core 135-841B-71M (this core representing rubble at the bottom of the hole with no advance), the drill string stuck. After several cycles of pumping mud and jarring of the drill string with the Hydrolex "jars," the pipe became free. The pipe became stuck again at 224 mbsf; after unsuccessful attempts to free the pipe using the jars, the bit was released with the mechanical bit release (MBR) and the pipe was dragged uphole to 50 mbsf where it finally came free. The poor, deteriorating hole conditions and the likely presence of both the bit and a portion of the MBR at 224 mbsf prevented use of the hole for logging.

Hole 841C

The scientific value in logging the sequence was deemed sufficient to drill a third hole dedicated to logging. The ship was moved 20 m to the north (23°20.720′S, 175°17.879′W), and Hole 841C was spudded in at 1525 UTC 10 January, with the seafloor estimated at 4821 m below the drillers datum. A 9-7/8-in. hole was then drilled from 0 to 775.0 mbsf, at which point drilling was stopped because of poor hole conditions. An attempt was made to drop the drill bit with the MBR, but it had apparently been damaged earlier when attempting to ream through a bridge in the hole at 657 mbsf. As a result of the MBR failure, a free fall funnel (FFF) was dropped to allow reentry into the hole for logging purposes after the bit had been removed from the drill string on the rig floor. After reentering the FFF, the reentry/logging bit was positioned at 78.1 mbsf; to save time, no conditioning of the hole was done.

Table 1. Coring summary, Site 841.

Core no.	Date (1991)	Time (UTC)	Depth (mbsf)	Cored (m)	Recovered (m)	Recovery (%)	Age
135-841A-							
1H	21 January	0125	0.0–8.5	8.5	8.57	101.0	?middle Pleistocene
2H	21 January	0225	8.5–18.0	9.5	9.83	103.0	Barren
3H	21 January	0320	18.0–27.5	9.5	10.08	106.1	Barren
4H	21 January	0550	27.5–37.0	9.5	9.18	96.6	Barren
5H	21 January	0655	37.0–46.5	9.5	8.89	93.6	Barren
6H	21 January	1050	46.5–56.0	9.5	8.40	88.4	Barren
7H	21 January	1240	56.0–65.5	9.5	0.61	6.4	upper Miocene
8H	21 January	1700	65.5–71.7	6.2	6.24	100.0	upper Miocene
9X	21 January	1940	71.7–81.4	9.7	1.00	10.3	upper Miocene
10X	21 January	2200	81.4–91.0	9.6	0.09	0.9	upper Miocene
11X	31 January	2355	91.0–100.7	9.7	1.44	14.8	upper Miocene
12X	1 February	0120	100.7–110.3	9.6	0.12	1.3	Barren
13X	1 February	0255	110.3–120.0	9.7	0.31	3.2	Barren
14X	1 February	0515	120.0–129.6	9.6	1.17	12.2	Undefined
15X	1 February	0655	129.6–139.3	9.7	0.82	8.5	upper Miocene
16X	1 February	0850	139.3–148.9	9.6	0.37	3.9	upper Miocene
17X	1 February	1100	148.9–153.9	5.0	1.18	23.6	upper Miocene
18X	1 February	1300	153.9–159.1	5.2	0.38	7.3	upper Miocene
19X	1 February	1500	159.1–168.7	9.6	0.66	6.9	upper Miocene–lower Pliocene
20X	1 February	1715	168.7–176.9	8.2	0.07	0.9	upper Miocene
21X	1 February	1915	176.9–186.6	9.7	0.84	8.7	Barren
Coring totals				186.6	70.25	37.6	
135-841B-							
1W	2 February	1615	0.0–169.8	169.8	2.84	(wash core)	
2R	2 February	1755	169.8–179.4	9.6	4.01	41.8	upper Miocene
3R	2 February	1935	179.4–189.1	9.7	1.84	18.9	Barren
4R	2 February	2125	189.1–198.7	9.6	2.53	26.3	upper Miocene
5R	2 February	2325	198.7–208.4	9.7	3.31	34.1	upper Miocene
6R	3 February	0105	208.4–218.1	9.7	2.41	24.8	upper Miocene
7R	3 February	0250	218.1–227.7	9.6	2.40	25.0	upper Miocene
8R	3 February	0425	227.7–237.4	9.7	1.49	15.3	upper Miocene
9R	3 February	0610	237.4–247.0	9.6	2.57	26.8	upper Miocene
10R	3 February	0755	247.0–256.7	9.7	1.36	14.0	upper Miocene
11R	3 February	0930	256.7–266.3	9.6	2.17	22.6	upper Miocene
12R	3 February	1115	266.3–275.6	9.3	3.31	35.6	upper Miocene
13R	3 February	1340	275.6–285.2	9.6	5.80	60.4	Miocene
14R	3 February	1605	285.2–294.9	9.7	0.08	0.8	upper Miocene
15R	3 February	2140	294.9–304.6	9.7	6.08	62.7	Miocene
16R	3 February	2335	304.6–313.8	9.2	8.33	90.5	Miocene
17R	4 February	0115	313.8–323.5	9.7	5.64	58.1	middle Miocene–upper Pliocene
18R	4 February	0300	323.5–333.2	9.7	3.06	31.5	Barren
19R	4 February	0450	333.2–342.5	9.3	3.99	42.9	upper Miocene–lower Pliocene
20R	4 February	0645	342.5–352.1	9.6	4.08	42.5	Barren
21R	4 February	0825	352.1–361.4	9.3	4.69	50.4	?late Miocene (reworked)
22R	4 February	1020	361.4–371.1	9.7	4.42	45.5	Miocene
23R	4 February	1205	371.1–380.7	9.6	4.83	50.3	middle Miocene–Quaternary
24R	4 February	1425	380.7–390.4	9.7	1.81	18.6	Barren
25R	4 February	1645	390.4–400.1	9.7	3.45	35.5	
26R	4 February	1845	400.1–409.7	9.6	2.39	24.9	Barren
27R	4 February	2045	409.7–419.4	9.7	0.55	5.7	Barren
28R	4 February	2305	419.4–429.1	9.7	1.93	19.9	middle Miocene–lower Pliocene
29R	5 February	0100	429.1–438.8	9.7	2.93	30.2	middle Miocene–lower Pliocene
30R	5 February	0250	438.8–448.5	9.7	2.03	20.9	Barren
31R	5 February	0445	448.5–458.1	9.6	0.16	1.7	Barren
32R	5 February	0640	458.1–467.8	9.7	2.31	23.8	middle Miocene
33R	5 February	0910	467.8–477.5	9.7	4.46	46.0	middle Miocene
34R	5 February	1115	477.5–487.1	9.6	3.10	32.3	middle Miocene
35R	5 February	1410	487.1–496.8	9.7	4.82	49.7	middle Miocene
36R	5 February	1655	496.8–506.4	9.6	4.47	46.5	middle Miocene
37R	5 February	1940	506.4–516.1	9.7	5.73	59.1	middle Miocene
38R	5 February	2215	516.1–525.7	9.6	5.31	55.3	Miocene
39R	6 February	0040	525.7–535.3	9.6	3.37	35.1	middle Miocene
40R	6 February	0240	535.3–545.0	9.7	5.42	55.9	middle Miocene
41R	6 February	0435	545.0–554.3	9.3	4.80	51.6	lower Oligocene
42R	6 February	0700	554.3–564.0	9.7	6.27	64.6	lower Oligocene
43R	6 February	0855	564.0–573.6	9.6	1.99	20.7	lower Oligocene
44R	6 February	1050	573.6–583.3	9.7	2.29	23.6	upper Eocene
45R	6 February	1415	583.3–592.9	9.6	1.80	18.7	upper Eocene
46R	6 February	1705	592.9–602.6	9.7	3.60	37.1	Undefined
47R	6 February	1945	602.6–612.3	9.7	3.20	33.0	Barren)

Table 1 (continued).

Core no.	Date (1991)	Time (UTC)	Depth (mbsf)	Cored (m)	Recovered (m)	Recovery (%)	Age
135-841B- (cont.)							
48R	6 February	2140	612.3–621.9	9.6	0.56	5.8	Barren
49R	6 February	2325	621.9–631.6	9.7	0.30	3.1	
50R	7 February	0130	631.6–641.3	9.7	0.28	2.9	Barren
51R	7 February	0330	641.3–650.9	9.6	4.52	47.1	Barren
52R	7 February	0530	650.9–660.6	9.7	3.41	35.1	
53R	7 February	0735	660.6–670.2	9.6	2.54	26.4	Barren
54R	7 February	0945	670.2–679.8	9.6	4.70	48.9	Barren
55R	7 February	1150	679.8–689.4	9.6	0.30	3.1	
56R	7 February	1420	689.4–699.1	9.7	0.48	5.0	
57R	7 February	1650	699.1–708.8	9.7	0.72	7.4	
58R	7 February	1905	708.8–718.1	9.3	0.40	4.3	
59R	7 February	2140	718.1–727.8	9.7	0.25	2.6	
60R	8 February	0020	727.8–737.5	9.7	0.15	1.5	Barren
61R	8 February	0250	737.5–747.2	9.7	0.22	2.3	Barren
62R	8 February	0505	747.2–756.9	9.7	2.94	30.3	Barren
63R	8 February	0800	756.9–766.5	9.6	1.79	18.6	Barren
64R	8 February	1040	766.5–776.2	9.7	0.07	0.7	
65R	8 February	1355	776.2–785.9	9.7	0.39	4.0	Barren
66R	8 February	1650	785.9–795.5	9.6	0.27	2.8	
67R	8 February	1915	795.5–805.2	9.7	0.22	2.3	
68R	8 February	2225	805.2–814.9	9.7	0.16	1.7	
69R	9 February	0235	814.9–824.6	9.7	0.16	1.7	Barren
70R	9 February	0540	824.6–834.2	9.6	0.03	0.3	
71M	9 February	1125	0.0–834.2	0	1.09	NA	
Coring totals				221.9	182.54	82.3	
Washing totals				169.8	2.84		
Combined totals				391.7	185.38		

Logs were then run as follows:

Run 1: formation microscanner (FMS)/gamma ray. During this logging run, the Schlumberger logging computer crashed twice after calibrating the FMS, but the third calibration was successful. The tool failed during its initial deployment as a result of a short in the logging head. After replacement of the logging head, a successful logging run was completed. The log found bottom 166.2 m above the driller's total depth and required 6.92 hr to run.

Run 2: "Quad combo"—induction/density/sonic/caliper/gamma ray. A Schlumberger computer malfunction required 1.75 hr to correct at the beginning of the logging run. The log found bottom 213.5 m above the driller's total depth and required 5.53 hr to run.

After this second logging run, logging was terminated because of time constraints. The hole was left full of seawater, and the reentry/logging bit cleared the seafloor at 1550 UTC on 14 February 1991 and reached the rig floor at 0200 UTC on 15 February 1991. The sea voyage to Pago Pago then began.

LITHOSTRATIGRAPHY

The lithostratigraphic summary (Fig. 5) is a synthesis of Holes 841A and 841B. Sediment recovery was approximately 76% for the interval 0–71.7 mbsf, but thereafter decreased to 7% between 71.7 and 186.6 mbsf. In Hole 841B the recovery was 27.3% from the interval 186.6–834.2 mbsf. The sedimentary sequence at Site 841 was divided into five lithologic units based on differences in texture, structure, and composition (Fig. 5). The generalized lithology for each unit is shown in Table 2.

Unit I

Interval: Cores 135-841A-1H through 135-841A-6H
Depth: 0.0–56.0 mbsf.
Age: middle Pleistocene to Pliocene (?)
Thickness: 56.0 m

Unit I is composed of a sequence of structureless clays, with very thin- to medium-bedded vitric sand, vitric silt, and coarse and fine ash interbeds. The age of Unit I, based on biostratigraphic and paleomagnetic data, is middle Pleistocene to Pliocene (?). The average sedimentation rate for the unit is 11 mm/k.y. (see "Sediment Accumulation Rates" section, this chapter).

The clay from 0.0 to 17.5 mbsf is grayish brown to greenish gray in color and consists mainly of clay minerals and clay-sized volcanic glass fragments (75–85 vol%), large volcanic glass shards (20–15 vol%), and up to 5 vol% nannofossils. From 17.5 to 54.9 mbsf, the clay is light yellowish brown and greenish gray to dark greenish gray and comprises 95 vol% clay-sized particles, with the remainder consisting of volcanic glass, feldspar, and accessory minerals (mainly pyroxenes). The clay appears homogeneous over long intervals and contains scattered, angular to rounded, altered pumice and claystone clasts (up to 2.5 cm across). Faintly mottled and planar laminated intervals are common.

Very thin- to medium-bedded (1–11 cm thick), normally graded vitric sands and silts occur within the clay. The sands are light to dark gray, while the silts are very dark grayish brown to dark gray. These beds show sharp, sometimes scoured basal contacts and gradational upper contacts. Internally the silts and sands show normal grading. Some silt layers contain planar laminae and burrows. The silts and sands consist of 70–95 vol% volcanic glass, up to 10% plagioclase, with minor amounts of clay, pyroxenes, and opaques. The sand layers typically contain greater concentrations of accessory minerals than adjacent silt intervals.

Fine and coarse-grained pyroclastic ash layers may have either sharp or diffuse upper and lower boundaries and commonly show normal grading. The ashes are olive gray to dark greenish gray, or brown to black. The lighter colored layers contain 80–90 vol% light brown glass, with feldspar and clay making up the remainder. The darker colored ash intervals comprise 75 vol% volcanic

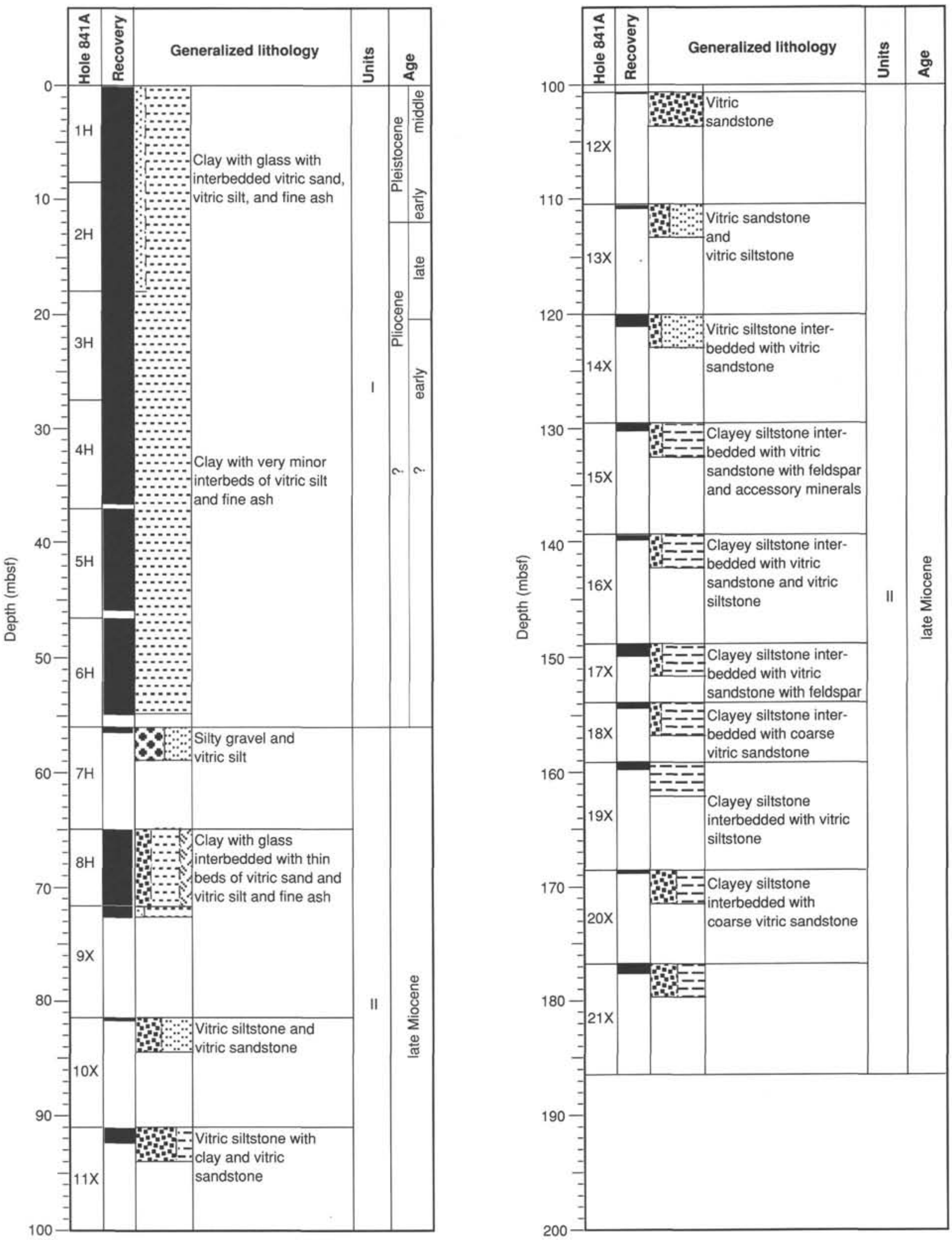

Figure 5. Lithologic summary diagram showing recovered lithologies from Hole 841A and 841B. Note that in cores with low recovery the generalized lithology column has been expanded vertically to clearly show the lithology present. The true recovery is correctly displayed in the recovery column.

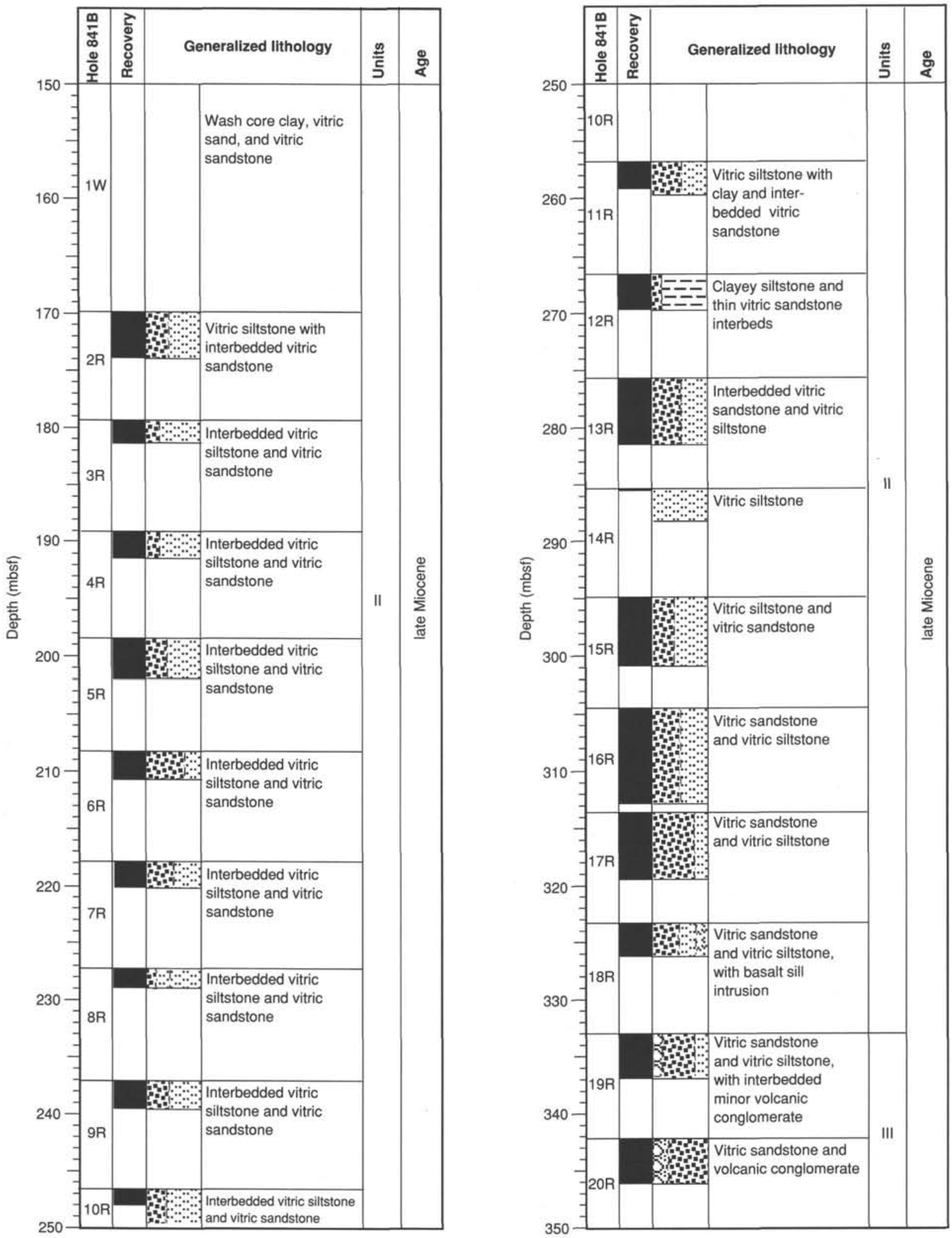

Figure 5 (continued).

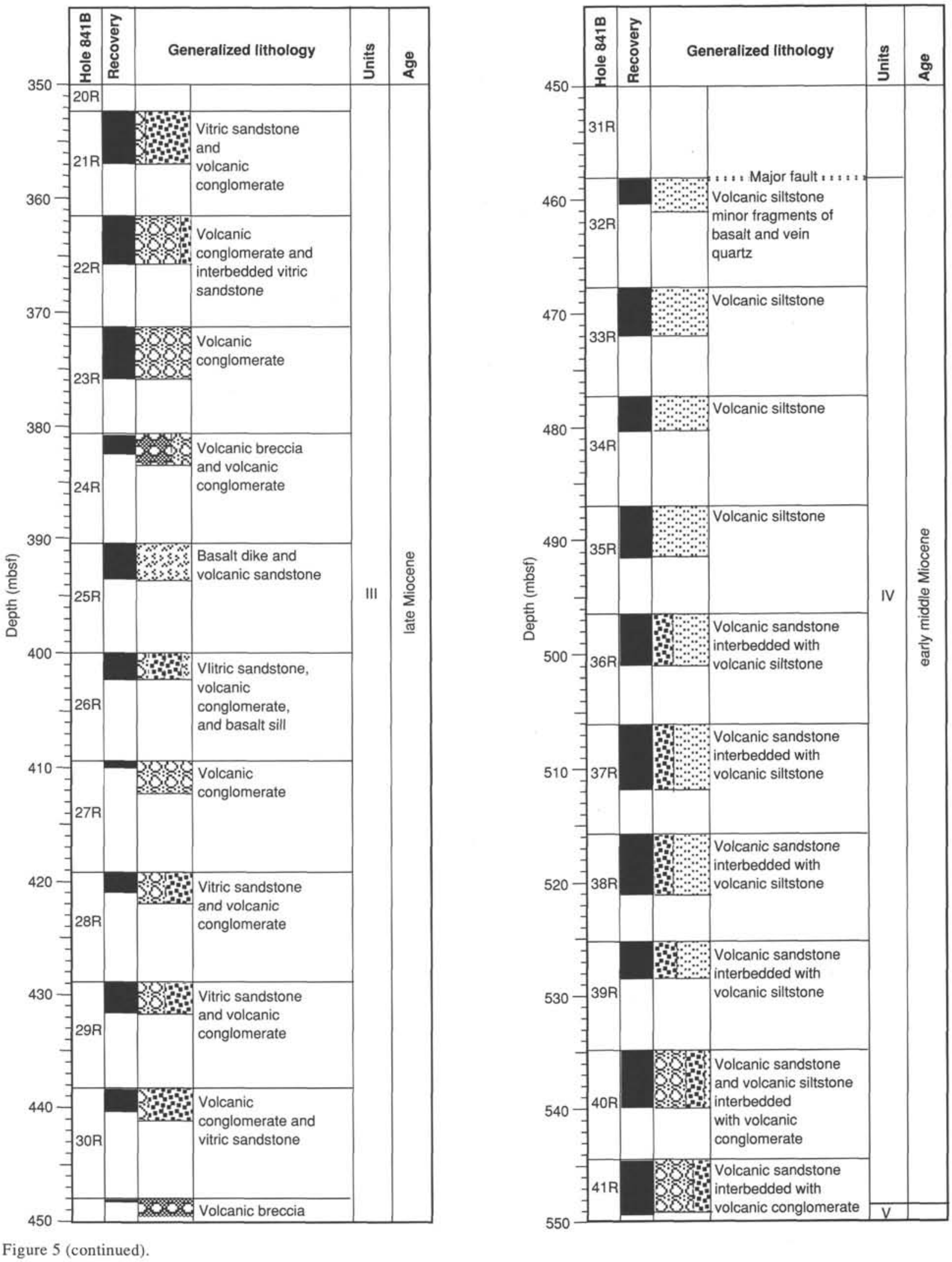

Figure 5 (continued).

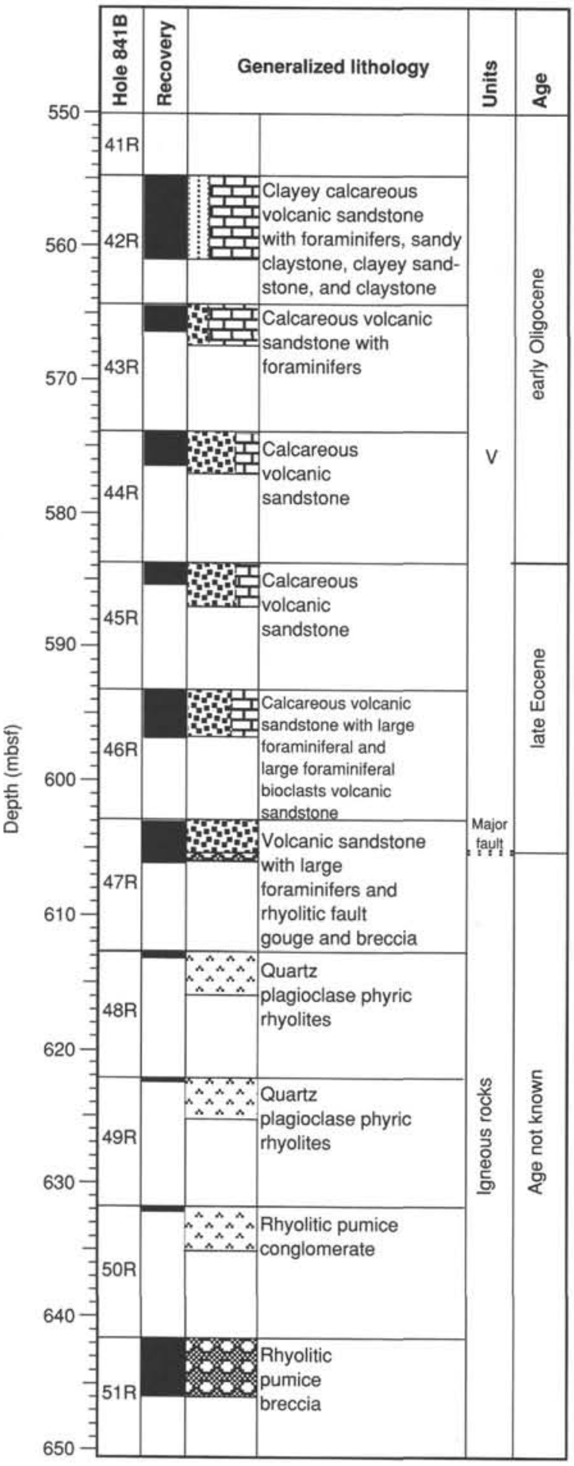

Figure 5 (continued).

glass, 10 vol% clay-sized particles, 10 vol% feldspar, and up to 5 vol% accessory minerals, mainly pyroxenes. Ash intervals are invariably thin to very thin bedded.

Planar laminated, normally graded layers may represent thin volcaniclastic turbidites, while thin, typically dark-colored volcaniclastic layers are interpreted to be the result of pyroclastic fallout.

Unit II

Interval: Cores 135-841A-7H through 135-841A-21X and Cores 135-841B-2R through 135-841B-18R
Depth: 56.0–186.6 mbsf and 169.8–333.2 mbsf
Age: late Miocene
Thickness: 277.2 m

The uppermost part of the Unit II is composed of clay with glass, vitric silt, and vitric sand. Clayey siltstone, vitric siltstone, and vitric sandstone increase in their abundance downward through the unit. The age of Unit II, based on paleomagnetic and biostratigraphic data, is late Miocene. The average sedimentation rate is estimated to be 53 mm/k.y. in the uppermost part of the unit and 142 mm/k.y. in the lower part of the unit (see "Sediment Accumulation Rates" section, this chapter).

The upper boundary of Unit II shows a downward transition from dark greenish-gray to dark gray clay (in Core 135-841A-6H, above the boundary) to polymict, dark greenish gray, poorly sorted silty gravel, and structureless, vitric silt with feldspar (in Core 135-841A-7H, below the boundary). In Cores 135-841A-8H and 135-841A-9X (65.5–81.4 mbsf) the predominant lithology is dark greenish gray and dark gray structureless clay with glass shards, which grades down into very dark grayish brown vitric clay. Individual clay beds are up to 50 cm thick. Structureless beds of black, dark gray and dark greenish gray vitric silt, vitric sand, and fine ash are interbedded with the clays. These vary in thickness from 2 to 10 cm and are normally graded. A thick bed of gray vitric sandy silt occurs in Section 135-841A-8H-3, 0–55 cm. This has a sharp base, and is faintly planar laminated in its lower part.

The sedimentary sequence in Cores 135-841A-10X through 135-841A-21X (81.4–186.6 mbsf) consists of interbedded black, dark greenish gray and dark gray vitric siltstone, clay, clayey siltstone, vitric siltstone, and vitric sandstone. Recovery from this interval was low (<7%), with a large proportion of the recovered material present as drilling breccia. The vitric sandstones usually rest on sharp, planar surfaces and are normally graded. Many of these beds grade up into vitric siltstone and are frequently mottled because of bioturbation in their upper parts. Vitric siltstones with clay, clayey siltstones, and vitric siltstones are all relatively structureless but some bioturbated intervals occur. Some beds have sharp basal contacts, show planar lamination in their lower parts, and are normally graded throughout. The basal sediment layer of some siltstones and sandstones comprises a vitric sand with feldspar.

The sedimentary sequence recovered in Cores 135-841B-2R through 135-841B-18R (169.8–333.2 mbsf) consists of interbedded, dark grayish green, very dark gray and dark gray vitric sandstones and vitric siltstones. The volume percentage of sandstone increases downward through the unit, from 40% to approximately 80% of the sequence. The sandstones also become coarser grained down sequence. Sandstone and siltstone beds increase in thickness downhole.

The vitric sandstone beds in Unit II range from a few centimeters up to 122 cm in thickness (Core 135-841-17R). The sandstones have planar or undulating basal contacts and show a variety of sedimentary structures. The lower part of each interval is often structureless or normally graded. This is overlain by a planar laminated or planar stratified interval followed by wedge-planar laminated, wavy laminated, lenticular laminated, trough cross-laminated, or cross-stratified intervals (Fig. 6). Convoluted laminae are relatively common in the cross-laminated and cross-stratified sandstones. Load-casts with flame structures and ball and pillow structures occur locally (Fig. 7). Bioturbation occurs in the upper parts of some of the thinner sandstone beds. Only a few of the sandstone beds contain the entire range of sedimentary structures described above.

Table 2. Lithologic units defined for Site 841.

Depth (mbsf)	Lithologic unit	Lithologies present	Age
0.0 to 56.0	I	Clay with minor vitric sand, vitric silt, and fine ash	middle Pleistocene to Pliocene(?)
56.0 to 333.2	II	Vitric siltstone, vitric sandstone, fine ash, and clay with glass	Pliocene(?) to late Miocene
333.2 to 458.5	III	Volcanic conglomerates/breccias and vitric sandstones	late Miocene
458.5 to 549.1	IV	Volcanic siltstone, sandstone, and conglomerates	early middle Miocene
549.1 to 605.0	V	Calcareous volcanic sandstone, claystone, calcareous volcanic sandstone with foraminifers, and large foraminifer bioclast volcanic sandstone	early Oligocene to late Eocene

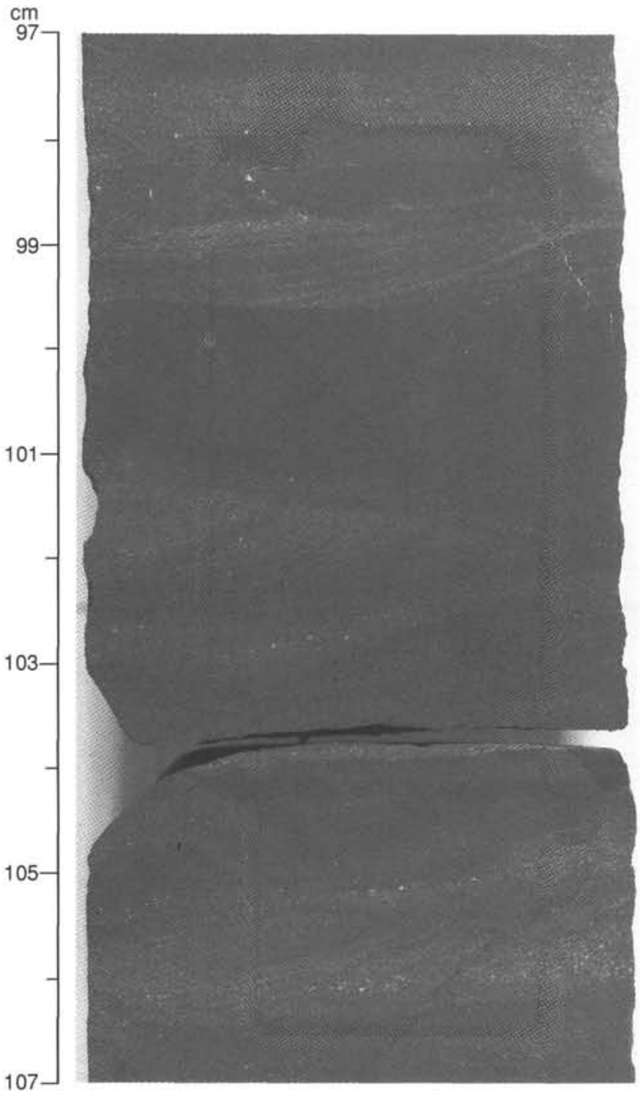

Figure 6. Vitric siltstone showing trough cross-lamination, trough cross-stratification, and planar lamination in Unit II, Section 135-841B-16R-2, 97–107 cm.

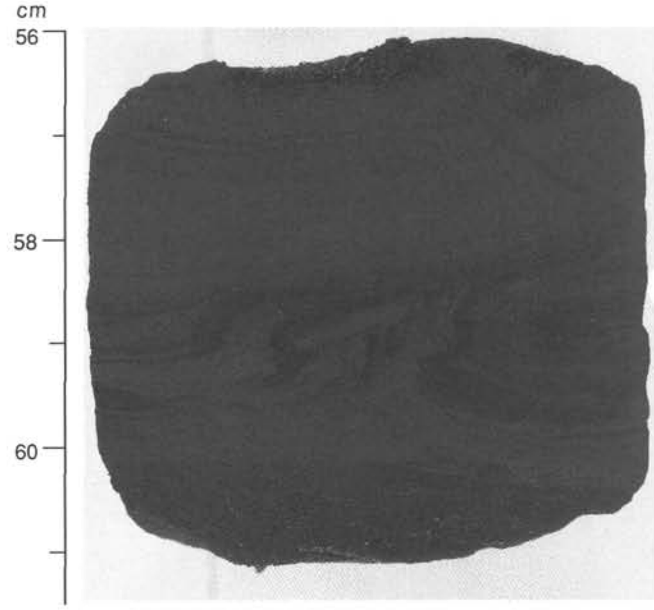

Figure 7. Convoluted bedding in a laminated sequence of vitric sandstone and siltstone (Unit II). Note flame and ball and pillow structures, Section 135-841B-6R-1, 57–61 cm.

Vitric sandstone is commonly overlain by vitric siltstone, which is either structureless or laminated, and is usually normally graded. Bioturbation is relatively common in siltstone beds. In addition, vitric siltstone appears as beds with sharp, planar, or undulating lower boundaries. These frequently show sedimentary structures similar to sandstone beds, with which they are interbedded. The thickness of individual volcanic siltstone beds varies from 1 to 90 cm, with bed thicknesses increasing downsequence.

The sediments and sedimentary rocks of Unit II are interpreted as a sequence of turbidites. The upward thinning and fining of individual turbidites throughout the units, and the increasing clay content of the deposits, may suggest an upward change from proximal to more distal deposition with an increase in water depth.

Unit III

Interval: Cores 135-841B-19R through 135-841B-31R
Depth: 333.26–458.1 mbsf
Age: late Miocene
Thickness: 124.9 m

Unit III is dated as late Miocene, based on biostratigraphic and paleomagnetic data. Recovery of the unit was variable, ranging from 5% to 50%, and is distinguished from Unit II by the presence of volcanic conglomerate interbedded within vitric siltstone and sandstones. Average sedimentation rates are calculated to be 142 mm/k.y. (see "Sediment Accumulation Rates" section, this chapter). The lower part of this unit is a 16-cm-thick breccia (in Core

135-841-31R) interpreted as a fault breccia. The top half of the unit fines upward from Core 135-841B-24R to 135-841B-19R. It is composed of coarse volcanic conglomerate and breccia. The conglomerate forms up to 24-cm-thick beds within a sequence of predominantly vitric sandstones and siltstones. Below Core 135-841B-24R the proportion of sandstone increases.

The top of the unit in Core 135-841B-19R (333.2–342.5 mbsf) is characterized by massive, dark grayish green, coarse-grained sandstone with thin interbeds of vitric siltstone. Very thick-bedded (up to 167 cm) vitric sandstones are normally graded and typically have 4- to 5-cm-thick conglomeratic layers at their base. The basal contacts of these beds are sharp and scoured. Sedimentary structures are rare, although planar laminae and, more rarely, planar cross-lamination occurs, especially toward the bases of sandstone beds. Microfaults are common throughout the sequence.

The volcanic conglomerates are poorly sorted, with granules and clasts ranging up to 1 cm in diameter. Individual clasts are subrounded to rounded and are supported by a matrix of vitric sandstone. A similar sedimentary sequence dominated by normally graded, massive sandstones was recovered in Cores 135-841B-20R to 135-841B-21R (342.5–361.4 mbsf). In Section 135-841B-20R-2 a reversely graded vitric sandstone coarsens upward into structureless, dark grayish green conglomerate. In Section 135-841B-21R-1 a volcanic conglomerate containing intraformational claystone fragments up to 15 cm across occurs. The matrix consists of angular to rounded grains of green and black sand. Thick-bedded vitric sandstones in Sections 135-841B-21R-2 to 135-841B-21R-CC show extensive wedge-planar laminae, planar cross-laminae, and planar laminae. Individual grains of feldspar, pyroxenes, opaques, and glass occur within the sandstone, as well as mudclasts up to 4 cm across.

Cores 135-841B-22R to 135-841B-24R (361.4–390.4 mbsf) comprise a sequence dominated by structureless volcanic conglomerate, with two interbeds, 61 and 16 cm thick, of vitric sandstone (in Section 135-841B-22R-3). These coarsen downward into conglomerates near their bases and contain planar cross-laminae. In Section 135-841B-23R-2 the conglomerate shows both normal and reverse grading. Individual clasts are up to 4.5 cm across, with the largest consisting of altered mafic lava. Altered pumice and greenish gray claystone clasts are found throughout the bed.

In Core 135-841B-25R and Section 135-841B-26R-1, 0–11 cm (390.4–400.2 mbsf), Unit III is intruded by a basaltic dike. Below this intrusion the unit comprises a series of poorly sorted, normally graded vitric sandstones. Planar laminae are found at the base of the sandstones, and in Section 135-841B-26R-2 three clasts of altered red basalt up to 12 mm across are present. Recovery in the lower half of Unit III varies from 5% to 30%; however, the recovered material indicates a sequence characterized by thick-bedded, normally graded volcanic conglomerates and vitric sandstones. In Sections 135-841B-28R-1, 135-841B-29R-1, and 135-841B-30R-1 vitric sandstones coarsen upward into massive conglomerates. This part of the unit is cut by microfaults and fractures, filled by silica and zeolites. The sandstones have few internal structures. In Sections 135-841B-29R-1 and 135-841B-29R-2 sandstones and conglomerates are found as a series of interbeds 2–9 cm thick. The deposits of Unit III are interpreted as proximal turbidites.

Unit IV

Interval: Core 135-841B-31R through Section 135-841B-41R-3, 113 cm
Depth: 458.1–549.1 mbsf
Age: early middle Miocene
Thickness: 91.0 m

Unit IV is composed of a sequence of black to dark gray and dark greenish gray volcanic siltstones, volcanic sandstones, and volcanic conglomerates. The unit shows an overall fining-upward trend with volcanic siltstone dominating the sequence in the upper part of the unit. Volcanic conglomerate is found only in the lowermost two cores. The age of Unit IV, based on paleomagnetic and biostratigraphic data, is early middle Miocene. The average sedimentation rate is estimated to be 160 mm/k.y. between 458.1 and 504 mbsf and 35 mm/k.y. between 504 and 549.1 mbsf (see "Sediment Accumulation Rates" section, this chapter).

The boundary between Units III and IV is marked by a change in lithology downward from vitric sandstones and volcanic conglomerates in Core 135-841B- 30R to volcanic siltstones in Core 135-841B-31R. At the boundary between the two units, in Core 135-841B-31R and in Section 135-841B-32R-1, 0–36 cm, there is a zone of dark gray to black volcanic breccia. This breccia consists of fragments of altered volcanic rocks, volcaniclastic sandstones, and siltstones and fragments of vein quartz. The boundary between Units III and IV is interpreted as a fault zone with associated fault breccia. The lower boundary of Unit IV is a major unconformity, spanning approximately 13 m.y. from the early Oligocene to the early middle Miocene (see "Biostratigraphy" section, this chapter).

Volcanic siltstone is the main lithology of the upper parts of Unit IV, and in Cores 135-841B-32R through 135-841B-35R (458.1–496.8 mbsf) it makes up almost 100% of the recovered sediments. In Cores 135-841B-36R through 135-841B-39R (496.8–535.3 mbsf) volcanic siltstone constitutes 60%–70%, with volcanic sandstone making up the remainder. The volcanic siltstone is usually finely planar laminated, wedge-planar laminated, and trough cross-laminated, with white to light gray laminae standing out against a background of black to gray siltstone (Figs. 8 and 9). Wavy lamination and trough cross-stratification is present within a few intervals. Tectonic deformation and soft-sediment deformation occur throughout the unit. In the upper part of the sequence, volcanic siltstone often occurs as normally graded beds, 2–15 cm thick, with planar basal surfaces. Mottling is rare. Lower down in the sequence normally graded beds up to 60 cm in thickness occur. These are planar laminated in their lower part and are overlain by trough cross-stratified and structureless siltstones (e.g., Section 135-841B-35R-3).

The volcanic sandstones in the lower part of the recovered sequence are usually dark greenish gray to dark grayish green. They are occasionally structureless, but they usually show planar laminated intervals overlain by trough cross-laminated and wedge-planar laminated sediments (Fig. 9). Individual beds of sandstone are up to 77 cm thick (in Sections 135-841B-38R-3 through 135-841B-38R-4) and may have planar or undulating, scoured lower contacts. Convoluted laminae are very common in the volcanic sandstones (e.g., Section 135-841B-37R-1, 30–40 cm). Volcanic sandstones are present both as normally graded beds and as laminated intervals interbedded with laminated siltstone (Fig. 10). Graded beds typically show scours, flame structures, and load casts at their basal contacts (Fig. 11).

Below Section 135-841B-40R-1, Unit IV consists of a series of very dark gray, medium-bedded, clast-supported, poorly sorted conglomerates and breccias, with thin interbeds of sandstone and siltstone. Bed thickness increases downsection, reaching a maximum of 102 cm in Core 135-841B-41R. Clasts within the conglomerates/breccias are angular to subrounded and range up to 3 cm in diameter (Fig. 12). They consist of very dark gray claystones, basalts, and very altered, mottled green lavas. The conglomerates/breccias are typically planar stratified, but toward the base of Core 135-841B-40R, wedge-planar stratification occurs. Clast imbrication and poorly developed cross-stratification also occur. The conglomerates/breccias have scoured basal contacts

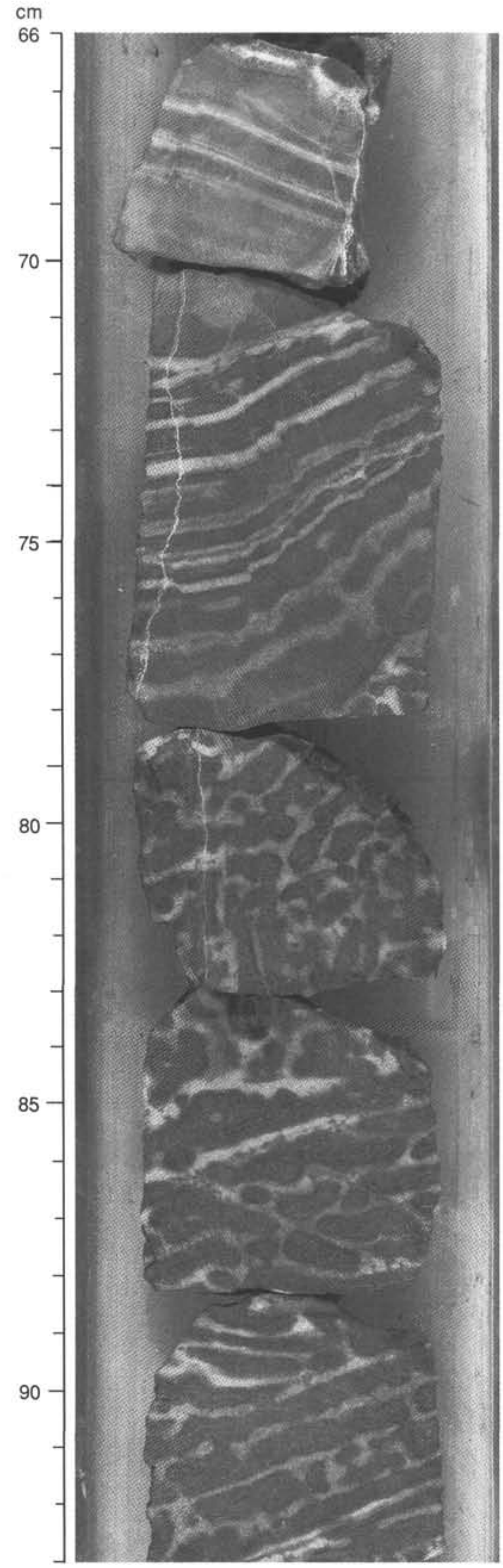

Figure 8. Volcanic siltstone of Unit IV showing a reticulate pattern, produced by leaching along fractures and coarser grained laminae, Section 135-841B-33R-1, 66–93 cm.

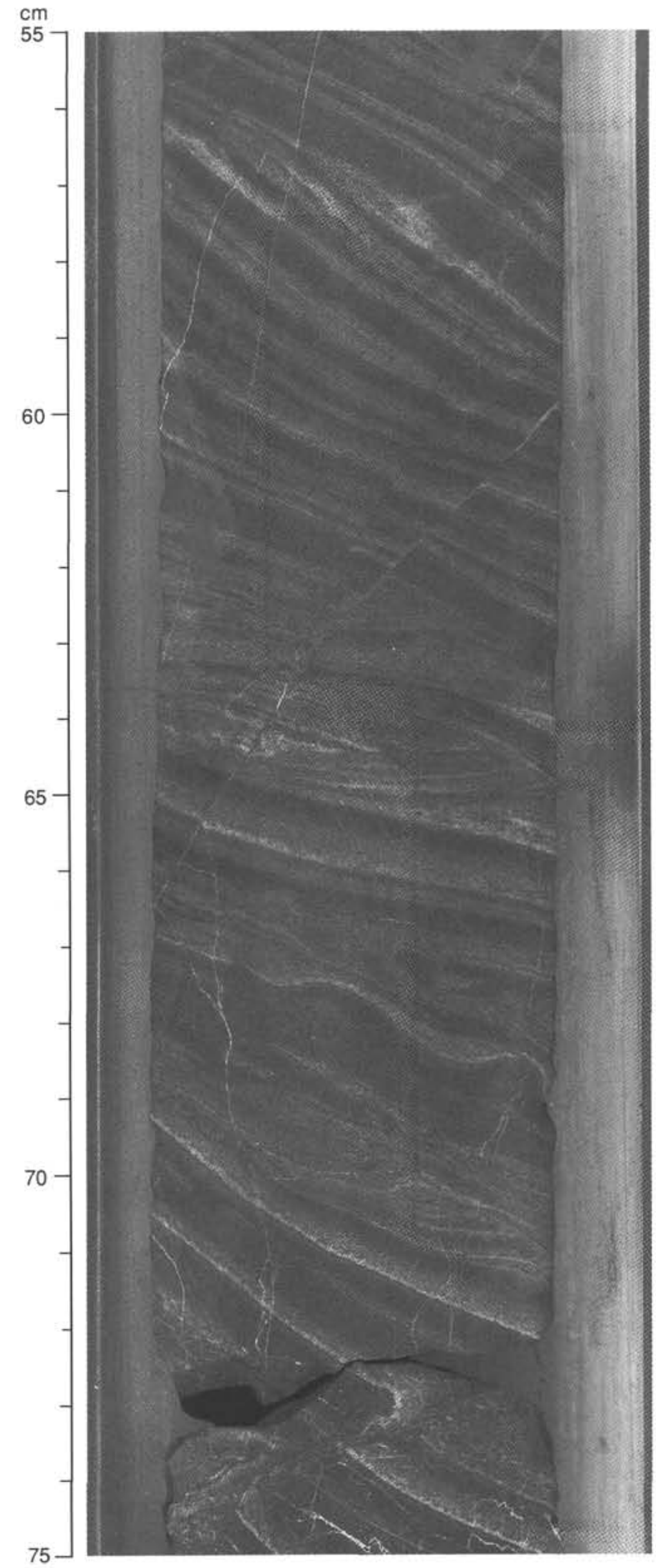

Figure 9. Volcanic siltstone in Unit IV showing wedge-planar laminae, trough cross-laminae, lenticular laminae, and convoluted laminae, Section 135-841B-37R-3, 55–75 cm. Note the normal fault in the central part and reverse fault in the lower part of the photograph.

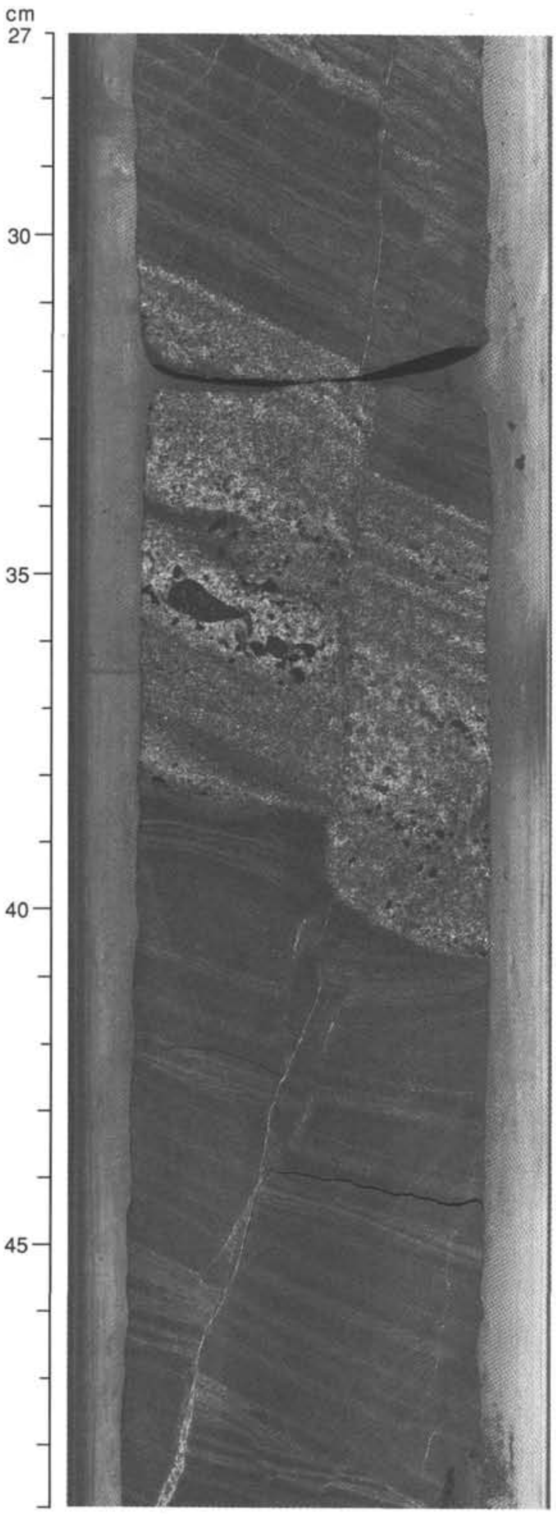

Figure 10. Vitric siltstone containing bed of volcanic sandstone (at 30–38 cm) in Unit IV, Section 135-841B-37R-3, 27–49 cm. Note high-angle fault, with normal sense of displacement with respect to the bedding.

and usually fine upward into sandstone. In Section 135-841B-40R-2 thin conglomerate beds are found as discrete, structureless intervals within sandstone. Microfaulting occurs throughout the unit.

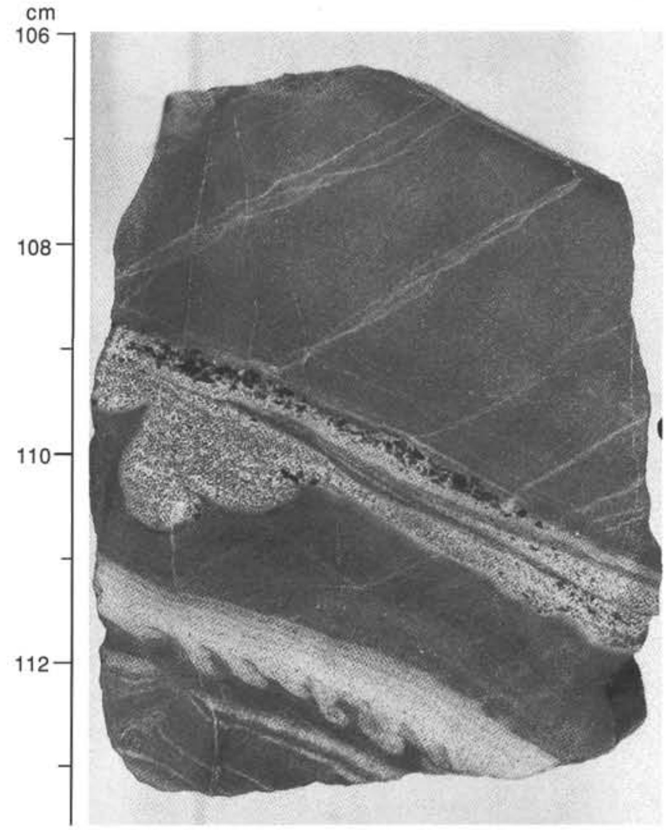

Figure 11. Load casts and flame structures in volcanic siltstone and sandstone of Unit IV, Section 135-841B-37R-3, 106–113.5 cm.

Tectonic Deformation

Unit IV forms the footwall to a major normal fault at 458 mbsf, and microfaults, offsetting lamination and bedding on a millimeter- to centimeter-scale, are common throughout the unit. Both normal and reverse faulting occur. These are discussed in detail in the "Structural Geology" section (this chapter).

Soft Sediment Deformation and Hydrothermal Alteration

Soft sediment deformation is common within the upper parts of Unit IV and in the coarser grained sediments in the lower part of the sequence. Soft sediment deformation is evident as flame structures, ball-and-pillow structures (e.g., in Section 134-841B-35R-2, 90–92 cm), load-casts (Fig. 11), and convoluted laminae. A characteristic reticulate pattern is present within the volcaniclastic siltstones of Unit IV and is especially prominent in Core 135-841B-33R (Fig. 8). The reticulate pattern is developed in siltstones with white to light gray laminae of planar and cross-laminated, coarse-grained silt or very fine-grained sand.

Hydrothermal fluids have probably circulated through these sediments, particularly along fractures, faults, and within coarser grained laminae where permeability is greatest, resulting in leaching and alteration of the sediment. These paler-colored, altered zones are typically 2–3 mm thick (Fig. 8; see "Structural Geology" section, this chapter).

Unit IV is interpreted as a series of turbidites possibly deposited on a submarine fan. Conglomerates and breccias in the lower part of the unit may be proximal gravity flow deposits, whereas turbidites higher in the sequence may have been deposited in a more distal position relative to the source area.

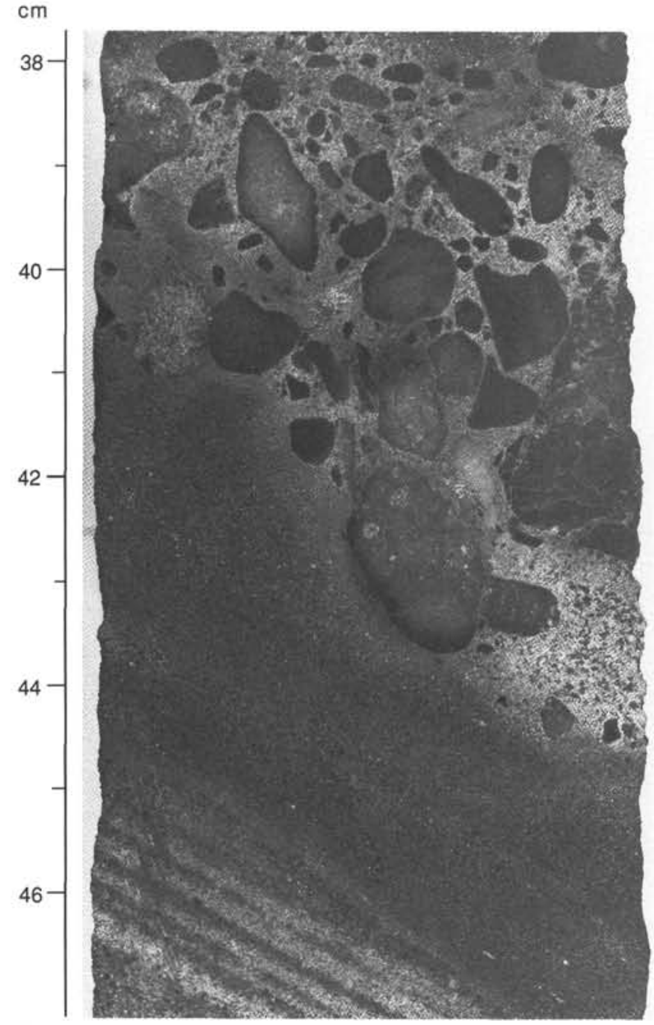

Figure 12. Coarse matrix-supported basaltic conglomerate/breccia in volcanic sandstone, Section 135-841B-40R-2, 37.7–47.2 cm.

Unit V

Interval: Sections 135-841B-41R-3, 113 cm, through 135-841B-47R-2, 90 cm Depth: 549.1–605.0 mbsf.
Age: early Oligocene to late Eocene
Thickness: 55.9 m

Unit V has an estimated sedimentation rate of 19 mm/k.y. (see "Sediment Accumulation Rates" section, this chapter). Total recovery was 18.35 m, representing approximately 37% of the stratigraphic section. The age of the unit ranges from late Eocene to early Oligocene, based on biostratigraphic and paleomagnetic data. In the uppermost part of Unit V there are beds of volcanic conglomerate (Sections 135-841B-41R-3, 113 cm, through 135-841B-42R-1, 42 cm, at 549.1-554.7 mbsf). Clayey calcareous volcanic sandstone with foraminifers is the main lithology in the upper part of the unit (in Sections 135-841B-42R, 42 cm, through 135-841B-42R-CC, at 554.7-564.0 mbsf). These sediments contain thin interbeds of sandy claystone, clayey sandstone, and claystone. Calcareous volcanic sandstone with foraminifers and calcareous volcanic sandstone are the dominant rock types in Cores 135-841B-43R through 135-841B-45R at 564.0–592.9 mbsf. In the lowermost part of Unit V (in Core 135-841B-46R through Section 135-841B-47R-2, 90 cm, at 592.9–605.0 mbsf), calcareous volcanic sandstone with large foraminifers and large foraminifer bioclast volcanic sandstone overlie a rhyolitic volcanic complex. This contains an interbedded series of rhyolitic lavas and pyroclastic sediments, including ignimbrites and welded tuffs (see "Igneous Petrology" section, this chapter).

Volcanic Conglomerate/Breccia

A reddish brown, matrix-supported volcanic conglomerate/breccia occurs in the uppermost part of Unit V (Sections 135-841B-41R-3, 113 cm, through 135-841B-42R-1, 42 cm, at 549.1–554.7 mbsf). This contains a polymict assemblage of brown, yellow, black, red, green, and white mafic rocks fragments, intraformational clasts of sedimentary rocks (mainly calcareous volcanic sandstone and claystone), and, possibly, silicic volcanic rocks. The clasts are up to 3 cm in diameter and are generally rounded to very angular. They are in a matrix of medium- to very coarse-grained reddish brown sandstone. The volcanic conglomerate/breccia is poorly sorted and contains very thin interbeds of volcanic sandstone. The volcanic conglomerates/breccias are extensively fractured, partly as a result of drilling brecciation, and are relatively strongly altered.

Clayey Calcareous Volcanic Sandstone with Foraminifers

This lithology is the dominant type in the upper part of Unit V (in Sections 135-841B-42R, 42 cm, through 135-841B-42R-CC, at 554.7–564.0 mbsf). The color of these sediments ranges from light gray or light pinkish gray to dark brown. The clayey calcareous volcanic sandstone with foraminifers contains very thin- to medium-bedded layers of dark red and reddish brown clayey sandstone, sandy claystone, and claystone. The clayey sandstones are generally medium- to coarse-grained and well-sorted, with subrounded grains of reddish or black mafic rock fragments and dark mafic crystals, including unaltered pyroxenes. These sandy interbeds are normally graded with sharp basal contacts and may be planar laminated. The interbedded sandy claystones and claystones are usually structureless. This sequence is heavily bioturbated and primary sedimentary structures and bedding are frequently absent because of reworking. The large influx of volcanic sand indicates proximity to an actively eroding volcanic center.

Calcareous Volcanic Sandstone and Calcareous Volcanic Sandstone with Foraminifers

Calcite-cemented, very dark gray, greenish gray or dark greenish gray calcareous volcanic sandstone and calcareous volcanic sandstone with foraminifers are the dominant sediments in the middle part of Unit V (Cores 135-841B-43R through 135-841B-45R, at 564.0–592.9 mbsf). These sediments are generally bioturbated, with common *Zoophycos* burrows, especially in Core 135-841B-45R. The volcanic sandstone is usually fine-grained and structureless; however, 1- to 8-cm-thick, normally graded, coarse- to fine-grained volcanic (mafic) sandstone layers occur. These contain abundant fresh pyroxene crystals. Some of these layers show load casts at their base.

Large Foraminifer Bioclast Volcanic Sandstone

This lithology was recovered only in Cores 135-841B-46R and 135-841B-47R and probably corresponds to the shallowest marine conditions present in Unit V. This lithology is characterized by an abundant benthic faunal assemblage, containing unbroken *Discocyclina* sp. tests (see "Biostratigraphy" section, this chapter; Fig. 13), indicating low-energy conditions and large (up to 4 cm), nearly complete, thin-walled bivalve shells. These are interpreted as representing shallow-water, normal marine salinity conditions at the time of deposition. Other common faunal constituents include red algae, and *Halimeda* sp. algae, indicating proximal, very shallow water depths.

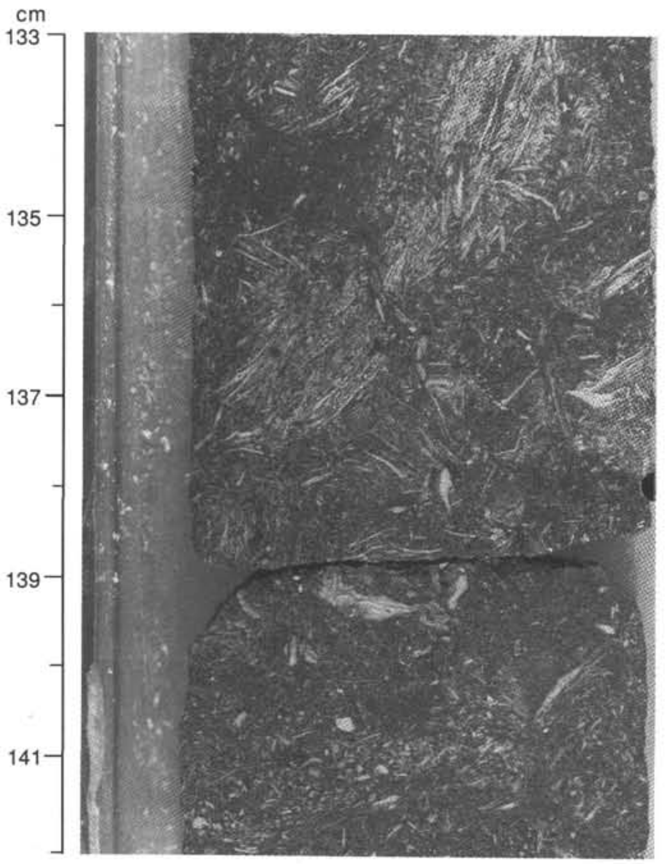

Figure 13. Calcareous volcanic sandstone with foraminifers, Section 135-841B-46R-2, 133–142 cm. Note the abundant large, unbroken *Discocyclina* sp. foraminifer tests present throughout the deposit.

The delicate nature of the *Discocyclina* sp. tests and the *Halimeda* sp. fragments preclude long transport histories. Proximity to an eroding volcanic terrain is suggested by the presence of angular quartz and feldspar fragments and by rounded grains of volcanic glass and ferromagnesian minerals within the sediment. The large foraminifer bioclast volcanic sandstone contains up to 48% $CaCO_3$.

Volcaniclastic Sedimentology

The sedimentary sequence at Site 841 is dominated by volcaniclastic deposits of early middle Miocene to late Miocene age, interpreted as turbidites. Previous volcaniclastic sedimentation was principally pyroclastic, with subaerial tuffs and ignimbrites intercalated with rhyolitic lava flows in the deepest levels of the sequence (see "Igneous Petrology" section, this chapter).

Low pelagic sedimentation rates and limited bioturbation have resulted in the preservation of abundant fallout tephras of middle Pleistocene to Pliocene age in the upper part of the sequence at Hole 841A (Unit I). More than 25 well-preserved coarse and fine ash layers, normally <5 cm thick, occur mainly in Cores 135-841A-1H to 135-841A-4H. They are interbedded within firm, slightly bioturbated clays, which often contain interspersed vitric shards in trace amounts. Also thin, distal turbidite sands occur interbedded with the hemipelagic clay. The number of epiclastic, normally graded beds is comparable to the number of pyroclastic beds. A significant component of the clay is clay-sized volcanic glass shards, locally constituting beds of almost 100% glass fragments.

In Unit V (early Oligocene to late Eocene) the volcaniclastic input is diluted by neritic carbonate material. For the remainder of the sequence recovered at Site 841 the sediments principally occur as normally graded beds, which form two major fining-upward cycles. The lower cycle, comprising Unit IV, is of early middle Miocene age, while the upper, comprising Units III, II and I, is of late Miocene age. These cycles are characterized by an upward reduction in grain sizes and thicknesses of individual beds. Figure 14 shows the variations in bed thickness plotted against depth for volcaniclastic beds in Hole 841A (0–186.5 mbsf). While beds 1–5 cm in thickness occur throughout the sequence, beds greater than 10 cm thick are generally restricted to the lower half of the sequence. It should be noted, however, that because of the relatively poor recovery in the lower part of Hole 841A compared to the good recovery in Cores 135-841A-1H through 135-841A-6H and 135-841A-8H, beds thicker than the recovered core, from this portion of the hole, are not represented in this chart.

Volcanic conglomerates/breccias in Units III and IV are generally structureless or planar stratified. These beds show sharp, scoured basal contacts and are normally graded.

Volcanic sandstones from all units show a variety of sedimentary structures indicative of high-energy current activity. Structureless, normally graded beds are very common, but planar laminae, cross-laminae, and wedge-planar laminae also occur throughout. Loaded and scoured bases, flame structures, soft sediment folds, and convoluted bedding testify to the rapid emplacement of volcanic sands and subsequent dewatering. We interpret these sediments as turbidite deposits.

Volcanic siltstones are present as normally graded, planar laminated, wedge-planar laminated, and trough cross-laminated intervals, but structureless beds and convoluted intervals are also common. Burrow structures are generally sparse and of the simple

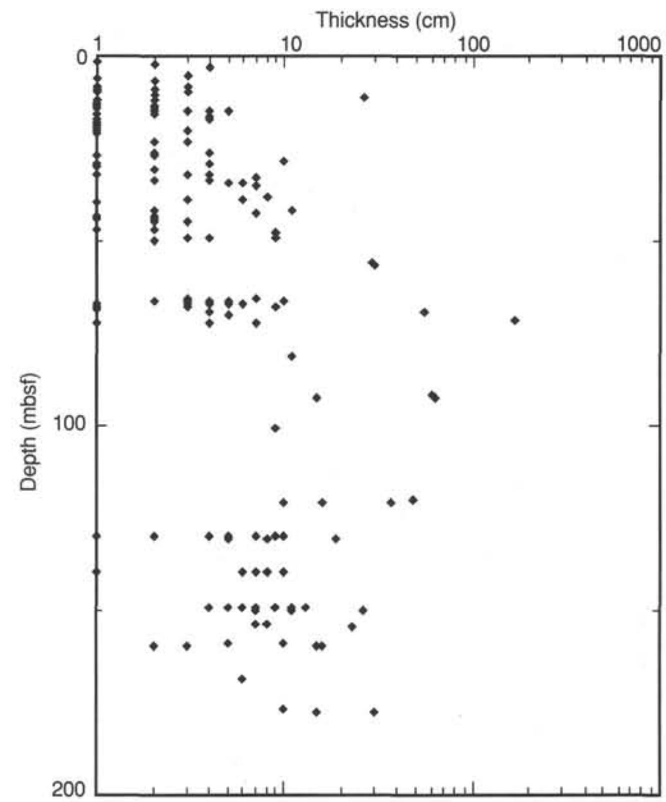

Figure 14. Variations in thickness vs. depth of volcaniclastic beds within Hole 841A (Unit I and the upper part of Unit II). Note that thickness is logarithmic.

vertical and horizontal tubular form (e.g., *Trichichnus* sp.) typical of deeper water environments (bathyal to abyssal >1000 m; Ekdale et al., 1984). High sedimentation rates coupled with the low organic carbon content of these sediments restrict the burrowing fauna to a minimum.

Chemical Variation

SiO_2 concentrations of vitric shards in the volcaniclastic sediments from the upper part of the sequence (Unit I and II) were estimated from refractive index measurements (after Church and Johnson, 1980, and Schmincke, 1981). For this analysis, the sediment sample was prepared following the method described in the "Lithostratigraphy" section of the "Site 834" chapter (this volume). The refractive indices of the different volcanic glass shard groups were then determined using standard reference optical oils and the total silica contents were calculated. The results of this analysis are shown in Table 3. Analyses are restricted to the upper parts of the recovered section (shallower than 270 mbsf), as sediments from the lower parts are more indurated and therefore more difficult to disaggregate efficiently in the short period of time available. In addition, higher degrees of alteration are found in volcaniclastic sediments from lower levels, affecting the reliability of the refractive index measurement.

Figure 15 shows the total calculated variability in silica contents for all samples from both Holes 841A and 841B. Due to the large number of glass types identified in some sands, it was often only possible to identify end-member compositions. This may partially contribute to the concentration of many data points at either end of the spectrum of observed compositions. In any case, the plot does demonstrate the wide range of glass compositions found, from basaltic (50 wt% SiO_2) to rhyolitic (72 wt% SiO_2). Figure 16 shows the change in total silica contents with depth below seafloor. Filled circles represent the largest single glass population in any one sample, whereas minor glass components are shown as open circles. It is evident that for much of the section, glasses of a number of different compositions are present in individual volcanic sandstone layers. Furthermore, the proportion of silica-poor to silica-rich glass is variable. Toward the top of the sequence, shallower than 100 mbsf (corresponding to the late Miocene), all but one of the sampled sands is dominated by silica-rich, dacitic to rhyolitic glass, although basaltic andesitic glasses are still an important component.

Table 3. Refractive indices (*n*) and SiO_2 concentrations (estimated from Church and Johnson [1980] and Schmincke [1981]) of vitric shards (63–36 μm size fraction) from volcanic sandstones in Holes 841A and 841B.

Sample (cm)	Depth (mbsf)	Comment	*n*	SiO_2 (wt%)
135-841A-				
1H-2, 107	2.57	Clear, dominant	1.504	71.7
2H-2, 110	11.10	Clear, dominant	1.514	68.8
2H-2, 110	11.10	Pale green	1.558	57.7
3H-1, 102	19.02	Clear, dominant	1.518	67.7
4H-5, 54	34.04	Clear, dominant	1.522	66.6
4H-5, 54	34.04	Clear	1.512	69.4
8H-1, 6	65.56	Greenish brown, dominant	1.576	53.8
8H-1, 6	65.56	Clear	1.518	67.7
8H-1, 6	65.56	Dark brown	1.574	54.2
11X-1, 120	92.20	Clear, dominant	1.514	68.8
11X-1, 120	92.20	Brownish green	1.568	55.5
12X-CC, 24	100.94	Greenish brown, dominant	1.566	55.9
12X-CC, 24	100.94	Dark brown	1.566	55.9
12X-CC, 24	100.94	Pale green	1.552	59.0
15X-1, 60	130.20	Clear, dominant	1.520	67.2
15X-1, 60	130.20	Clear	1.542	61.4
15X-1, 60	130.20	Greenish, altered	1.566	55.9
17X-CC, 18	149.08	Clear, dominant	1.518	67.7
17X-CC, 18	149.08	Pale green	1.542	61.4
17X-CC, 18	149.08	Green, altered	1.558	57.7
21X-1, 68	177.58	Green	1.594	50.3
21X-1, 68	177.58	Greenish brown	1.580	53.0
21X-1, 68	177.58	Very pale green, dominant	1.524	66.1
21X-1, 68	177.58	Green, dominant	1.558	57.7
135-841B-				
7R-1, 145	219.55	Clear	1.518	67.7
7R-1, 145	219.55	Clear	1.568	55.5
7R-1, 145	219.55	Greenish brown	1.574	54.2
9R-1, 82	238.62	Clear	1.520	67.2
9R-1, 82	238.62	Greenish brown	1.570	55.0
10R-1, 12	247.12	Clear	1.526	65.5
10R-1, 12	247.12	Greenish brown	1.568	55.5
12R-CC, 14	269.42	Clear	1.524	66.1

Alteration

Vitric shards are optically clear to slightly hydrated in the uppermost part of the sequence in Hole 841A. Volcaniclastic sediments in Hole 841B are nearly all altered to varying degrees. The intensity and inferred temperatures of alteration, however, do not appear to increase downhole.

The most common alteration effect found throughout Hole 841B is the replacement of volcanic glass in both vitric shards and the groundmass of volcanic lithic clasts by fine-grained clay minerals, presumably mainly smectite (Fig. 17). Clay minerals are only rarely found, filling veins, vesicles, and other pore spaces. Colors of clay minerals range from pale yellowish, brown to dark brown, and slightly greenish brown. Rare bright green clay minerals, which occasionally completely fill small vesicles, are tentatively interpreted as celadonite (e.g., Sample 135-841B-15R-1, 24–28 cm). Optically clear to slightly hydrated glass is abundant above Core 135-841B-7R (above 220 mbsf), and in smaller amounts deeper in Hole 841B (e.g., in Sample 135-841B-33R-2, 24–27 cm; 469.54 mbsf, and Sample 135-841-34R-2, 81–85 cm; 479.81 mbsf). Some volcanic glass has also been preserved in lithic fragments which are imbedded in lower Oligocene calcareous sandstone (Sample 135-841B-42R-3, 118–122 cm; 558.52 mbsf).

Iron hydroxide minerals are found in trace amounts in most of the samples. They occur either as thin coatings of clastic grains and minerals, or more rarely partly replacing the vitric groundmass of volcanic lithic fragments. Authigenic calcite occurs less frequently, but may constitute as much as 10 vol% in individual samples (e.g., Sample 135-841B-2R-2, 6–8 cm; 171.36 mbsf, and Sample 135-841B-15R-1, 24–28 cm; 295.14 mbsf). Small, granular, pore-filling aggregates of secondary quartz have been identified only in Samples 135-841B-18R-CC, 15–17 cm, and 135-841B-20R-3, 1–4 cm, at 324.97 mbsf and 345.51 mbsf, respectively.

Zeolites mainly occur in two intervals of the sedimentary sequence, at 364.48 to 421.12 mbsf, and from 519.22 to 574.90 mbsf. Several types of zeolites occur, some of which were tentatively identified by optical methods. Often fibrous aggregates of natrolite-thompsonite partly or completely fill interparticle pore spaces (e.g., Sample 135-841B-28R-CC, 1–2 cm; 421.12 mbsf; Fig. 18). Almost isotropic, equant, euhedral grains of analcime frequently replace plagioclase (e.g., Sample 135-841B-22R-3, 8–10 cm; 364.48 mbsf; Fig. 19). More rarely, analcime occurs as a pore-filling phase (e.g., Sample 135-841B-22R-1, 64–67 cm; 362.04 mbsf). A third type of zeolite, probably heulandite, is found to completely replace pumiceous shards farther down in the sequence (e.g., Sample 135-841B-38R-3, 12–15 cm; 519.22 mbsf).

Prehnite is a major pore-filling phase in the same two intervals where zeolites are abundant. It forms aggregates of bladed,

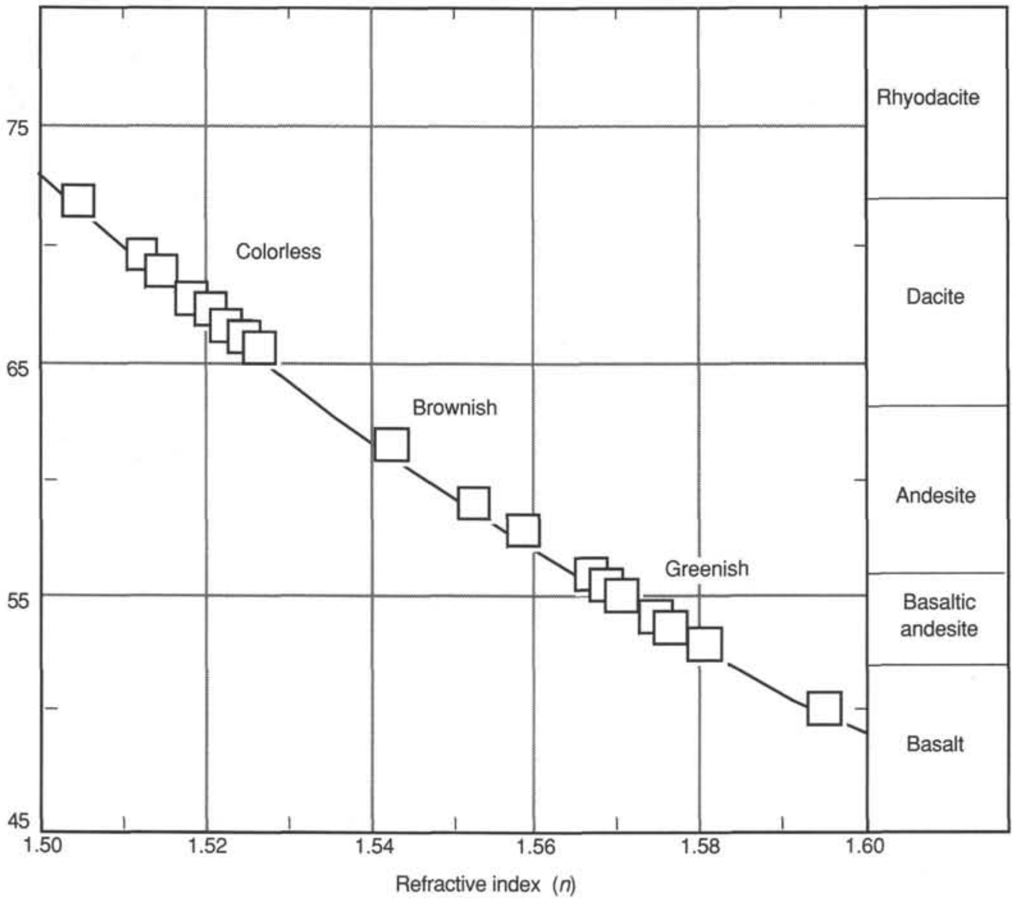

Figure 15. Variation in refractive indices and calculated silica content of volcanic glass shards extracted from volcanic sandstones from Holes 841A and 841B (estimated after Church and Johnson [1980] and Schmincke [1981]). Plot contains data from all sampled levels of both holes and shows the variability found at this site.

slightly elongate crystals in the center of the vesicles, which are up to 300 μm long and randomly oriented. At the vesicle margins these crystals are smaller grained and oriented subparallel to the vesicle rims (Fig. 20).

Epidote, usually with distinctive yellowish green pleochroism, is found in four samples, and in one instance, intergrown with pumpellyite (Sample 135-841B-22R-3, 8–10 cm; 364.48 mbsf; Fig. 21). Epidote is not common in these samples but occurs as rare, isolated grains.

The abundance of unaltered volcanic glass in the upper part of the Holes 841A and 841B (0–170 mbsf) is indicative of normal, low-temperature diagenetic conditions. Replacement of glass by clay minerals starts at about 170 mbsf and increases gradually downsequence. At about 270 mbsf increasingly abundant zeolites indicate slightly enhanced alteration temperatures, probably well below 100°C (Evarts and Schiffmann, 1983). At about 325 mbsf, the appearance of prehnite suggests an increase in alteration temperatures. The occurrence of rare epidote (with or without pumpellyite) in a few samples is consistent with an even higher alteration temperature of at least 200°C (Browne, 1978; Ellis, 1979). However, the occurrence of epidote as clastic grains may indicate that it was not formed *in situ* but is of detrital origin. Below 421 m, the degree of alteration decreases to an almost pure clay mineral assemblage before returning to a zeolite + prehnite ± calcite ± clay minerals (+ epidote?) assemblage in the interval from 519.22 to 574.90 mbsf.

The two intervals with evidence of enhanced alteration temperatures show a close spatial relationship to basaltic andesitic intrusions, which have a minimum total thickness of about 18 m (see "Igneous Petrology" section, this chapter). These intrusions indicate one or more episodes of active volcanism, younger than 10 Ma, in the proximity of Site 841. It is likely that the two intervals of zeolite to probable lower greenschist-facies metamorphism in Hole 841B are related to this volcanism.

Depositional History

The date of the earliest sedimentation at Site 841 is unknown, but paleontological data suggests it is at least late Eocene in age. The first sediments deposited were the products of subaerial pyroclastic airfall events. In addition to welded rhyolitic tuffs (ignimbrites), proximal volcanic rhyolitic tuff breccias are present. The presence of rare dark pebbles, tentatively identified as basalt, within these sediments indicates that the exposed landmass had basaltic volcanic rocks of Eocene or older age in addition to active silicic volcanic centers. The oldest dated sediments recovered from Site 841 show that shallow-marine carbonate sedimentation was established over eroding volcanic arc basement by the late Eocene. Paleo-water depths were shallow (10–60 m), with normal marine salinity and a rich fauna. Episodic emplacement of volcanic sands suggest that the site was still close to an exposed volcanic arc, although it is not clear if it was active at this time. Carbonate sedimentation continued until the early Oligocene. A sedimentary hiatus occurs between the early Oligocene and early middle Miocene, after which a sequence of volcanic conglomerates, breccias, and sands were deposited. These sediments fine

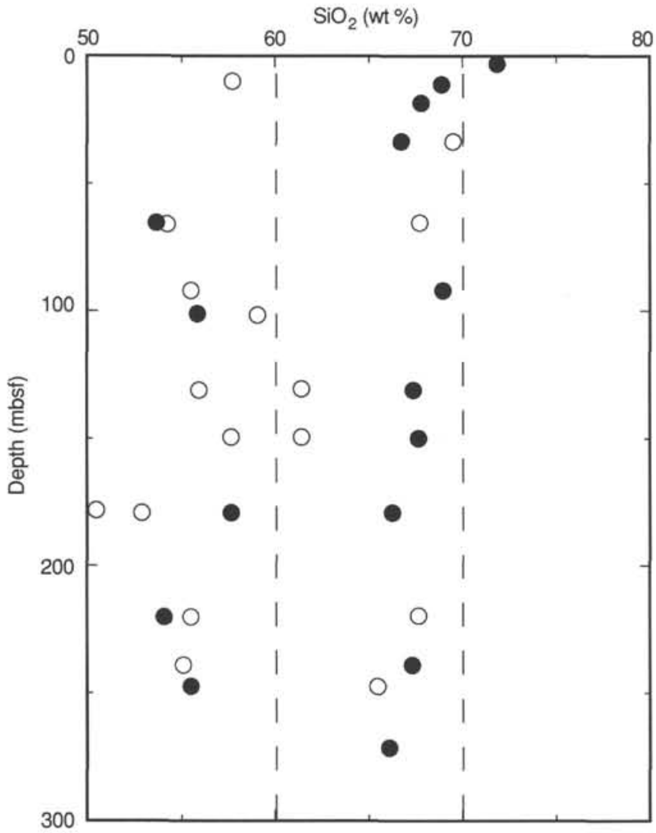

Figure 16. Variability of total silica contents with depth (mbsf) at Site 841. Where more than one glass type was identified in a sample the most abundant type is marked by a solid circle and the minor glass types by an open circle.

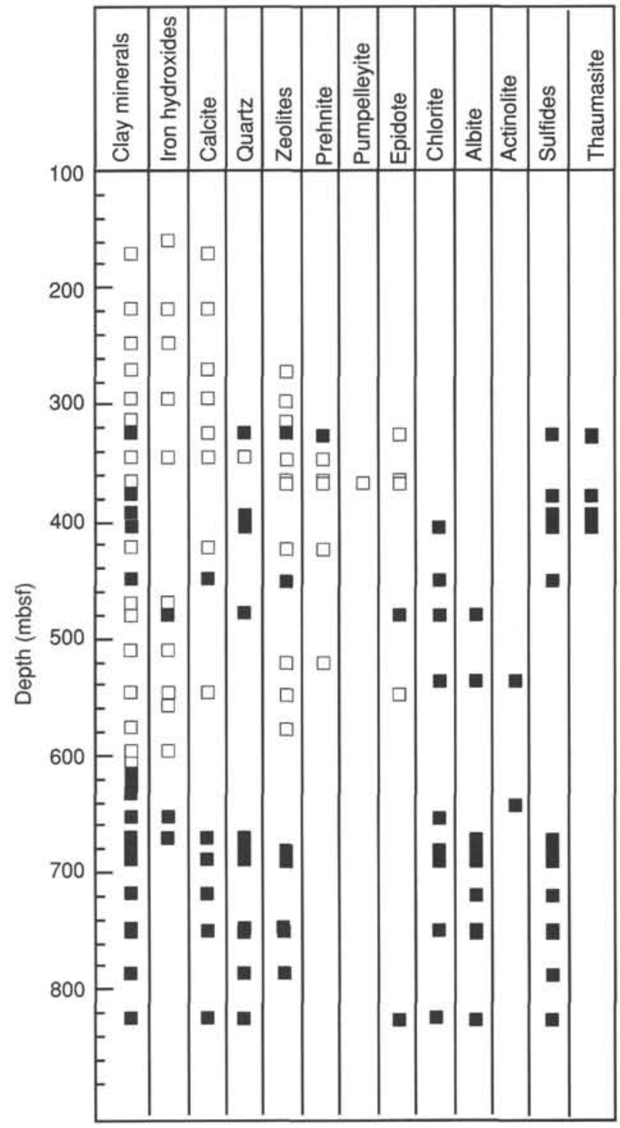

Figure 17. Downhole plot showing the occurrence of secondary minerals in Hole 841B. Open squares indicate sedimentary samples; solid squares indicate igneous rock samples, including rhyolitic tephras, pumice breccias, welded tuffs, and lapilli tuffs.

upward into interbedded volcanic sandstones and siltstones, interpreted as turbidites.

Volcaniclastic sediments in the lower part of the upper Miocene again comprise volcanic sandstones and conglomerates. These sediments accumulated rapidly, possibly on a proximal submarine fan. Upward there is a transition into thin-to medium-bedded sandy and silty deposits, and finally into clayey siltstones with thin sandstones. These sediments are interpreted as distal turbidites.

From the late Miocene to the middle Pleistocene, hemipelagic clays with minor interbedded volcaniclastic turbidites and thin pyroclastic ash layers were deposited.

STRUCTURAL GEOLOGY

Site 841 is located 48 km to the east of Site 840. It is situated on the upper trench slope in 4810 m of water, 40 km to the west of the axis of the Tonga Trench and positioned on a minor NNE-SSW elongate topographic arch trending parallel to the strike of the slope.

Microfaults

Site 841 is unique among Leg 135 sites in that abundant evidence for significant tectonic disruption of the succession was encountered. Sedimentary bedding, inclined in excess of 15°, even within a meter of the mudline, and microfaults, with throws of <1 mm to several centimeters, are preserved throughout the succession. The majority of microfaults have normal displacements (Fig. 22, although see below) which, when their slip vectors can be determined with precision, are very close to pure dip slip. Normal microfaults have been identified as high in the succession as Core 135-841A-2H, corresponding to a depth of 9.3 mbsf. Paleomagnetic data suggest that sediment from this depth has polarity consistent with magnetization during the Jaramillo Subchron, of early Pleistocene age (0.93–0.98 Ma; see "Paleomagnetism" section, this chapter). Normal faulting must therefore have been taking place in the region at least until the early Pleistocene, and multichannel seismic reflection data (see Fig. 4) suggest that this has continued in the Holocene.

Major Fault Zones

Brittle, deformed rocks are intersected at several different intervals at Site 841, and are taken to correspond to fault zones. These zones of deformation are discussed individually in this and the following section. Two of the zones are considered to be significant fault zones as they juxtapose substantially different lithologies, although their actual displacements are not known. The remaining fault zones are not associated with stratigraphic hiatuses, are therefore thought to be associated with lesser dis-

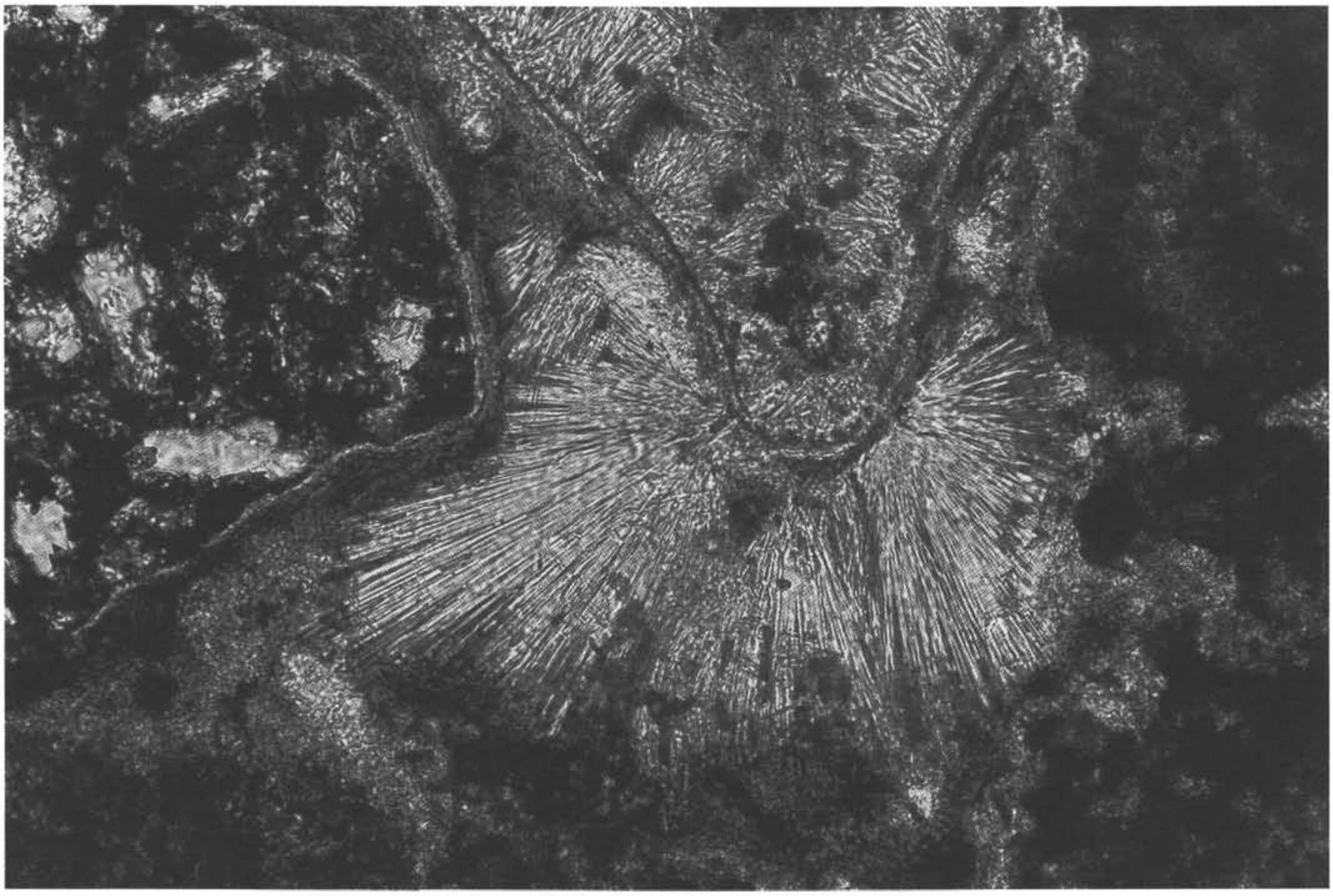

Figure 18. Photomicrograph of radial aggregate of fibrous zeolite, probably natrolite-thompsonite in Sample 135-841B-28R-CC, 1–2 cm (Unit III); plane polarized light; long side of photomicrograph = about 0.6 mm.

placements, and are described below under the heading "minor fault zones."

Higher Fault Zone: Sections 135-841B-31R-1 and -32R-1 (449–458 mbsf)

Earthy-textured fault gouge and fault breccia, including epidote-bearing fragments of tonalite, are present at the base of Core 135-841B-31R and in the uppermost 35 cm of Core 135-841B-32R (Fig. 23). Only 0.16 m of rock was recovered from Core 135-841B-31R and it is possible that fault rock was also present over much of the intervening 9.5 m. The fault zone separates upper Miocene volcaniclastic sediments above from lowest middle Miocene volcaniclastic sediments. Three nannofossil and at least seven foraminiferal zones are absent, implying that the structure had a normal sense of displacement. This is corroborated in adjacent cores by offsets of steeply dipping microfaults (sometimes apparently conjugate; Fig. 24) that are thought to be sympathetic to the major structure.

The fault zone coincides with major changes in rock physical properties; peak values of sonic velocity and thermal conductivity occur at this level (see "Physical Properties" section, this chapter). Significant hydrothermal alteration of the sediments is observed over a depth of more than 100 m below the fault zone, but does not appear to affect the hanging wall strata at all. Footwall sediments are traversed by large numbers of veins belonging to several generations of fracturing, and sometimes cleavage may be formed, although whether this is an extension or a pressure solution phenomenon is not obvious from hand specimens alone. The earliest and most pervasive phase of alteration involves the formation of pale halos around veins (Fig. 25) and normal microfaults (Fig. 24). The veins are typically very narrow (<0.5 mm) and may be filled with a chalky white mineral that preliminary shipboard X-ray diffraction (XRD) analysis suggests may include thaumasite, a sulfate of calcium and silicon (see "Igneous Petrology" section, this chapter). The pale halos around the veins and fractures may be several millimeters wide and appear to be formed by leaching of the volcaniclastic wall-rock rather than by the addition of any other mineral. The leaching is also concentrated along bedding planes, preferentially in the coarser grained sandy sediments, which were presumably more permeable to fluid flow (Fig. 25; see also Fig. 10). The alteration gives rise to a distinctive "zebra-striped" appearance to the rocks and often accentuates original sedimentary structures. The extent of the leaching of more than 100 m into the footwall of the fault zone, and its absence on the hanging wall, are significant.

The leached veins, fractures, and bedding are cut by large numbers of irregular, often anastomosing, thaumasite-filled veins up to 4 mm in width (Fig. 25). Several generations of veins may be recognized. They largely postdate the normal faulting but may occasionally display small, normal offsets themselves.

Lower Fault Zone: Section 135-841B-47R-2 (605 mbsf)

The second major fault zone in Hole 841B separates calcareous volcanic sandstone and shallow-water bioclast volcanic sand-

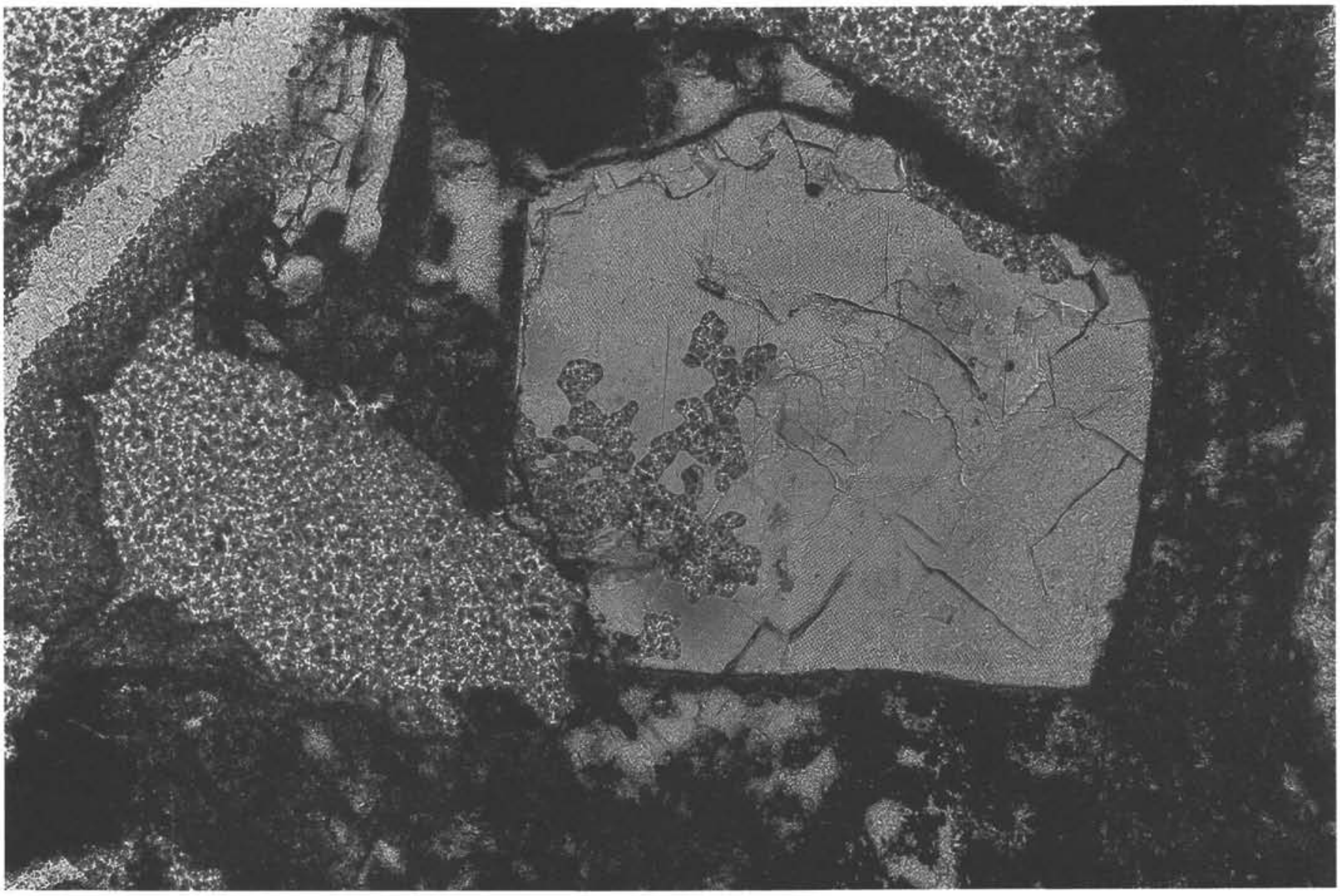

Figure 19. Photomicrograph of euhedral plagioclase crystal in Sample 135-841B-22R-3, 8–10 cm (Unit III). The plagioclase is partly replaced by analcime/chabazite. Zeolite can be recognized in the lower right half of the crystal where cleavage parallel (010) is replaced by a pattern of diagonal fractures and crystal boundaries. Partly crossed nicols; long side of photomicrograph is about 1.5 mm.

stones of late Eocene age above from a 230-m-thick sequence of rhyolitic tuffs and ignimbrites below. The magnitude and displacement sense of the fault zone is not known but general stratigraphic relationships and the offset of associated smaller scale faults in Cores 135-841B-44R to 135-841B-46R, within 30 m of the fault zone, suggest that it, too, is normal. The uppermost preserved part of the fault zone itself starts in Section 135-841B-47R-2 at a depth of 90 cm (605.0 mbsf), with a 12-cm interval containing several nonoriented polished clasts of limestone and rhyolite. One rhyolite clast has a foliated cataclastic fabric indicative of high strain. Beneath these clasts, 64 cm of extremely soft white clay was recovered. The clay contains abundant millimeter-sized quartz grains (often euhedral), occasional pumice fragments up to 1 cm in diameter, and mineralized lithic fragments, including a 2-cm pebble of strained vein quartz, dark gray fine-grained (andesitic?) lava fragments and jasper. The lithic fragments contain disseminated pyrite, and grains of sulfide are dispersed widely throughout the clay. The clay is undeformed except for a narrow, gently-dipping schistose shear band in Section 135-841B-47R-2, 106–109 cm (Fig. 26), and a series of low-angle shear structures in Section 135-841B-47R-CC, 108–127 cm, that appear to have brecciated and disaggregated a preexisting foliated clay-bearing rock of uncertain origin (Fig. 27).

Formation of the soft white mineralized clay is thought to be largely post-kinematic, with the exception of the minor fault strands described above. The shear strength of the clay appears to be so low that any significant displacement along the main fault zone would have obliterated these faults entirely.

Minor Fault Zones

Minor fault zones are defined for the purposes of this discussion as those intervals within the core over which faulted rock or significant shattering of the core (demonstrably pre-drilling) has been recognized and whose displacement is greater than the scale of the core, but which do not give rise to detectable hiatuses or repetitions of the stratigraphic sequence. They are therefore assumed to be of lesser magnitude than those structures described in the previous section, although this assumption need not be valid if the lithologies are homogeneous. We envisage them to be comparable in magnitude to outcrop-scale mesofaults that have displacements on the order of tens of centimeters to tens of meters.

Section 135-841B-36R-1, 87–120 cm (497.7–498.0 mbsf)

A total of 33 cm of indurated, foliated, faulted rock was recovered from lithologic Unit IV at a depth of 498 mbsf (Fig. 28). No reliable kinematic indicators were observed in hand specimens of the faulted rock; analysis of its slip history will be based upon post-cruise petrofabric studies. The faulted rock lies within the zone of leaching described above from the footwall of the fault zone at 449–458 mbsf, and has itself been heavily modified by hydrothermal alteration in the form of cross-cutting anastomosing veins of a fine gray-white mineral that is similar in

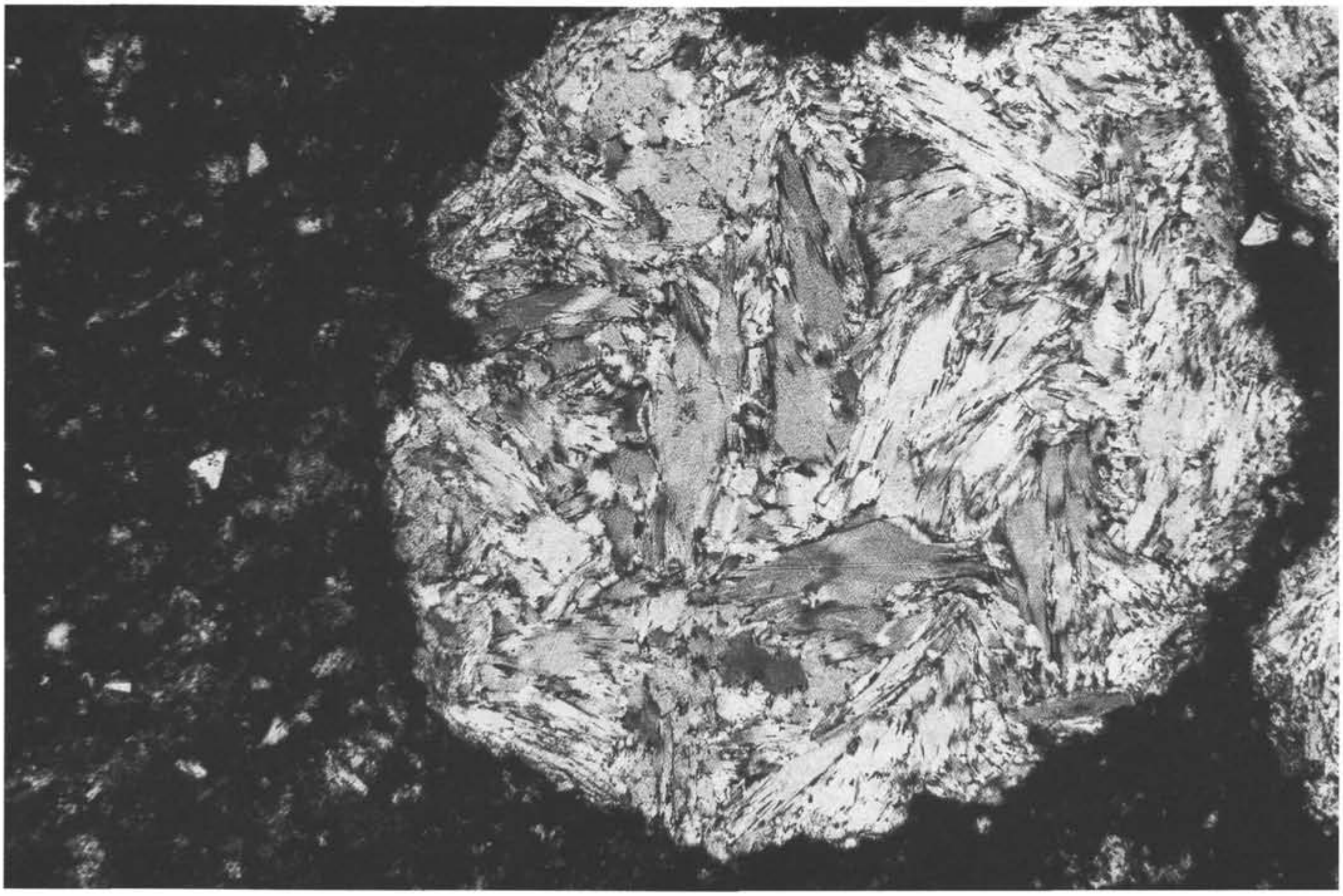

Figure 20. Photomicrograph of vesicle completely filled by slightly elongate, bladed crystals of prehnite in Sample 135-841B-23R-3, 18–24 cm (Unit III). Partly crossed nicols; long side of photomicrograph is about 1.5 mm.

appearance to the thaumasite vein fill described above. It is considered probable that the minor fault zone at 498 mbsf is subsidiary to the major structure that lies 40 m above it (see above).

Sections 135-841B-44R-1 to -46R-2 (~574–595 mbsf)

Minor faults are distributed throughout the 25–30 m of core that lies above the major mineralized fault zone at 605 mbsf. Slickensides are common and many surfaces are coated with soft talc-like or clay minerals. Where the core is sufficiently coherent for the orientation of fractures relative to the borehole axis to be discernible, the striations fall on steeply dipping planes and display almost pure dip-slip normal senses of motion.

Section 135-841B-51R-3 (645 mbsf)

In Section 135-841B-51R-3 coherent but hydrothermally altered green rhyolitic tuffs at the top of the section change abruptly to a gouge, formed of comminuted fragments of the same lithology. No discrete fracture planes were observed at or close to the transition from competent to crushed rock, but a fault zone is the most reasonable explanation for the sudden transition.

Section 135-841B-63R-1 (757 mbsf)

Core 135-841B-63R marked the transition to very poor recovery at the base of Hole 841B. Recovery in Core 135-841B-63R was 1.79 m, but only 1.3 m in total was recovered from the succeeding seven cores, until unstable rock caused termination of the hole at 834.2 mbsf. Core 135-841B-63R, which is made up of pale green tuffaceous breccia, is cut by a large number of fault strands and associated gouge zones throughout. Discrete fracture planes are occasionally preserved, dipping steeply with respect to the axis of the borehole, and a pair of conjugate normal faults with moderately to steeply plunging slickenside surfaces was recognized. The poor recovery beneath Core 135-841B-63R may be an indication that the brittle fracturing continues below.

Reverse Faults

The history of normal faulting presented above from the entire depth range of Holes 841A and 841B is complicated by the presence of microfaults with reversed senses of motion (e.g., Fig. 29) at certain depth intervals. Some apparent reversed senses of motion on steeply dipping microfaults are actually normal with respect to the sedimentary bedding (see Fig. 10) and may therefore represent tilted normal faults. However, reverse motion on the majority of the microfaults, some of which dip at a shallow angle, cannot be explained in this manner and appears to represent genuine although perhaps localized compressional faulting. The true reverse microfaults appear to be restricted to the approximate intervals 170–360 mbsf and 460–530 mbsf (i.e., entirely within the Miocene parts of the succession). None has been observed that has a displacement of more than a few centimeters. In the higher stratigraphic levels, at ~200–220 mbsf, slump folds and other structures clearly indicative of soft-sediment deformation are preserved (see "Lithostratigraphy" section, this chapter). Mi-

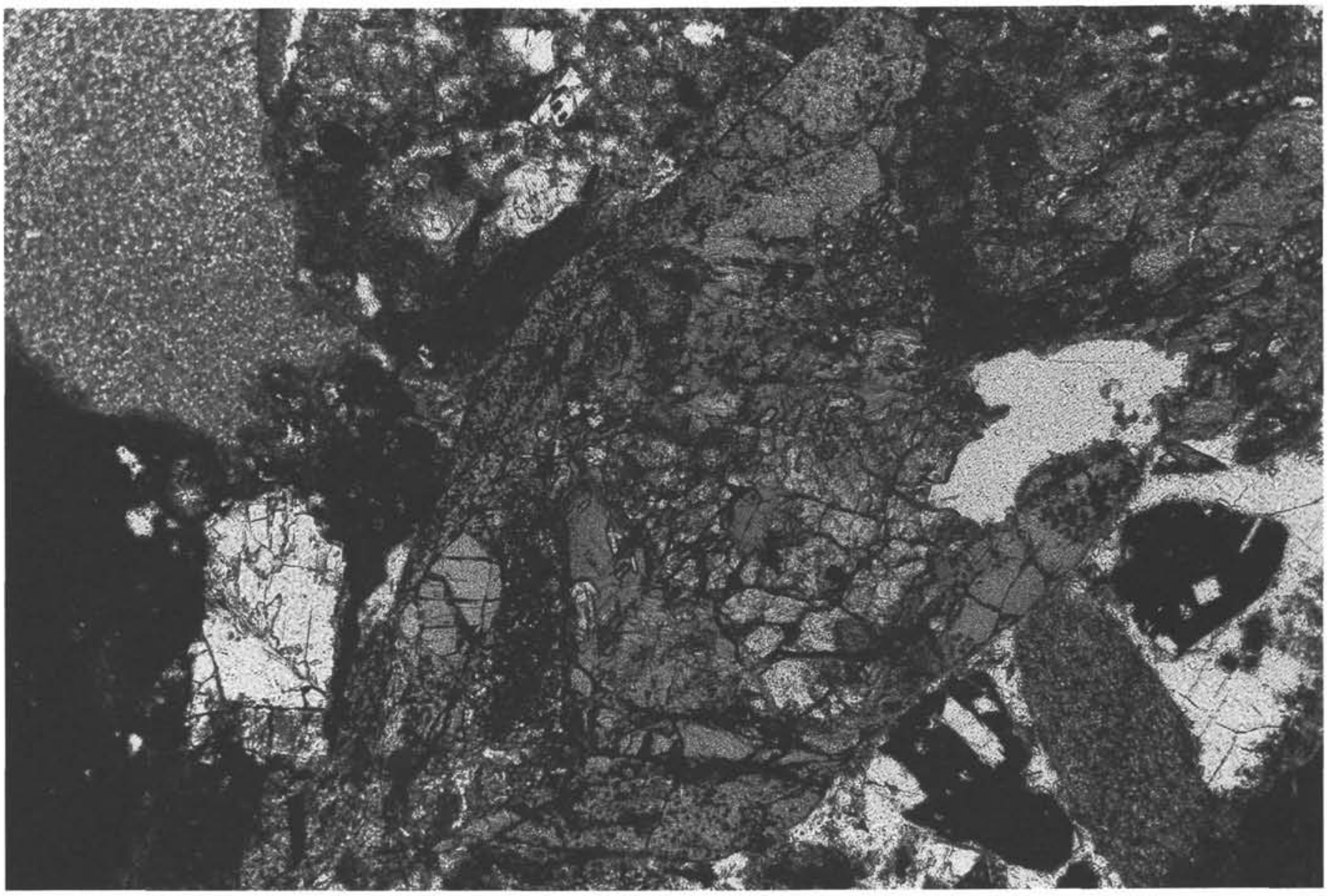

Figure 21. Photomicrograph of detrital(?) epidote/pumpelleyite intergrowth. Sample 135-841B-22R, 8–10 cm (Unit III).

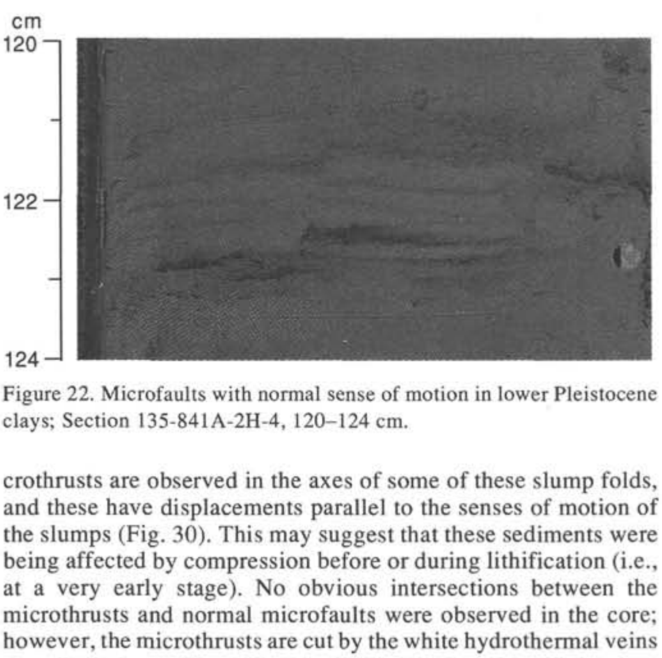

Figure 22. Microfaults with normal sense of motion in lower Pleistocene clays; Section 135-841A-2H-4, 120–124 cm.

crothrusts are observed in the axes of some of these slump folds, and these have displacements parallel to the senses of motion of the slumps (Fig. 30). This may suggest that these sediments were being affected by compression before or during lithification (i.e., at a very early stage). No obvious intersections between the microthrusts and normal microfaults were observed in the core; however, the microthrusts are cut by the white hydrothermal veins described above. These observations, when considered together, suggest that the reverse faulting probably predated at least some of the normal faulting. If this is so, a possible change in the tectonic regime in the Tonga forearc between the Miocene and the early Pleistocene (at the oldest) may be implied. The relationship between the normal and reverse faulting will be established with more certainty following detailed integration of paleomagnetic and logging data post-cruise.

BIOSTRATIGRAPHY

The sedimentary section at Site 841 yielded planktonic foraminifer and calcareous nannofossil assemblages of middle Pleistocene, late Miocene, early middle Miocene, early Oligocene, and late Eocene ages. The middle Pleistocene assemblages found in Core 135-841A-1H are separated from those of late Miocene age by a barren interval spanning Cores 135-841A-2H through 135-841A-6H. Dissolution effects from deposition below the CCD are probably responsible for the lack of preserved faunas and floras in this interval. The upper Miocene section continues through the rest of the section recovered in Hole 841A and in Cores 135-841B-2R through 135-841B-12R. Assemblages in this interval continue to show varying degrees of dissolution resulting from both deposition at or near the CCD together with diagenetic effects. Poor preservation in the Miocene assemblages from Cores 135-841B-13R through 135-841B-29R prevent more exact age determination. A barren interval followed by a fault (see "Structural Geol-

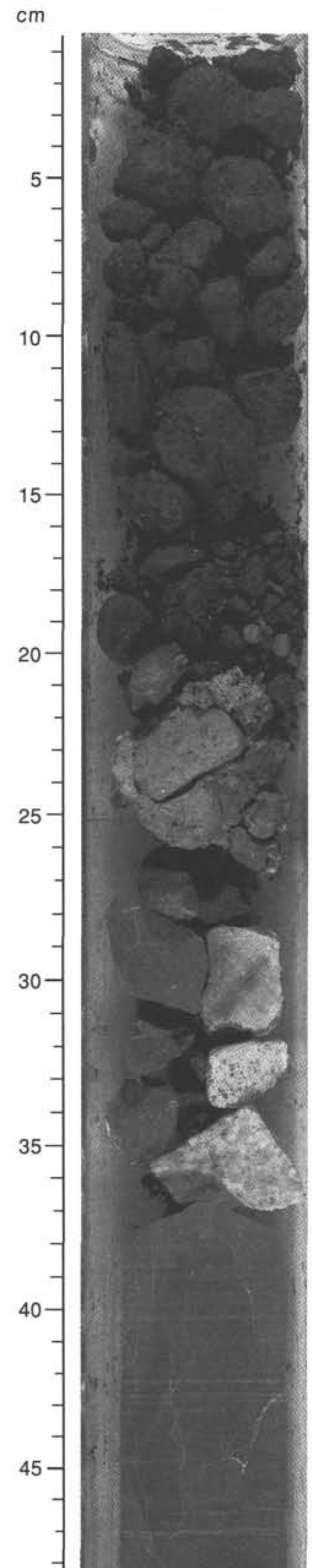

Figure 23. Faulted rock from the major fault zone at 458 mbsf; Section 135-841B-32R-1, 0–49 cm. The pale clast at 22–24 cm contains epidote. Note veining and normal faulting in laminated volcaniclastic sediments beneath the faulted rocks.

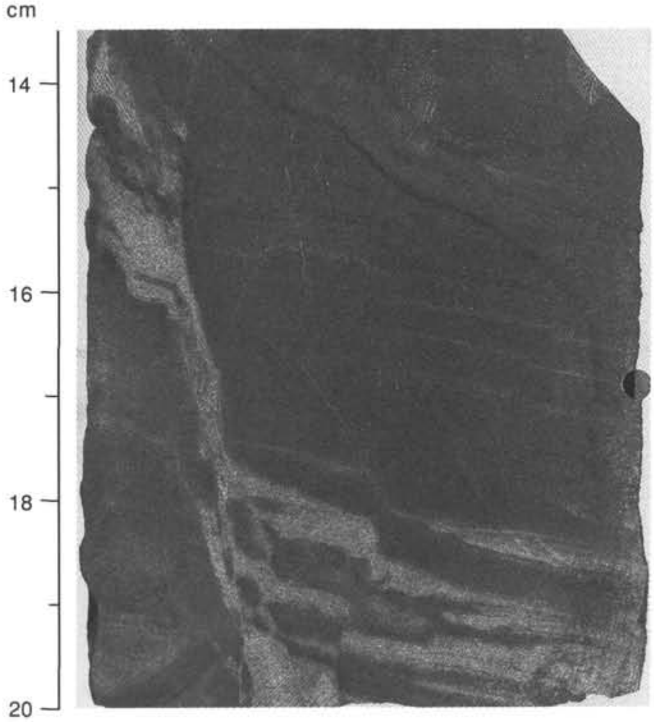

Figure 24. Leaching associated with a normal microfault, suggesting that motion on the fault predated or was coeval with leaching; Section 135-841B-34R-2, 13–20 cm. Note the slight normal faulting on either side of a small horst structure in the center of the piece; these tiny faults form a conjugate pair.

ogy" section, this chapter) separates lower middle Miocene faunas and floras in Cores 135-841B-32R through 135-841B-40R from the overlying section. This section rests unconformably on a section of lowermost Oligocene to upper Eocene in Cores 135-841B-41R through 135-841B-47R. Larger benthic foraminifers from the lower part of the Eocene section (Cores 135-841B-46R and 135-841B-47R) indicate that it was deposited in warm, shallow water. These cores also contain reduced planktonic assemblages. A fault (see "Structural Geology" section, this chapter) separates the Eocene section from volcanic units below.

The biostratigraphic results for Sites 841A and 841B are summarized in Figures 31, 32, and 33.

Calcareous Nannofossils

Pleistocene

Pleistocene calcareous nannofossils were encountered in only one sample from near the top of Hole 841A. Other samples from Core 135-841A-1H through Section 135-841A-6H-CC are barren. This paucity is attributable most likely to dissolution effects associated with deposition below the CCD.

Sample 135-841A-1H, 50 cm, contains a flora including *Gephyrocapsa oceanica* and *G. caribbeanica* but not *Emiliania huxleyi* or *E. ovata*. On this basis this sample is assigned to Subzone CN14b. This sample also contains a reworked flora including *Discoaster* spp. and *Cyclicargolithus* spp.

Upper Miocene

Nannofossil assemblages in the Miocene part of the sedimentary section show variable signs of dissolution effects. Preservation in most samples is moderate to poor. In some assemblages, however, dissolution appears to have removed some taxa while

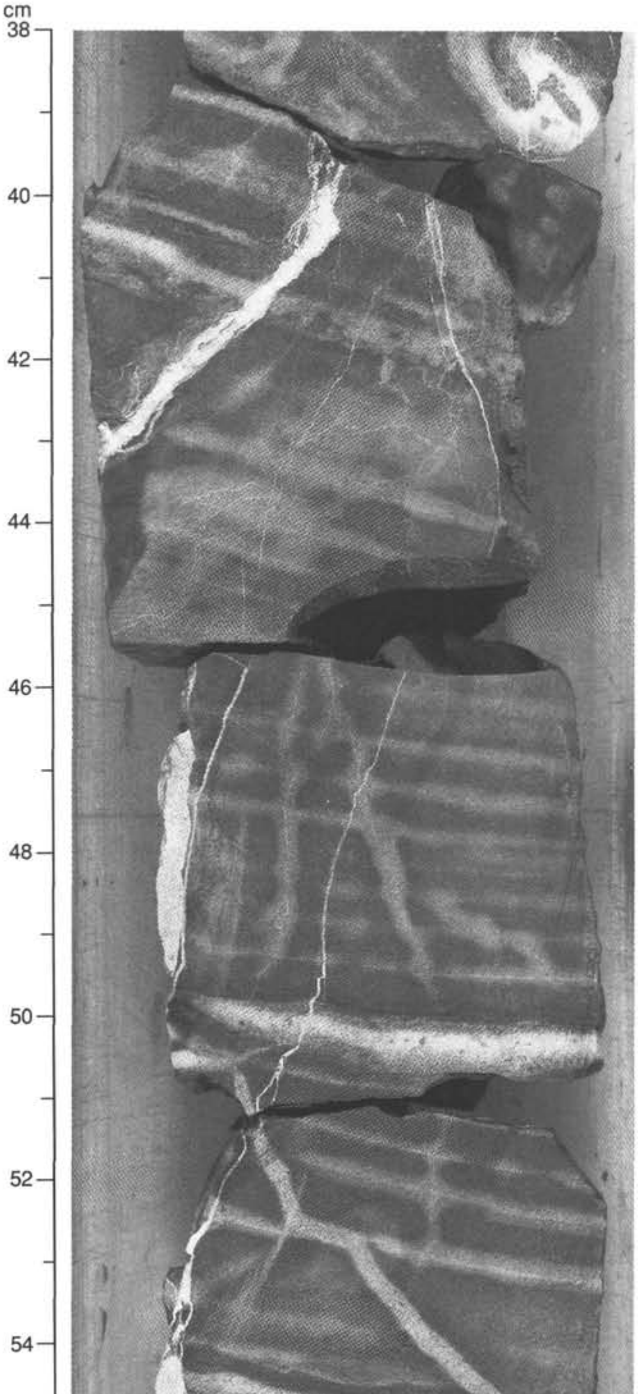

Figure 25. Two generations of veining; Section 135-841B-33R-2, 38–57 cm. Earlier narrow veins, with white ?thaumasite infilling, are associated with leaching of the volcaniclastic silts to a pale color. Leaching also occurs along bedding planes, preferentially along coarser grained sediment layers. A later generation of broader veins, filled by white minerals, including thaumasite, cuts the bedding and zones of earlier leaching.

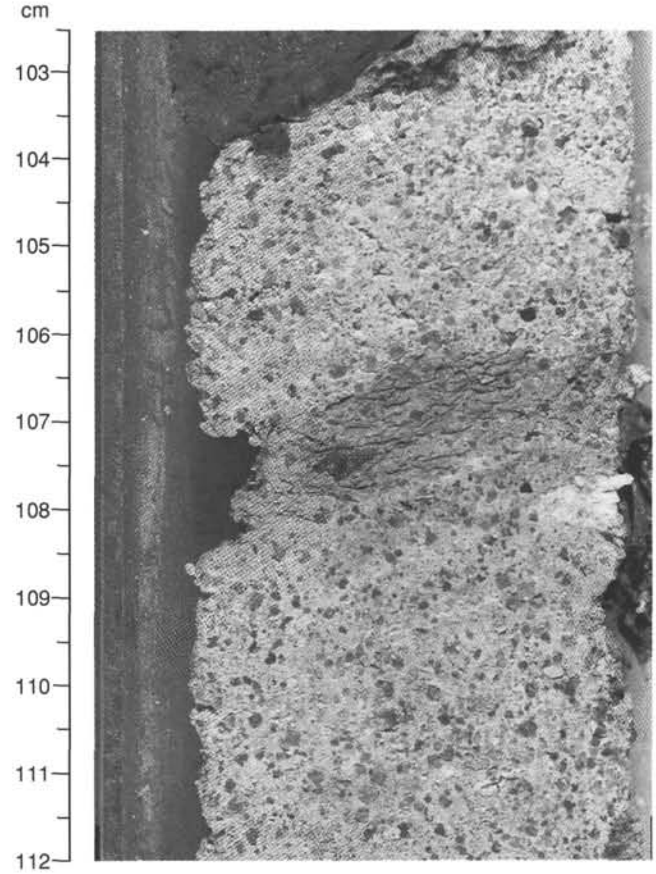

Figure 26. Minor schistose shear strand in mineralized white clay infilling major fault zone at 605 mbsf; Section 135-841B-47R-2, 102.5–112 cm. Detrital material within the clay is quartz and sulfide; the edge of a larger lava pebble is also visible at the top left-hand corner.

leaving those remaining quite pristine. High in the section dissolution is associated with deposition below the CCD. In more lithified sections lower in the hole dissolution may be due to diagenesis.

Sample 135-841A-7H-CC contains a flora including only discoasters. Coccoliths are absent. The flora includes *Discoaster brouweri, D. surculus, D. variabilis, D. challengerii,* and *D. berggrenii.* The first evolutionary occurrence of *D. berggrenii* falls at the base of Zone CN9 (Okada and Bukry, 1980) and the extinction falls within Subzone CN9b (Bukry, 1973). On this basis this sample is assigned to Zone CN9. Samples 135-841A-8H-CC through 135-841A-11X-CC yielded more diverse floras, also including *D. berggrenii.* They are assigned to Zone CN9.

Samples 135-841A-16X-CC through 135-841A-18X-CC, 135-841A-20X-CC, and 135-841B-2R-CC contain floras including *Minylitha convallis.* This taxa first occurs within Subzone CN8a and sometimes ranges to within Subzone CN9a (Bukry, 1973). On this basis these samples are assigned an age of Subzone CN8a to Subzone CN9a.

Sample 135-841B-4R-CC yielded a flora including *Discoaster neorectus, D. variabilis, D. pentaradiatus, Sphenolithus abies, S. neoabies,* and *Reticulofenestra pseudoumbilica.* This sample is assigned to Subzone CN8b.

Samples 135-841B-5R-CC through 135-841B-12R-CC, 135-841B-14R-CC, and 135-841B-16R-CC contain floras with *M. convallis.* They are assigned to Zone CN8. Sample 135-841B-14R-CC contains rare reworked Oligocene/lower Miocene *Cyclicargolithus* spp.

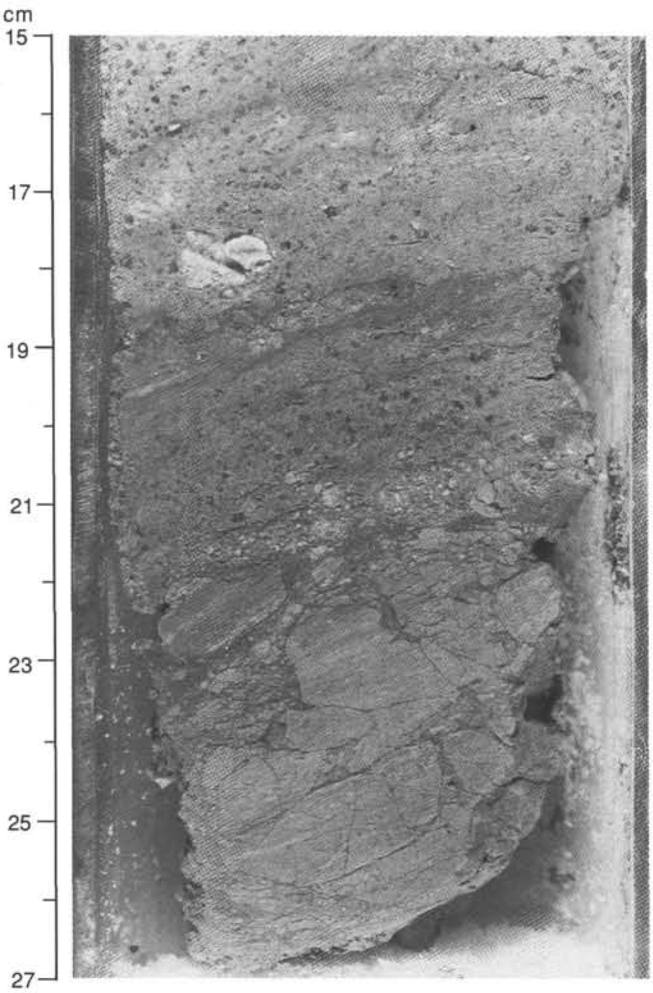

Figure 27. Deformation within mineralized white clay infilling major fault zone at 605 mbsf; Section 135-841B-47R-CC, 15–27 cm. Note foliated protolith at 22–27 cm becoming disaggregated and sheared.

Samples 135-841B-15R-CC through 135-841B-17R-4, 33 cm, yield sparse, poorly preserved floras containing *Calcidiscus macintyrei*. This species initially occurs at the base of Subzone CN3 (Bukry, 1973). These samples are therefore assigned an age of Zones CN3 to CN8.

Sample 135-841B-13R-CC yielded a sparse flora including only two taxa: *Sphenolithus neoabies* and *Cyclicargolithus floridanus*. *Sphenolithus neoabies* ranges from Miocene to Pliocene. *Cyclicargolithus floridanus* ranges from upper Oligocene to lower Miocene. This flora could be entirely reworked, but it indicates a Miocene age.

Sample 135-841B-22R-2, 125 cm, taken from the sandy matrix of a conglomerate, yielded a single specimen of the early to middle Miocene taxon *Sphenolithus heteromorphus*. Although this specimen is almost certainly reworked, it indicates that the conglomerate still represents Miocene deposition.

Samples 135-841A-14X-CC, 135-841A-15X-CC, 135-841B-17R-CC, 135-841B-19R-3, 21 cm, 135-841B-19R-CC, 135-841B-21R-CC, 135-841B-22R-CC, and 135-841B-28R-CC contain floras too sparse and poorly preserved for age determinations.

Samples 135-841B-3R-CC, 135-841B-18R-2, 64 cm, 135-841B-18R-CC, 135-841B-20R-CC, 135-841B-24R-CC, and 135-841B-29R-CC through 135-841B-31R-CC are barren of calcareous nannofossils.

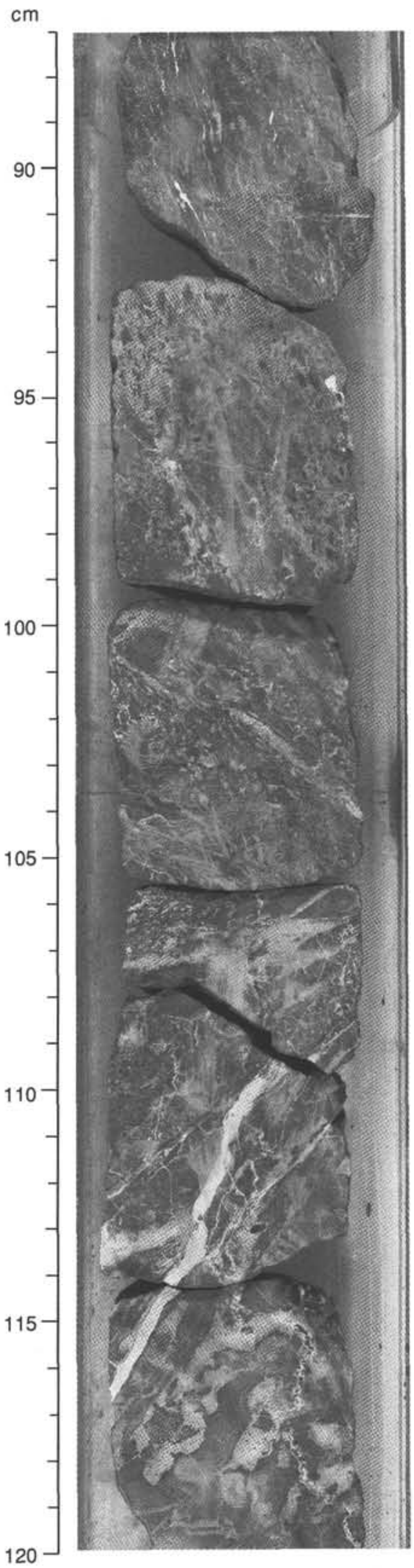

Figure 28. Foliated hydrothermally altered faulted rock from within the zone of leaching of the foot wall of the major fault at 458 mbsf; Section 135-841B-36R-1, 87–120 cm.

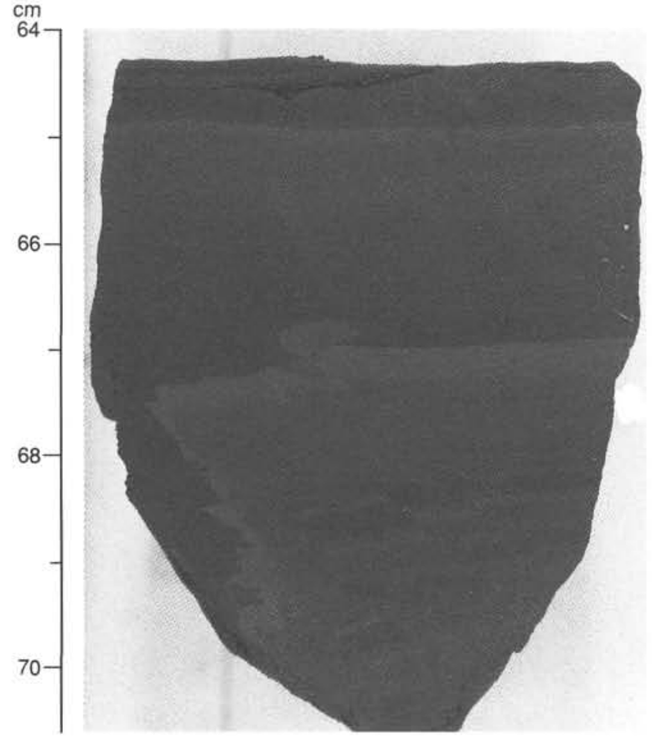

Figure 29. Reverse microfaults in upper Miocene sediments; Section 135-841B-2R-1, 64–71 cm.

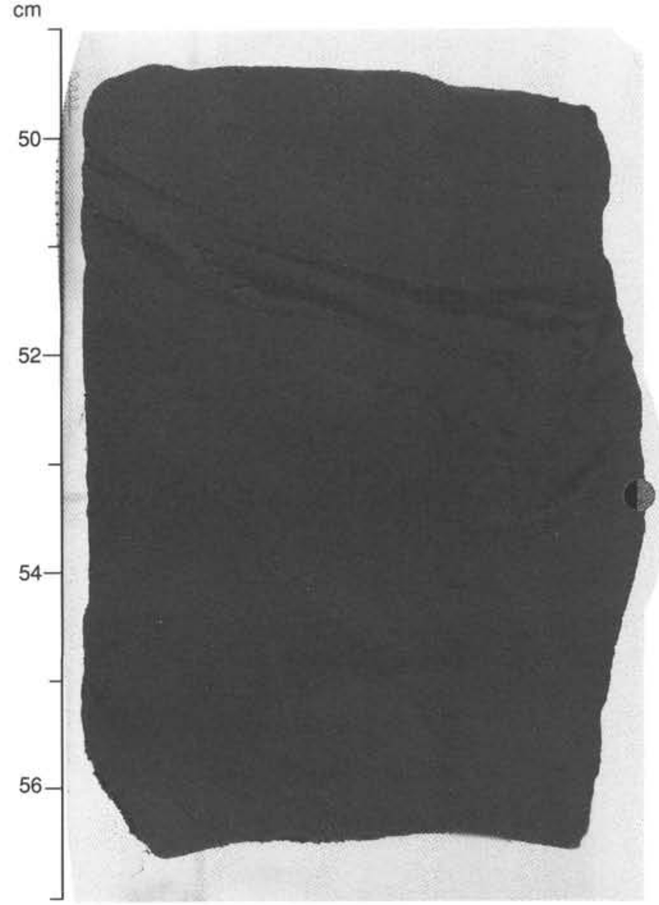

Figure 30. Microthrusts in the hinge of a soft-sediment fold in upper Miocene sediment, possibly indicating early syn-lithification reverse faulting; Section 135-841B-6R-1, 49–57 cm.

Middle Miocene

Samples in this part of the section show diagenetic dissolution similar to those in the upper Miocene.

Samples 135-841B-32R-CC through 135-841B-36R-CC, 135-841B-39R-CC, and 135-841B-40R-CC contain floras including *Sphenolithus heteromorphus* and *Cyclicargolithus floridanus* but not *Helicosphaera ampliaperta.* On this basis these samples are assigned to Zone CN4. Samples 135-841B-33R-CC and 135-841-34R-CC also yielded the reworked Oligocene/early Miocene taxa *Cyclicargolithus abisectus.*

Samples 135-841B-37R-CC, 135-841B-38R-CC, and 135-841B-41R-CC are barren of calcareous nannofossils.

Lower Oligocene/Eocene

Floras in this part of the section are generally abundant and fairly well preserved.

Samples 135-841B-42R-CC and 135-841B-43R-CC yielded floras including *Reticulofenestra umbilica, R. hillae, Dictyococcites bisectus, Dictyococcites scrippsae, Ericsonia formosa, Ericsonia subdisticha, Zygrhablithus bijugatus, Discoaster deflandrei,* and *Discoaster tanii nodifer.* This flora is characteristic of Subzones CP16b or CP16a. A single specimen of *Discoaster saipanensis* identified from Sample 135-841B-42R-CC, if in place, could indicate placement of these samples in Zone CP15.

Sample 135-841B-44R-CC contains a flora including *Discoaster saipanensis* and *Discoaster barbadiensis* and lacks *Chiasmolithus grandis.* On that basis this sample is assigned to Zone CP15.

Sample 135-841B-45R-CC yielded a flora with limited diversity including *Discoaster barbadiensis* and *Ericsonia formosa* but dominated by *Pemma* spp. The genus *Pemma* ranges from middle to upper Eocene. The flora in this sample is assigned that age.

Sample 135-841B-46R-CC yielded only tiny placoliths and small, overgrown sphenoliths. No age determinate taxa were identified from this sample.

Sample 135-841B-47R-CC and deeper samples are barren of calcareous nannofossils.

Planktonic Foraminifers

A total of 68 core-catcher samples were examined for planktonic foraminifers at Site 841. Of these 29 were barren and seven contained faunas too poor to permit any detailed age determination. Most barren samples and those with poor faunas probably coincide with stratigraphic intervals deposited below the CCD or within conglomeratic beds. The remainder contain faunas from the middle Pleistocene to upper Miocene, lower middle Miocene and upper Eocene.

Pleistocene

Sample 135-841A-1H-CC contains a very poorly preserved foraminiferal fauna of a few minute forms and radiolarians which may be Pleistocene in age. Downcore, Samples 135-841A-2H-CC to 135-841A-7H-CC lack foraminiferal faunas, probably the result of deposition below the CCD.

Pliocene to Upper Miocene

Several samples above and below 135-841A-8H-CC and 135-841A-10X-CC are barren. Although diversity is low in both samples, the presence of *Globorotalia (Gr.) merotumida* in both

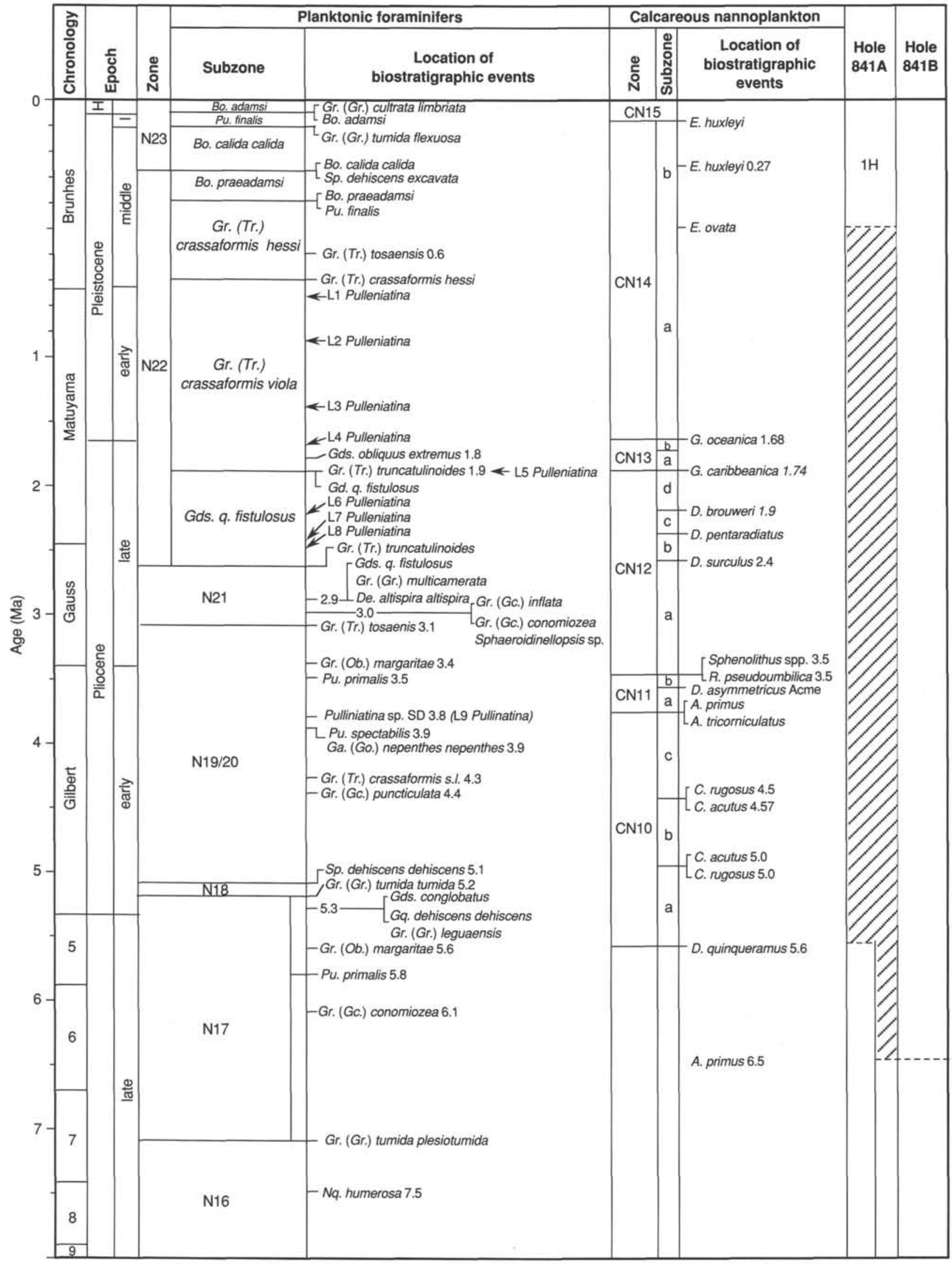

Figure 31. Biostratigraphic results, Site 841.

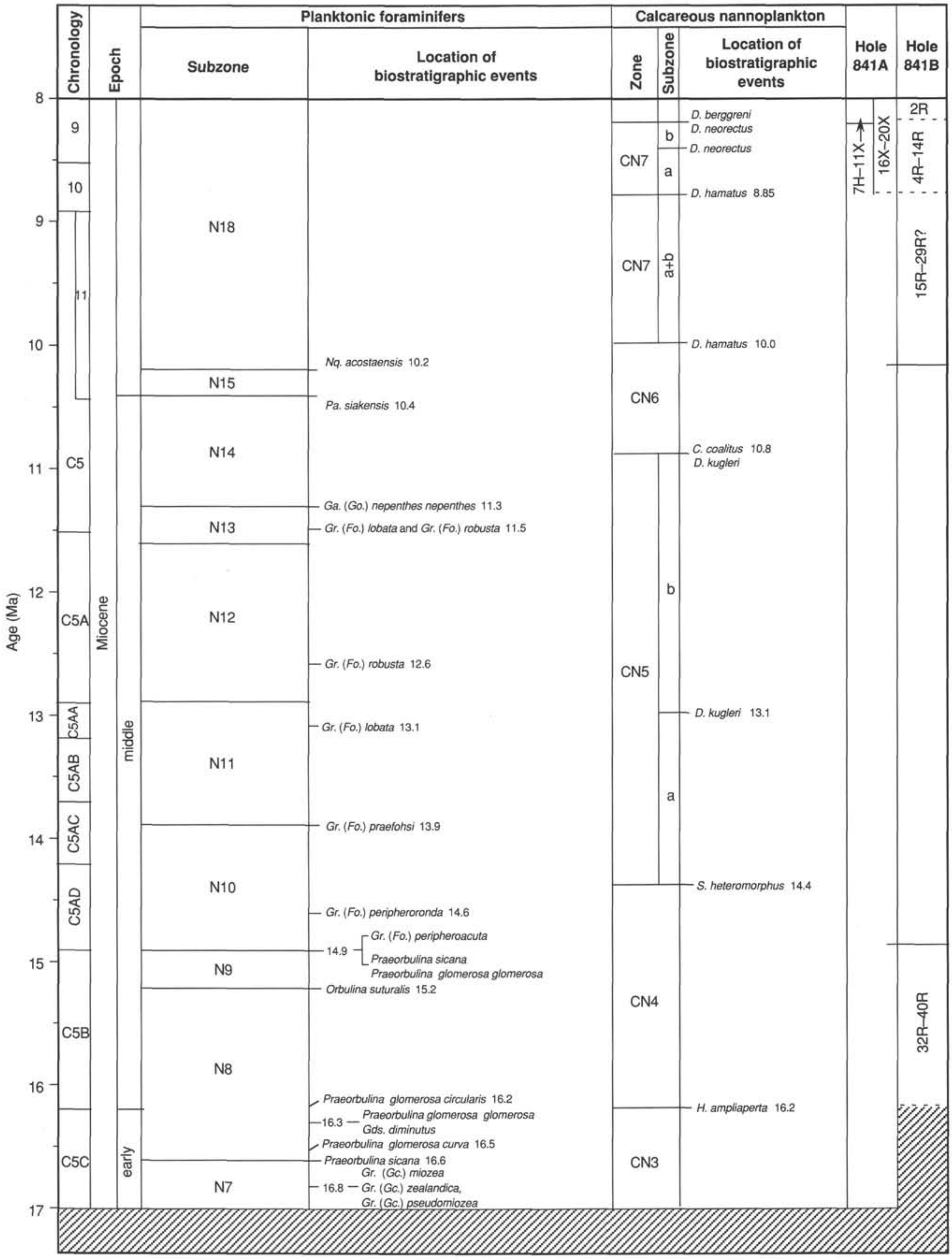

Figure 31 (continued).

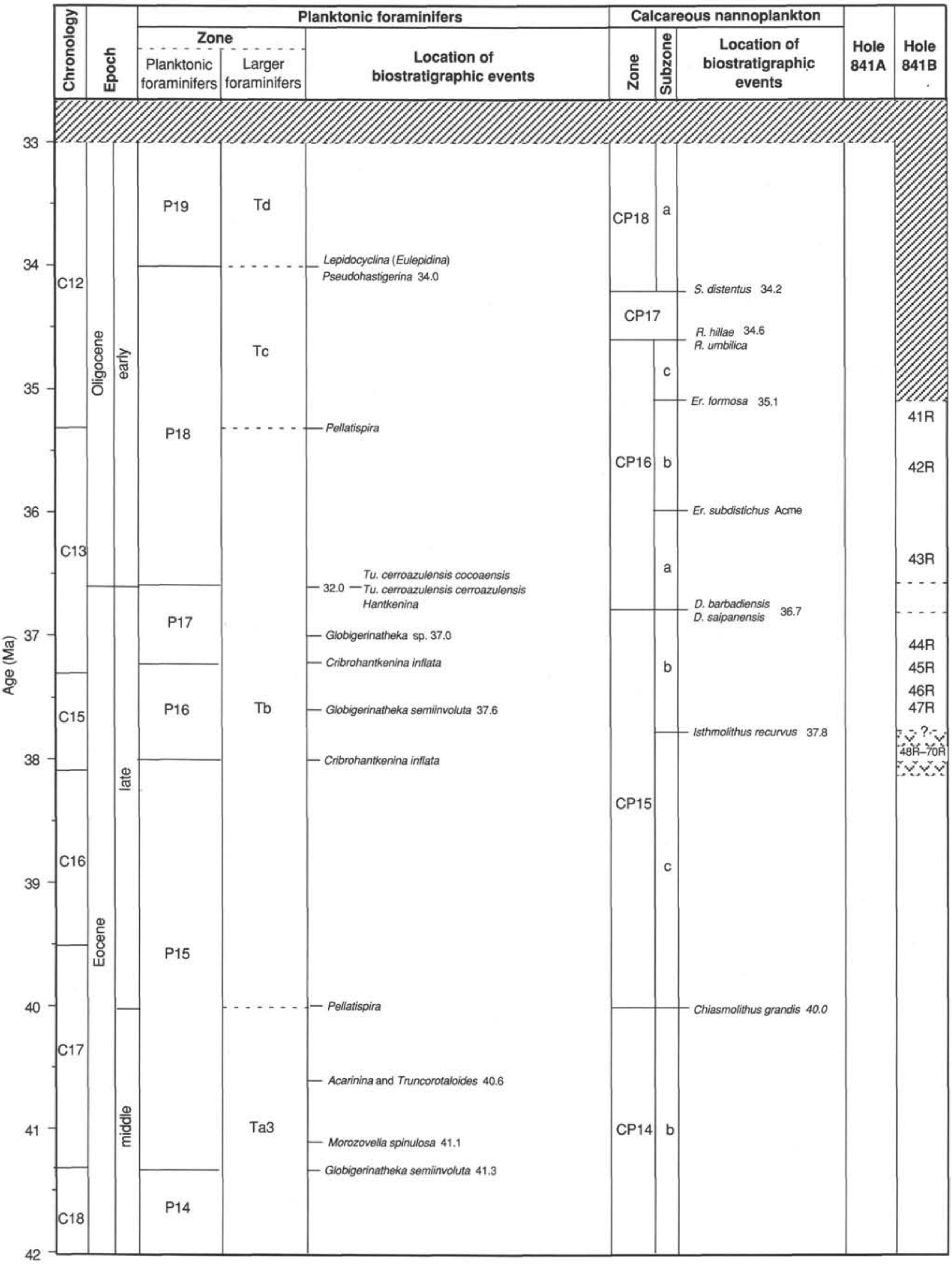

Figure 31 (continued).

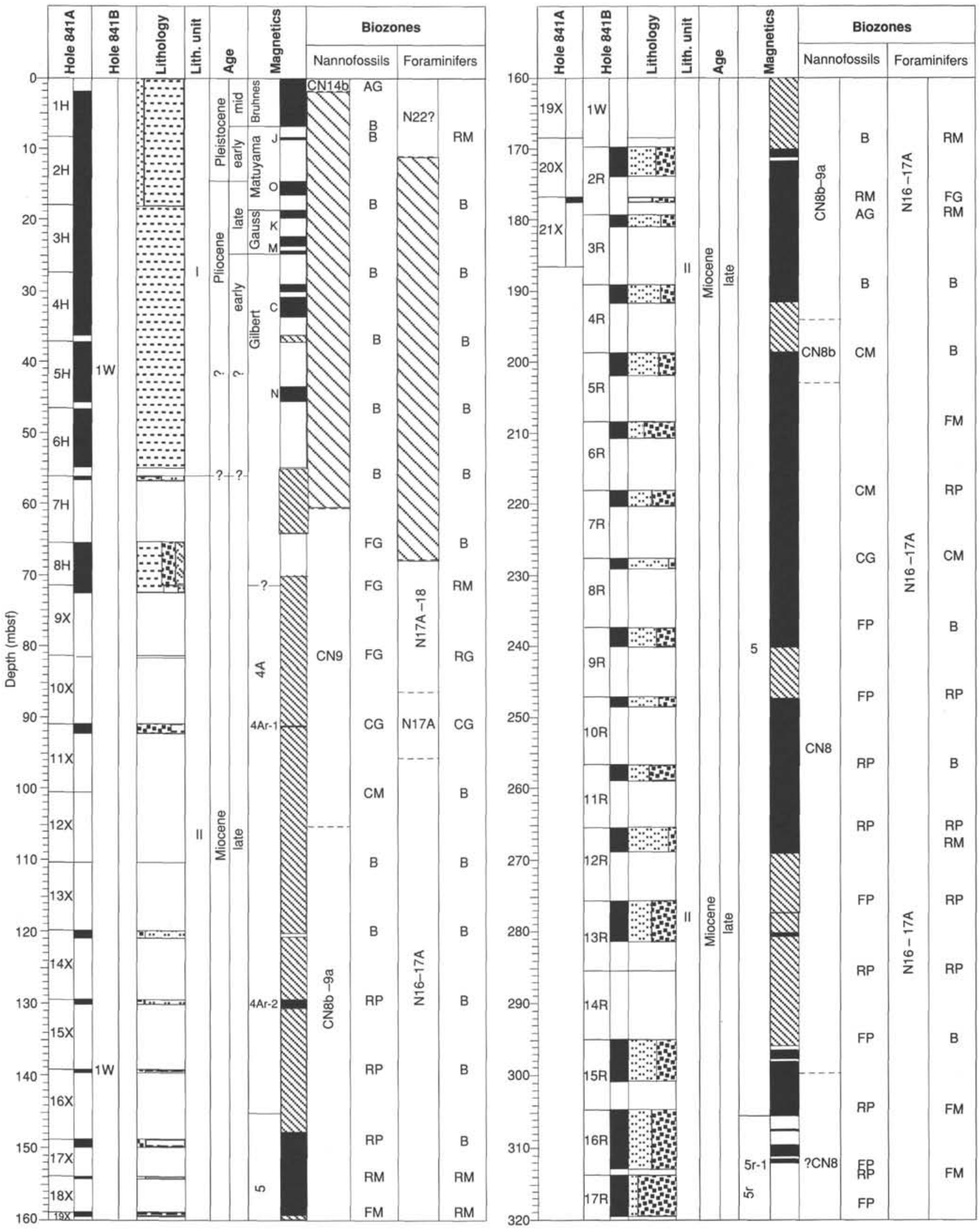

Figure 32. Paleontology summary chart, Site 841. See Figure 1 caption for an explanation of the abbreviations used.

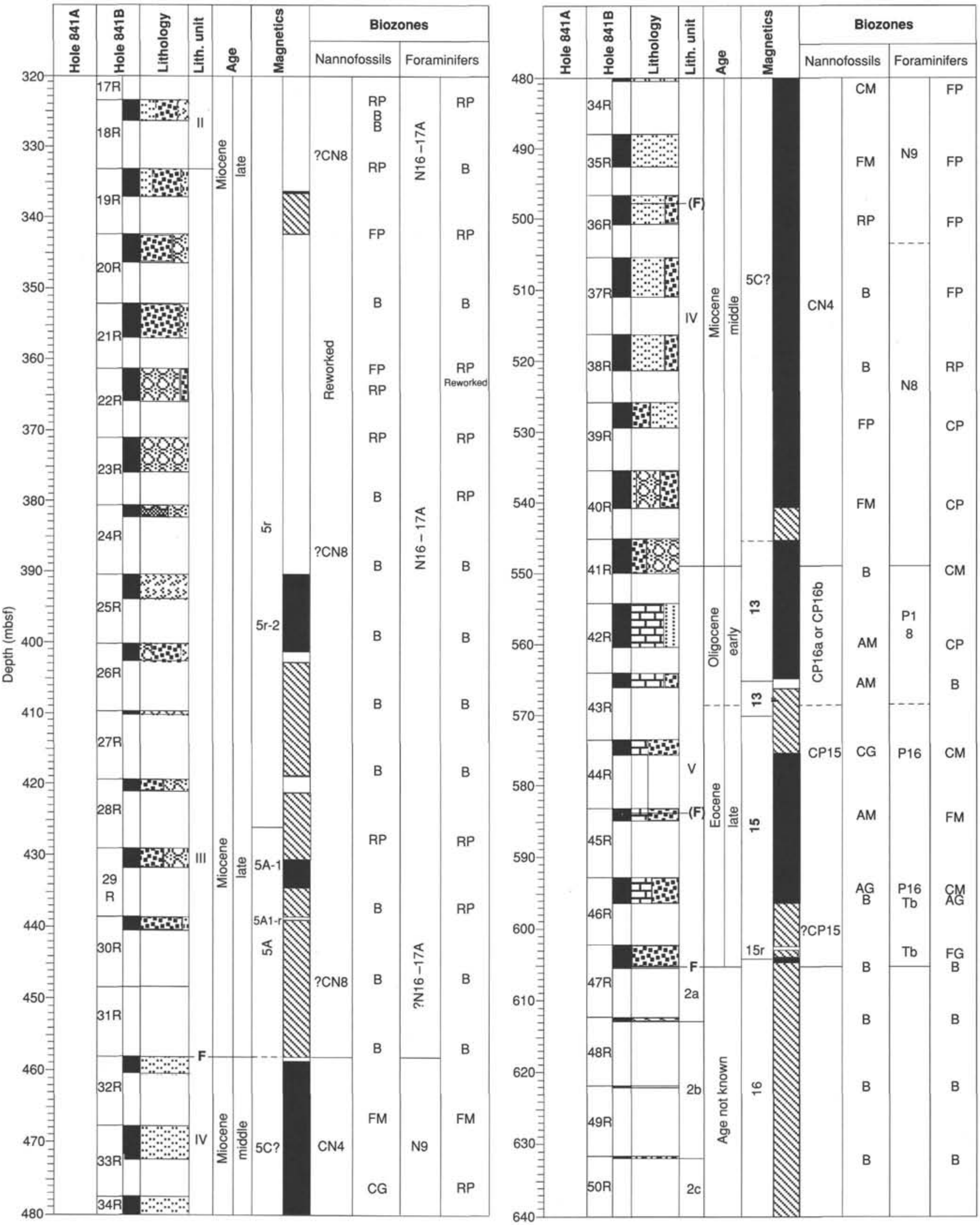

Figure 32 (continued).

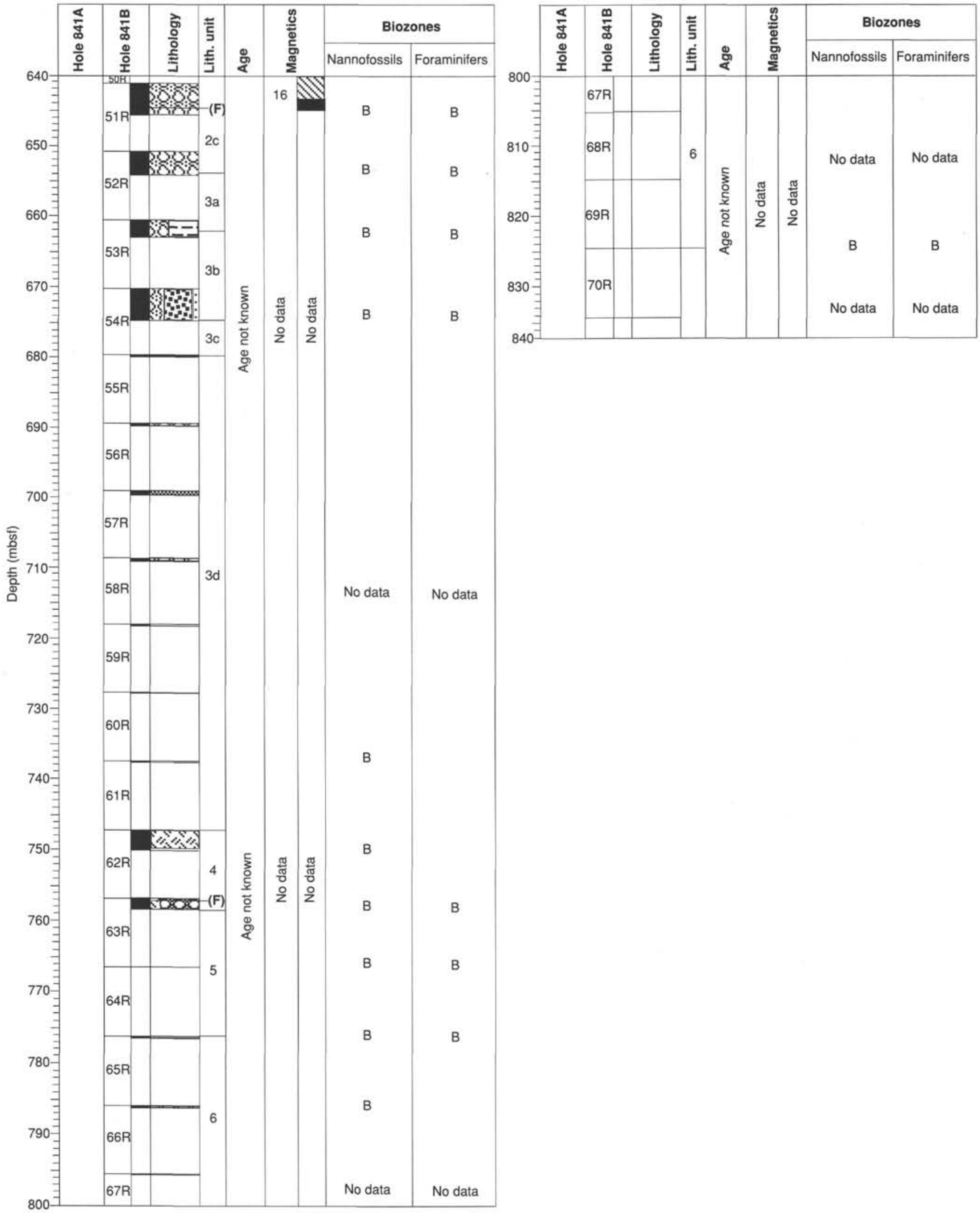

Figure 32 (continued).

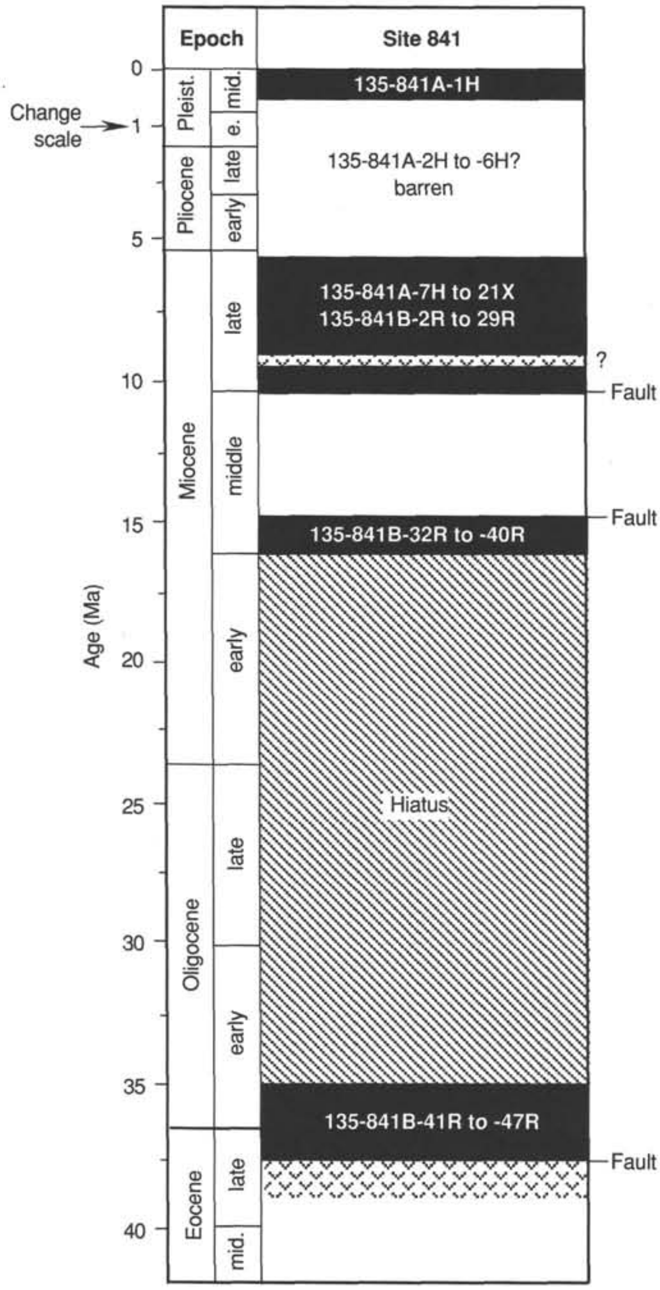

Figure 33. Time-stratigraphic summary, Site 841.

samples and *Gr. (Gr.) tumida plesiotumida* with *Gr. (Gr.) lenguaensis* in Sample 135-841A-10X-CC indicates Zone N17A. Samples 135-841A-11X-CC to 135-841A-16X-CC are barren. Samples 135-841A-17X-CC to 135-841A-19X-CC contain low-diversity faunas, including *Neogloboquadrina acostaensis,* indicating an age no older than Zone N16 (Kennett and Srinivasan, 1983). The presence of *Gr. (Gr.) lenguaensis* in Sample 135-841A-10X-CC indicates that these levels are no younger than Zone N17A. Sample 135-841A-20X-CC contains *Globigerina (Globoturborotalita) nepenthes* with a few small, nondiagnostic forms, giving a maximum age of Zone N14. Because *Ga. (Go.) nepenthes* is present in most higher assemblages, it is considered unlikely that the age is any older than Zone N16, and, in addition, nannofossil data indicates a maximum age of Zone CN8 for this sample, a level which correlates to the middle part of Zone N16. Sample 135-841A-21X-CC is barren of foraminifers.

Sample 135-841B-2R-CC contains an impoverished fauna with both *Ga. (Go.) nepenthes* and *Globogerinoides obliquus extremus,* indicating a level within Zones N16 to N19/20. Nannofossils in this sample indicate Zones CN8a to CN9a, which correlate with a part of the planktonic foraminiferal zonal interval N16 to N17A. Many samples from 135-841B-3R-CC to 135-841B-19R-CC are barren of foraminifers but the lowest contains a low-diversity fauna, including *Gds. kennetti,* a species ranging from Zone N16 to Zone N17 (Kennett and Srinivasan, 1983), giving a maximum age for this part of the sequence as within Zone N16; nannofossils give indeterminate results for this sample. Several samples from 135-841B-20R-CC to 135-841B-29R-CC are barren and most others contain impoverished faunas, probably the result of deposition close to the CCD. The lowest of these samples contains *Ga. (Go.) nepenthes,* indicating a level no older than Zone N14. Though this suggests that Zone N14 (middle Miocene) may be represented in these samples, the faunas and floras are too poor to permit an accurate assessment. A similar impoverished fauna within the zonal interval N16 to 17A, and the lack of lithologic evidence for a stratigraphic break between Cores 135-841B-19R and 135-841B-31R implies that these lower samples may also be referred to Zones N16 to N17A. Reworking of both upper Eocene and upper Oligocene to lower Miocene faunas is evident within samples assigned to the zonal interval N16 to N17A. Sample 135-841B-21R-CC contains an upper Oligocene to lower Miocene fauna (zonal interval ?P22 to N5) and Sample 135-841B-22R-CC contains *Discocyclina* sp. Reworking also is found in Sample 135-841B-22R-2, 125 cm, which contains a nannofosssil flora from Zones CN3 to CN5, correlating to within the foraminiferal Zones N7 to N14.

Middle Miocene

Samples 135-841B-32R-CC to 135-841B-36R-CC contain both *Orbulina* spp. and *Praeorbulina* spp., indicating Zone N9. Samples 135-841B-37R-CC to 135-841B-40R-CC contain *Praeorbulina* spp. without *Orbulina* spp. and are referred to Zone N8. These foraminiferal assemblages, though of low species diversity, show no sign of dissolution effects and were probably deposited at depths above the CCD.

Lower Oligocene to Upper Eocene

Samples 135-841B-41R-CC and 135-841B-42R-CC contain *Pseudohastigerina barbadoensis* and *Turborotalia ampliapertura* without *Tu. cerroazulensis,* indicating Zone P18 (Berggren and Miller, 1988). Samples 135-841B-41R-CC and 135-841B-45R-CC contain *Tu. cerroazulensis* with *Ps. barbadoensis,* indicating the P16 to P17 zonal interval. Though the extinction level of *Cribrohantkenina inflata* defines the top of Zone P16 (Blow, 1969), this species is globally very rare, and its absence from these samples, which were probably deposited in neritic conditions, is possibly of little biostratigraphic consequence. Furthermore, *Tu. ampliapertura,* which first appears at the base of Zone P17 (Blow, 1969), is absent from these samples though present in Samples 135-841B-41R-CC and 135-841B-42R-CC, again suggesting a level below Zone P17. In addition, the presence of *Subbotina linaperta* in both Samples 135-844B-44R-CC and 135-841B-45R-CC, which becomes extinct within Zone P16 (Blow, 1969), gives further support to referring these samples to Zone P16. Sample 135-841B-46R-1, 35–39 cm, contains a more restricted planktonic foraminiferal assemblage including *Tu. cerroazulensis,* as well as larger benthic foraminifers (see below), and must also be referred to Zone P16. Sample 135-841B-43R-CC was barren of foraminifers.

Larger Benthic Foraminifers

Eocene larger benthic foraminifers *Asterocyclina, Discocyclina, Operculina,* and *Pellatispira* are scattered throughout the matrix of Cores 135-841B-22R to 135-841B-30R (lower part of the upper Miocene section). These have been reworked from upper Eocene sediments in the vicinity. The specimens are slightly rounded and appear to have been transported only a short distance. Of interest is the absence of *Pellatispira* from the upper Eocene sediments intersected at this site. This form is present in some limestones from 'Eua Island, and is used to define the Tb letter stage boundary of Adams (1970). Reworked specimens are present in the upper Miocene sequence but none are present in the upper Eocene samples.

Samples 135-841B-46R-1, 35–39 cm, to 135-841B-47R-2, 79–83 cm, contain *Amphistegina waireka, Asterigerina tectoria, Asterocyclina matanzensis, Discocyclina omphala,* and *Operculina pacifica*; nodular and articulated coralline algae and bryozoa are also present. The number of specimens gradually increases downcore from the top of Core 135-841B-36R to Sample 135-841B-46R-CC and become rare in the underlying Core 135-841B-47R, disappearing at the fault contact with the underlying volcanic sequence. Larger foraminifers are most concentrated in Sample 135-841B-46R-CC. In this sample additional forms *Heterostegina saipanensis, Spiroclypeus vermicularis, Sherbornina carteri,* and *Gypsina ?discus,* together with *Halimeda,* also occur. Throughout the section in Core 135-841B-46R the sediments are fine-grained and poorly sorted, and the larger foraminifers are delicate with only parts of the outer flange broken. These features suggest that there was little or no postmortem reworking and that it is a live assemblage. Throughout most of Core 135-841B-47R the sediments are well-sorted fine sands with very low numbers of foraminifers, but at the base of these sands there is a very thin, hard calcarenite (Sample 135-841B-47R-2, 90–92 cm) containing fragments of the larger foraminifers together with planktonic forms. The occurrence of these benthic species with planktonic forms and the absence of miliolids suggests normal marine salinities; the presence of planktonic forms in the samples from Core 135-841B-46R and Sample 135-841B-47R-2, 90–92 cm, suggest contact with the open ocean. In contrast, however, the fine sands from within Core 135-841B-47R lack planktonic forms, suggesting that contact with the open sea ceased for a period until the sediments within Core 135-841B-46R were deposited. The assemblage of larger foraminifers from both cores is distinctly tropical. The absence of *Pellatispira* would normally place this assemblage in the Ta3 letter stage, which is equivalent to planktonic foraminifer Zones P10 to P14 (Adams, 1970; Chaproniere, 1983), but the presence of a Zone P16 planktonic assemblage within the upper part of Core 135-841B-46R suggests a correlation with the Tb letter stage.

SEDIMENT ACCUMULATION RATES

The three marine sedimentary sequences present at Site 841 are either separated by disconformities (between the lower middle Miocene and lower Oligocene) or faulting (between the upper Miocene and lower middle Miocene). Barren intervals or very impoverished faunas and floras throughout the upper Miocene to Pleistocene interval of Site 841 have limited the use of datum levels for sedimentation accumulation rate calculations. Faulting within the lower middle Miocene and lower Oligocene to upper Eocene parts of the section has also made accurate positioning of datums difficult because it has not been possible to estimate how much of the section is missing. Furthermore, in the shallow-water Eocene sequence only a few datums are available. For these reasons the figures used to calculate the sediment accumulation rates (Table 4) are, at best, approximations.

Table 4. Depths and ages of bioevents used to plot sediment accumulation rates for Site 841.

Depth (mbsf)	Age (Ma)	Events
60.0	5.6	LAD *Discoaster quinqueramus*; top CN9
203.0	8.3	FAD *Discoaster neorectus*; base CN8b
458.0	10.1	FAD *Gr. merotumida*; base N16
458.1	14.9	LAD *Praeorbulina glomerosa*; top N9
504.0	15.2	FAD *Orbulina suturalis*; base N9
549.0	16.5	FAD *Praeorbulina glomerosa curva*; within N8
549.1	36.0	FAD *De. tapuriensis*; base P18
604.0	37.5	Within Zone P16

Note: LAD = last appearance datum and FAD = first appearance datum.

Figure 34 illustrates the sedimentation accumulation rates based on the estimated bioevents in Table 4. The curve has been divided into six sections. The interval (A) from 604 to 549 mbsf, which covers the upper Eocene larger foraminiferal limestone sequence, has a low sediment accumulation rate of 14 mm/k.y. This figure is similar to that obtained from the paleomagnetic data. Between 549 and 458 mbsf (B), the sedimentation rate increases from 35 mm/k.y. in the lower part to 160 mm/k.y. for the upper part (C), covering an interval of lower middle Miocene volcanic siltstone, sandstone, and conglomeratic sequence. No paleomagnetic data are available for this interval. The lower boundary of this unit is an unconformity and the top is fault bounded. The base of the upper Miocene to Pleistocene section, between 458 to 203 mbsf (D), is an interval of volcanic conglomerates and sandstones, with high sedimentation rates of 142 mm/k.y. similar to the rate inferred from the paleomagnetic data. Between 203 and 60 mbsf (E), sediment accumulation rates fall to 53 mm/k.y. as the sequence becomes more fine grained. Above 60 mbsf (F), sedimentation rates fall to 11 mm/k.y. within a sequence of clays barren of calcareous microfossils which was deposited below the CCD.

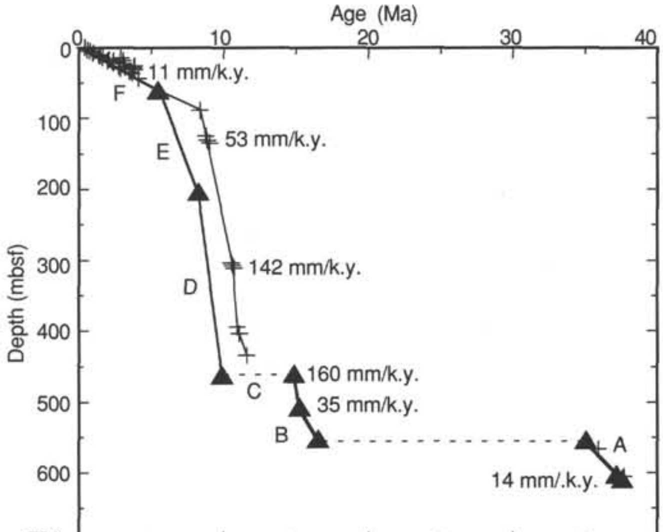

Figure 34. Graphic representation of age vs. depth data illustrating the sedimentation rates at Site 841 using bioevents and depths given in Table 4. Filled triangles = biostratigraphic datum points. A plot of the paleomagnetic data is also included for comparison, indicated by plus signs.

PALEOMAGNETISM

Remanent Magnetism

Nearly all remanent magnetization measurements were made with the pass-through cryogenic magnetometer on 7-cm^3 (soft sediment) or 8-cm^3 (consolidated sediment) cubes sampled from the working-half core sections. After measuring the natural remanent magnetization (NRM), the cubes were remeasured at the pass-through cryogenic magnetometer after alternating field (AF) demagnetization at 1, 2, 4, 7, 10, 15, 20, 25, 30, 40, 50, and 60 mT (and in some cases 80 and 100 mT) using the Schonstedt AF demagnetizer above 25 mT. A few discrete samples were also analyzed using the Molspin Minispin spinner magnetometer and the Molspin pulse magnetizer to investigate the type of magnetic grains contained within the samples.

Archive-half sections from APC-drilled Cores 135-841A-1H through 135-841A-8H were measured with the pass-through cryogenic magnetometer to determine magnetic stratigraphy, and also in oriented Cores 135-841A-4H through 135-841A-8H to determine paleomagnetic declination. XCB-drilled cores were not measured with the pass-through magnetometer because they suffered moderate to heavy drilling disturbance and were unlikely to produce reliable results.

Magnetic Properties

The sediments at Site 841 are strongly magnetic. Their NRM intensities range between 4 and 1000 mA/m with a mean of 360 mA/m in Hole 841A, between 1.5 and 1220 mA/m with a mean of 230 mA/m in Hole 841B, and between 10 and 930 mA/m with a mean of 300 mA/m in Hole 841C. The strong magnetizations probably result from volcanic material ubiquitously present in the sediments. In contrast to other Leg 135 sites, the sediment color at this site is dominantly light gray to light brownish gray because of a high content of vitric volcanic silt and sand (see "Lithostratigraphy" section, this chapter).

Isothermal remanent magnetization (IRM) acquisition curves (Fig. 35) show a rapid saturation with increasing magnetizing field strength, indicating that the magnetic grains within both the sediments and the igneous rocks behave like magnetite.

Another factor in producing the strong magnetizations is a pervasive upward-oriented overprint that gives the sediments NRM inclinations near –90° and completely masks their polarities. The vertical direction of the overprint implies that it results from exposure of the sediments to strong magnetic fields (an IRM) in the core barrel and/or drill string. The sediments acquire this strong drill-string-induced IRM because some of their magnetic grains have low coercivities, although median destructive field (MDF) values are sometimes as high as 20 to 40 mT (Fig. 36). At times when the drill-string-induced IRM was not excessively high the original polarity of the sediment was not obscured by the overprint, although the inclination is usually biased to a shallower value (Fig. 36). In other samples with a stronger drill-string IRM, reversed polarity samples have been overprinted to appear normally polarized (Fig. 36). However, because it mainly resides in low coercivity grains, this overprint is often removed with moderate AF demagnetization (often 5–15 mT but sometimes higher; Fig. 36) leaving a stable characteristic remanence that holds geologic information.

In the basaltic andesite samples (325 to 326 mbsf and 390.5 to 393.7 mbsf) the NRM magnetization intensities ranged from about 0.5 to 30 A/m. The magnetic remanence carriers appear to be magnetite, as evidenced by the low field saturation of IRM (Fig. 35).

Because AF demagnetization of the core archive halves during Leg 135 was limited to 15 mT, characteristic magnetizations were not always isolated. As a result, measurements made with the pass-through magnetometer of the archive halves of the APC cores must be regarded as reconnaissance results only.

Magnetic Polarity Stratigraphy

Determination of magnetostratigraphy at Site 841 proved a difficult task. Apart from the inevitable problem with the IRM overprint in sediments, the determination of magnetic polarity stratigraphy was complicated by volcaniclastic silt and gravel layers, which were quite abundant (see "Lithostratigraphy" section, this chapter). These sediments were probably deposited rapidly, some perhaps as turbidites. Thus, they are likely to record

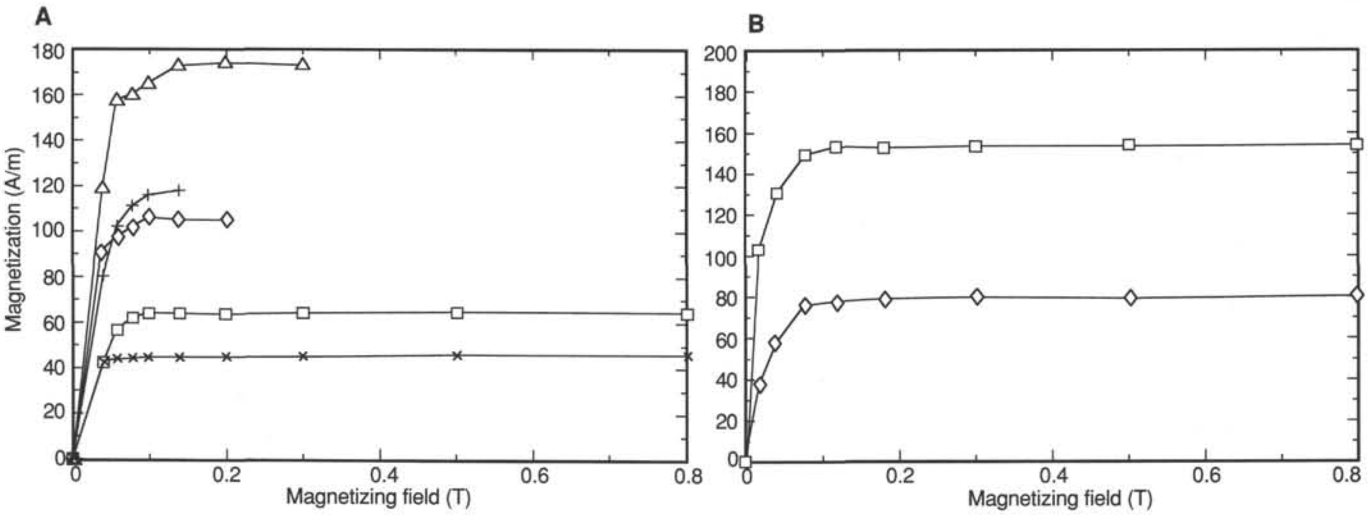

Figure 35. **A.** Isothermal remanent magnetization (IRM) acquisition curves for five sediment samples from Site 841. Samples 135-841A-19X-1, 2–4 cm; 135-841B-7R-1, 101–103 cm; and 135-841B-15R-1, 34–36 cm, are vitric siltstones. Sample 135-841B-38R-2, 145–147 cm, is a volcanic siltstone and Sample 135-841B-42R-3, 34–36 cm, is a clayey calcareous sandstone. The curves all display saturation in low applied fields between 0.08 and 0.14 T, indicating that the remanence carrier is magnetite in these sediments. **B.** Isothermal remanent magnetization (IRM) acquisition curves for two samples of basaltic andesite at about 392 mbsf in Hole 841B. The samples display saturation in applied fields between 0.08 and 0.12 T, indicating the remanence carrier to be magnetite.

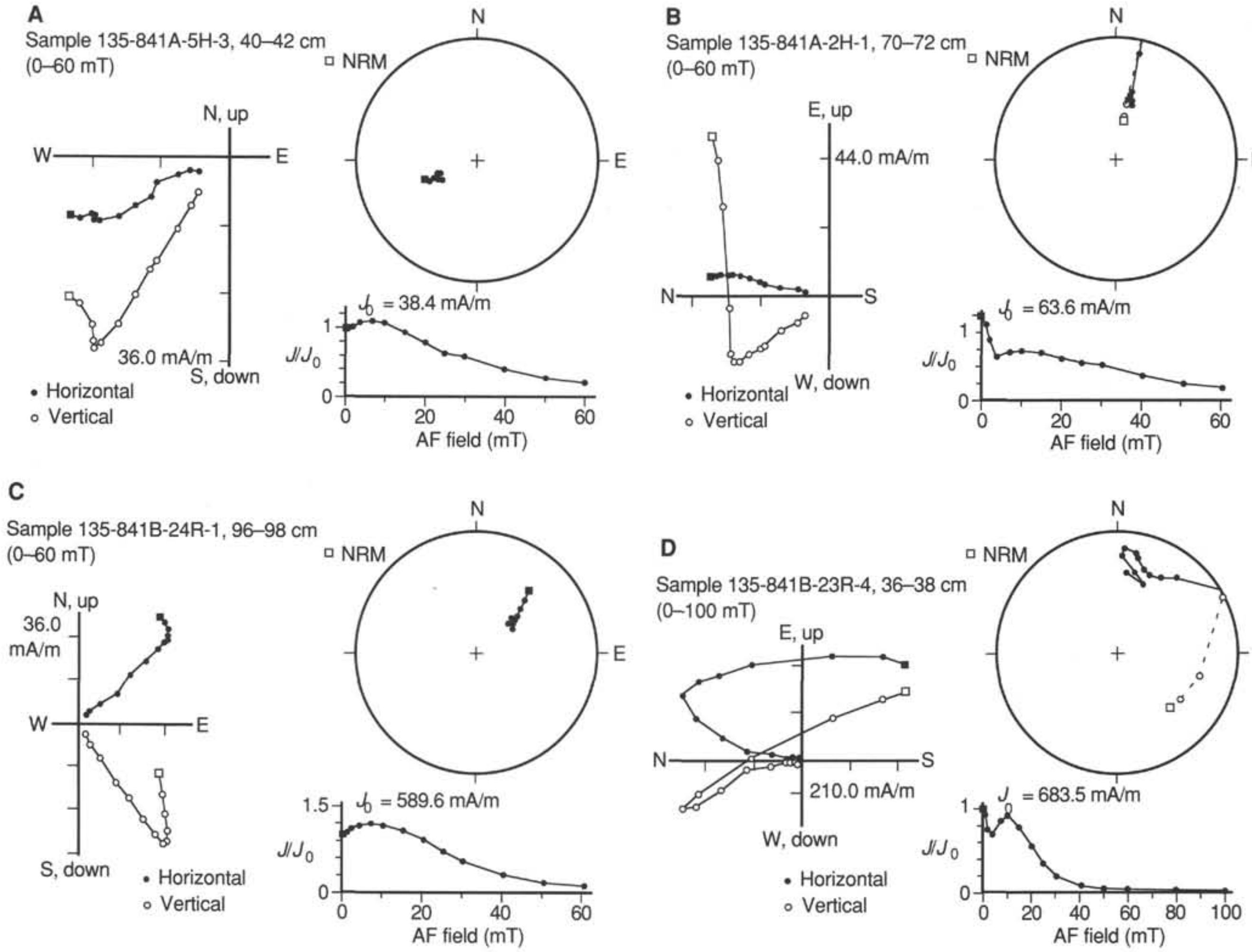

Figure 36. Behavior of Site 841 sediment samples during alternating field (AF) demagnetization. **A.** Sample of brown nannofossil ooze from Hole 841A does not change polarity and reveals a characteristic magnetic component above 7 mT AF, although the median destructive field (MDF) is about 40 mT. **B.** Sample of gray, vitric mud from Hole 841A changes polarity at 4 mT AF. It shows two magnetization components with distinctly different MDF; one value is due to the strongly remagnetized but low coercivity components (the drill-string IRM, MDF = 4 mT), and one is due to the intrinsic NRM of the sediment (MDF = 25 mT). **C.** Volcaniclastic silt sample from Hole 841B does not change polarity, although the inclination is steepened and reveals a characteristic magnetic component above 7 mT AF demagnetization, even though the MDF is about 30 mT. **D.** Another sample from Hole 841B changes polarity by 4 mT but does not show a characteristic stable remanence until after 25 mT AF demagnetization. The MDF is 22 mT and the drill-string IRM severely biases the remanence. In each set of plots an equal area plot of vector endpoints is shown at upper right, a normalized intensity decay plot is at lower right, and an orthogonal vector endpoint plot is shown at left.

the magnetic field only for an "instant" of geologic time. Furthermore, because of their large grain sizes, these sediments are often poor recorders of magnetic field direction.

Because the drill-string overprint is directed upward, it gives the sediments an artificial "normal" polarity (for the Southern Hemisphere) with magnetic inclinations approaching –90°. Furthermore, in the NRM, this overprint almost always masks the inherent polarities of the sediments. Even after AF cleaning to 15 mT, the magnetic inclinations are not distributed symmetrically around zero, as expected if the overprint had been completely removed. As the APC archive sections could only be AF demagnetized to 15 mT, this was insufficient to remove drill-string-induced IRM in many sections. Hence, many reversed polarity sediments are overprinted with negative (i.e., apparently normal) inclinations, so they are not reliable indicators of polarity. Furthermore, declination was disturbed in some core sections, so it also was not always a reliable polarity indicator. Hence, polarity zones were defined by examining both declination and inclination. Where both were consistent, a reliable polarity determination was possible. Inconsistent zones have been classified as either "probably normal," "probably reversed," or "indeterminate."

Polarity determination in XCB and RCB cores of Holes 841A and 841B were hampered by low recovery. Hence, it is difficult to locate polarity boundaries and determine the sequence of reversals. Because of these limitations, magnetostratigraphy interpretations at Site 841 given here are somewhat tentative.

The magnetostratigraphy of the APC cores of Hole 841A (Fig. 37; Table 5) can be interpreted as a relatively continuous sedimentary sequence extending from the Brunhes to the Gilbert chrons. The Brunhes Normal Chron, the Brunhes/Matuyama boundary, and the Jaramillo Subchron are all clearly seen in Cores 135-841A-1H and -2H. The majority of the sections beneath Jaramillo are reversely polarized, with relatively short-duration normal subchrons. The biostratigraphic data in this section are poor (see "Biostratigraphy" section, this chapter), but they indicate a late Miocene age for Core 135-841A-7H.

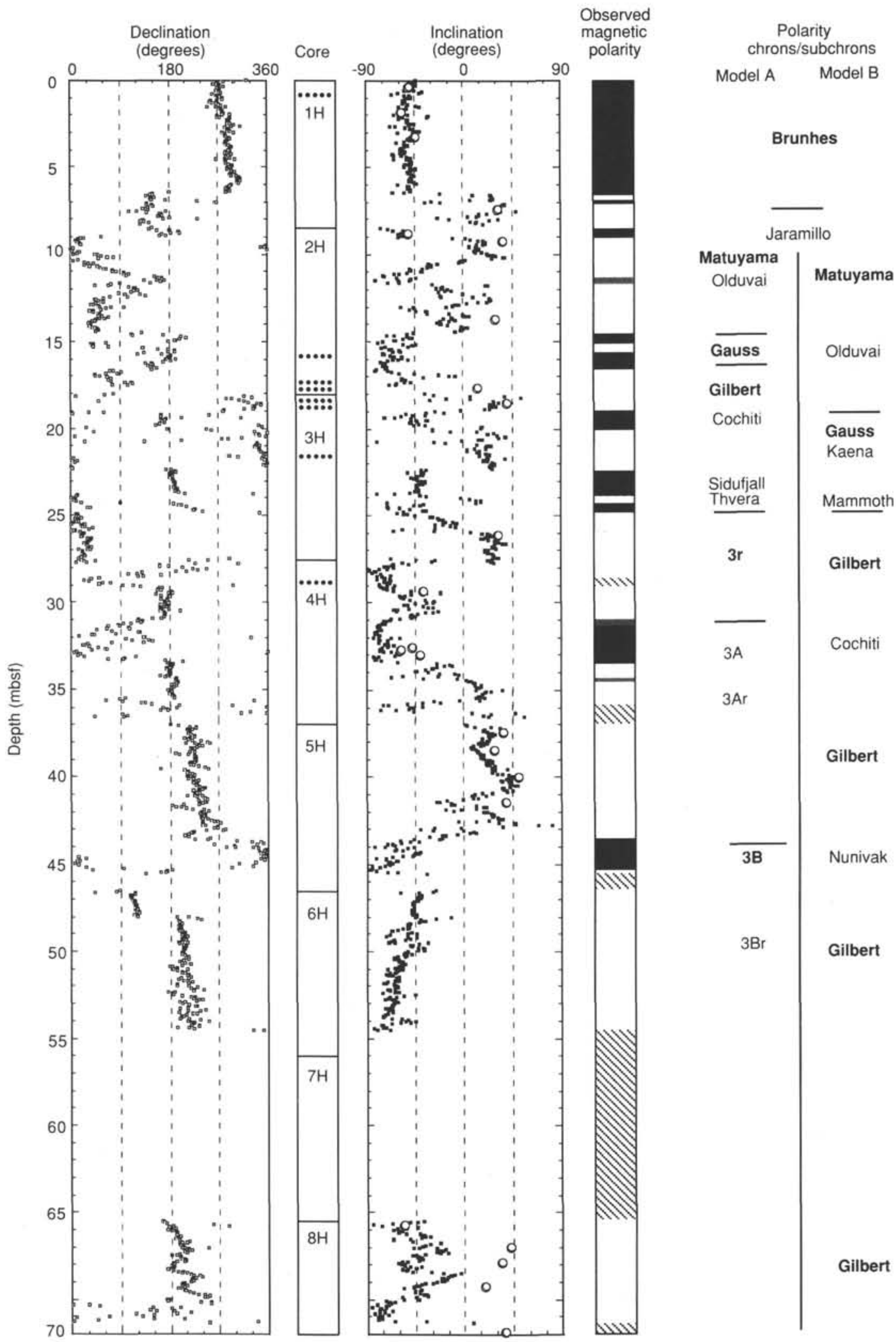

Figure 37. Magnetic polarity stratigraphy from Hole 841A, based upon pass-through cryogenic magnetometer measurements on core archive halves (squares) supplemented by discrete specimens (circles). Wide columns at middle and left show the magnetic inclination and declination, respectively. The narrow column in the middle shows core boundaries; disturbed zones are indicated by dots. Columns at right show observed and interpreted magnetic polarities (black = normal, dark stipple = probably normal, hachure = indeterminate, light stipple = probably reversed, and white = reversed). At far right, chron and subchron names are shown in large and small type, respectively. Below the Jaramillo Subchron, models A and B are shown, indicating two possible polarity interpretations. For further discussion, see text.

Table 5. Magnetic polarity of Site 841.

Depth (mbsf)	Polarity	Age (Ma)	Chron/subchron		
0.0					
	N		BRUNHES		
6.5					
	R				
6.8					
	N		BRUNHES		
7.0		0.73			
	R		MATUYAMA		
8.5		0.91			
	N		Jaramillo		
9.0		0.98			
			Model A:		**Model B:**
10.4					
	R?				
11.3		1.66			
	N?		Olduvai		
11.7		1.88			
	R?				
12.4					
	R				
12.7					
	R?				
14.5		2.47		1.66	
	N		GAUSS		
15.0					
	R?				Olduvai
15.5					
	N				
16.5		3.40		1.88	
	R?		GILBERT		
17.5					
	I				
18.9		3.88		2.47	
	N		Cochiti		GAUSS
19.8		3.97		2.92	
	R?				Kaena
20.8					
	R				
22.3		4.40		2.99	
	N		Sidufjall		
23.8		4.47		3.08	
	R				Mammoth
24.3		4.57		3.18	
	N		Thvera		
24.8		4.77		3.40	
	R?				
25.9					
	R		3r		GILBERT
27.7					
	R?				
28.5					
	I				
29.0					
	R?				
30.9		5.35		3.88	
	N?				
31.3					
	N		3A		Cochiti
33.5				3.97	
	R?				
34.2					
	N?				
34.4		5.89			
	R				
35.6					
	I		3Ar		
37.0					
	R				
41.3					
	R?				
41.6					
	R				
41.8					
	R?				
42.0					
	R				
42.8					
	R?				

Table 5 (continued).

Depth (mbsf)	Polarity	Age (Ma)	Chron/subchron		
43.0					
	R				
43.2					
	R?				
43.6		6.37		4.10	
	N		3B		Nunivak
45.3		6.50		4.24	
	R?				
45.5					
	I				
46.5					
	R		3Br		
54.5					
	I				
65.5					
	R?				
71.4					
71.9					
	R				
72.3					
	I				
91.2					
	N	(8.46)	4Ar-1		
91.5					
	I				
100.8					
	R				
100.9					
	I				
120.3					
	R				
120.5					
	I				
129.6					
	N	(8.76)	4Ar-2		
130.4					
	I	(8.92)			
139.3					
	R				
139.5					
	I				
148.9					
	N		5		
159.5					
	I				
170.0					
	N				
171.3					
	R				
171.8					
	N				
191.1					
	R				
191.2					
	I				
198.8					
	N		5		
239.3					
	I				
247.0					
	R				
247.2					
	N				
268.9					
	I				
277.1					
	R		5		
277.2					
	I				
280.1					
	N				
280.7					
	I				
295.9					
	R				
296.4					
	N				
297.7					

Table 5 (continued).

Depth (mbsf)	Polarity	Age (Ma)	Chron/subchron
	R		
298.1			
	N		5
305.5		(10.42)	
	R		
307.3			
	N		
307.5			
	R		5r
309.5		(10.54)	
	N		
311.2			5r-1
	R		
311.4			
	N		
313.0		(14.59)	
	R		5r
336.3			
	N		
336.5			
	I		
343.3			
	R		
392.8		(11.03)	
	N		5r-2
401.0		(11.09)	
	R		
402.0			
	I		
419.0			
	R		
421.1			
	I	(11.64)	
430.8			
	N		5A-1
431.6			
	I		
439.2			
	R		
439.1			
	I		
458.3			
	R		
458.7			Hiatus
	N		5C ?
540.2			
	I		Hiatus
545.4			
	N		13
564.9		(35.87)	
	R		13r
565.4			
	I		
575.2		(37.24)	
	N		15
596.0			
	I		
602.6			15r
	R		
602.7			
	I		
604.0		(37.68)	
	N		16
604.6			
	I		
643.4			
	N		
645.0			
	I		
TD			

Notes: Ages from magnetic polarity reversal time scales of Berggren et al. (1985) and Harland et al. (1982). Models A and B are two different interpretations of the polarity intervals from the lower part of Hole 841A (10.4–71.4 mbsf). Chron names in capital letters, subchrons in lowercase letters. TD = total depth of hole.

Normal polarity subchrons between 15 and 45 mbsf, however, do not closely match the magnetic polarity reversal time scale. As a result, two possible models are shown in Figure 37. Model "A" uses a probably normal polarity zone at 11.3 to 11.7 mbsf to represent the Olduvai Subchron, the two normal polarity zones from 14.5 to 16.5 mbsf to represent the Gauss Chron, the three normal zones at 18.9 to 19.8 mbsf, 22.3 to 23.8 mbsf, and 24.3 to 24.4 mbsf to represent the Gilbert Chron, and the two normal zones at 30.9 to 34.4 mbsf and 43.6 to 45.3 mbsf to represent anomaly 3A and 3B chrons. In Model "B" the normal zone at 14.5 to 16.5 mbsf is interpreted as Olduvai. The next three normal zones are modeled as the Gauss Chron with intervening Kaena and Mammoth reversed subchrons, although the Kaena appears much longer than expected. Finally, the normal polarity zones at 30.9 to 34.4 mbsf and 43.6 to 45.3 mbsf are interpreted as the Cochiti and Nunivak subchrons of the Gilbert Chron.

Model B is more satisfying because it does not leave out major subchrons as does Model A; it also accounts for large intervals of reversed polarity in Cores 135-841A-4H to -8H as part of the Gilbert reversed chron. The sedimentation rate of the Brunhes through Jaramillo section implies a slow sedimentation rate of 8.8 mm/k.y., while the rate appears to increase to 62.5 mm/k.y. in Gilbert (Model B).

In contrast to the top part of the core, the polarity record of Site 841 below the APC section is remarkably simple (Fig. 38; Table 5). The polarity is mostly normal from 148.9 to 307.5 mbsf and mostly reversed from 313.0 to 392.8 mbsf. Biostratigraphic data (see "Biostratigraphy" section, this chapter) imply that the normal interval is Miocene Chron 5; hence, the reversed interval below is probably reversed Chron 5r. The normal intervals between 72 and 149 mbsf are hypothesized to be normal subchrons in Chron 4Ar, whereas those from 392.8 to 458.7 mbsf are assigned to subchrons in Chron 5r. The sedimentation rate during anomaly 5 was 113.3 mm/k.y. (Fig. 39).

The biostratigraphy shows hiatuses at 459 and 545 mbsf, both occurring within normal polarity zones. It also gives an age of about 15.2 to 16.5 Ma for the interval of the upper hiatus. The nearest long normal polarity zone is anomaly 5C which ended at 16.2 Ma. Below the older hiatus, biostratigraphy gives an age of 36 Ma at 549 mbsf, implying an age near anomaly 13. Hence the three normal polarity zones between 545 and 604 mbsf are assigned to anomalies 13, 15, and 16, respectively. The sedimentation rate during this period was about 31.5 mm/k.y. (Fig. 39).

Magnetic Susceptibility

Sediments

Volume magnetic susceptibility was measured on a routine basis on whole (i.e., unsplit) core sections of sediments (and basalts) from both holes at Site 841, whenever the core sections appeared to be relatively full in cross section. Magnetic susceptibility values in Hole 841A sediments range from 25×10^{-6} to 2620×10^{-6} cgs, with a mean value of 250×10^{-6} cgs, and display both long and short wavelength variations (Fig. 40).

The broad-scale variation in susceptibility of Hole 841A of APC sediment cores (Fig. 40) consists of half an order of magnitude oscillation over 10–20 m of depth. Most likely, these broad peaks reflect variations in the general input of more strongly magnetic volcanic material into the nannofossil ooze, which in itself is only weakly magnetic.

Magnetic susceptibility values in Hole 841B sediments range from 3×10^{-6} to 3100×10^{-6} cgs, with an average of 630×10^{-6} cgs, and a plot of the data displays rather long wavelength variations (Fig. 41) for the interval 170 to 800 mbsf. Minima in the susceptibility are seen at 250, 470, 670, and 790 mbsf, whereas the maxima are found at 205, 395, 550 and 760 mbsf, respectively.

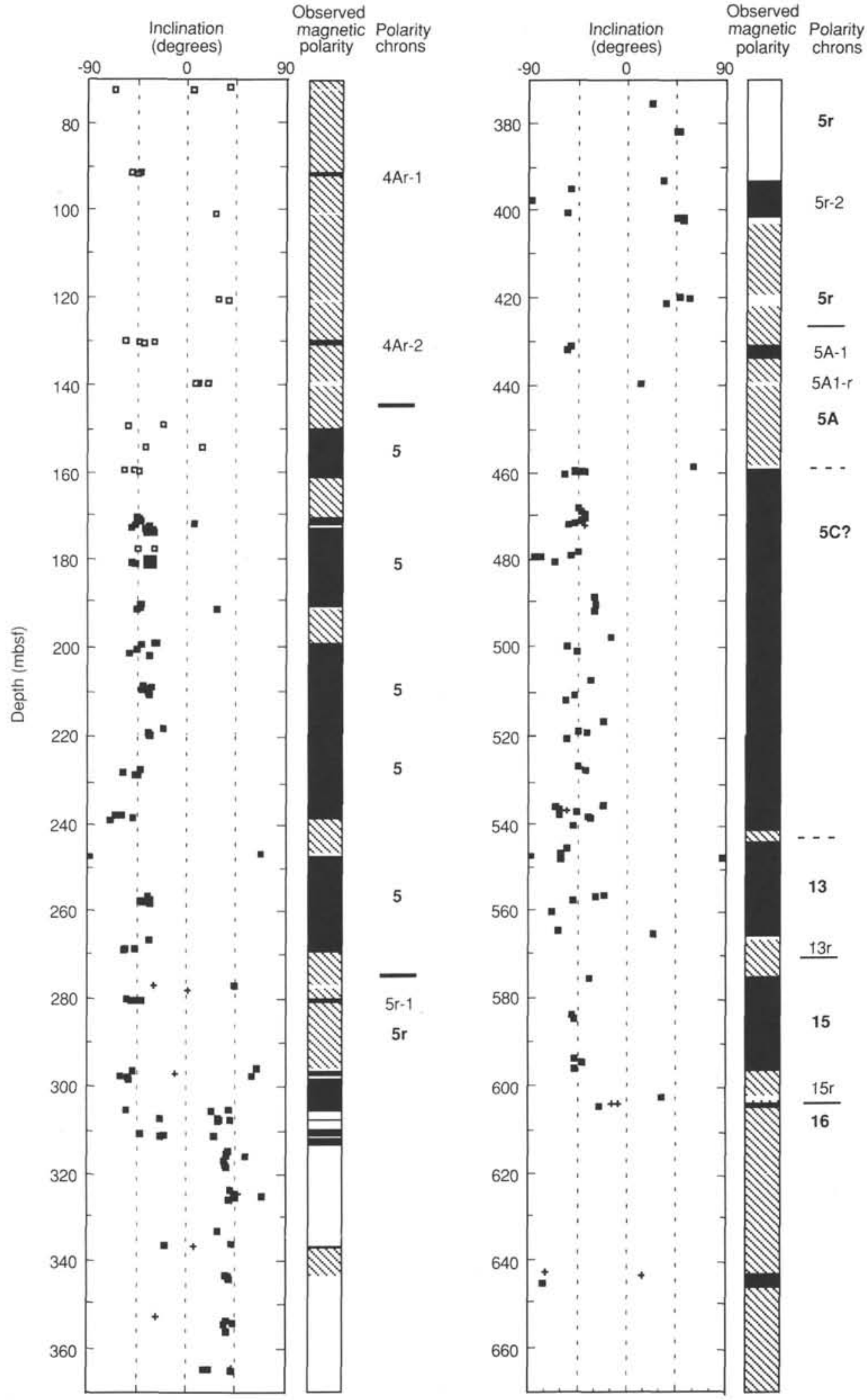

Figure 38. Magnetic polarity stratigraphy below 70 mbsf for Site 841, based upon cryogenic measurements of discrete samples. Open squares are from Hole 841A, solid squares are from Hole 841B. The wide column shows the magnetic inclination. Narrow columns show observed magnetic polarities (black = normal, hachure = indeterminate, and white = reversed). At right, numbers of interpreted polarity chrons are indicated.

The latter cyclicity is likely to indicate broad lithological variations in the vitric sediments, and hence perhaps in the regional volcanic activity in the area, showing variations either in the ash concentrations or in the concentration of iron-bearing minerals in the ash.

Core Orientation

APC-drilled Cores 135-841A-4H through 135-841A-8H were oriented using the multishot camera (see "Explanatory Notes" chapter, this volume). Usable orientation photographs were obtained for all five cores (Table 6); however, Core 135-841A-7H encountered a resistant sediment layer and returned nearly empty.

Magnetic measurements were made with the pass-through cryogenic magnetometer on archive-half core sections and discrete samples. It was not possible to calculate mean paleomagnetic poles using the archive-half core measurements because the inclinations were inconsistent and apparently biased by the drill-string IRM, even after AF demagnetization at 15 mT. It was also impossible to calculate mean poles with the shipboard discrete samples because not enough reliable results were available from undisturbed core sections.

Declination measurements from the archive halves, however, appeared to be more reliable. Even though most of the cores have apparently disturbed sections that yielded scattered declination values, each has sections with good serial correlation. Interestingly, each of the four oriented APC cores displayed a clockwise shift in declination downcore. Least-square line regressions on the declination measurements gave shifts of 2.7°–5.5°/m (Table 7). Apparently, the APC rotates as it is injected into the sediments.

To calculate mean declinations for each oriented core, the least-squares line regressions were used to extrapolate the declination value at the top of each core. Because the multishot tool orients the APC just before it is fired, the top-of-core declination value is assumed to be the most nearly correct. Corrected declinations ranged from 164.8° to 212.3°, with an average of 189.4° ± 9.7° (Table 7).

INORGANIC GEOCHEMISTRY

A total of 20 interstitial water samples were collected at Site 841, six in Hole 841A and 14 in Hole 841B. In Hole 841A, interstitial water was collected from every core in the uppermost 31 m. Below this depth, samples were taken every second core. However, below 70.5 mbsf (Core 135-841A-8H), low recovery prevented water sampling. In Hole 841B, the sediments were relatively hard and well lithified, and the least indurated samples were chosen. Standard ODP squeezing techniques were used for the removal of water samples (see "Explanatory Notes" chapter, this volume). The volumes retrieved from the sediment samples range from 3 to 34 mL. One sample collected in Section 135-841B-37R-3 was so well indurated that no pore water could be squeezed from it at a pressure of 35,000 psi. Results of the interstitial water chemical analysis are listed in Table 8. Hole 841B was drilled 20 m north of Hole 841A. Because we assume that a comparison of data can be made between the two holes, the depth-concentration distributions are combined in Figure 42.

In Holes 841A and 841B, dissolved major constituents (chloride, sodium, calcium, magnesium, potassium, and sulfate) were determined. Subsequent charge balance calculations yielded sodium concentrations. Ammonia, phosphate, silica, strontium, and manganese were also carried out using colorimetric methods and flame AA spectrophotometry.

Chemical Components

To assist with drilling operations at Hole 841B, drilling mud was pumped between alternate cores. Therefore, special attention was paid to possible contamination of the pore water by drilling-mud filtrate. The composition of the drilling-mud filtrate is given in Table 8. On the basis of chloride analyses, we estimated that no sample was contaminated with more than 2% drilling-mud filtrate. The chemical distributions presented in Figure 42 show that the data obtained in Hole 841A can be favorably compared to those obtained in Hole 841B. In Hole 841A, the distribution of the major cations follows the pattern commonly described for marine sediments (Gieskes, 1983): chloride and sodium concentrations are fairly uniform and similar to the average seawater concentrations; and the concentration-depth profiles of calcium, magnesium, and potassium indicate an increase in Ca and a decrease in Mg and K.

The calcium and magnesium distributions, however, show an almost linear relationship with a $\Delta Ca/\Delta Mg$ ratio of about –0.78. This feature reflects the alteration of volcanogenic material in sediment characterized by high sedimentation rates. In the uppermost 70 mbsf, the decrease in alkalinity must be related to a downward diffusive exchange with the low alkalinity value determined in Hole 841B.

In the upper Miocene sediments of Hole 841B (from 171.3 to 257.4 mbsf), the increase in calcium and chloride associated with the decrease in magnesium, potassium, and sodium is unusual. At 257.4 mbsf, the chloride and calcium concentrations reach values of 142.6 mM and 612 mM, respectively, the concentrations of potassium and magnesium drop toward zero, and the sodium concentration reaches a minimum value of 347 mM. These drastic changes in concentrations of the dissolved major ions define a reaction zone situated within the interval 250 to 640 mbsf. The lower boundary of this zone is well defined by a calcium decrease and chloride, sodium, magnesium, and potassium increases below 640 mbsf. These trends in concentration are opposite to those observed during seawater/basalt interactions. The chloride and sodium concentrations are higher than those of "average" seawater (Broecher and Peng, 1982) and rule out the possibility of dilution by an advection of seawater to the basement below the sediment cover. The very low porosity determined below 650 mbsf (e.g., about 15%; see "Physical Properties" section, this chapter) also argues against a fluid circulation in this section of rhyolitic breccias, tuffs, and welded tuff (see "Igneous Petrology" section, this chapter).

In the interval between 250 and 640 mbsf, the chemistry of the pore water indicates that the collected interstitial water is some of the most intensively modified pore water of seawater origin yet sampled by the ODP/DSDP programs, and can be defined as $CaCl_2$-rich brine. The porewater chemistry of the Site 841 is similar to that obtained in only three other drilling sites in the world: Sites 792 and 793 occupied during Leg 126 in the Izu-Bonin arc sedimentary basin (Taylor, Fujioka, et al., 1990) and Site 802 occupied during Leg 129 in the Central Mariana Basin (Lancelot, Larson, et al., 1990). On Leg 126, a $CaCl_2$-rich brine was observed at depth in Oligocene sediments. At Site 792, a maximum Ca concentration of 163.3 mM was observed at 599 mbsf and no chloride deviation was observed. At Site 793 the concentrations of Ca and Cl reach stable levels of about 300 and 710 mM below 997 mbsf. At Site 802, maximum Ca and Cl concentrations of 130 and 627 mM were determined at 109 mbsf in Miocene sediment.

The changes in Ca, Mg, K, and Na at Site 841 are much more pronounced than are usually observed in porewater-depth profiles, and are probably caused by the combined effect of chemical exchange with abundant volcanogenic material and high rates of sedimentation. Increased sedimentation rates cause diminished diffusive exchange with the overlying ocean water (Gieskes and Johnston, 1984), thus allowing steeper concentration gradients to be maintained. Nevertheless, quantitative estimates of the diagenetic processes at Site 841 await isotope measurements of pore

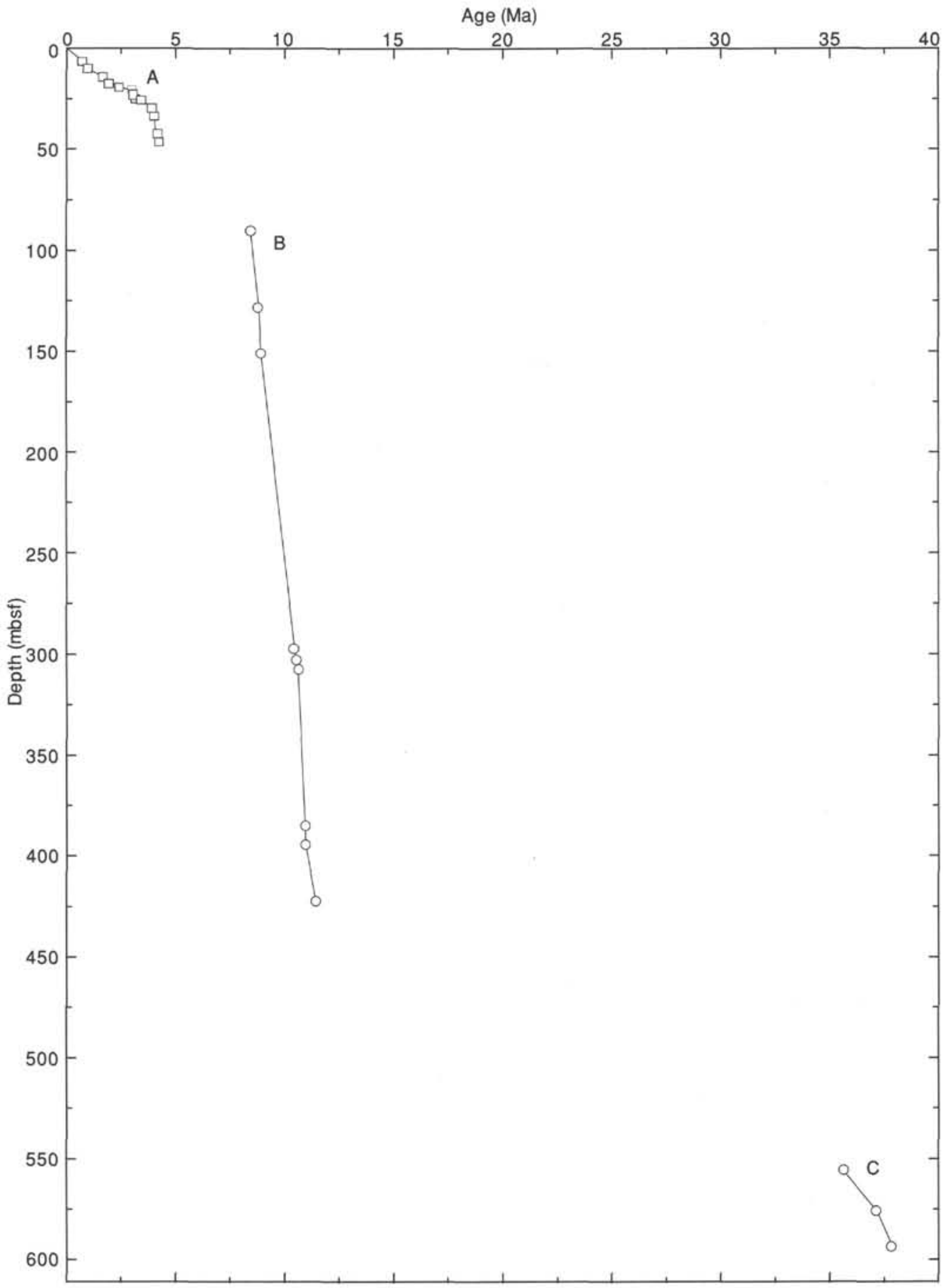

Figure 39. Age vs. depth plot from magnetic polarity stratigraphy, Holes 841A and 841B combined. Age/depth points are connected with solid lines. Index figure shows relative positions of parts A, B, and C (insets). **A.** Age vs. depth plot from magnetic polarity stratigraphy of APC cores, Hole 841A. Two possible models (A and B) below the Jaramillo Subchron are shown. **B.** Age vs. depth plot from magnetic polarity stratigraphy between 90 and 430 mbsf, Holes 841A and 841B. **C.** Age vs. depth plot from magnetic polarity stratigraphy between 540 and 620 mbsf, Hole 841B.

waters and quantitative determinations of the secondary mineralogical phases (including clays, zeolites, sulfates, and other secondary minerals).

Processes leading to enhanced Cl concentrations in pore waters include dissolution of evaporites, gas hydrate formation, shale membrane filtration, and uptake of water by secondary hydrous minerals. As evaporites are absent and concentrations of organic carbon and methane are low (see "Organic Geochemistry" section, this chapter), the first two processes may be discounted here. If the elevated Cl concentrations were caused by shale membrane filtration, a corresponding Cl minimum should also be observed (Gieskes et al., 1990; Blanc et al., 1991). We suggest,

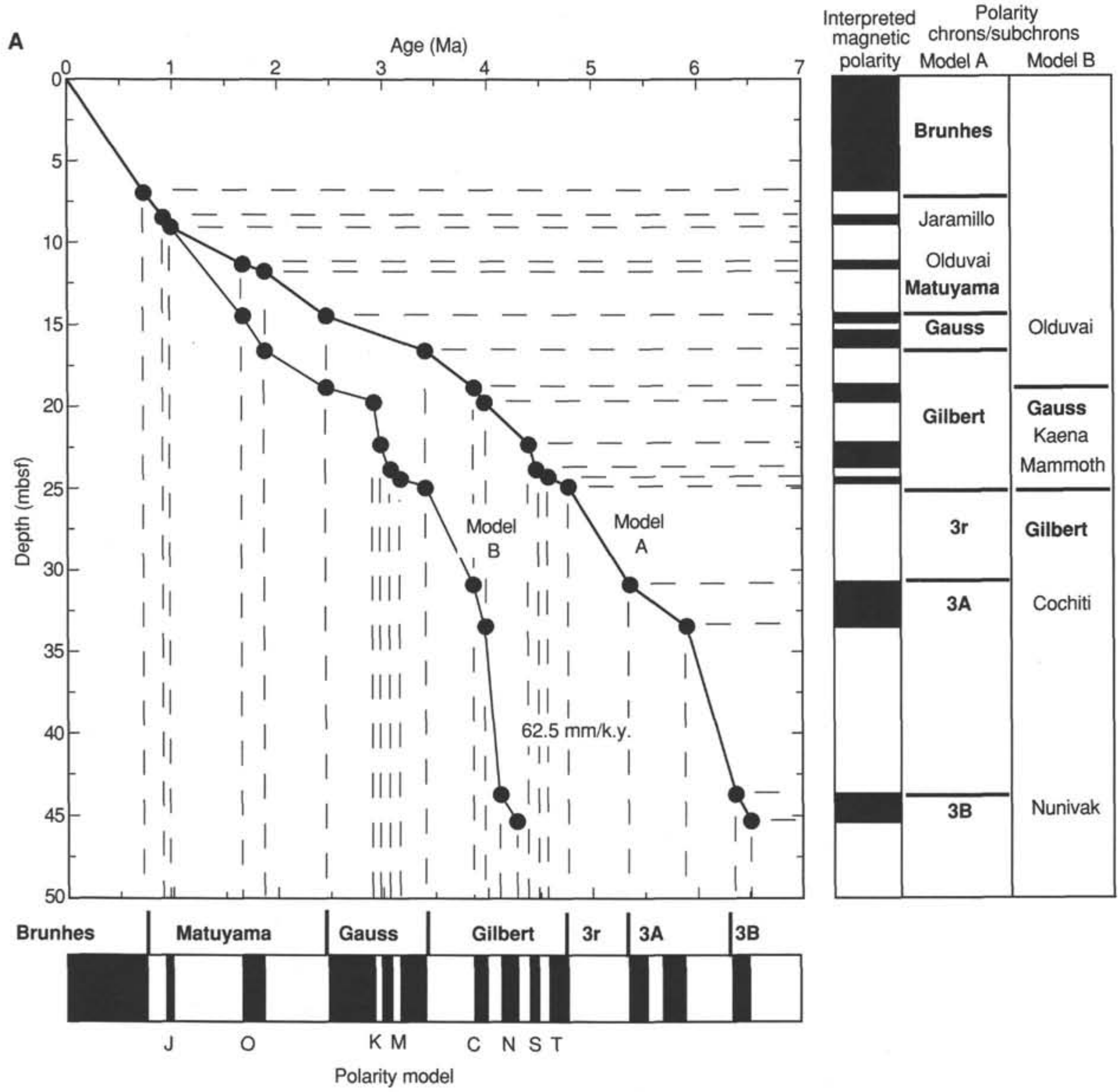

Figure 39 (continued).

Table 6. APC core orientation data, Hole 841A.

Core no.	Camera no.	Compass	Inclination Direction	Inclination Drift	Declination
135-841A-					
4H	3250	A	N50°E	1.5°	321°
5H	3250	A	65°	1.5°	157°
6H	3209	B	75°	1.5°	348°
7H	3209	B	75°	1.8°	154°
8H	3250	A	75°	2.0°	303°

Notes: Magnetic declination at site is 14.5°E. Compass B was misaligned; to correct declination values, add 13°. Inclination is the off-vertical angle of the core; drift and direction are the dip angle and dip direction (clockwise from north) of a plane perpendicular to the core axis. Declination is the angle between the double line on the core liner and magnetic north (measured clockwise).

Table 7. Oriented APC paleomagnetic declination data, Hole 841A.

Core	Declination (corrected)	Rotation
135-841A-4H	164.8°	2.7°/m
135-841A-5H	212.3°	5.2°/m
135-841A-6H	192.2°	3.3°/m
135-841A-8H	188.4°	5.5°/m
Mean:	189.4° ± 9.7°	

therefore, that the high chloride concentrations are probably caused by uptake of water by secondary minerals, as also recorded at the ODP Leg 126 and 129 sites.

The sulfate concentration decreases from 28.7 mM at 6 mbsf to 11.9 mM at 257.4 mbsf (Fig. 42). From this depth to 651.5 mbsf, the sulfate concentrations show values fairly uniform of about 1.3 ± 0.3 mM. Below 651.5 mbsf, the sulfate concentration increases

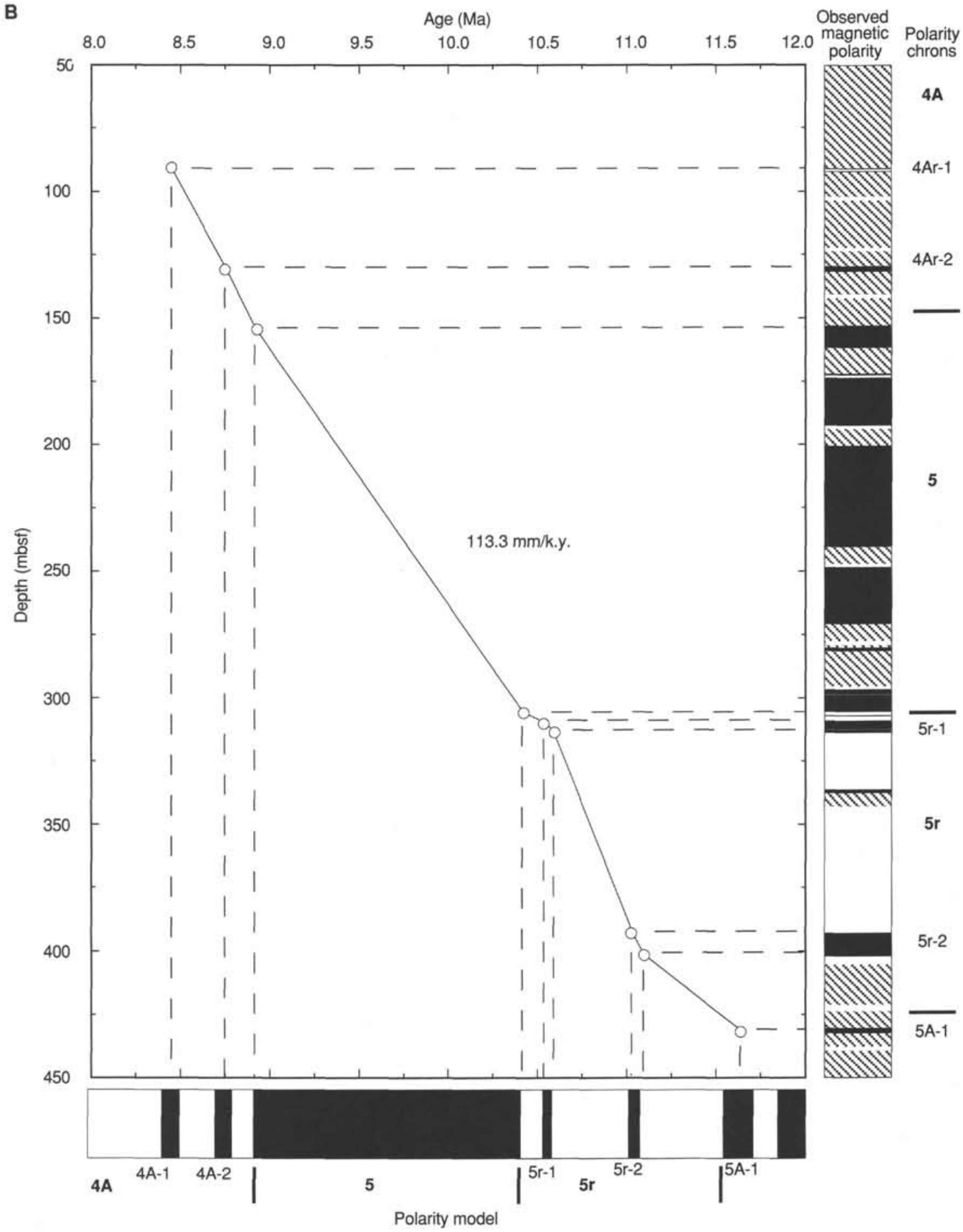

Figure 39 (continued).

and reaches a value of 21.8 mM at 748.7 mbsf. The distribution of sulfate observed in the uppermost 257.4 mbsf probably results from bacterially mediated sulfate reduction. The ammonia maximum of 210 μM at 200.2 mbsf and the phosphate maximum at 24 mbsf also argue for biogenic oxidation of the organic matter. Because phosphate is preferentially released during degradation of organic matter, the phosphate maximum occurs at a shallower depth than the ammonia maximum (Gieskes, 1983). Below 257.4 mbsf, sulfate concentrations are probably not controlled by bacteria activity. The absence of an increase in the alkalinity in the uppermost 250 mbsf indicates that alkalinity is not controlled by the sulfate reduction processes. The relatively low alkalinity below 228.5 mbsf probably results from the precipitation of carbonate in response to the release of calcium from altered volcanogenic material. The amount of calcium carbonate precipitated is expected to be very low; thus, this hypothesis does not conflict with the very low amount of sedimentary carbonate present (see "Organic Geochemistry" section, this chapter).

The distributions of dissolved silica, strontium, and manganese show great complexity and are causally related to the local

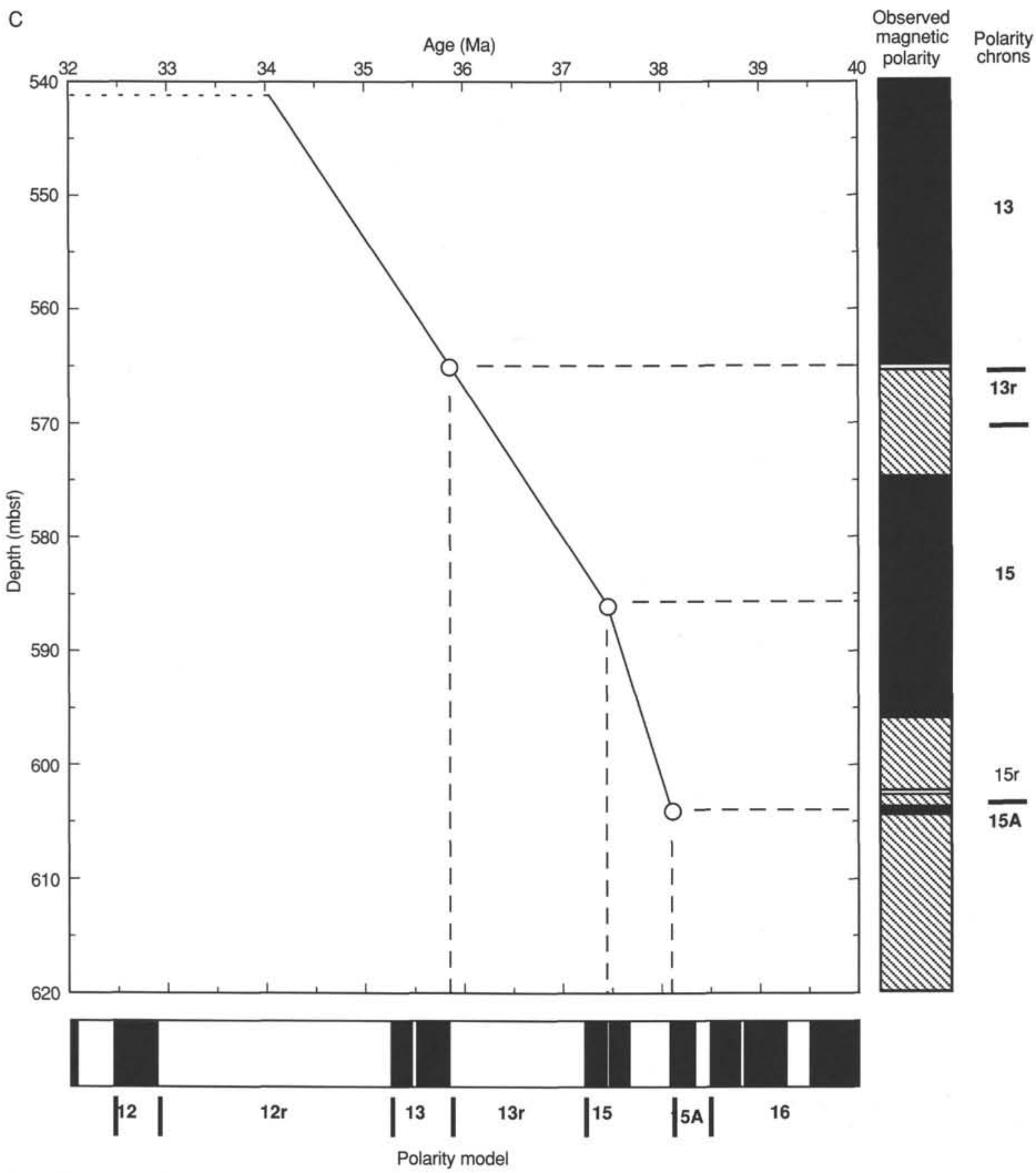

Figure 39 (continued).

diagenetic processes (Table 8 and Fig. 42). Further lab-based investigations on shore are necessary to define the possible reactions affecting their concentration. The steep gradients observed in silica between 257.4 and 296.4 mbsf, however, indicate a high reaction rate leading to an uptake of silica in solid phases.

Conclusions

At Site 841, the pore waters have been extensively modified from standard seawater values and include a $CaCl_2$-rich brine. The variations in concentrations of Ca, Mg, K, Na, and Cl are abnormal for average marine sediments and are probably caused by the combined effect of abundant volcanogenic material and high rates of sedimentation leading to very low diffusivity. The observed changes of dissolved sulfate, ammonia, and phosphate in the uppermost 200 mbsf are likely to be related to the decomposition of organic matter by sulfate-reducing bacteria. The observed changes in silica, strontium, and manganese concentrations are probably controlled by diagenetic reactions involving the alteration of the volcanogenic material.

ORGANIC GEOCHEMISTRY

Shipboard organic geochemical analysis of samples from Holes 841A and 841B consisted of 47 determinations of volatile hydrocarbons in sediments using the Carle gas chromatograph, 30 determinations of total nitrogen, carbon, and sulfur using the Carlo Erba NCS analyzer, 99 determinations of total inorganic carbon using the Coulometrics 5011 coulometer equipped with a System 140 carbonate/carbon analyzer, and 11 analyses with the

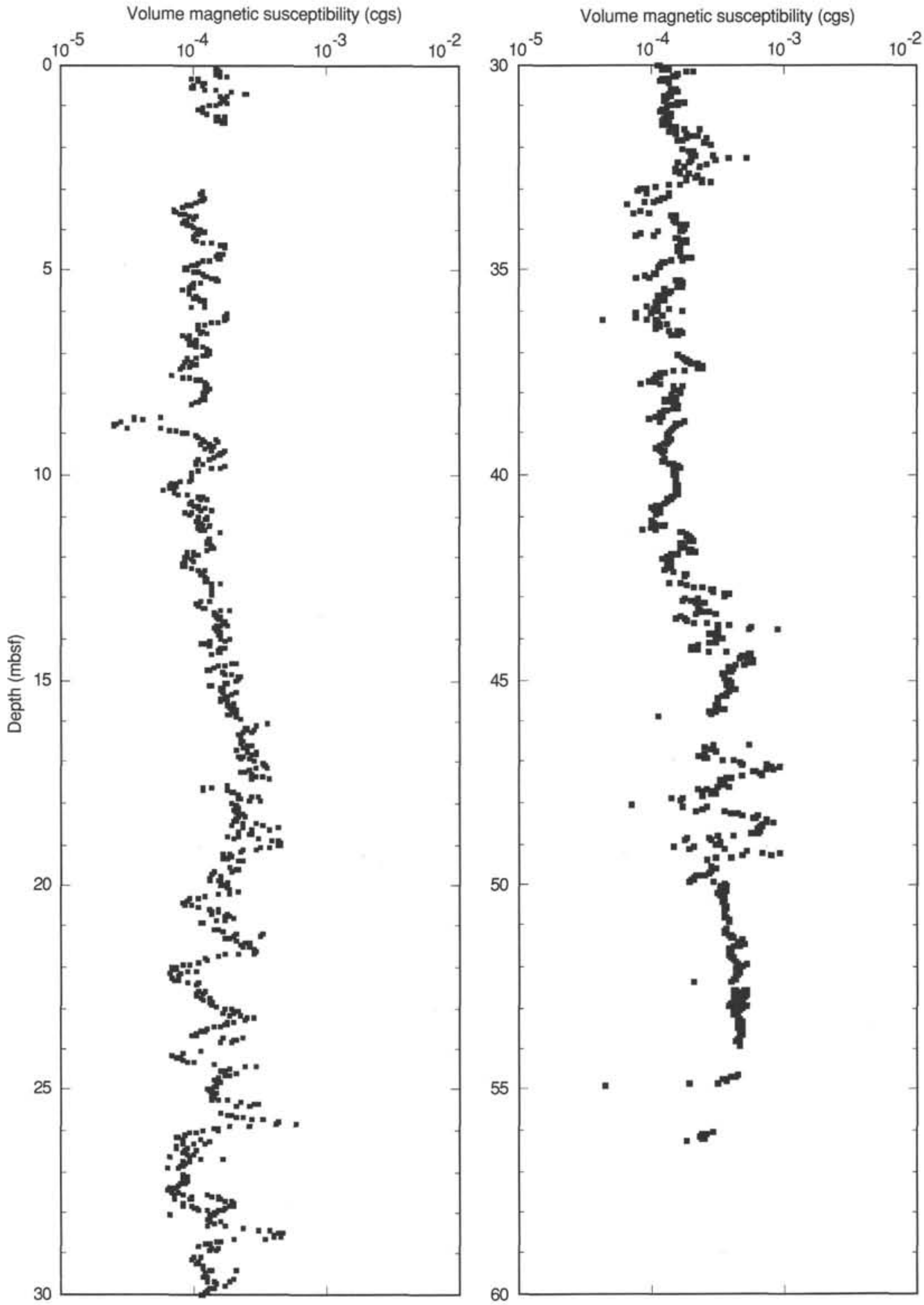

Figure 40. Volume magnetic susceptibility of Hole 841A, 0–60 mbsf. Both columns show susceptibility values plotted on a logarithmic scale.

Rock-Eval instrument. Details of the analytical procedures used are outlined in the "Organic Geochemistry" section, "Explanatory Notes" chapter (this volume) and are described in detail by Emeis and Kvenvolden (1986).

The volatile hydrocarbon gases were obtained from the bulk sediment using the headspace sampling technique and were routinely monitored for methane, ethane, and propane. The cores from which headspace samples were taken are given in Table 9. Methane concentrations in most samples were between 2 and 3 ppm, which is very low and at the laboratory background level. Ethane and propane were not detected in any sample. Sulfate levels remain at relatively high levels throughout this hole (see "Inorganic Geochemistry" section, this volume) and consequently conditions were not favorable for methanogenesis. As at the other

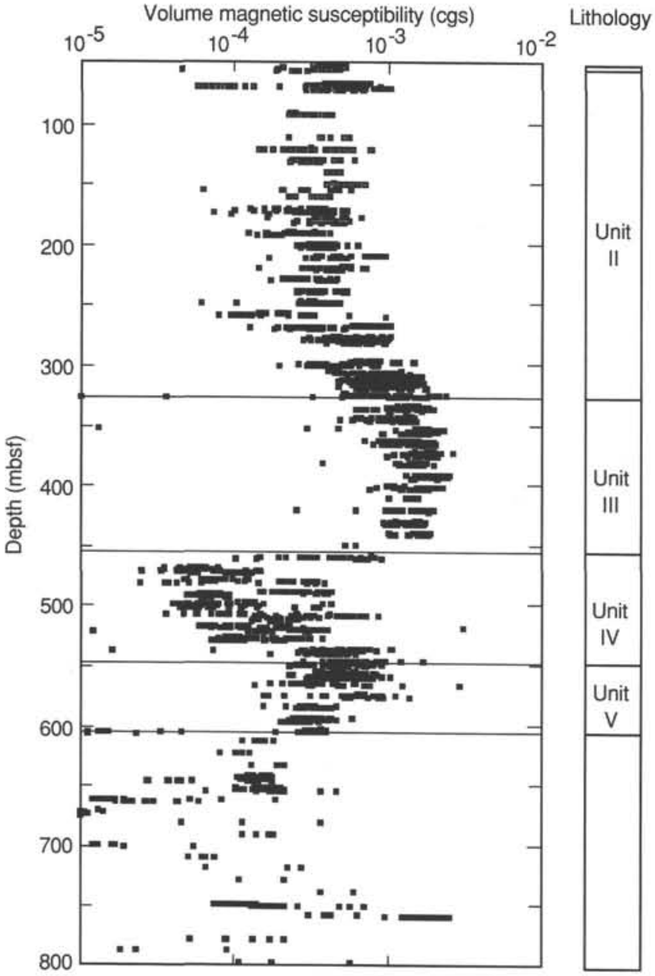

Figure 41. Volume magnetic susceptibility, 50 to 800 mbsf, Holes 841A and 841B combined. Susceptibility scale is logarithmic. Column at right shows sedimentary unit boundaries.

Leg 135 sites, this is probably because the very low levels of organic carbon (see below) in these sediments were not enough to sustain microbial activity. Slightly higher levels of methane were recorded from some samples taken in the lower part of Hole 841, notably the sample from Section 135-841B-62R-1, which contained 15 ppm methane. While this is a very low value when compared to the methane concentrations commonly observed in marine sediments, it is the highest methane concentration recorded during Leg 135. More surprising is that this core contained igneous rocks (welded rhyolite tuffs). Since methane is only associated with cores containing igneous rocks at this site, it could be derived from a nonbiological process. The amounts of the other gaseous hydrocarbons relative to methane can often be used to help elucidate the origin of a gas (Claypool and Kvenvolden, 1983). In this case, methane is in such low concentrations that ethane and propane would not be expected to be present in detectable quantities, whatever the origin of the gas.

Determinations of inorganic carbon (IC) contents were performed on the samples used for physical properties and on additional samples selected by the sedimentologists. Percentage of $CaCO_3$ is calculated according to the equation:

$$CaCO_3 = IC \cdot 8.334.$$

This equation assumes that all the carbonate is present as calcite. The data from these analyses are presented in Table 10. Carbonate values range from 0.1% to 48.4%. Most sediments at this site have a very low carbonate content. This is partly because, as at the other Leg 135 sites, most of the sediments at Site 841 contain a large component of volcaniclastic material. An additional factor at Site 841 is that most sediments were deposited in deep water, below the CCD. The CCD is between the depth at which the rate of carbonate dissolution exceeds that of the supply of pelagic carbon, and the deep sea (e.g., Hay, 1988). The only samples to show high carbonate values were from Core 135-841B-46R, which contained abundant large foraminifers. Based on the presence of these organisms and on other sedimentological features (see "Biostratigraphy" and "Lithostratigraphy" sections, this chapter), this interval has been interpreted as being deposited in a shallow platform lagoon. Soon after deposition, the platform was drowned and then progressively submerged. The carbonate values obtained from samples obtained below these sediments are low because they contain rhyolitic and other igneous rocks.

Also shown in Table 10 are the percentages of total carbon and organic carbon. Total organic carbon (TOC) is defined here as the difference between the total carbon and the inorganic carbon values. Nitrogen and sulfur contents were also measured but not detected in any of the samples analyzed. The sediments from Site 841 have organic carbon contents between 0.0% and 0.67%. However, the four samples with the highest TOC values were all from Core 135-841B-46R. This unit was probably deposited in an environment with higher primary productivity (as indicated by the presence of foraminifers) and a lower volcaniclastic input than other sediments analyzed from this site.

Eleven samples with higher TOC values were analyzed using the Rock-Eval instrument, and the results are shown in Table 11. S1 represents the amount of "free hydrocarbons" in the sample, and S2 and S3 values represent the amount of hydrocarbons and carbon dioxide, respectively, that can be released from the kerogen during pyrolysis or thermal maturation of the sediment. When normalized to the amount of organic carbon, the derived parameters hydrogen index (HI) and oxygen index (OI) are obtained, which can provide an indication of the type of organic matter (Espitalié et al., 1977). T_{max} is the temperature where the maximum release of hydrocarbons from the pyrolysis of the kerogen occurs and the production index (PI) is calculated by $S1/S1 + S2$. A more detailed explanation of these parameters is provided in the "Explanatory Notes" chapter (this volume). TOC measurements were not provided by the Rock-Eval instrument because the TOC module was not working. The TOC values given in Table 11 represent the difference between the total carbon and inorganic carbon values and hence are the same as those given for these samples in Table 10.

Gatliff (1990) suggested that Eocene limestones, equivalent to those outcropping on 'Eua, may be the source rocks for the seeps on Tongatapu. Such rocks have not been penetrated by the exploration wells drilled in the Tongatapu area. The TOC contents of the Eocene carbonates from Core 135-841-46R are higher than those reported by Buchbinder and Halley (1985) for Pleistocene to Eocene sediments from the Tonga-'Eua area, and those reported by Sandstrom (1985) for Miocene and younger sediments dredged from the southern Tonga Platform. However, the results of Rock-Eval analyses on these samples (Table 11) indicates that this organic matter has no hydrocarbon potential, as it has been completely oxidized to inertinite. These results do not rule out Eocene limestones as the source of the seeps on Tongatapu. Although Site 841 is over 250 km from Tongatapu (Fig. 2), in the vicinity of the seeps there could have been better preservation of the organic matter in this unit.

Table 8. Interstitial water chemistry data, Holes 841A and 841B.

Core, section, interval (cm)	Collected water (mL)	Depth (mbsf)	pH	Alkalinity (mM)	Salinity (‰)	Ca^{2+} (mM)	Mg^{2+} (mM)	K^{+} (mM)	Cl^{-} (mM)	SO_4^{2-} (mM)	NH_4^{+} (µM)	PO_4^{3-} (µM)	Si^{4+} (µM)	Sr^{2+} (µM)	Mn^{2+} (µM)	Na^{+} (mM)
135-841A-																
1H-4, 140–150	50	6.0	7.58	3.406	35.6	11.2	50.0	11.7	548	28.7	4	3.6	487	105	<10	471
2H-4, 140–150	50	14.5	7.89	3.430	35.8	13.0	49.3	11.6	546	28.4	15	4.8	514	111	60.6	466
3H-4, 140–150	50	24.0	7.67	2.986	35.5	13.9	48.4	11.4	547	27.6	21	7.9	527	107	137.2	466
4H-4, 140–150	50	33.5	7.53	3.081	35.4	15.5	46.6	11.1	548	28.2	21	5.7	607	107	145.7	469
6H-4, 140–150	30	52.5	8.07	2.640	35.0	17.3	43.3	10.5	549	26.5	59	2.2	543	98	75.8	470
8H-3, 140–150	50	70.0	8.23	2.121	35.8	20.0	41.2	10.3	547	27.5	84	1.9	431	105	57.1	468
135-841B-																
2R-1, 142–150	34	171.3	8.47	1.149	36.2	49.6	30.5	7.5	570	22.9	188	0.8	493	95	42.9	448
5R-1, 142–150	20	200.2	8.45	1.135	38.4	84.9	18.5	5.5	584	18.4	210	1.4	462	75	27.9	409
8R-1, 75–85	22	228.5	8.84	0.749	40.8	134.6	3.1	2.6	613	12.3	185	0.9	442	50	10.6	360
11R-1, 61–74	20	257.4	9.12	0.929	41.7	142.6	1.5	1.9	612	11.9	141	ND	456	55	<10.0	347
15R-1, 135–150	18	296.4	8.93	0.967	40.1	138.3	0.5	1.2	605	11.4	120	0.3	139	60	<10.0	349
18R-2, 77–95	7	325.9	ND	ND	40.4	136.5	0.0	1.9	600	11.1	74	0.5	149	95	<10.0	347
21R-1, 13–32	18	352.4	8.72	0.896	41.0	126.2	0.0	1.1	607	10.5	72	0.3	122	121	<10.0	375
29R-1, 130–150	4	430.6	ND	ND	ND	120.5	0.0	1.4	609	11.9	45	ND	ND	ND	ND	390
37R-3, 0–13	0	**	**	**	**	**	**	**	**	**	**	**	**	**	**	**
40R-2, 8–21	7	536.5	ND	ND	40.3	126.6	0.0	0.9	609	10.6	31	0.6	157	103	<10.0	376
42R-3, 0–9	8	557.4	ND	ND	40.1	124.4	0.0	1.5	607	10.6	10	0.5	239	127	18.7	378
51R-2, 0–19	35	641.5	8.10	0.885	42.5	125.1	7.6	2.6	618	15.0	25	1.4	832	265	42.8	380
53R-1, 132–150	3	662.1	ND	ND	42.2	107.3	13.9	4.0	621	19.1	36	ND	142	274	14.1	413
62R-1, 130–150	6	748.7	ND	ND	42.0	66.5	19.3	4.2	649	21.8	26	ND	107	217	<10.0	517
Drilling mud filtrate			10.00	ND	14.8	4.25	12.0	2.5	212	18.3	9	3.4	124	77	<10.0	214

Note: ND = not determined.

The results of the other samples shown in Table 11 also suggest that their organic matter is oxidized and is inertinite. This is supported by the high OI, PI, and T_{max} values. Some samples show very high HI values (e.g., the sample from a depth of 0.88 mbsf), suggesting that their organic matter has considerable hydrocarbon potential. However, the other parameters indicate that these are spurious results. Examination of the shape of the S2 peaks using the Laboratory Automation System confirmed that this was true. The S2 peaks, with the exception of the sample from 673.85 mbsf, were almost flat, barely rising above the baseline and had been integrated incorrectly by the Rock-Eval instrument. This would also explain why the T_{max} values fall outside the range of those normally observed in sedimentary organic matter.

The results obtained from the NCS and Rock-Eval analyses of the sample from 673.85 mbsf are also suspicious because this sample is taken from a welded tuff interval. Hence it is unlikely to contain organic matter other that which has been exposed to high temperatures and no longer gives a significant S2 peak. As the organic matter of this sample does show a significant S2 peak, we concluded that our sample has been contaminated, either during drilling or subsequently aboard ship. As the organic carbon content of this sample is only 0.14%, it would take very little input of extraneous material for the contamination to be apparent during analysis.

IGNEOUS PETROLOGY

The two principal objectives of the site were to recover a section of volcaniclastic sediments in order to examine the early evolution of arc volcanism in the Tonga region and to identify the age and composition of the forearc basement. The latter objective, in particular, would test hypotheses for the origin of the forearc as a trapped fragment of old oceanic crust (Hawkins et al., 1984) or as an Eocene arc volcanic complex equivalent to the basement on 'Eua (Bloomer and Fisher, 1985).

Two major igneous sequences were recovered from Hole 841B. The first (Unit 1, 324.76 to 497.68 mbsf) is a series of thin basaltic andesite units within upper Miocene volcanic siltstones and sandstones (Fig. 43). The contacts between the basaltic andesite and sediments include chilled margins, hyaloclastite brecciation, and induration of the adjacent sediment, all suggesting intrusive emplacement of the igneous material into the sedimentary pile. Nine basaltic andesite units have been identified, ranging from 7 cm to almost 18 m in recovered thickness. The orientations of the chilled margins suggest that some are steeply inclined and may represent dike margins, while others are flatter lying and probably represent sills. Some may have been flows or pillows but the contact features commonly found in the adjacent sediment make this unlikely.

The second major igneous sequence (Units 2 through 6) comprises a series of low-K rhyolites, low-K rhyolitic tuffs, breccias, welded tuffs, and lapilli tuffs (Fig. 43). This silicic complex constitutes the lower 210 m of Hole 841B. Evidence for welding in some of the rhyolitic clasts and tuffs, the complete absence of interbedded sediments and fossil flora or fauna, and the coexistence of dense clasts and highly vesicular pumice suggest subaerial emplacement. The silicic rocks are structurally overlain by upper Eocene shallow-water calcareous volcanic sandstones (approximately 38 Ma).

Igneous rocks also occur as diverse clasts and cobbles in sedimentary breccias and sandstones from Holes 841A and 841B. The lithologies represented in clasts include highly altered variolitic basalt, rhyolite, and altered granodiorite or tonalite. These are particularly prominent in breccias within early Oligocene (Cores 135-841B-41R and -42R) and upper Miocene (Cores 135-841B-21R through -30R) sediments.

Unit 1 was defined on the basis of the petrographic and lithologic similarities of the basaltic andesite intrusions. Subunits were defined as continuous intervals of volcanic rocks bounded by sedimentary layers. Subunit 10 includes two short (10–20 cm) sedimentary rubble intervals mixed along a steeply dipping chill margin. Unit divisions in the thick sequence of rhyolitic volcanics and volcaniclastic rocks in the lower part of Hole 841B are based on significant changes in lithology. Subunits are defined on the basis of more subtle lithologic breaks within each unit, some of which may represent cooling unit discontinuities within single complex eruptive events. A summary of the lithologic divisions is given in Table 12.

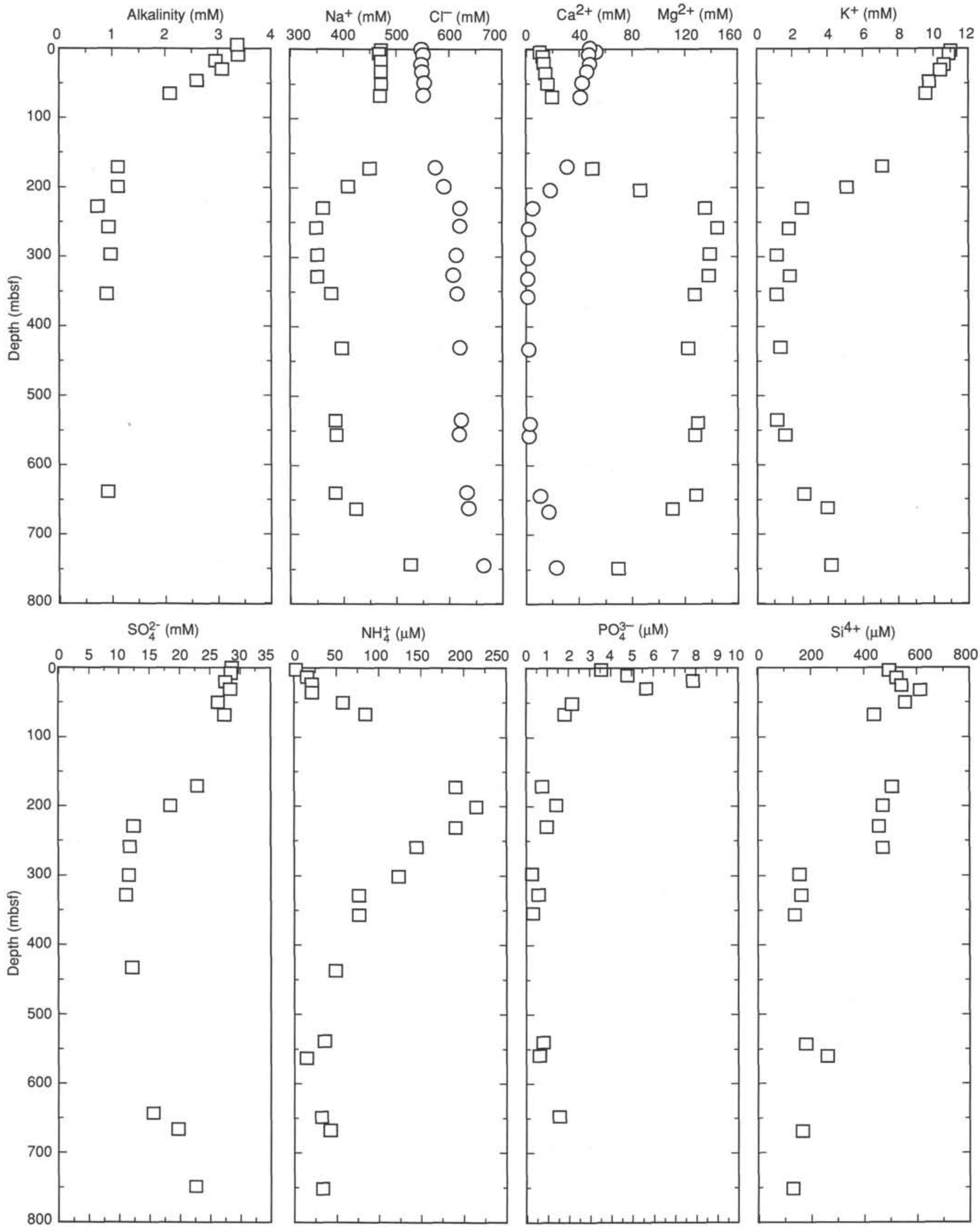

Figure 42. Concentration-depth profiles for alkalinity, sodium and chloride, calcium and magnesium, potassium, sulfate, ammonia, phosphate and silica, Site 841.

Table 9. Locations in Site 841 cores where headspace samples were taken and their concentrations of methane were obtained using the Carle gas chromatograph.

Core, section, interval (cm)	Depth (mbsf)	Methane (ppm)
135-841A-		
1H-5, 0–3	6.00	2
2H-5, 0–3	14.50	2
3H-5, 0–3	24.00	2
4H-CC, 0–3	36.63	2
5H-4, 0–3	41.05	2
6H-5, 0–3	52.50	2
8H-CC, 0–3	71.36	4
9X-CC, 0–3	72.67	2
14X-CC, 0–3	120.91	3
15X-CC 0–3	130.39	2
17X-1, 0–3	148.90	3
18X-1, 0–3	153.90	2
19X-CC, 0–3	159.66	3
135-841B-		
2R-1, 142–150	171.22	3
135-841A-		
21X-1, 0–3	176.90	2
135-841B-		
4R-2, 97–100	191.57	3
6R-1, 0–3	208.40	2
7R-2, 0–3	219.60	3
8R-1, 0–3	227.70	3
10R-1, 0–3	247.00	2
11R-1, 0–3	256.70	3
12R-CC, 0–3	269.30	2
13R-CC, 0–3	281.14	2
15R-1, 132–135	296.22	2
17R-1, 0–3	313.80	3
18R-2, 0–3	325.00	2
20R-1, 0–3	342.50	3
21R-1, 0–3	352.10	2
22R-1, 0–3	361.40	3
24R-CC, 0–3	382.32	3
27R-1, 0–3	409.70	3
29R-CC, 0–3	431.71	3
30R-CC, 0–3	440.61	2
35R-CC, 0–3	491.64	2
45R-2, 0–3	584.80	3
47R-CC, 0–3	605.50	3
53R-1, 147–150	662.07	4
54R-1, 0–3	670.20	5
56R-CC, 0–3	689.73	3
57R-CC, 0–3	699.69	4
58R-1, 0–3	708.80	3
59R-1, 0–3	718.10	3
62R-1, 130–133	748.50	15
63R-1, 0–3	756.90	6
65R-CC, 0–3	776.20	4
66R-CC, 0–3	785.90	3
68R-CC, 0–3	805.20	3

Lithology and Petrography

Unit 1: Basaltic Andesite Dikes and Sills

Unit 1 comprises nine dark gray to black, moderately to highly phyric orthopyroxene-clinopyroxene-plagioclase basaltic andesites which occur as 0.07 to 18 m (recovered interval) sills or dikes separated by sedimentary interbeds (Fig. 43). These nine basaltic andesites have been defined as Subunits A through I. Several of the rocks show devitrified glassy chilled margins, some of which appear to be subvertical to steeply dipping in orientation. Many contacts, however, occur on pieces too small to be oriented. As a result, it is not clear whether these glassy margins represent the near vertical edges of dikes or subhorizontal contacts from sills or pillows. The volcanic sediment contacts include baked sediments (Fig. 44) and brecciated or glassy zones.

Vesicle contents are low in most samples of Unit 1 and become significant (3%–5%) only toward fine-grained margins, being concentrated in a zone within approximately 1 cm of the contact (Fig. 44). The vesicles are generally irregular in shape and are occasionally lined with quenched, frothy magma. The cavities are clear of infillings or have only thin linings of colorless zeolites.

Plagioclase is the dominant phenocryst phase (up to 12%) and tends to occur in glomerocrysts, which may be up to 4 mm in maximum dimension. Plagioclase phenocrysts are euhedral to subhedral, ranging in size from 0.3 to 2 mm across, giving the rocks a seriate porphyritic texture. The size of both the phenocrysts and the glomerocrysts increases away from the glassy margins. Melt inclusions, narrow sodic rims, and well-developed normal oscillatory zoning are common features of the plagioclase phenocrysts.

Clinopyroxene is present as a phenocryst phase; it is typically less than 0.7 mm across but ranges up to 1 mm in length. The proportion of clinopyroxene phenocrysts present in the rocks of Unit 1 varies from only trace amounts up to a maximum of 3%–5%; it is always subordinate in abundance to plagioclase phenocrysts (Table 13). The crystals are generally subhedral to anhedral and occur both as isolated equant to elongate crystals and associated with plagioclase glomerocrysts, some in radiating clusters. Many of the clinopyroxene crystals have ragged, corroded outlines associated with alteration to brownish clays. Some exhibit lamellar twinning.

Orthopyroxene is a rare phenocryst phase and is not found in all samples, but when present it forms euhedral to subhedral crystals generally less than 0.5 mm, ranging up to a maximum of 1 mm across. The crystals are typically partially to completely altered to brownish clays. Orthopyroxene grains occasionally include irregular clinopyroxene cores or have thin clinopyroxene rims. In other cases, the orthopyroxene and clinopyroxene phenocrysts are intergrown.

The groundmass varies in its degree of crystallinity, ranging from cryptocrystalline mesostasis to a fine-grained interlocking network of plagioclase, pyroxene, and opaques. The ratio of plagioclase to clinopyroxene is approximately 2:1, with minor orthopyroxene and a few percent of opaque minerals (Table 13). Plagioclase is generally less than 0.5 mm in length and occurs as euhedral elongate laths. Close to the glassy margins, quenched plagioclases show swallowtail terminations and skeletal equant and tabular habits (Fig. 45).

Clinopyroxene abundance in the groundmass averages approximately 15%. It is euhedral to anhedral, and present in a variety of habits that include equant crystals, acicular and plumose aggregates, and rounded grains. It also occurs as interstitial grains intergrown with plagioclase and orthopyroxene. Orthopyroxene forms euhedral to subhedral crystals which are randomly distributed throughout the groundmass. The crystals are typically less than 0.5 mm in length and are present in small amounts that range up to a few percent. Magnetite is the dominant opaque mineral, up to approximately 5% in abundance, and ranges up to 0.05 mm in maximum dimension. It occurs as skeletal laths or equant crystals (sometimes in aggregates) and may display cruciform morphologies in the more quenched zones. Opaques also occur as dust-like grains in the cryptocrystalline mesostasis. Interstitial cryptocrystalline mesostasis constitutes up to 50% of the volume of the Unit 1 rocks and may show significant replacement by fine-grained greenish brown clays.

The chilled contact zones exhibit varied quench textures, some with strong gradations. These include devitrified, ribbed glassy

Table 10. Concentrations of inorganic and organic carbon at Site 841.

Core, section, interval (cm)	Depth (mbsf)	Total carbon (%)	Inorganic carbon (%)	Organic carbon (%)	$CaCO_3$ (%)
135-841A-					
1H-1, 88–89	0.88	0.16	0.03	0.13	0.2
1H-3, 80–81	3.80		0.96		8.0
1H-5, 80–81	6.80	0.12	0.02	0.10	0.2
1H-6, 38–39	7.88		0.02		0.2
2H-1, 101–102	9.51		0.21		1.7
2H-3, 70–71	12.20		0.02		0.2
2H-4, 15–16	13.15	0.12	0.03	0.09	0.2
2H-5, 88–89	15.38		0.02		0.2
2H-7, 35–36	17.85		0.02		0.2
3H-1, 78–79	18.78		0.02		0.2
3H-3, 82–83	21.82	0.09	0.02	0.07	0.2
3H-5, 71–72	24.71		0.02		0.2
3H-7, 36–37	27.36		0.02		0.2
4H-1, 68–69	28.18		0.02		0.2
4H-2, 121–122	30.21		0.02		0.2
4H-3, 76–77	31.26	0.21	0.02	0.19	0.2
5H-2, 33–34	38.38		0.02		0.2
5H-3, 97–98	40.52		0.02		0.2
5H-5, 65–66	43.22		0.02		0.2
6H-2, 9–10	48.09	0.13	0.02	0.11	0.2
6H-4, 4–5	51.04		0.02		0.2
8H-1, 88–89	66.38		0.16		1.3
8H-2, 36–37	67.36		0.45		3.7
8H-3, 117–118	69.67		0.02		0.2
11X-1, 10–11	91.10		0.03		0.2
15X-1, 62–63	130.22	0.26	0.22	0.04	1.8
135-841B-					
2R-1, 47–48	170.27	0.26	0.15	0.11	1.2
2R-2, 69–70	171.99		0.78		6.5
2R-3, 37–38	173.17		0.04		0.3
135-841A-					
21X-1, 80–81	177.70	0.21	0.09	0.12	0.7
135-841B-					
3R-1, 0–1	179.40		0.36		3.0
4R-1, 99–100	190.09	1.00	0.98	0.02	8.2
4R-2, 15–16	190.75		0.18		1.5
5R-1, 16–17	198.86		0.99		8.2
5R-2, 7–8	200.27		0.78		6.5
6R-1, 45–46	208.85	0.38	0.38	0	3.2
7R-1, 16–17	218.26		0.44		3.7
7R-2, 22–23	219.82		0.27		2.2
8R-1, 3–5	227.73		0.21		1.7
8R-2, 21–23	228.76	0.35	0.30	0.05	2.5
9R-1, 85–86	238.25		0.11		0.9
9R-2, 37–38	239.27		0.17		1.4
10R-1, 3–4	247.03	0.73	0.73	0	6.1
10R-1, 117–118	248.17		0.04		0.3
11R-2, 18–19	257.62		0.20		1.7
12R-1, 102–103	267.32	0.39	0.39	0	3.2
13R-1, 48–49	276.08		0.44		3.7
13R-2, 12–13	277.22		0.42		3.5
13R-3, 97–98	279.57	0.69	0.69	0	5.7
16R-1, 111–112	305.71		0.50		4.2
16R-2, 73–74	306.83		0.36		3.0
16R-3, 30–31	307.90	0.52	0.50	0.02	4.2
16R-4, 128–129	310.38		0.41		3.4
16R-5, 103–104	311.63		0.44		3.7
18R-1, 109–110	324.59		0.04		0.3
18R-2, 61–62	325.61		0.05		0.4
19R-1, 16–17	333.36	0.25	0.25	0	2.1
19R-2, 24–25	334.94		0.55		4.6
19R-3, 7–8	336.27		0.90		7.5
20R-1, 76–77	343.26		0.16		1.3
20R-2, 7–8	344.05	0.16	0.13	0.03	1.1
23R-3, 90–91	374.89		0.03		0.2
26R-1, 32–34	400.42		0.03		0.2
26R-2, 49–50	402.06	0.06	0.03	0.03	0.2
27R-1, 41–42	410.11		0.03		0.2
28R-1, 35–36	419.75		0.21		1.7

Table 10 (continued).

Core, section, interval (cm)	Depth (mbsf)	Total carbon (%)	Inorganic carbon (%)	Organic carbon (%)	$CaCO_3$ (%)
135-841B- (cont.)					
29R-2, 94–95	431.54		0.27		2.2
30R-1, 64–65	439.44		0.13		1.1
32R-1, 104–105	459.14		0.11		0.9
33R-1, 8–9	467.88	0.31	0.26	0.05	2.2
33R-3, 66–67	471.44		0.26		2.2
34R-1, 120–121	478.70		0.15		1.2
34R-2, 110–111	480.08		0.04		0.3
35R-1, 108–109	488.18		0.09		0.7
35R-3, 125–126	491.39	0.13	0.09	0.04	0.7
36R-1, 56–57	497.36		0.15		1.2
36R-2, 102–103	499.32		0.20		1.7
36R-3, 68–69	500.48		0.33		2.7
37R-1, 77–78	507.17	0.40	0.34	0.06	2.8
37R-3, 119–120	510.46		0.07		0.6
37R-4, 89–90	511.65		0.30		2.5
38R-1, 55–56	516.65		0.89		7.4
38R-2, 144–145	518.90		0.13		1.1
38R-3, 112–113	520.08		0.15		1.2
40R-1, 85–86	536.15		0.10		0.8
40R-2, 35–36	537.08	0.17	0.08	0.09	0.7
45R-1, 6–8	583.36	1.61	1.57	0.04	13.1
45R-2, 12–13	584.92		0.74		6.2
46R-1, 71–73	593.61	4.09	3.68	0.41	30.7
46R-2, 12–13	594.52	6.48	5.81	0.67	48.4
46R-2, 72–73	595.12	5.15	4.58	0.57	38.2
46R-3, 8–10	595.94	5.72	5.50	0.22	45.8
47R-1, 6–7	602.66		0.30		2.5
47R-1, 143–144	604.03	0.42	0.35	0.07	2.9
47R-2, 48–49	604.58		0.29		2.4
51R-2, 61–62	643.41		0.03		0.2
51R-3, 79–80	645.00		0.03		0.2
52R-1, 76–77	651.66		0.02		0.2
54R-3, 65–66	673.85	0.15	0.01	0.14	0.1

Note: Parameters are explained in the text.

zones (Fig. 46) and cryptocrystalline, nearly opaque, contorted zones (Fig. 47) at the sediment-igneous interfaces. These commonly grade into cryptocrystalline variolitic zones (Fig. 47), which then grade (over an interval of <0.5 cm) into a microcrystalline zone exhibiting veinlet structures (~0.05 mm wide), forming networks parallel to the glassy margin (Fig. 44). The distance between veinlets increases from 0.4 mm apart close to the contact, to 3 mm apart at a distance of 2 cm into the rock interior.

Cross-cutting veins and fractures are common in the Unit 1 basaltic andesites (up to several percent of the rock by volume). These veins are filled with quartz, feldspar, thaumasite, and minor carbonate (see "Alteration and Metamorphism," this section). Some of the silicic veins are associated with the development of sulfides, including pyrite, chalcopyrite, pyrrhotite, and marcasite.

Rhyolitic Pyroclastic Units 2 through 6 (605.05–815.06 mbsf)

The thick sequence of silicic volcaniclastic rocks recovered from the lower part of Hole 841B was first intersected in Section 135-841B-47R-2, 95 cm, in which sandy limestone fragments are faulted against volcaniclastic fragments (Fig. 43). The volcanic sequence can be identified at least through 815 mbsf and has a minimum thickness of 210 m. Unit designations exist only through the recovered interval in Section 135-841B-69R-CC; only a small clast of greenstone of unknown origin was recovered in Section 135-841B-70R-CC. These rocks are referred to here as low-K rhyolites (K_2O <1.5%, SiO_2 >68%; Taylor et al., 1981).

Five units have been distinguished within the silicic volcanic complex. Unit 2 consists of 41.9 m of highly phyric vitreous quartz-plagioclase rhyolites and poorly welded pumice breccias (Subunits 2B and 2C) separated from the overlying upper Eocene

Table 11. Results of Rock-Eval analysis for Site 841.

Core, section, interval (cm)	Depth (mbsf)	S_1 (mg/g)	S_2 (mg/g)	S_3 (mg/g)	TOC	HI	OI	T_{max} (°C)	PI	S_2/S_3
135-841A-										
1H-1, 88–89	0.88	0.25	1.33	0.54	0.13	1023	415	496	0.16	2.46
4H-3, 76–77	31.26	0.35	1.37	0.29	0.19	721	153	532	0.20	4.72
135-841B-										
2R-1, 47–48	170.27	0.14	0.48	0.70	0.11	436	636	545	0.23	0.68
135-841A-										
21X-1, 80–81	177.70	0.21	0.86	0.65	0.12	717	542	545	0.20	1.32
135-841B-										
40R-2, 35–36	537.08	0.12	0.10	0.60	0.09	111	667	443	0.55	0.16
46R-1, 71–73	593.61	0.13	0.05	1.01	0.41	12	246	323	0.72	0.04
46R-2, 12–13	594.52	0.24	0.03	1.00	0.67	4	149	320	0.92	0.03
46R-2, 72–73	595.12	0.06	0.06	0.78	0.57	11	137	326	0.50	0.07
46R-3, 8–10	595.94	0.03	0.03	0.66	0.22	14	300	313	0.50	0.04
46R-CC, 14–15	596.37	0.06	0.10	1.07	0.59	17	181	365	0.37	0.09
54R-3, 65–66	673.85	0.06	0.63	0.23	0.14	450	164	453	0.09	2.73

Notes: The total organic carbon (TOC) values are not from the Rock-Eval analysis but are the difference between the total carbon and inorganic carbon values. Parameters are explained in the text. HI = hydrogen index, OI = oxygen index, and PI = production index.

calcareous sandstones by a rhyolitic fault gouge (Subunit 2A). The overall recovery of the rhyolitic units was 19%, whereas recovery in Subunit 2B was only 4%.

Unit 3, about 93 m thick, is divided into four subunits and consists of a generally upward-fining sequence of rhyolitic breccias (Subunit 3D), laminated crystal tuffs and lapilli tuffs (Subunit 3C), welded tuffs (Subunit 3B), and rhyolitic tuffs and lapilli tuffs (Subunit 3A). The overall recovery was 15%. The lower boundary of Subunit 3D is somewhat arbitrary, as recovery was low and the Unit 3/Unit 4 boundary was not recovered.

Unit 4, 10.2 m thick, comprises a well-defined welded rhyolitic lapilli tuff which is sheared at the base and quickly grades into the underlying Unit 5. It contains lenticular pumice fragments and abundant rhyolitic lithic clasts. The recovery in Unit 4 was 34%.

Unit 5 is an intensely sheared breccia. It is estimated to be 18.8 m thick, but its lower boundary was not recovered. The base of the unit was defined as the top of Section 135-841B-65R-CC, where a distinct change in lithology occurred. Core 135-841B-64R recovered only 7 cm of material; it has been included in Unit 5 although its origin is uncertain. The recovered thickness of Unit 5 is only 1.3 m.

Unit 6 is at least 39 m thick (recovery was only 2.1%) and consists largely of clasts and fragments mixed with drilling rubble. The fragments recovered are welded rhyolitic lithic lapilli tuffs, containing strongly deformed altered pumice lenticles, lapilli tuffs, and fragments of mafic greenstone.

The rhyolitic rocks from Site 841 are quartz- and plagioclase-bearing, and in fresh samples contain clinopyroxene, orthopyroxene, and magnetite. The thickness drilled suggests that the hole has intersected a pre–upper Eocene voluminous rhyolitic province, previously unknown and unsuspected, occurring within part of the outer Tonga forearc. The Site 841 volcanic units are inferred to be subaerial based on the occurrence of welded lapilli tuffs and the absence of unambiguously subaqueous sediments. Their thickness (>210 m), the intensity of alteration (except in the uppermost portion of Unit 2B), and the diversity of eruptive lithologies all point toward an "intra-caldera" environment rather than an "outflow" facies environment. Moreover, the vitric rhyolitic lavas and associated pumice breccias of Subunits 2B and 2C are consistent with late-stage resurgent phase eruptives in which lava domes and flows with associated localized poorly welded ash-flow deposits are commonly present (e.g., the Taupo Volcanic Zone, New Zealand; Healy et al., 1964; Ewart, 1965; the Valles Caldera or Long Valley; Bailey et al., 1976).

Unit 2: Moderately to Highly Phyric Quartz-Plagioclase Rhyolites and Rhyolitic Pumice Breccias

The top of this unit, designated Subunit 2A, is predominantly a soft, rhyolitic fault gouge with smaller amounts of a rhyolitic breccia. The unit is immediately overlain by upper Eocene–lower Oligocene, shallow-water calcareous sandstones (see "Biostratigraphy" and "Lithostratigraphy" sections, this chapter).

The light greenish gray rhyolitic fault gouge contains prominent euhedral, often bipyramidal, quartz grains (up to 3 mm diameter), euhedral to subhedral plagioclase, chlorite, disseminated pyrite, and sparse silicified rhyolitic fragments. The crystal fragments are from rhyolitic rocks, and the whole subunit is interpreted as the sheared equivalents of the underlying Subunits 2B and 2C.

Subunit 2B (recovered from Cores 135-841B-47R through -50R, 612.30–631.81 mbsf) consists of a mixture of loose clasts of black, highly phyric quartz-plagioclase vitric rhyolite (pitchstone) and grayish green, moderately phyric quartz-plagioclase pumice breccia fragments (Fig. 48). Some fragments are sheared locally, and black pitchstone clasts are included within some of the pumiceous fragments.

The black pitchstone lithologies contain euhedral to subhedral phenocrysts of quartz (7%–12%; 0.4–2.5 mm in diameter), occurring as single crystals, some of them slightly resorbed, and less commonly as glomerocrysts. Euhedral to subhedral plagioclase (8%–15%; 0.1–2.5 mm diameter) occurs as single crystals and less commonly as glomerocrysts. Plagioclase exhibits normal oscillatory zoning, often with sharp internal compositional discontinuities (Fig. 49), while very rare crystals are strongly resorbed (Fig. 50). Plagioclase:quartz ratios are approximately 2. Euhedral to subhedral prismatic clinopyroxene (<1%; 0.2–1.5 mm in length) occur as single phenocrysts and less commonly as glomerocrysts with plagioclase or orthopyroxene. Some have magnetite inclusions. Euhedral to subhedral prismatic orthopy-

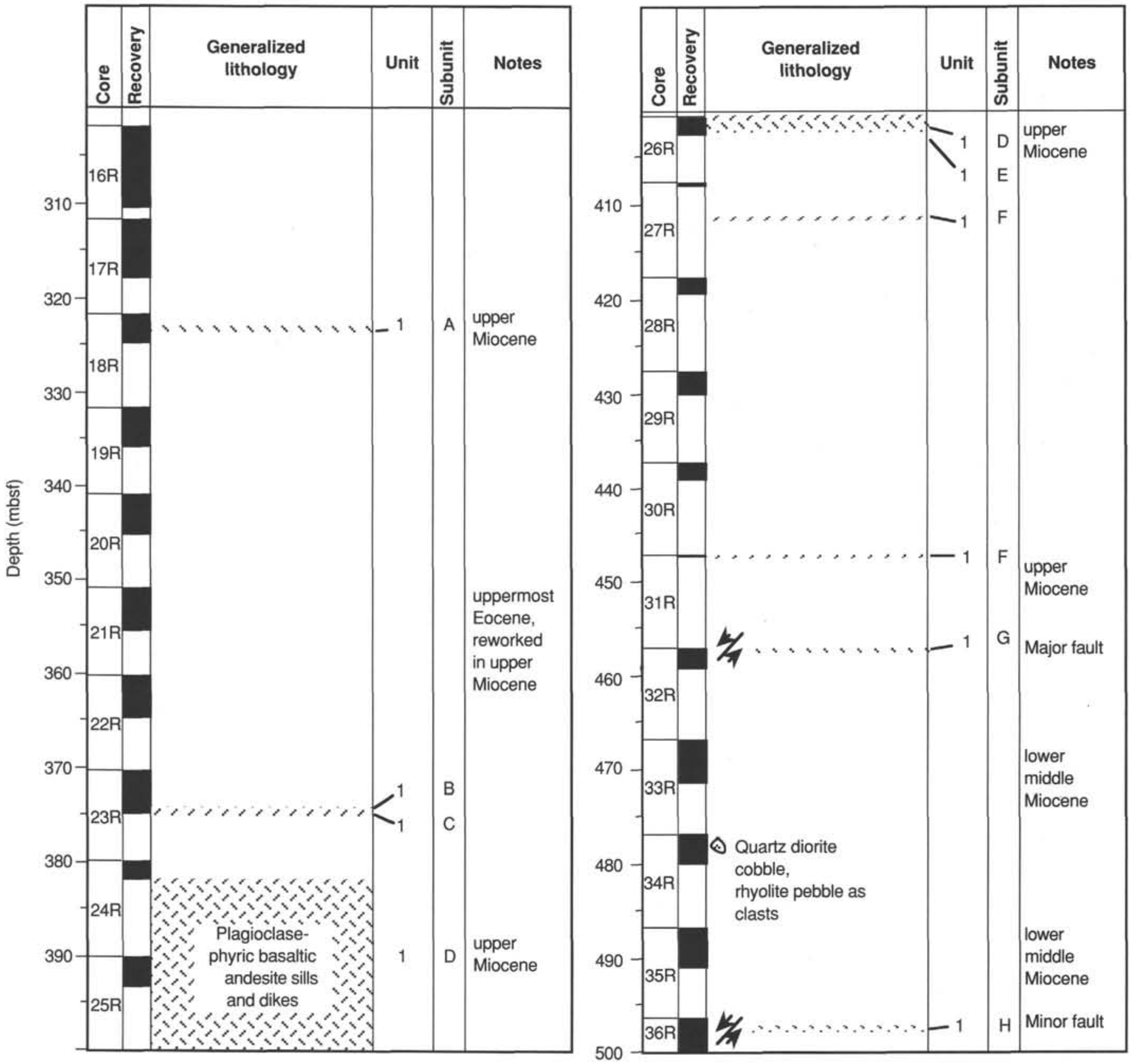

Figure 43. Schematic summary of igneous rock units recovered in Hole 841B. Black infilled areas indicate length of core recovery. Faults and biostratigraphic data are taken from the relevant sections in this chapter. Stippled areas from Cores 135-841-18R through -40R indicate basaltic andesite dikes or sills. When unit boundaries were not recovered, units were arbitrarily extended downward to the next distinct change in lithology that was recovered. Such extrapolated unit boundaries are shown as dashed lines.

roxene phenocrysts (<1%; 0.1–1.5 mm in length) typically contain magnetite microphenocryst inclusions. Rarely, they form glomerocrysts with plagioclase. Euhedral to subhedral equant magnetite (<1%; up to 0.4 mm) occurs as single crystals but is more commonly included in plagioclase and the pyroxenes. The matrix is optically fresh glass; abundant perlitic fractures that have typically developed around phenocrysts are evidence of enhanced hydration of the glass. Crystallites occur in some samples.

The pitchstone exhibits a low degree of vesiculation (5%–11%) with irregular and elongated vesicles up to 4 mm in length. Their alignment suggests that they are a primary flow feature. These rhyolites are interpreted as the rapidly quenched part of a lava flow and/or dome.

The pumiceous fragments are mineralogically similar to the pitchstone clasts, although with lower phenocryst abundances. They comprise interlocking, strongly elongated to tubular pumice fragments (>10 mm; Fig. 51). No compaction of the fragments is evident and welding is slight. Traces of clay and iron-oxyhydroxides occur, lining some vesicles and between clasts. In most fragments alteration is minimal. Pitchstone clasts (and their devitrified equivalents) occur within the pumice breccia lithology, and in some specimens shearing of the pitchstone has occurred adjacent to the pumice lithologies. In these sheared zones, pheno-

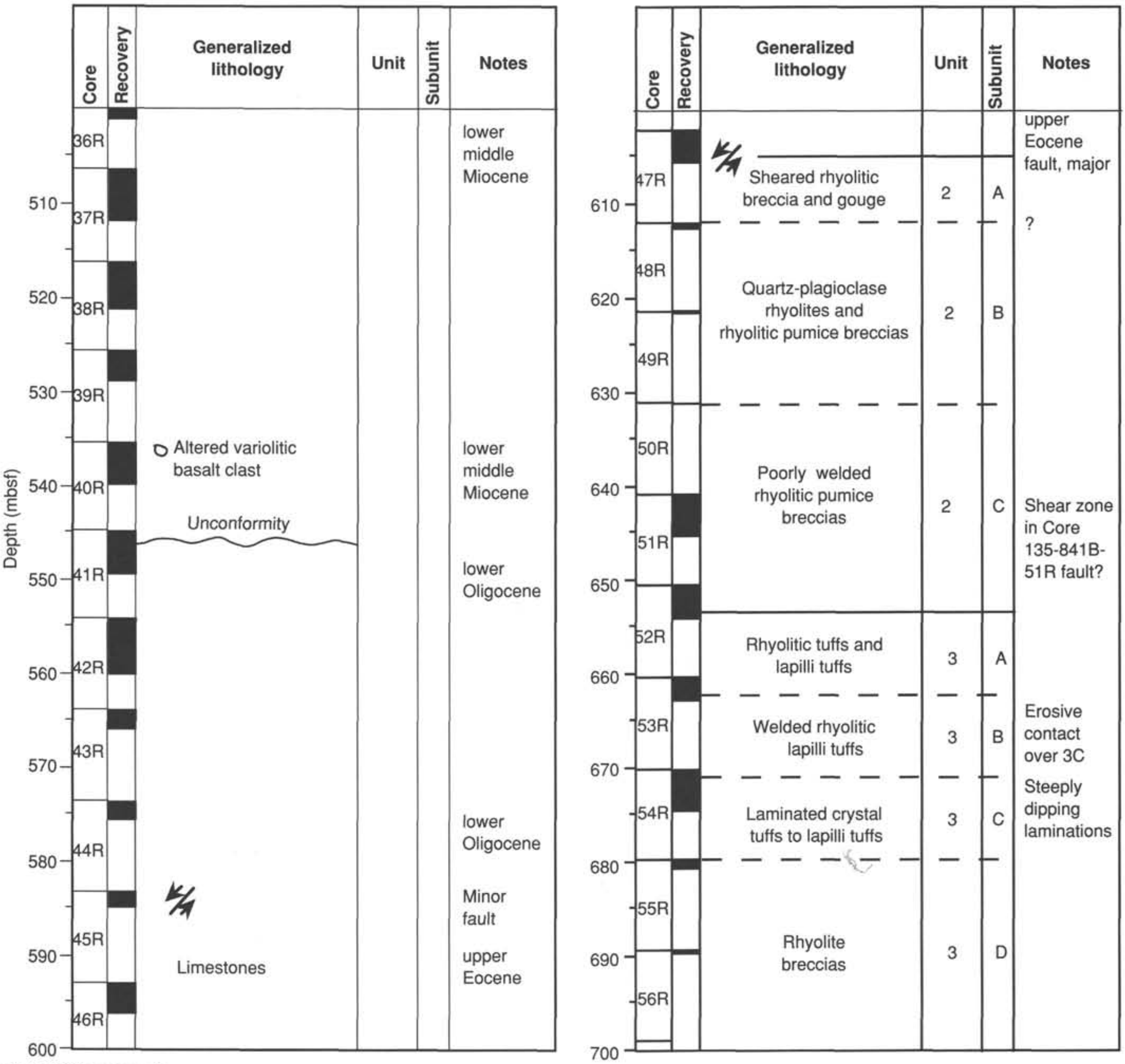

Figure 43 (continued).

crysts are only locally fragmented, suggesting that shearing occurred during cooling within the original lava. The green coloration seen in hand specimen is thought to be the result of degrees of hydration higher than was observed in the pitchstones.

Subunit 2C (Sections 135-841B-50R-1, 21 cm, to -52R-CC, 30 cm) consists of green to gray-green, poorly welded rhyolitic pumice breccias that contain interlocking, randomly oriented clasts of highly vesicular, moderately to highly phyric pumice. Individual fragments range from 1 to 25 cm in length, and they exhibit little if any compaction or postdepositional deformation. Sparse clasts of rhyolite, altered, moderately phyric clinopyroxene-plagioclase basalt or basaltic andesite occur, especially toward the lower part of the section (Fig. 52). Alteration appears to increase downward, with the rocks becoming soft and soapy, apparently the result of infilling by clays and chlorite. Fractures, some with slickensides and 1–2 mm wide, are observed within and bounding many fragments.

The pumice breccias are moderately to highly phyric and have phenocrysts of subhedral equant quartz (some fractured and partially resorbed; 0.1 to 1.5 mm in diameter and varying from 2%–12%) and subhedral plagioclase (1%–10%, up to 2 mm across; some present as crystal fragments). Also present are euhedral, prismatic clinopyroxene (<1%; up to 0.15 mm in size), traces of orthopyroxene (up to 0.9 mm), and magnetite (euhedral to subhedral equant crystals, up to 0.1 mm size, which form isolated crystals but are more often included in plagioclase). The groundmass is highly vesicular pumice with tubular vesicles (0.004 to 0.4 mm wide). The glass is fresh; the alteration seen in

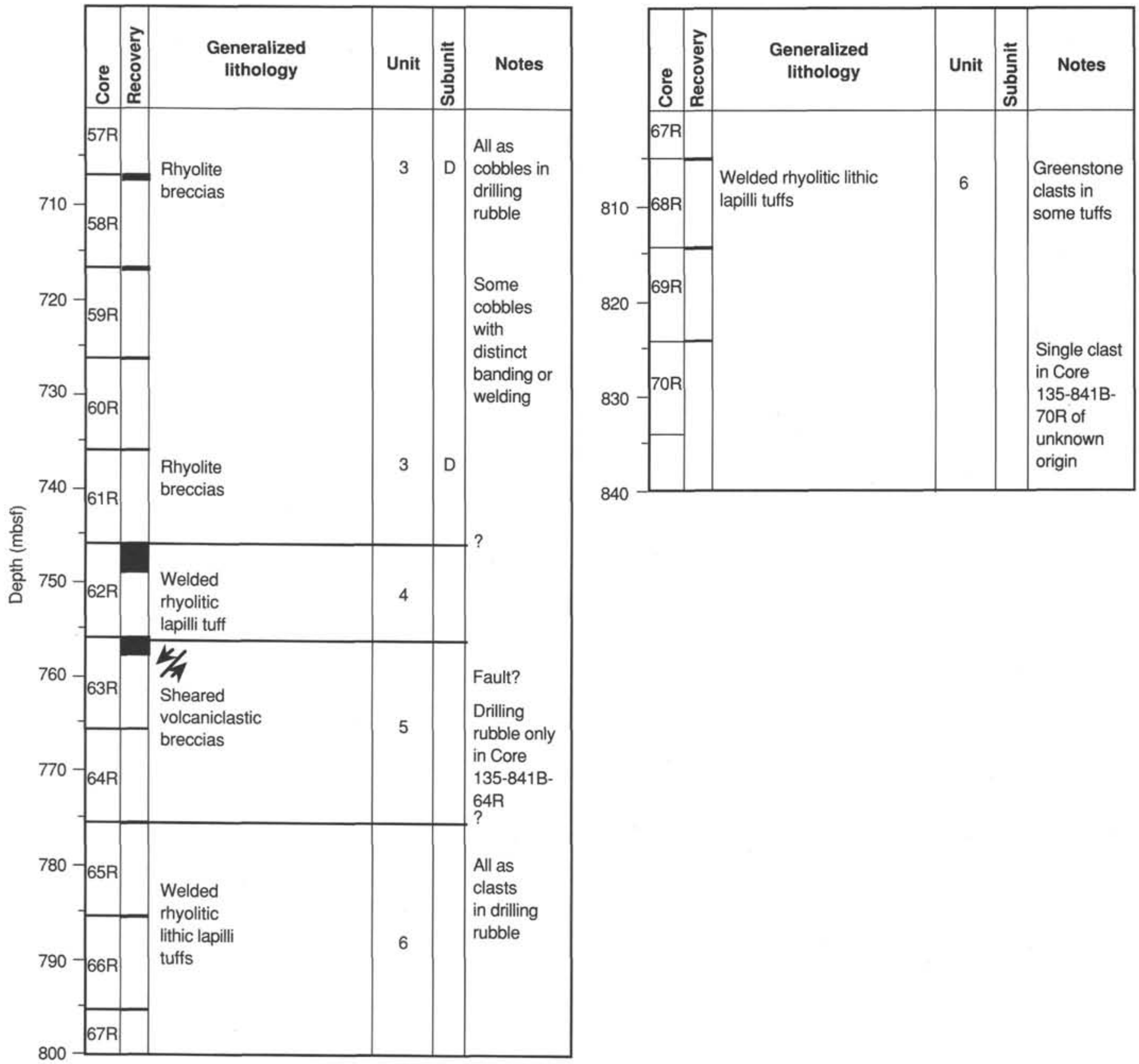

Figure 43 (continued).

hand specimen is due predominantly to infilling by chlorite, clays, and minor iron-oxyhydroxides, although localized replacement does occur in the pumice fragments.

Petrographic examination of a rhyolite clast (Section 135-841B-51R-3, 89–91 cm) shows phenocrysts of quartz (3%–5%), plagioclase (5%–7%), hornblende (2%–3%, pseudomorphed by actinolite), clinopyroxene (trace), and magnetite (1%). The groundmass is relatively coarse grained (0.2–0.3 mm) and well crystallized, suggesting that the fragment may be derived from an intrusive plug or dike. Two mineralogical features in this clast are of interest. First is the presence of what is considered to be phenocrystal (and groundmass) hornblende, partially to completely pseudomorphed by actinolite. Second is the occurrence of irregular symplectic overgrowths on some quartz phenocrysts, which are interpreted as having developing during groundmass recrystallization.

The pumice breccias are interpreted as poorly welded ash-flow deposits, and analogies can be made with similar deposits in New Zealand (Ewart, 1965). They seem to predate the rhyolitic lava (Subunit 2B), but interrelationships between the two subunits suggest that they are successive phases of the same volcanic event.

Unit 3: Tuffs, Lapilli Tuffs, Welded Tuffs, and Rhyolite Breccias

Unit 3 comprises a series of rhyolitic tuffs and lapilli tuffs, welded rhyolitic lapilli tuffs, and rhyolitic breccias. We have divided it into Subunits 3A to 3D. Subunit 3A includes rhyolitic tuffs and lapilli tuffs (654.20–662.97 mbsf) and was first recovered from Section 135-841B-52R-CC, 30 cm, as 5 cm of rhyolitic sandy material underlying the pumice breccias (Subunit 2C) along a sharp contact dipping at approximately 30°. It is estimated to be 8.77 m thick (21.5% recovery) and overlies Subunit 3B on an

Table 12. Igneous and volcaniclastic units defined at Site 841.

Unit		Subunit	Sample Top depth (mbsf)	Sample Bottom depth (mbsf)	Features
1	Moderately to highly phyric orthopyroxene-clinopyroxene-plagioclase basaltic andesite sills and dikes or pillows	A	18R-1, 126 cm 324.76	18R-2, 37 cm 325.37	Intruding upper Miocene sediments; baked sediment occurs adhering to some margins; glassy margins, brecciation common in some pieces; 5%–7% plagioclase, trace amounts of clinopyroxene and orthopyroxene; altered glassy margins common; steep dips on some margins suggest intrusion as dike-like bodies; variously altered with vein materials, including thaumasite and disseminated pyrite.
		B	23R-4, 0 cm (Piece 1) 375.1	23R-4, 66 cm (Piece 8) 375.76	
		C	23R-4, 85 cm (Piece 9) 375.95	23R-4, 97 cm (Piece 10B) 376.07	
		D	24R-CC, 0 cm 383.31	26R-1, 10 cm (Piece 3) 400.20	
		E	26R-2, 75 cm (Piece 1) 402.20	26R-2, 93 cm (Piece 3) 402.63	
		F	28R-1, 0 cm 419.40	28R-1, 7 cm 419.47	
		G	31R-1, 0 cm (Piece 1) 448.50	31R-1, 9 cm (Piece 2) 448.59	
		H	32R-1, 26 cm 458.36	32R-1, 33 cm 458.43	
		I	36R-1, 80 cm (Piece 1) 497.60	36R-1, 88 cm (Piece 2) 497.68	
2	Quartz-plagioclase rhyolites, rhyolitic pumice breccias				
	Sheared and altered rhyolite breccias and fault gouge	A	47R-2, 95 cm 605.05	48R-1, 0 cm 612.30	Pyrite, quartz, clay throughout; quartz grains floating in white matrix; minor rhyolitic clasts with shear fabrics; virtually completely altered.
	Moderately to highly phyric quartz-plagioclase vitric rhyolites and rhyolitic pumice	B	48R-1, 0 cm 612.30	50R-1, 21 cm 631.81	5%–10% euhedral quartz phenocrysts, 10%–15% euhedral plagioclase phenocrysts; rare pyroxene phenocrysts; vitric groundmass with perlitic cracks; hydration of glass gives it a dark resinous luster like pitchstone; internal shear zones and transitions from massive rhyolite to poorly welded rhyolite pumice with plagioclase-quartz phyric pumice clasts.
	Poorly welded rhyolitic pumice breccias	C	50R-1, 21 cm 631.81	52R-CC, 30 cm 654.20	Highly vesicular pumice clasts in matrix of pumice fragments, quartz, and plagioclase grains, and occasional rhyolite lithic clasts; alteration appears very high in hand sample because of green-white color but shards are actually quite fresh in thin section; fractures and faults with clay/chlorite coatings are common.
3	Tuffs, lapilli tuffs, welded tuffs, rhyolite breccias				
	Rhyolitic tuffs to lapilli tuffs	A	52R-CC, 30 cm 654.20	53R-CC, 13 cm 662.97	Fragments of rhyolite, pumice and altered pumice, disaggregated plagioclase, and quartz phenocrysts.
	Welded rhyolitic lapilli tuffs	B	53R-CC, 13 cm 662.97	54R-1, 55 cm 670.75	Erosive contact over Unit 3C; lenticular altered pumice fragments with steep and irregular orientations in matrix of disaggregated pumice grains.
	Laminated crystal tuffs to lapilli tuffs	C	54R-1, 55 cm 670.75	55R-1, 0 cm 679.80	Steeply dipping wavy lamination; convoluted locally and truncated by 60° faults and fractures filled by clastic dikes; lamination truncated by Unit 3B; shows fining upwards overall, with some shorter coarse to fine intervals in the unit as a whole; well-sorted mixture of altered glass, microcrystalline quartz and fe

Unit		Subunit	Sample Top depth (mbsf)	Sample Bottom depth (mbsf)	Features
	Rhyolite breccias	D	55R-1, 0 cm 679.80	62R-1, 0 cm 747.20	Angular to subrounded sparsely to moderately phyric rhyolite cobbles with lithyic inclusions; 3–5% quartz phenocrysts; 1–3% plagioclase phenocrysts; range from massive to welded.
4	Welded rhyolitic lapilli tuff		62R-1, 0 cm 747.20	63R-1, 49 cm 757.39	Lenticular flattened grey pumice fragments, abundant rhyolitic lithic fragments; sheared at base, grading into Unit 5; pumice clasts are somewhat more abundant near top, lithic clasts more abundant near base; pyrite common.
5	Sheared volcaniclastic breccias		63R-1, 49 cm 757.39	65R-CC, 0 cm 776.20	Highly sheared, extensive replacement by mixed clays and chlorite(?); abundant dark fine-grained clasts of shale/siltstone or highly altered mafic volcanics.
6	Welded rhyolitic lapilli tuffs		65R-CC, 0 cm 776.20	69R-CC, 15 cm 815.60	Pumice lenticles strongly deformed and irregular; quartz and feldspar grains occur as phenocrysts in lithic fragments and as disseminated grains; original feldspars and matrix are intensely altered; pyrite is common; large lithic fragments of mafic greenstones are also common.

Notes: Subunits in Unit 1 are lithologically homogeneous. The subunits in Units 2 through 6 are described separately. Units have been defined as lithologies with textural or mineralogic similarities in hand sample and thin section. Subunits are defined as lithologies separated by sedimentary interbeds in the case of the sills and dikes of Unit 1, or as changes of facies within apparently compositionally similar volcaniclastic deposits in the case of Units 2 through 6. If the contact between two units was not recovered, the upper unit was arbitrarily extended downward to the first recovered interval of the lower unit.

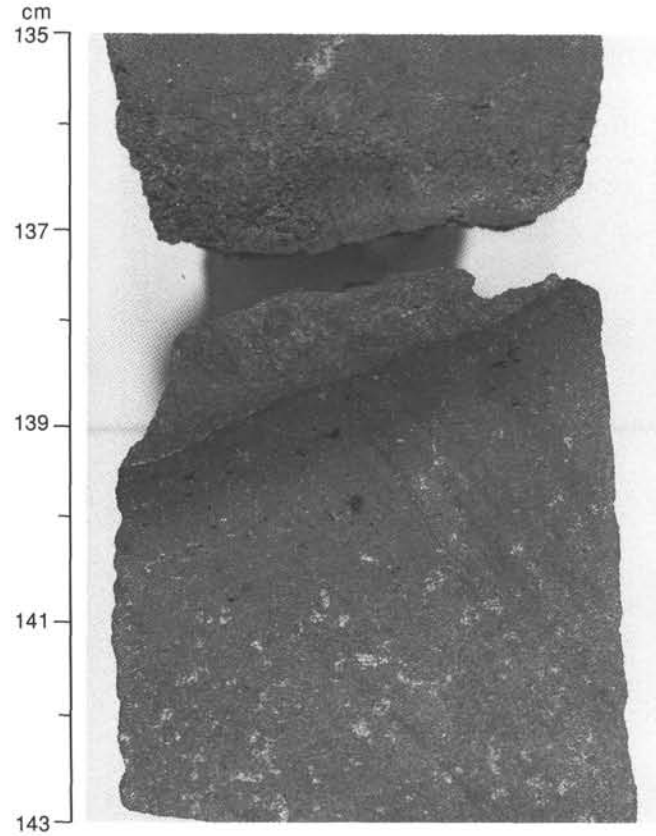

Figure 44. Contact between basalt with glassy, chilled margin and baked sediment, with a concentration of vesicles within a 1-cm zone near the contact; Subunit 1B, interval 135-841B-18R-1, 135–143 cm.

irregular, steeply dipping sharp contact that appears erosive in origin. Sharp erosive or sheared contacts occur within Unit 3 in Section 135-841B-53R-1 between lapilli tuffs and tuffs. Most of the tuffs show no clearly defined bedding or lamination. Lithic fragments of phyric quartz-plagioclase rhyolite ranging from 1 to 6 mm in size (occasionally up to 25 mm) occur in a fine-grained altered matrix that contains small, scattered grains of quartz and plagioclase. Alteration is pervasive and includes disseminated pyrite, clay, and chlorite.

Subunit 3B is a welded lithic tuff; it was recovered in only a narrow interval (approximately 7.84 m) and has steep, irregular, sharp, erosive contacts with both the overlying and underlying units (Fig. 53). The bottom 10–20 cm of Subunit 3B shows evidence of admixture with the underlying Subunit 3C. Subunit 3B contains phenocrysts of quartz (5%–7%) and plagioclase (3%–5%) set in a fine-grained altered matrix that contains highly deformed and flattened, greenish gray lenticular altered pumice clasts. The orientation of the clasts is random, possibly the result of deposition on a steep and irregular surface. The rock is intensely altered, with development of clays, calcite, quartz, albite, and disseminated irregular aggregates of pyrite. This alteration has destroyed original matrix textures.

Subunit 3C comprises 9.05 m (45.3% recovery) of laminated crystal tuffs to lapilli tuffs. The top is a sharp, very irregular contact with Subunit 3B (Fig. 53). The tuffs have an irregular, steeply dipping wavy lamination with dips in excess of 70° (Fig. 53). This lamination is developed on a millimeter scale and is defined by subtle light and dark banding accompanied by slight grain-size variations. Thin clastic dikes crosscut the tuffs at high angles (Fig. 54). The overall texture, as seen in hand specimen, is of a relatively well-sorted, fine-grained sandy deposit. The grain size increases in the lowermost 50 cm of the unit, with increasing abundance of lithic fragments up to 2.5 cm in diameter at the base. Alteration is pervasive, with development of pyrite, clays, and chlorite. One thin section (Section 135-841B-54R-1, 97–99 cm)

Table 13. Modal analyses of representative basaltic andesites from Unit 1 and rhyolitic lavas from Units 2 and 3 in Hole 841B.

Core, section	18R-1	25R-3	48R-1	49R-1	50R-1	51R-3	55R-1	59R-1
Interval (cm)	137–140	117–118	53–56	20–21	14–17	89–91	1–3	8–12
Piece	—	—	—	—	—	—	1	—
Unit	1A	1D	2B	2B	2B	2C	3D	3D
Rock type	Basaltic andesites		Rhyolite	Pumice	Rhyolite	Rhyolite clast	Rhyolite clast	Rhyolite clast
N	782	808	1003	1016	1043	1141	1003	1235
Phenocrysts:								
Plagioclase	8.8	12.2	14.1	8.0	15.1	7.4	3.5	4.1
Quartz	—	—	6.7	3.9	8.1	4.1	6.5	4.6
Clinopyroxene	2.1	2.5	0.4	0.1	0.8	Tr	—	—
Orthopyroxene	0.6	0.9	0.7	<0.1	0.6	—	—	—
Opaques	0.6	0.7	0.5	0.2	0.4	1.2	—	—
Amphibole	—	—	—	—	—	1.8	—	—
Pyrite	—	—	—	—	—	—	2.2	2.4
Quartz-feldspar aggregates	—	—	—	—	—	—	1.9	2.4
Open vesicles	—	—	10.9	44.0	6.8	—	0.4	0.1
Filled vesicles	—	—	<0.1	0.3	0.4	—	—	—
Mesostasis	87.7	83.4	66.8	43.5	67.9	85.5	85.8	85.9

Notes: Plagioclase phenocryst count includes plagioclase partially or totally pseudo morphed by clays, carbonate, and albite. Quartz-feldspar aggregates rim large quartz phenocrysts and occur throughout the groundmass; they are similar to the "snowflake" structures that have been described in similar rhyolitic lavas (Anderson, 1969; van der Lingen, 1973). The largest of these may be replacements of plagioclase feldspar. All samples appear to be fragments of massive lavas, except for Sample 135-841B-49R-1, 20–21 cm, which is a rhyolitic pumice. Opaque percentages refer to primary opaque phases; the pyrite in the rhyolites is a secondary phase. The mesostasis includes crystallites, recrystallized quartz and feldspar, and alteration products. The amphibole in Sample 135-841B-51R-3, 89–91 cm, is partially replaced by actinolite and traces of sphene; it occasionally has cores of apparently unaltered amphibole. Tr = trace.

Figure 45. Photomicrograph of skeletal and equant quenched plagioclase and magnetite in cryptocrystalline mesostasis; Subunit 1I, Sample 135-841B-36R-1, 84–86 cm; crossed polarized light; field of view = 0.3 mm.

shows scattered subhedral to angular fragments of quartz (0.05–0.2 mm) and less common plagioclase (0.05–0.15 mm) in a finer grained matrix of devitrified and recrystallized glass shards (0.01–0.025 mm).

The origin of this subunit is problematic. One possible interpretation is that it represents a ground surge deposit underlying Subunit 3B. Surge deposits range from sandwave bedforms, to massive bedforms, to planar bedforms (see review in Fisher and Schmincke, 1984). The lithology of Subunit 3C would seem most similar to the massive bedform facies, which tends to be thicker, although more poorly sorted, than the other types, and which possesses pebble trains or faint internal stratification that can be either planar or wavelike.

An alternative interpretation is that the sands in Subunit 3C result from local reworking of primary tephras, which may be consistent with the wavy laminations and the overall, small-scale normal grading of the deposit. Erosion and redeposition of unconsolidated tephra on a local scale (e.g., due to rainwash and changing surface drainage patterns) is a common process associated with the sedimentation of voluminous pyroclastic deposits. The steep dip indicates either deposition on unusually irregular and steep topography, or more plausibly, post- (or syn-) depositional slumping or bulk disturbance during emplacement of the overlying units. The general form of the laminations and the absence of distinctly graded bedded intervals within the unit are considered to be inconsistent with an airfall origin.

Subunit 3D consists of a sequence of rhyolite breccias (recovered interval is 67.4 m thick). These consist of broken fragments (up to about 5 cm diameter) of rhyolite, siltstone, and light gray pumiceous fragments set in a poorly sorted, finer matrix of smaller rhyolite fragments grading down to clay-like, soft interstitial material (Fig. 55). Most of this matrix seems to have been lost during drilling. The rhyolitic clasts themselves often contain small rhyolitic lithic fragments (up to 5.5 cm), and some exhibit irregular banding, suggesting that some of the clasts are welded lithic tuffs; thin-section examination shows that the clasts include rhyolite lavas and poorly welded rhyolitic pumice breccias.

The rhyolite lava clasts are mineralogically and texturally very uniform, indicating a common source. Phenocryst phases are quartz (3%–5%; equant euhedral to anhedral crystals, occasionally showing partial resorption, 0.2 to 1.5 mm in diameter), plagioclase (1%–5%; up to 1 mm, euhedral to subhedral crystals, showing prominent oscillatory zoning), and magnetite (<1%; up to 0.15 mm diameter, commonly included in plagioclase phenocrysts). The groundmass is a microcrystalline (mostly <0.02 mm) mosaic of quartz, plagioclase, and interstitial alkali feldspar. A common textural feature is the development of quartz-feldspar symplectite that encloses some (but not all) of the quartz and

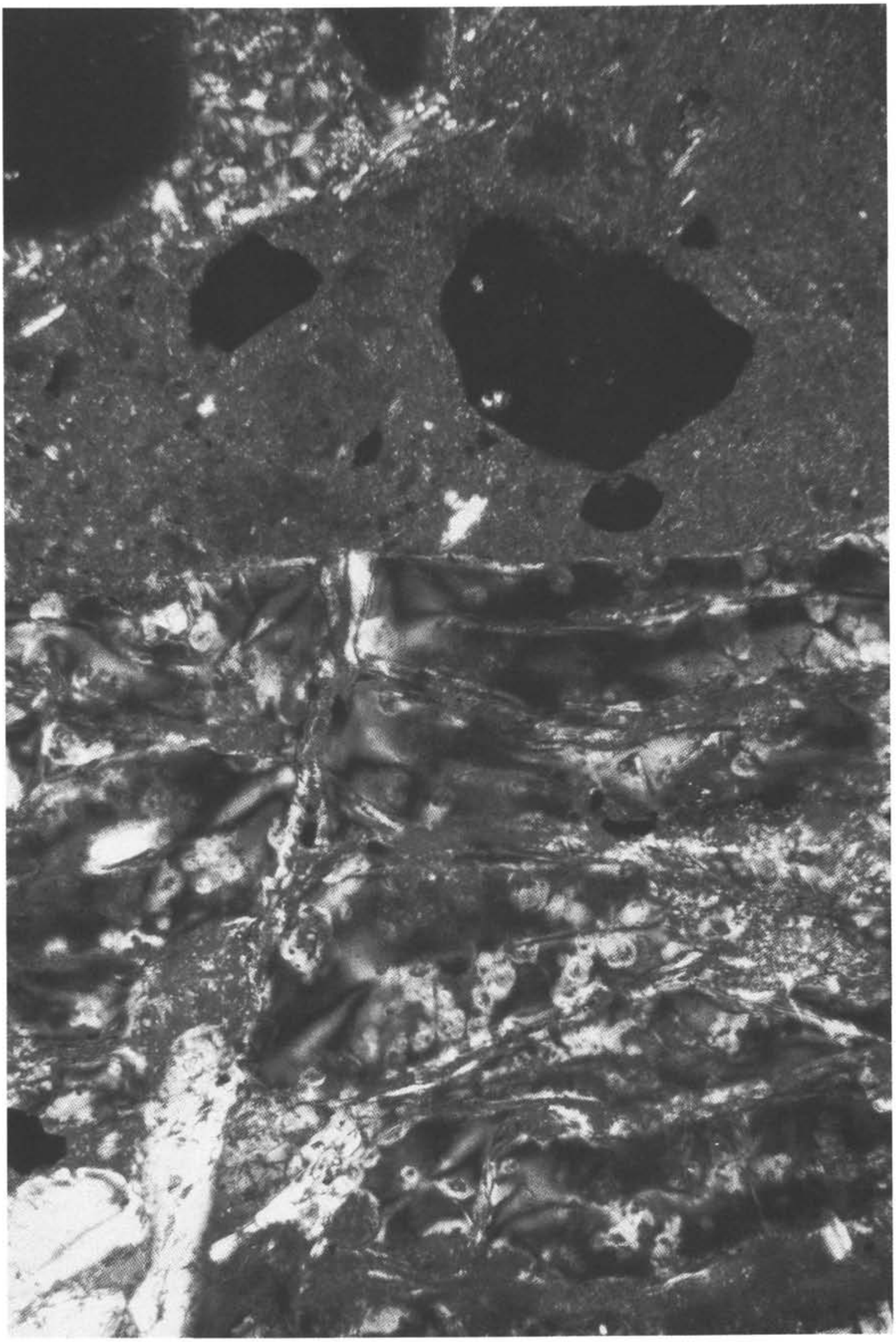

Figure 46. Photomicrograph of devitrified, ribbed glassy contact against sediment (left side of photo); Subunit 1D, Sample 135-841B-25R-3, 117–118 cm (Piece 12A); ordinary light; field of view = 1.5 mm.

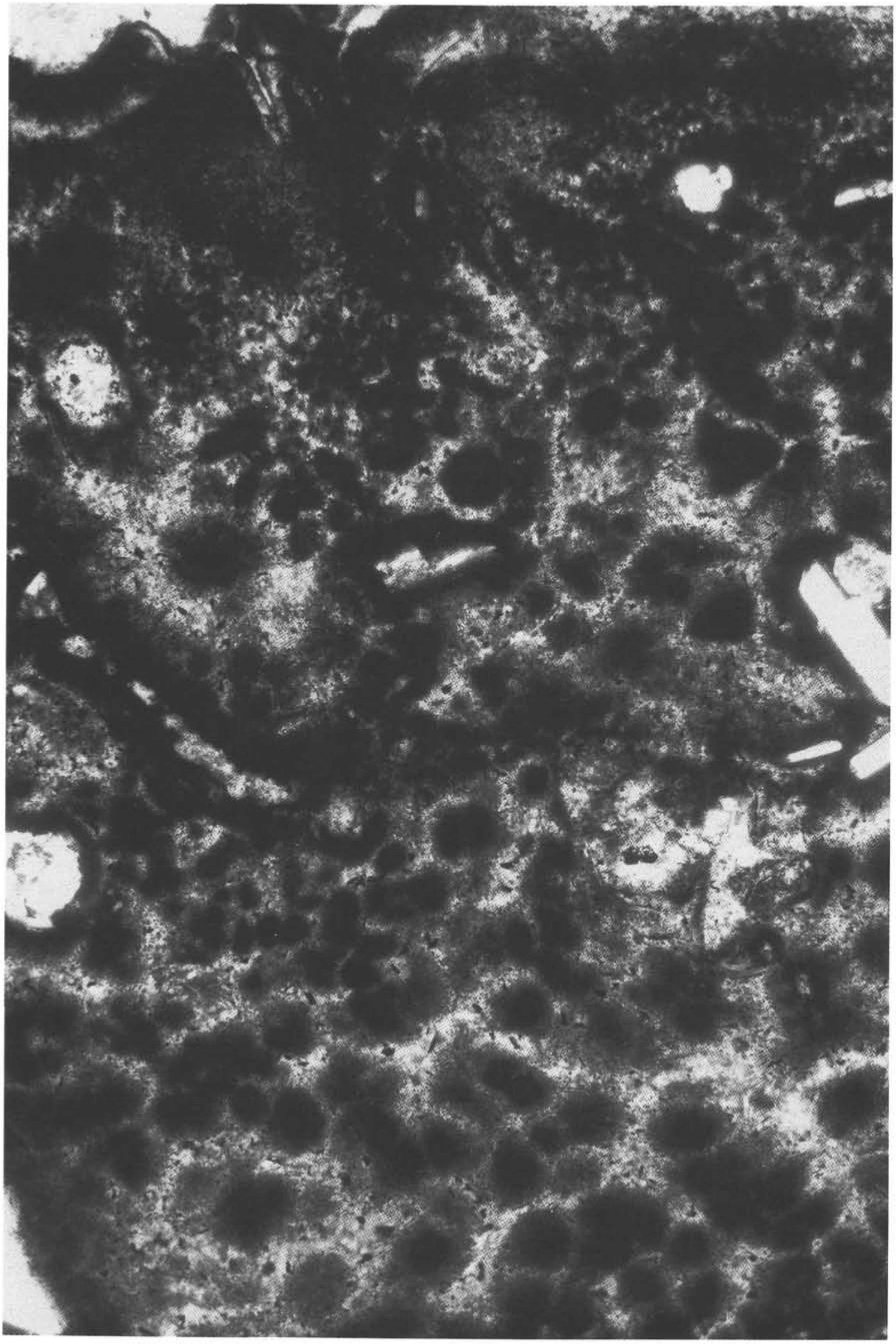

Figure 47. Photomicrograph of a chilled contact zone (contact in left bottom corner) showing transition from nearly opaque contorted zone into variolitic zone; Subunit 1A, Sample 135-841B-18R-1, 137–140 cm; plane light; field of view = 1.5 mm. Phenocrysts of plagioclase are visible.

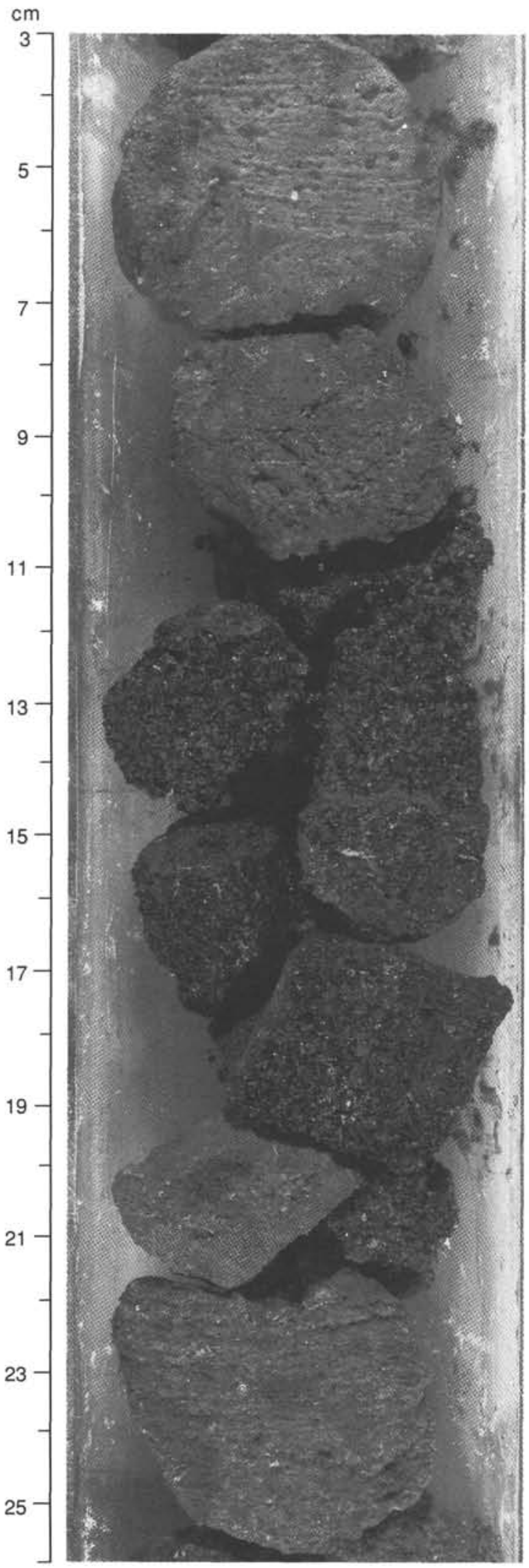

Figure 48. Black pumice pitchstone and paler fragments of pumice and pumice breccia fragments; Subunit 2B, interval 135-841B-49R-1, 3–26 cm.

plagioclase phenocrysts (Fig. 56). This texture is interpreted as the result of post-emplacement recrystallization of the original lavas. All samples have undergone alteration, with replacement by pyrite as skeletal aggregates scattered through the groundmass of samples. In rare instances, these replace original ferromagnesian phenocrysts. Other secondary minerals are clay, chlorite, albite, and quartz.

The rhyolite pumice breccia (Sample 135-841B-56R-1, 0–3 cm) contains phenocrysts of quartz (5%) and plagioclase (2%–3%) set in a matrix of recrystallized and altered fragments of original volcanic glass and pumice clasts. The fine matrix textures have been destroyed by recrystallization, but the outlines of the shapes and structures of the original abundant pumice clasts are visible. Recrystallization has also resulted in the local development of quartz-feldspar symplectite adjacent to the rims of some quartz phenocrysts.

The poor recovery of Subunit 3D makes interpretation of its origin difficult. The coarse clasts and the poorly sorted (and poorly recovered) matrix may be consistent with a coarse lag in a poorly welded ash-flow tuff unit.

Unit 4: Welded Rhyolitic Lapilli Tuff

Unit 4 is a greenish gray welded rhyolitic lapilli tuff unit, with an estimated thickness of 10.19 m (33.6% recovery). The tuffs are moderately to highly phyric, with quartz and plagioclase phenocrysts, and contain abundant, highly altered, elongated and flattened pumice clasts set in a fine-grained matrix (Fig. 57). The lenticular pumice imparts a planar foliation to the rock. The dip of the foliation is often steep, but is highly variable between fragments (Fig. 57). Lithic fragments (rhyolitic and basaltic/basaltic andesitic) are also common. There is an increase in the size (2–7 cm) and abundance of lithic clasts at the base of the unit, while the concentration of flattened pumice lenticules increases upward. This upward increase in pumice is not a typical characteristic of many welded tuff deposits, raising the possibility of deposition as locally reworked rhyolitic material. The base of the unit is strongly sheared and is gradational into Unit 5.

Petrographic examination of three tuff samples shows phenocrysts of quartz (3%–7%; 0.1–1.6 mm), which range from euhedral equant crystals to fragmented crystals. Some are partially resorbed. Plagioclase phenocrysts (1%–5%; 0.2–1.3 mm) also occur as euhedral to subhedral tabular crystals and glomerocrysts. Prominent oscillatory zoning is well developed in the plagioclase crystals. Pumice shapes and structure, although altered and recrystallized, are still readily discernible in most samples. Only in the topmost sample examined in thin section (135-841B-62R-1, 23–27 cm) have devitrification and alteration completely destroyed the original shard textures. In the two lower thin-section samples (135-841B-62R-2, 16–20 cm, and -62R-2, 113–116 cm), there are patches in the finer grained groundmass in which the original interlocking shard outlines (i.e., vitroclastic texture) can still be recognized in spite of the recrystallization. These original shard outlines are not intensely deformed and compacted, which suggests only a moderate degree of original welding. Alteration of all samples is intense, with development of secondary pyrite, calcite, chlorite, albite, and quartz.

Rhyolitic clasts within the tuff have phenocrystal quartz (3%; up to 2 mm), plagioclase (5%–7%; up to 2 mm, with oscillatory normal zoning), and magnetite (<1%; up to 2 mm, most commonly associated with plagioclase phenocrysts). These are set in a microcrystalline and microspherulitic groundmass. Secondary calcite is conspicuous.

Unit 5: Sheared Volcanic Breccias

This unit has an estimated thickness of 18.8 m (from Section 135-841B-63R-1, 49 cm, to 135-841B-65R-CC, 0 cm; Table 12)

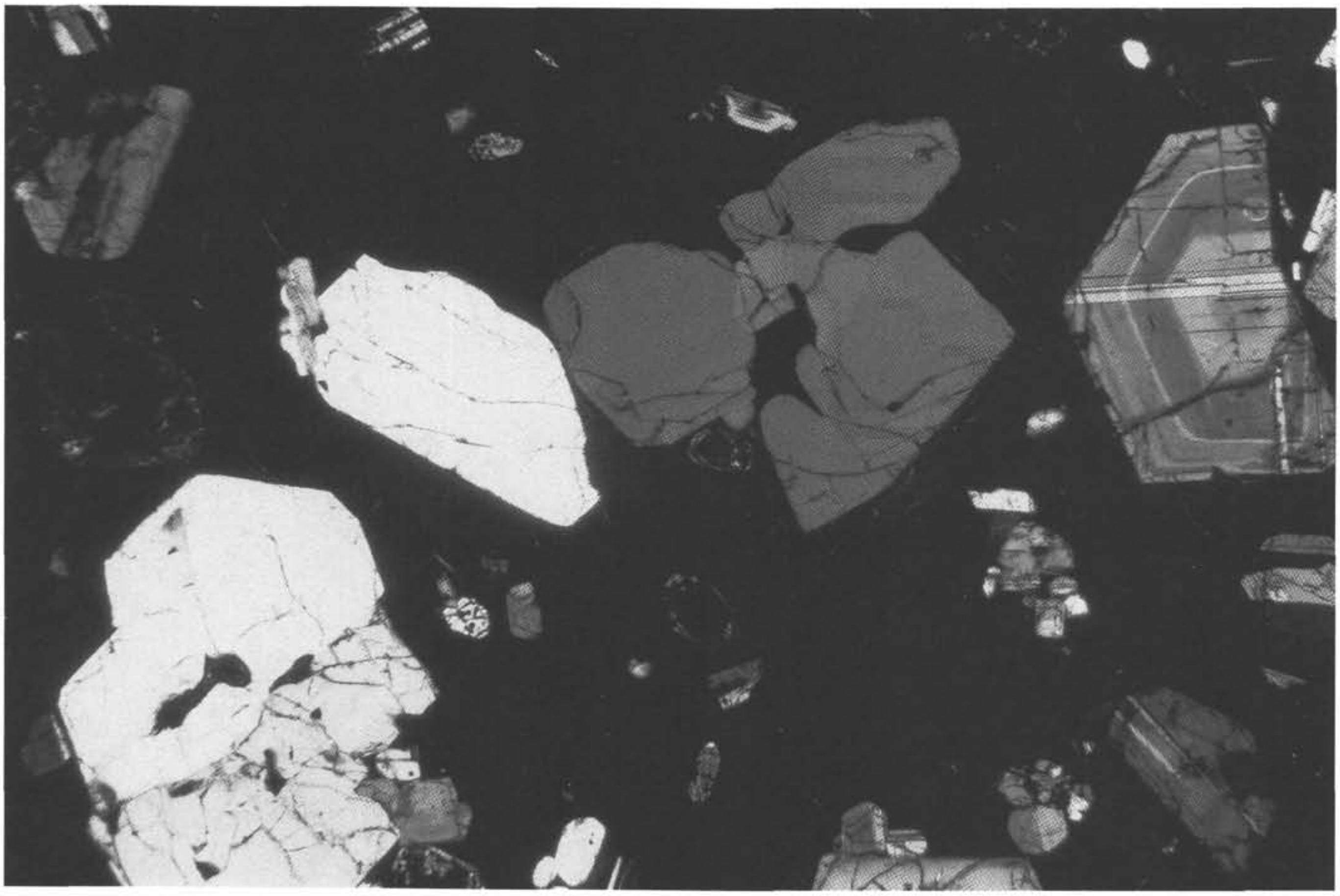

Figure 49. Photomicrograph of phenocrysts of quartz (showing partial resorption) and zoned plagioclase in a vitreous matrix; Subunit 2B, Sample 135-841B-50R-1, 14–17 cm; crossed polarized light; field of view = 6 mm.

and includes highly sheared volcanic breccias which grade downward from Section 135-841B-63R-1, 49 cm, in Unit 4. The contact zone between Units 4 and 5 is taken where there is a relatively abrupt increase in the proportions of dark-colored fragments (up to 3 cm diameter). Recovery in core was 7.1%. The breccia is a grayish green to dark bluish gray with individual clasts of rhyolite, vesicular rhyolite, and dark siltstone or shale, set in a fine, friable rhyolite-dominated matrix. Secondary clays and chlorite are abundant.

Unit 6: Welded Rhyolitic Lithic Lapilli Tuffs

This unit comprises loose fragments of welded lithic lapilli tuffs, together with clasts of rhyolite and less common dark, altered aphyric basalt. It is defined from Section 135-841B-65R-CC, 0 cm, to Section 135-841B-69R-CC, 15 cm (38.9 m; with 3% recovery). The base of the unit was set arbitrarily in Core 135-841B-69R, as Core 135-841B-70R recovered only a single, rounded clast whose origin was uncertain; no drilling advancement was made below that core. The gray to grayish green fragments in Unit 6 exhibit strongly deformed, irregular pumice lenticules and are moderately phyric with a microcrystalline matrix (Fig. 58). Some welded tuff fragments clearly contain lithic inclusions of rhyolite and dark basalt.

Petrographic examination of the welded tuff shows phenocrystal quartz (5%; up to 0.4 mm) which ranges from equant euhedral to subhedral crystals to broken fragments; resorption is evident in some crystals. Recrystallization and alteration is intense and has affected both the matrix and lithic fragments alike. The outlines and structures of original deformed pumice fragments are still clearly visible (as these are usually more coarsely recrystallized than the enclosing matrix). Remnants of highly deformed original shard outlines (i.e., vitroclastic texture) are still barely discernible where recrystallization has been less intense. Alteration minerals include clays, chlorite, quartz, calcite, albite, and zeolites.

The dark, aphyric basalt fragments contain traces of phenocrystal plagioclase set in a groundmass of plagioclase (radiating laths, largely recrystallized and replaced), pyroxene (completely replaced by chlorite and clays), magnetite grains, and completely replaced mesostasis. Metamorphic and alteration phases include calcite, clays, chlorite, albite, pyrite, zeolite, epidote, and quartz.

Miscellaneous Volcanic Rocks

A variety of volcanic and plutonic rocks occur as clasts in sedimentary breccias or as drilling rubble in intervals of little recovery. Most of these clasts are moderately to highly altered

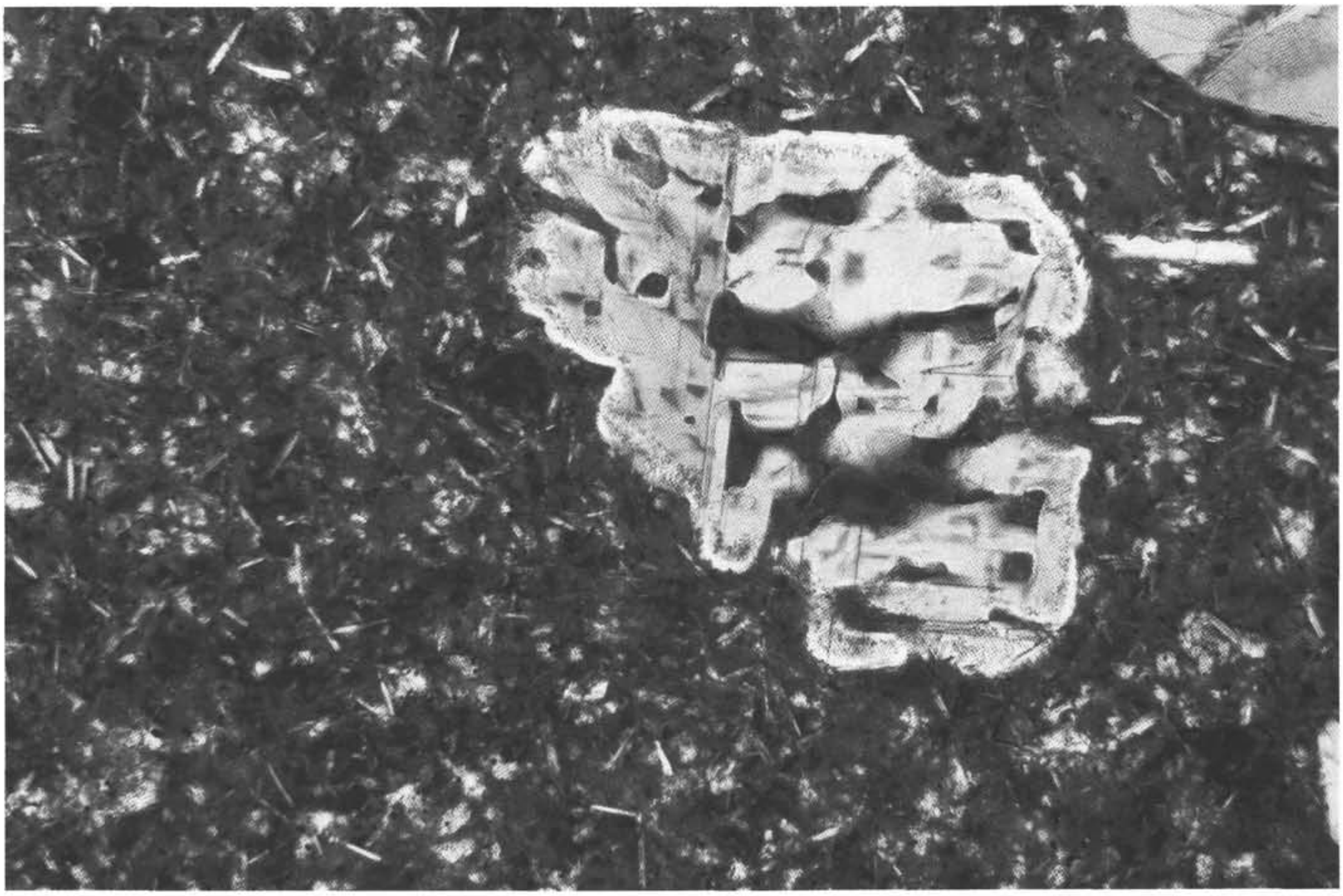

Figure 50. Photomicrograph of strongly resorbed plagioclase in rhyolitic clast in pumice matrix; Subunit 2B, Sample 135-841B-49R-1, 4–7 cm; crossed polarized light; field of view = 1.5 mm.

mafic to intermediate volcanic rocks. Three distinctive clast types were examined in thin section.

A tonalite cobble occurs in Core 135-841B-34R. It is characterized by a coarse-grained texture, alkali feldspar, and aggregates of epidote and chlorite replacing Fe-Mg minerals, and plagioclase. The proportion of potassic to sodic feldspar cannot be reliably determined without a stained thin section. The occurrence of coarse-grained epidote is noteworthy, as clastic fragments of epidote and pumpellyite occur in some of the sedimentary breccias. A fine-grained, aphyric rhyolite clast occurs in the same interval as the granodiorite.

A highly altered variolitic basalt fragment occurs in Core 135-841B-40R. It is completely recrystallized to an assemblage of albite-chlorite-actinolite-quartz, but has extensive retrograde development of clays. This greenschist metamorphic assemblage does not occur in the basaltic andesites higher in the hole. This fragment is also one of the few mafic volcanic fragments positively identified.

Alteration and Metamorphism

A variety of alteration and metamorphic minerals occur in the core above the rhyolitic basement. The basaltic andesite sills generally show only slight development of clay in the mesostasis (e.g., Section 135-841B-25R-1, Piece 14). The variolitic basalt in Section 135-841B-40R-1 is completely recrystallized to a greenschist facies assemblage consisting of actinolite, albite, magnetite, and chlorite. Calcite and zeolites are present variously in the core (Fig. 17). X-ray diffraction determination of a hand-picked, white, soft mineral that occurred in veins in Section 135-841B-18R-2 revealed thaumasite ($Ca_3Si(OH)_6(CO_3)(SO_4) \cdot 12H_2O$) as the main constituent (Fig. 59). Quartz-feldspar veins are common in the basaltic andesite sills, sometimes carrying relatively large amounts of sulfides. Thaumasite is also thought to be present in these veins. Vein-filling sulfide minerals are mainly pyrite with lesser marcasite and chalcopyrite. Pyrite in these veins contains abundant silicate inclusions and is rimmed by at least two generations of marcasite (Figs. 60 and 61). In addition, pyrite and chalcopyrite occur as secondary sulfide minerals in the groundmass. Sample 135-841B-40R-1 (Piece 1), a volcanic clast occurring in sediments, is completely replaced by actinolite (~70%), albite (15%–20%), and chlorite (Fig. 62). Abundant titanomagnetite is also observed but no sulfides are present. The tonalitic clast occurring at Section 135-841B-34R-1, 2–4 cm, contains abundant epidote, clinozoisite, and chlorite as secondary phases (Fig. 63). Anomalous brownish interference colors suggest a

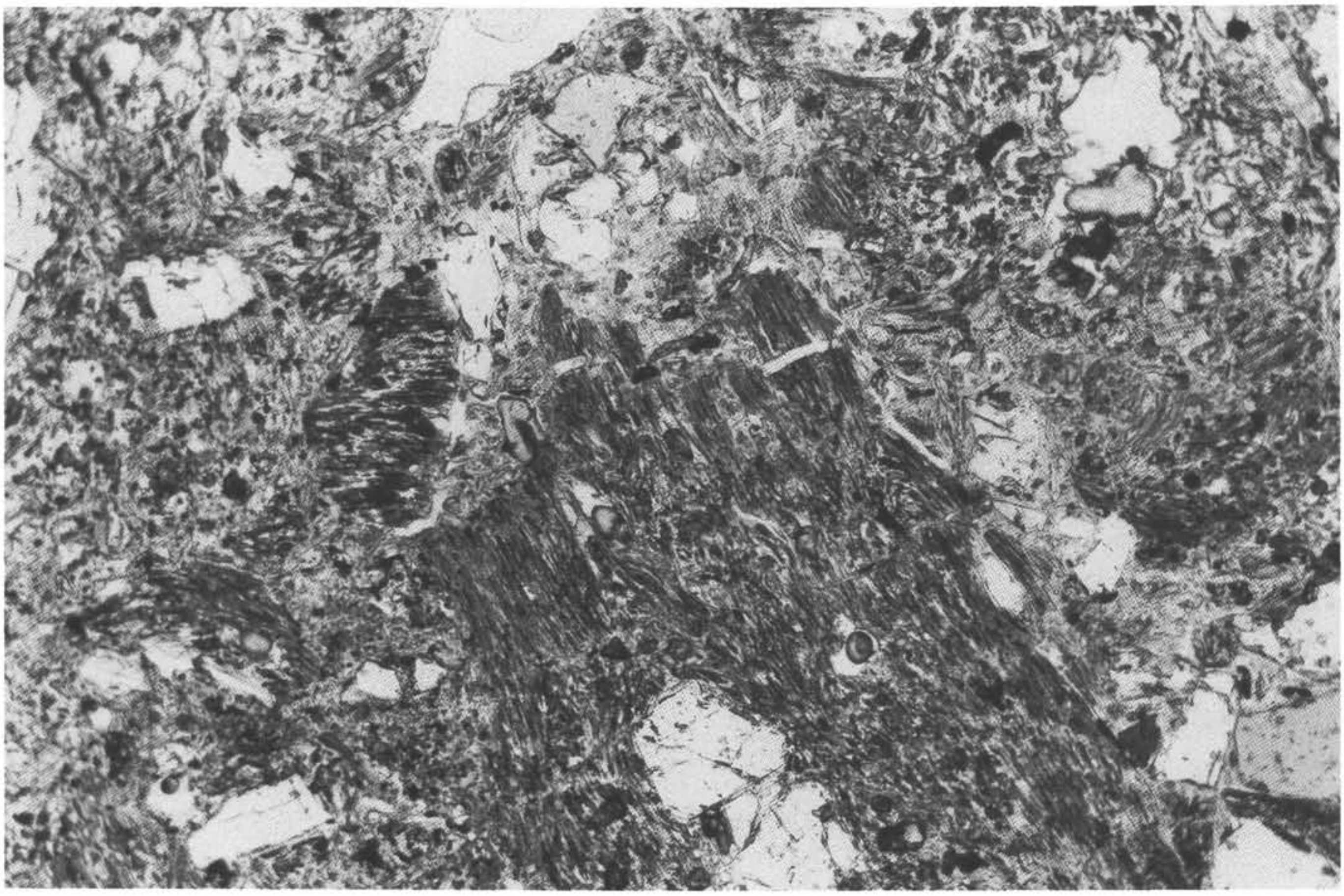

Figure 51. Photomicrograph of pumice fragments in pumice breccia; Subunit 2B, Sample 135-841B-48R-1, 52–56 cm; plane light; field of view = 1.5 mm. The pumice shows prominent attenuated tubular vesicle structure.

magnesium-rich composition of the chlorite; coexisting titano-magnetite is also abundant.

The first of the pyroclastic rhyolitic breccias and lavas occurs below Section 135-841B-47R-2. These become more altered deeper in the sequence. The rhyolitic breccias exhibit kaolinite and illite development, together with pervasive low-grade disseminated sulfide mineralization. In fresher rock fragments, sulfide-filled veins also occur. Pyrite is the dominant sulfide, but occasionally pyrrhotite inclusions occur in the pyrite (Fig. 64). In the lowermost part of the section, magnetite(?) rims pyrite and fills cracks. Some pyrite grains in the groundmass are surrounded by Fe-rich chlorite.

Different pyrite morphologies in the rocks may be related to different stages of pyrite formation. One pyrite morphology is highly porous and exhibits a large amounts of rounded inclusions (Fig. 64), whereas a second form has a more idiomorphic character. No time relationships can be drawn between these two pyrite morphologies.

The intense alteration of the rhyolitic breccias suggests a high-temperature (>300°C) hydrothermal fluid circulation. Hydrothermal processes may also have produced extensive low-grade mineralization within the upper drilled rock sequence (see "Lithostratigraphy" section, this chapter).

Geochemistry

Eight samples from Hole 841B, including five from Unit 1 and one each from Units 2, 3 and 4, were selected for shipboard X-ray fluorescence (XRF) geochemical analysis (Table 14). The rocks of Unit 1 are classified as low-K basaltic andesites and the limited variation between the five representative samples supports the designation of a single unit for this group. These rocks are clearly derived from more primitive magma compositions. They have an average MgO content of 4.7 wt%, and average Ni and Cr contents of only 20 and 14 ppm, respectively. The lack of geochemical variation precludes any rigorous discussion of the likely fractionation history of these rocks, but it is apparent from the petrography that plagioclase would have been important in controlling the liquid line of descent. It is also likely that orthopyroxene and clinopyroxene were included in the fractionated mineral assemblage.

The trace element abundances of the five samples normalized to N-MORB are illustrated in Figure 65. The variation in Sr, P, Zr, Ti, and Y is very limited and the five patterns are remarkably coherent. In contrast, Rb, Ba, K, and Ce show considerable scatter, with ranges approaching an order of magnitude difference between some samples. The variation in concentrations of some

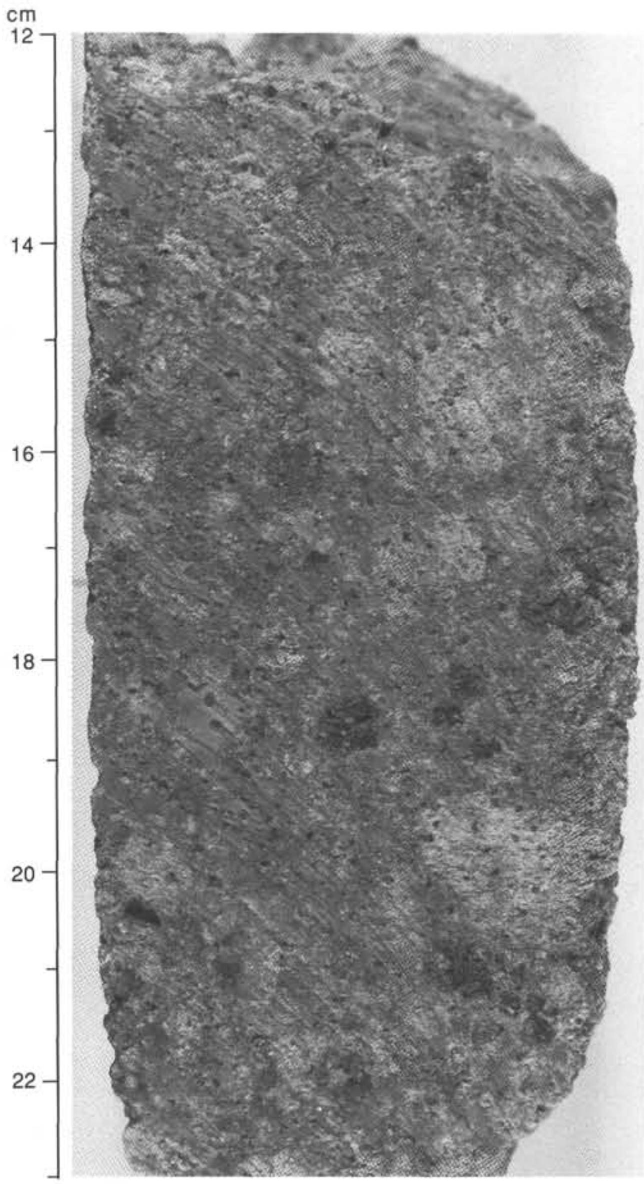

Figure 52. Pumice breccia from near the top of Subunit 2C consisting of pumice fragments and darker, vesicular rhyolitic fragments; Subunit 2C, interval 135-841B-51R-1, 12–23 cm.

of the more incompatible elements could be caused by their mobility during alteration.

Despite the element mobility, it is clear that these basaltic andesites are enriched in large-ion-lithophile elements relative to Nb in a manner similar to rocks from island arcs, and that the Site 841 samples carry an arc-like signature. The uniformity in concentration of the elements from Sr to Y on this diagram indicates that these are likely to represent true magmatic values. The concentrations of these elements are either similar to, or higher than, those observed in basaltic andesites from the Tonga-Kermadec arc. Zr, in particular, is relatively high when compared to Tofua Arc data (Fig. 66), and, together with the relatively elevated Ti and Y, suggests that these rocks were derived from melting a more fertile mantle source compared to the source of the modern Tofua Arc lavas.

Although the Unit 1 rocks show significant differences compared to the Tonga Arc, they share some of the characteristics of the volcanic rocks from the Lau Ridge (Table 15). This is illustrated in Figure 66, which compares the variation in Ba and Zr between samples from the active Tofua Arc, tholeiites from the Lau Ridge, samples from 'Eua and the Tonga forearc, and the samples from Site 841. Although two of the Unit 1 samples plot at high Ba contents, this is interpreted as reflecting mobility during alteration. The lower Ba concentrations are more likely to approximate original magmatic values, and these plot within the field for the Lau Ridge tholeiites, close to the field for the forearc and 'Eua. In this regard, the Unit 1 basaltic andesites more closely

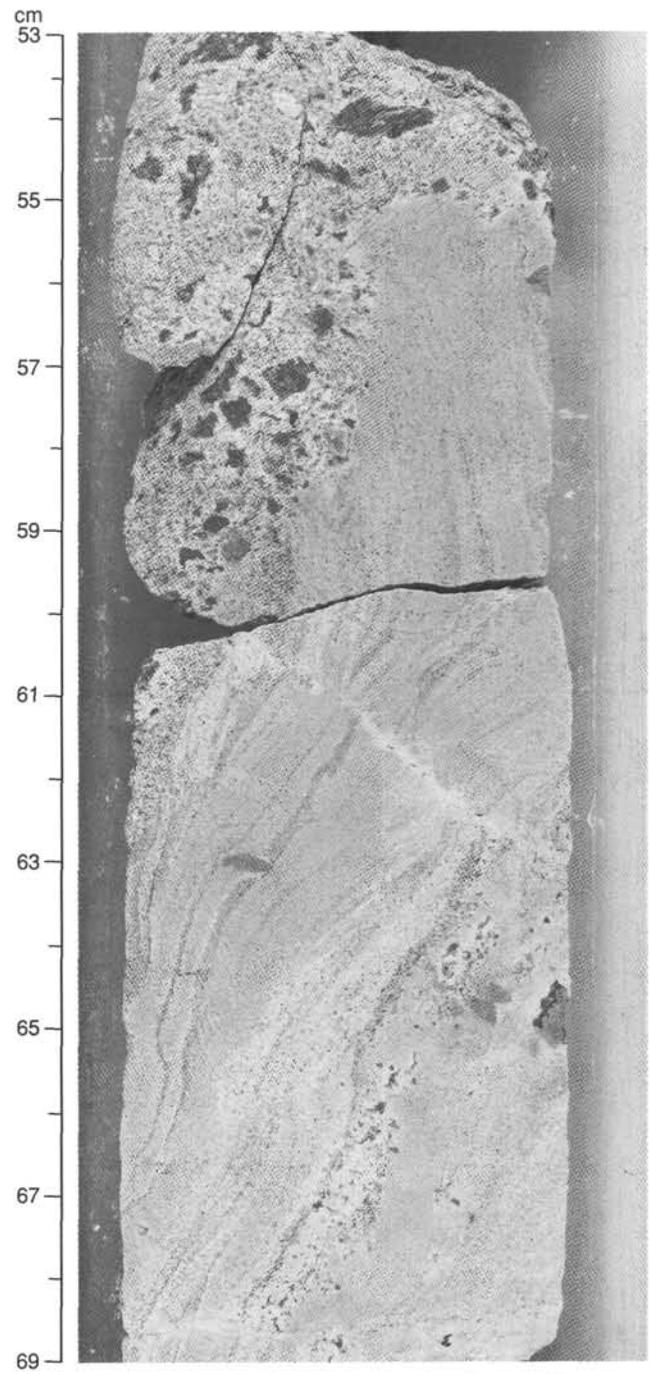

Figure 53. Steep, irregular erosive contact between Subunit 3B (coarse pumice breccia) and Subunit 3C; Subunit 3C, interval 135-841B-54R-1, 53–69 cm. The darker altered pumice clasts are visible in Subunit 3B as are the fine, wavy laminae with thin coarser bands which are characteristic of Subunit 3C.

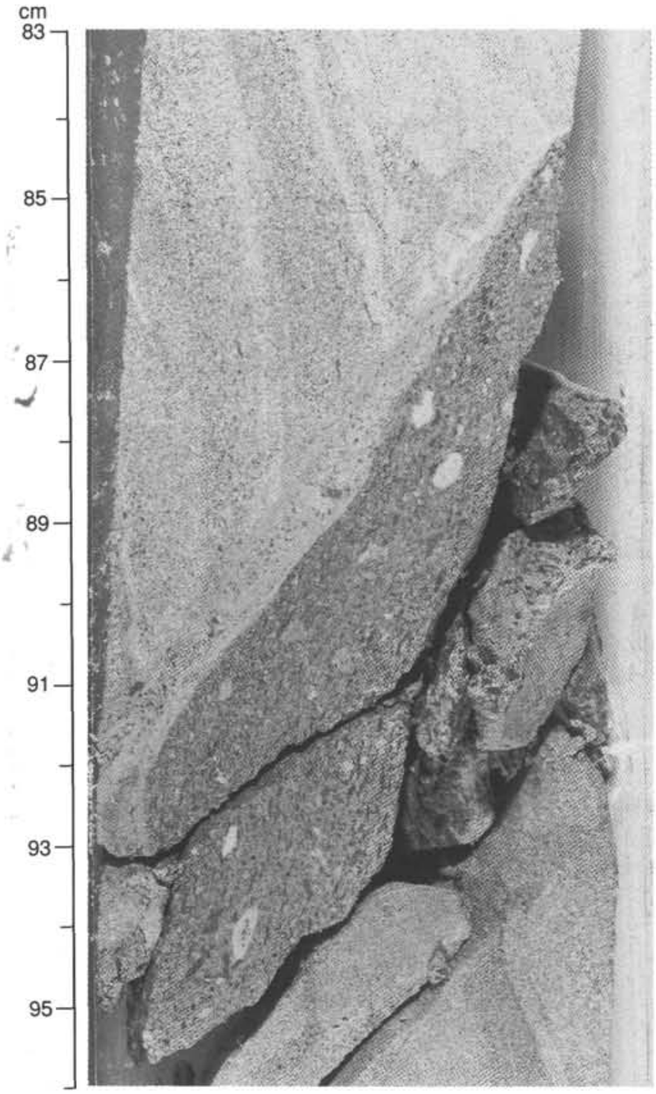

Figure 54. Steeply cross-cutting clastic dikes; Subunit 3C, interval 135-841B-54R-2, 83–96 cm.

resemble older lavas erupted from the Lau Ridge arc system than they do those of the modern arc lavas.

Most high-silica rocks in Units 2 through 6 are altered, recrystallized, tuffaceous, or some combination of the three, so most are poor choices for bulk-rock geochemical analysis. The only samples analyzed, therefore, were massive rhyolitic clasts in tuff breccia from Subunits 2B and 3D and Unit 4, all of which are low-K rhyolite (Table 14; Taylor et al., 1981). Inspection of thin sections, and the very high value for SiO_2 in the Subunit 3D sample, suggest that the Subunit 3D sample was too altered to represent a primary composition. With this exception, these samples can be compared with the geochemical trends and fields defined by other forearc samples, by the high silica-pumice and lavas recovered from previous Leg 135 sites, and by pumices from the two localities in the Tofua Arc for which data on siliceous volcanic rocks are available. For this discussion "high silica" is defined as SiO_2 >68 wt%. The only modern analyses from the Tofua Arc that meet this criterion are the glass from the Metis Shoal dacite pumice, and the matrix from several of the dacites of Fonualei (Ewart et al., 1972).

Selected incompatible trace element pairs indicate that both similarities and certain differences are likely to be related to

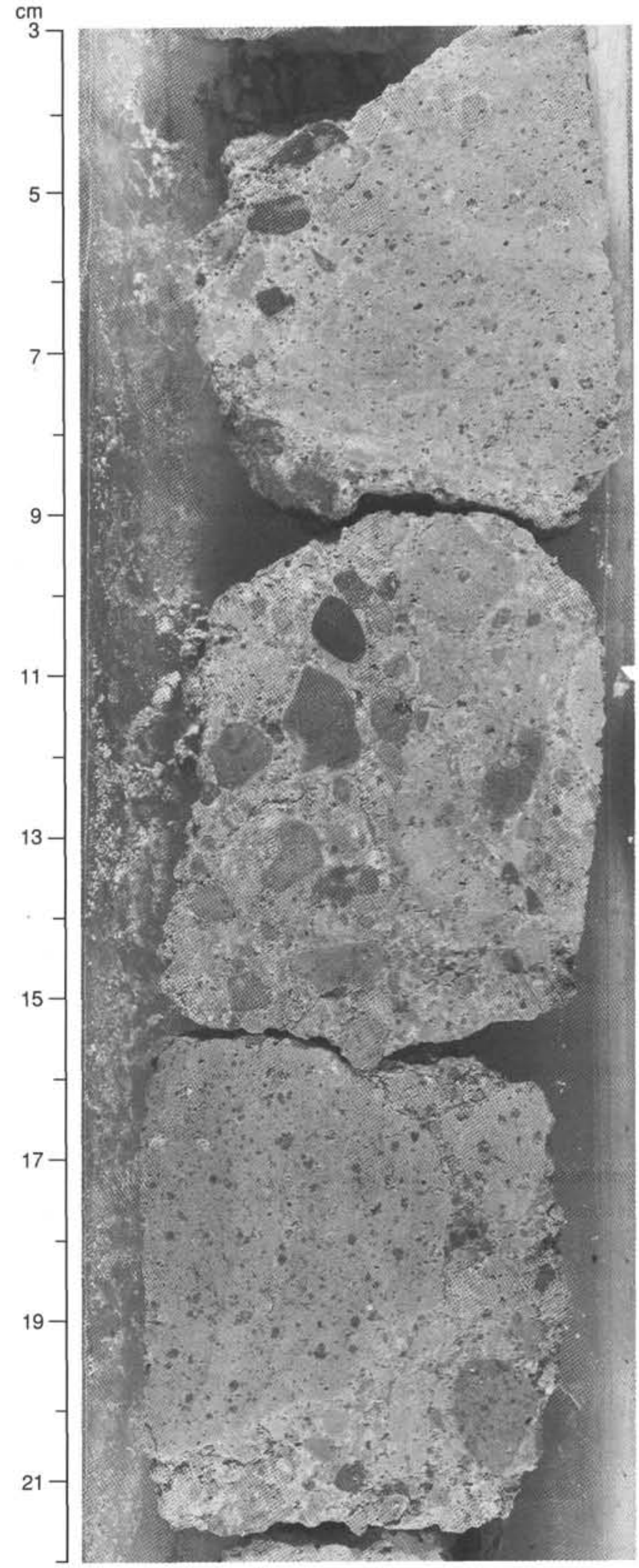

Figure 55. Rhyolite breccia showing clasts up to 5 cm in a soft interstitial matrix; Subunit 3C, interval 135-841B-56R-1, 3–22 cm.

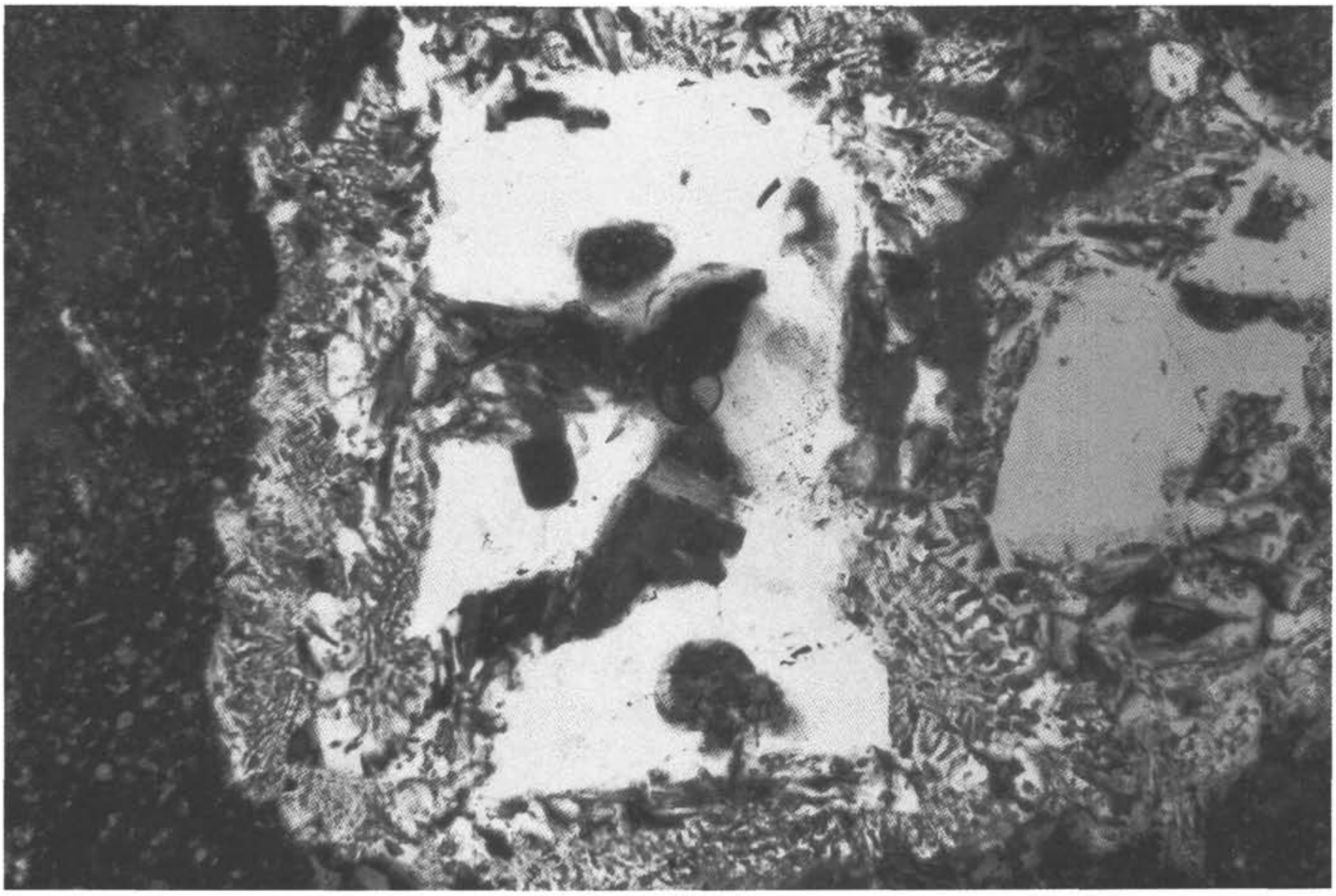

Figure 56. Photomicrograph of quartz-feldspar graphic intergrowths enclosing a highly resorbed quartz phenocryst in a rhyolite lava clast in Subunit 3D; Sample 135-841B-56R-CC, 0–2 cm; crossed polarized light; field of view = 1.5 mm.

mantle source depletions in the different magmatic settings in this area. There is a generally coherent trend for Ce vs. Y for all of the Site 841 igneous samples, similar to other forearc analyses (Fig. 67). Note the small excursion in Ce at almost constant Y in the basaltic andesites, similar to the effect noted for Ba in the same rocks. Overall, the data define a trend through the origin with a Ce/Y ratio of about 0.3.

Although the data are limited, several important conclusions can be drawn. The Site 841 rocks as a group are comparable in their geochemical signature with other fresh to moderately altered volcanic rocks from 'Eua and farther to the north on the trench slope and the Tonga Ridge. This suggests they are sufficiently well preserved to yield some information on eruptive setting and source characteristics. It is also apparent that the pumices from each region retain a geochemical coherence (e.g., the low and high Ba contents in Site 841 and Site 840 pumices, respectively; Table 15), which suggests that they represent materials that are locally derived, not rafted in to the site.

Table 15 shows averaged analyses for Unit 1 from Site 841 for pumices analyzed from Site 840 (clasts in Miocene sediments) and for the three rhyolites from Site 841, and compares them to data from relevant volcanic provinces within the western and southwestern Pacific, including the Lau Ridge. It can be seen that the Unit 1 compositions correspond more closely to volcanics from the Lau Ridge than to those from the Tofua Arc in the major and trace elements. The most notable discrepancies are in total Fe and V (the differences in Sr, Ba, and Rb are most likely attributable to alteration as previously discussed).

The rhyolites of Subunits 2B and 3D show both gross similarities in major element chemistry as well as some striking differences in trace element abundances when compared to silicic volcanic rocks from the Mariana and Bonin forearcs and Site 840 pumice. The rocks from Site 841, the Mariana and Bonin forearcs, all have relatively low Ba when their high SiO_2 content is considered. This suggests that all were derived from Ba-poor parental melts. The Site 841 samples have higher Ba than the Bonin samples and markedly higher Ba (up to 4 times greater) than the Mariana forearc boninite and tholeiite series. Zr and Y are also higher in the Site 841 rhyolites, but Sr is relatively depleted when compared to the Mariana and Bonin rocks. Site 841 rhyolites differ from the nearby Site 840 pumice, which represents a much younger phase of volcanism, in that the rhyolites contain lower Ba (about half as much) and lower Sr (about a third as much). Pumice from Site 840 exhibits similarities closer to the Mariana forearc island- and tholeiite-series dacite, although the pumice has higher Ba (e.g., MARA-D36; Table 15).

Rhyolitic rocks from Site 841 may be genetically related to the younger Lau Ridge, 'Eua, and Tonga Ridge arc series, and thus

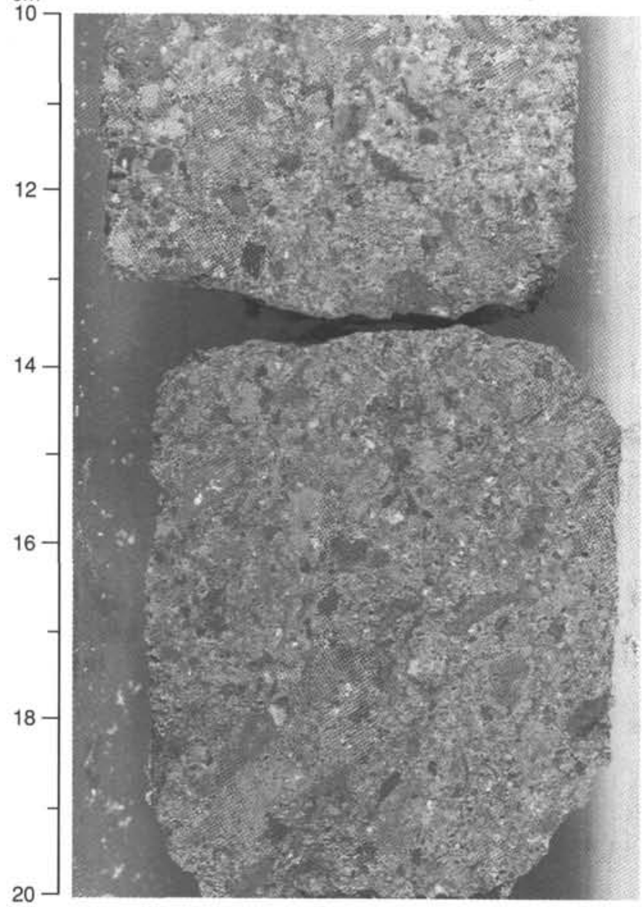

Figure 57. Unit 4, interval 135-841B-62R-1, 10–20 cm. Lithic and pumiceous fragments in welded tuff. The pumiceous clasts are compacted and, in this part of the core, variously oriented.

Figure 58. Unit 6, Sample 135-841B-66R-CC, 24–28 cm. Strongly deformed pumice lenticles and rhyolitic clasts in fragment from Unit 6.

representative of an early stage in the development of the Melanesian proto-arc. An alternative and highly speculative interpretation is that they may be related to the rhyolites found at Lord Howe Rise and therefore represent a far-traveled exotic terrane. In either case, they constitute part of the igneous basement on which the Lau Ridge and Tofua Arc were constructed.

Summary

Two major igneous sequences were recovered from Hole 841B. The first (Unit 1, 324.76–497.68 mbsf) is a sequence of nine basaltic andesite intervals within upper Miocene and lower middle Miocene volcanic siltstones and sandstones. The contacts between the basaltic andesites and sediments include chilled margins in the volcanics, hyaloclastite breccias, and indurated sedimentary material, all of which suggest intrusion of the volcanics into the sedimentary pile. Chilled margins suggest intrusion as relatively steep dikes or possibly as sills. Their occurrence in upper Miocene forearc sediments indicates that volcanic activity existed a significant distance outboard of the Lau Ridge when it was active. The basaltic andesites are extensively veined with thaumasite and a suite of sulfide minerals, including mainly pyrite with lesser marcasite and chalcopyrite.

The second major igneous sequence recovered at Site 841 (Units 2 through 6, 605.05–815.1 mbsf) comprises a series of low-K rhyolites, rhyolitic tuffs, breccias, welded tuffs, and lapilli tuffs and appears to constitute volcanic basement in this part of the forearc. Evidence for welding in some of the rhyolitic clasts and tuffs, and the complete absence of interbedded sediments and fossil flora or fauna, requires the occurrence of subaerial emplacement. The silicic rocks are structurally overlain by upper Eocene, very shallow-water calcareous volcanic sandstones. The eruptives are predominantly low-K_2O rhyolites; they generally have lower contents of Ba than do similar high-SiO_2 pumices from the modern Tonga Arc (Hawkins, 1987) and pumices in Miocene to Pleistocene sediments recovered at Site 840. The rhyolitic breccias are locally kaolinitized and illitized, accompanied by extensive, disseminated sulfide mineralization.

The identification of these rhyolitic eruptives is important in several respects. First, their subaerial origin indicates that this portion of the forearc was at or above sea level when erupted and has subsequently subsided more than 5000 m. The age of eruption is not known but the oldest sediments overlying the rhyolitic volcanics are upper Eocene. These upper Eocene calcareous sandstones are probably normally faulted (see "Structural Studies" section, this chapter) against the volcanics but they do contain abundant rhyolitic debris that must have been eroded from a nearby source. The absence of any older reworked fauna, the lack of any flora or fauna within the volcanic sequence, and the lack of any radiometric or biostratigraphic ages older than middle Eocene from any part of the Tonga ridge, forearc, or trench all suggest that latest Eocene is a reasonable minimum age for rhyolitic volcanic complex.

This thick, high-SiO_2 eruptive complex is unusual for an intraoceanic island arc. High-silica rocks do occur in the Pacific (e.g., on Saipan and in the Mariana forearc; Meijer, 1983; Bloomer, 1983) but most are dacitic and few form true ignimbritic complexes. While intraoceanic arcs may indeed produce high-SiO_2 eruptives, perhaps in part by remelting of older arc material, the position and composition of the forearc basement rocks raises the intriguing possibility that they are related to similar rocks from rhyolitic complexes in northeastern Australia and from the Lord Howe Rise in the Tasman Sea. In DSDP Hole 207 on the Lord Howe Rise, 140 m of Upper Cretaceous (93.7 ± 1.2 Ma) rhyolitic lavas were cored (Burns, Andrews, et al., 1973). The rhyolites, tuffs, and fragmental rocks are interpreted as having formed subaerially or in shallow water (van der Lingen, 1973). The bottom of the rhyolitic series was not reached; they are overlain by Upper Cretaceous (Maestrichtian) silty claystone deposited in a shallow-marine environment (van der Lingen, 1973; Burns and Andrews, 1973). Cretaceous rhyolites are also recorded from New Caledonia (Paris and Lille, 1977). The Lord Howe Rise and New

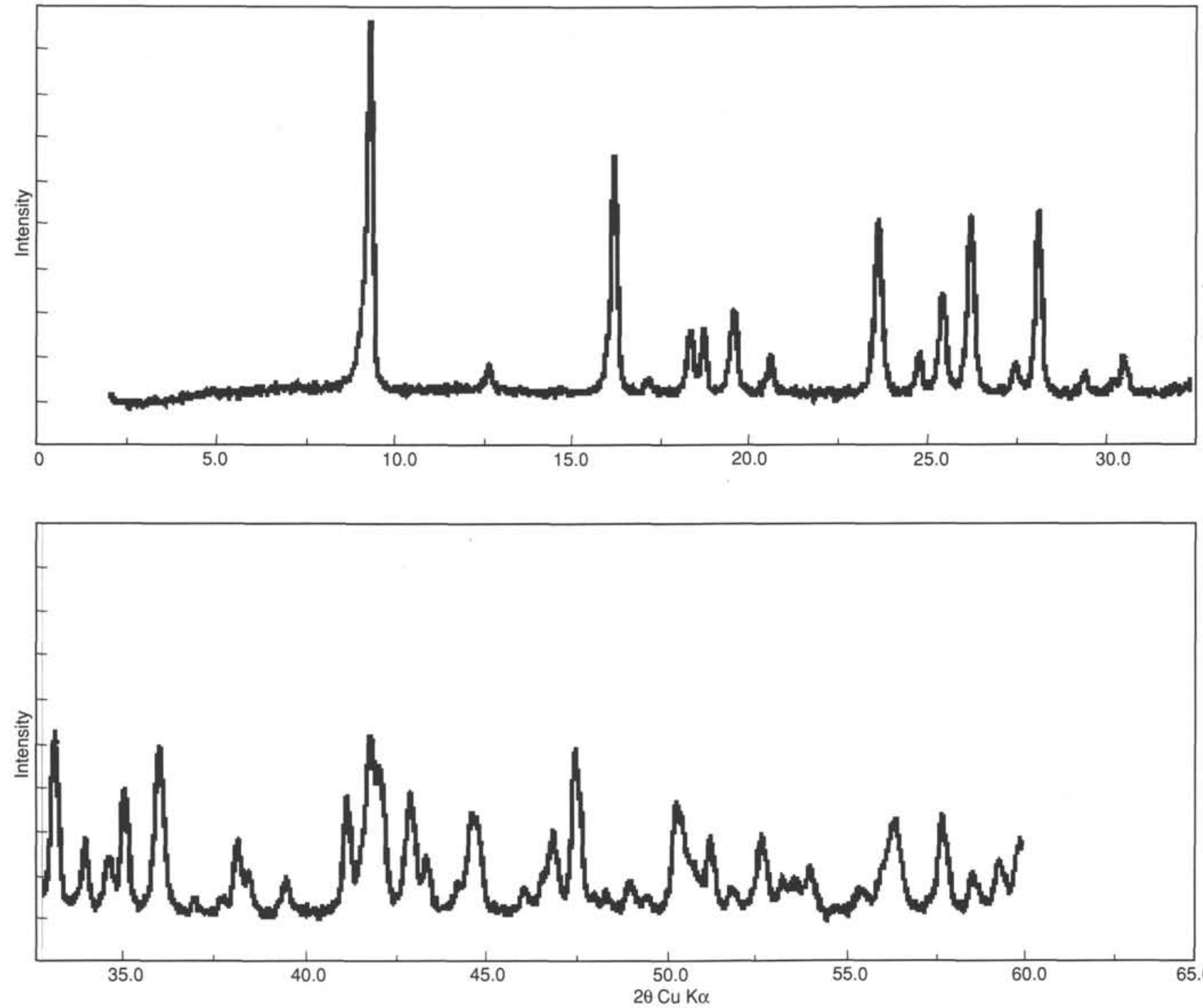

Figure 59. X-ray diffraction pattern of white, soft vein mineral, identified as thaumasite [$Ca_3Si(OH)_6(CO_3)(SO_4) \cdot 12H_2O$] in Sample 135-841B-18R-2, 13–14 cm. Note that peak at 44.58° belongs to an Fe peak from the sample chamber.

Caledonian sequences are both overlain by dolomite and shallow-water detrital sediments of Coniacian-Campanian age (89–72 Ma; Paris and Lille, 1977). Both of these occurrences are interpreted to be associated with the formation of a small rift basin along the extension of the present eastern Australian coast which preceded the breakup of eastern Australia and the opening of the Tasman Sea (Wilcox et al., 1980).

The occurrence of such a crustal fragment in the Tonga forearc would require a major reevaluation of tectonic models for the Southwest Pacific. It should be noted, however, that both the Australian and Tasman Sea occurrences are Cretaceous in age. As no fossiliferous horizons were encountered within the Site 841 rhyolitic units, their age is unknown, except as pre–late Eocene. It should be noted, however, that no fauna or flora older than late Eocene have been identified anywhere in the Tonga region (e.g., Vallier et al., 1985; Cawood, 1985).

The simplest explanation may be that the silicic rocks are genetically related to younger volcanic rocks on the Lau and Tonga ridges and formed during the early stages of evolution of the ancestral Melanesian proto-arc. In either case, the Site 841 rhyolites are important as an indication of rocks that constitute part of the igneous basement on which the Lau Ridge and Tofua Arc were constructed.

PHYSICAL PROPERTIES

A full suite of standard ODP physical properties measurements was made at Site 841. Index properties on sediments and sedimentary rocks from Holes 841A and 841B were determined by using a pycnometer and balance, and include bulk density, grain density, porosity, water content, and void ratio. Bulk density was also measured using the continuous gamma-ray attenuation and porosity evaluator (GRAPE) on full APC cores from Hole 841A.

Compressional wave velocities were measured both on whole cores using the continuous *P*-wave logger and on discrete samples using the Hamilton Frame apparatus. Velocities of unconsolidated sediments that could not be removed from the core liner were measured in only one direction. Velocities were measured in both horizontal and vertical directions when possible in unconsolidated sediments and on most of the consolidated sedimentary rocks and basalts.

Vane shear strength was measured on selected undisturbed intervals of the core samples from Hole 841A until degrees of

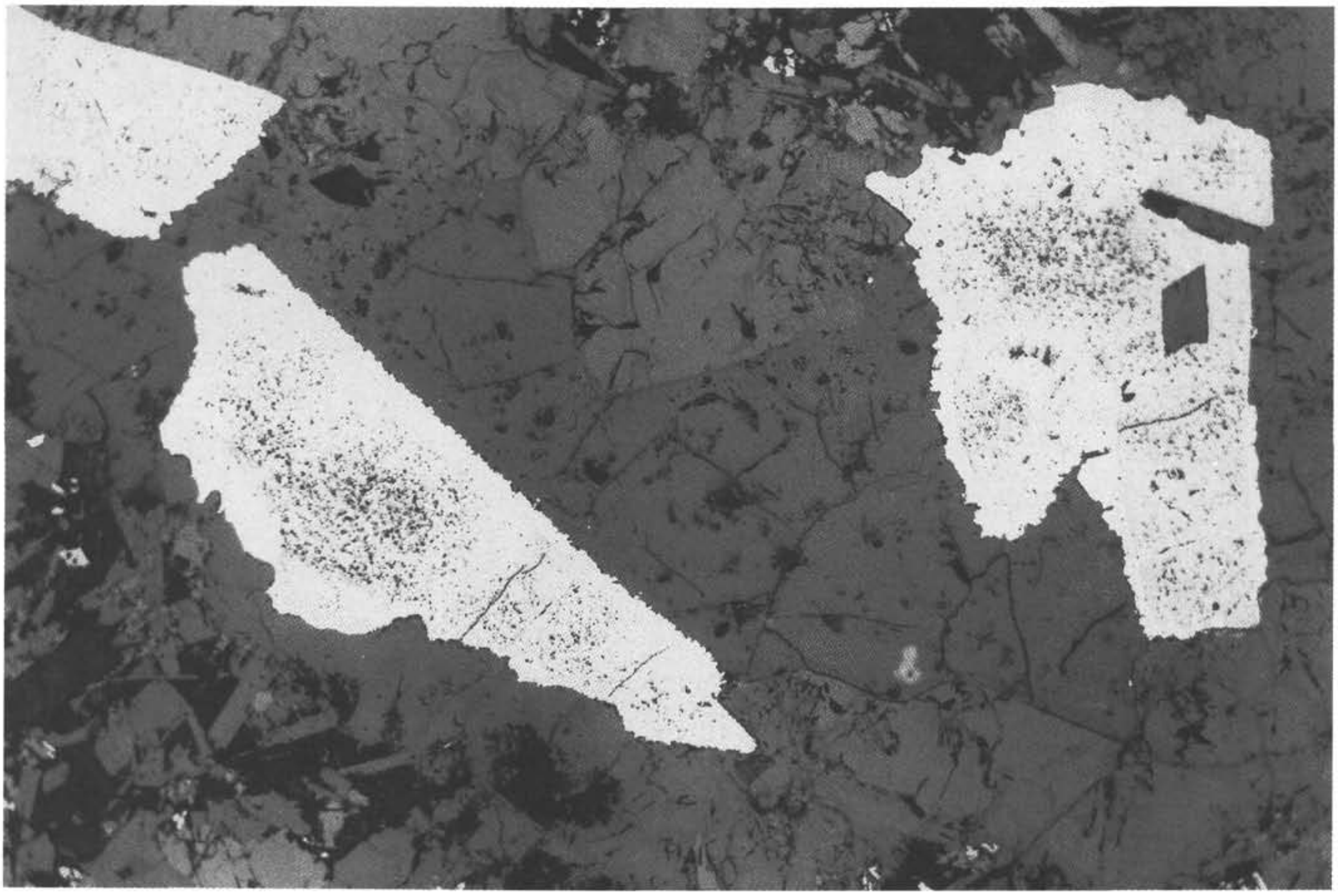

Figure 60. Reflected light photomicrograph of sulfide aggregates in a thaumasite vein in Sample 135-841B-18R-2, 7–10 cm; field of view = 1.5 mm.

rotation exceeded 90° or the sediment cracked, indicating that the assumption of uniform shear by the vane was no longer valid. Thermal conductivity was measured on whole undisturbed sediment cores from Hole 841A and on half rounds from lithified sediments from Hole 841B.

The lithologic units referenced in this section are those described in the "Lithostratigraphy" section (this chapter). Results from laboratory measurements are listed in Table 16 and plotted in Figures 68 through 77.

Index Properties

Hole 841A

Wet-bulk density, grain density, water content, porosity, and void ratio for sediments and sedimentary rocks from Hole 841A are plotted vs. depth in Figure 68, and values for the gravimetrically determined index properties are listed in Table 16.

The index properties measured on samples from Hole 841A show several distinct trends. Between 0 and 7 mbsf, bulk density and grain density increase while water content, porosity and void ratio decrease. Between 7 and about 30 mbsf, the trend is reversed, bulk density decreases, and grain density remains constant, while water content, porosity, and void ratio increase to values greater than those measured within the upper 7 m. Between 30 and about 55 mbsf, bulk density increases, grain density remains constant, while water content, porosity, and void ratio decrease. Below 55 mbsf to the bottom of the hole, the bulk density increases and other index properties decrease slightly with depth. Bulk density increases from 1.75 to 1.95 g/cm^3. Water content decreases from about 70% to about 60%, porosity decreases from about 65% to 47%, and void ratio decreases from about 2 to 1.5.

The index property trends outlined above show a limited correlation with the lithostratigraphy. The clay within the upper 7 mbsf is undergoing rapid dewatering, as shown by the rapidly increasing bulk density. Between 7 and about 30 mbsf, the increased water content of the sediment suggests that the upper 7 m of clay are acting as a barrier preventing normal consolidation and dewatering of the sediments within this zone. Since the grain density remains constant, the increased water content, porosity, and void ratio are probably not related to the lithology of the sediments. A possibility exists that the upper 30 m of sediment may not be in place; rather it may be part of a slump overlying the normally consolidating section below 30 mbsf. The sediments below 30 mbsf display an initial high water loss to 55 mbsf and then a smaller water loss gradient throughout lithologic Unit II (see "Lithostratigraphy" section, this chapter). Most of Unit II below 54 mbsf consists of siltstones and sandstones with varying grain sizes and percentages of foraminifers. These variations, sampled as representatively as possible from discrete measurements, are reflected in the scatter in the data below 55 mbsf.

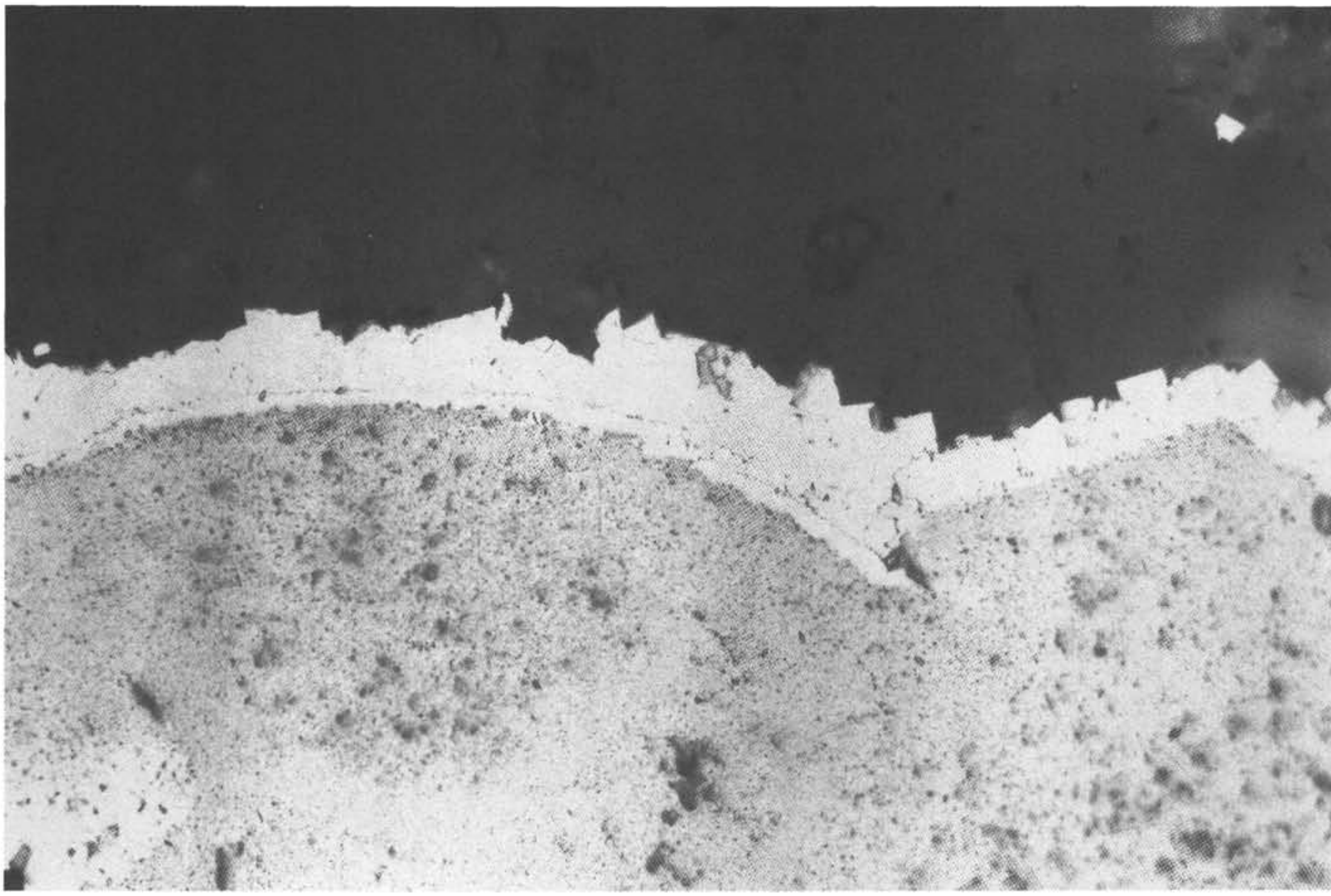

Figure 61. Close-up of sulfides in Figure 61 showing "dirty" pyrite rimmed by two generations of marcasite; field of view = 0.3 mm.

The GRAPE bulk density data have been processed by initially averaging at 5-cm intervals to remove spurious data points caused by core section ends and void spaces within the core (Fig. 69A) and then by applying a 5-point running average (Fig. 69B). GRAPE bulk density was measured continuously only in the upper 55 mbsf (e.g., within Unit I) and between 65 and 75 mbsf because the core liners were not completely filled throughout the remainder of the hole.

Within Unit I, the GRAPE bulk density shows trends similar to those illustrated by the discrete bulk density measurements. There is an increase within the upper 7 mbsf, a decrease between 7 and 24 mbsf, and an increase between 24 and 55 mbsf.

Hole 841B

Gravimetrically measured index property results for Hole 841B (Fig. 70 and Table 16) show several distinct trends down hole. Bulk density increases from 1.87 to 2.04 g/cm^3 between 170 and 248 mbsf. Between 248 and 260 mbsf, the density of the sediment is low (1.75 to 1.85 g/cm^3), and the low values may reflect an increase in clay content. Between 260 and about 390 mbsf, bulk density increases to a high-density basaltic andesite unit (2.98 g/cm^3) that is present from 390.4 to 400.2 mbsf in the core (see "Igneous Petrology" section, this chapter). The basalt may function as a cap preventing the loss of water and normal consolidation processes, as immediately below the igneous unit, bulk density decreases down to 459 mbsf. Below 495 mbsf, the bulk density again increases gradually. A fault is present at about 460 mbsf, and correlates with a change from decreasing or low bulk density values above 460 mbsf to more normal consolidation below 460 mbsf. Below this fault, the scatter in the data reflects the varied grain size and water content in the variable lithology of the sampled sandstones and siltstones. A second fault is present around 600 mbsf. Below this fault, measured values show considerably more scatter, and a marked increase in bulk density and decrease in water content, porosity, and void ratio occurs. Below 690 mbsf, bulk densities reach a maximum value of 2.91 g/cm^3 measured on rhyolitic breccias.

Grain density is relatively constant with depth, averaging about 2.6 g/cm^3. However, the grain density also partly mirrors the bulk density trends, suggesting that the trends illustrated by the index properties are affected by changes in lithology. Water content, porosity, and void ratio vary inversely with density. However, below the fault at 600 mbsf, values for all three properties are much lower than above 600 mbsf. Also, more scatter is present in the water content, porosity, and void ratio measurements than in those of the bulk and grain densities, reflecting the more varied composition of the altered rhyolitic lavas, breccias, and tuffs sampled from 600 to 786 mbsf.

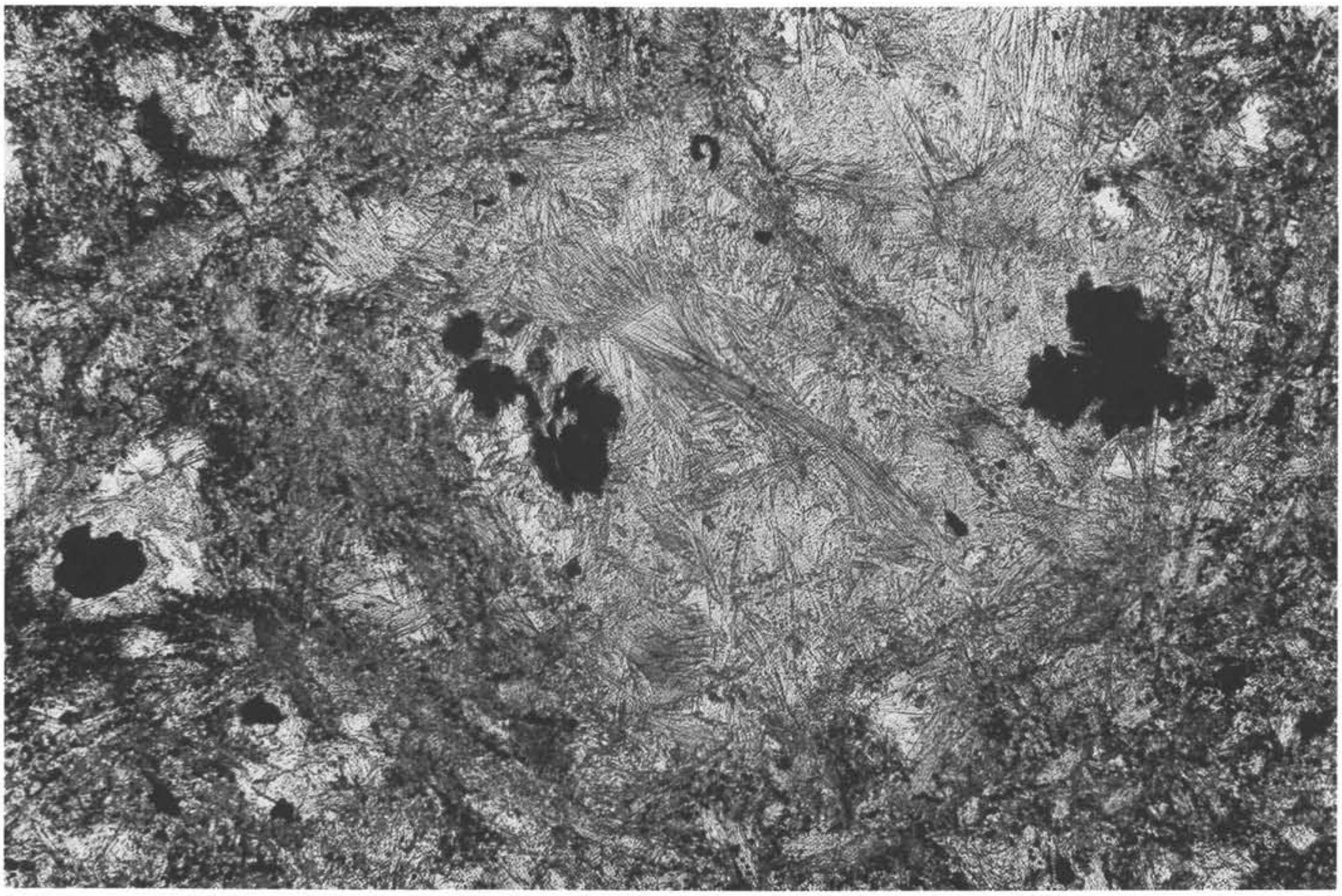

Figure 62. Transmitted light photomicrograph, Sample 135-841B-40R-1, 0–3 cm; field of view = 1.5 mm. Total replacement of plagioclase (?) phenocryst in a volcanic clast by actinolite, albite, chlorite, and magnetite.

Compressional Wave Velocity

Compressional wave velocity data measured with a Hamilton Frame device and the *P*-wave logger are shown in Figures 71 and 72, respectively, and are listed in Table 16. Fewer compressional wave velocity measurements than index property measurements were made on samples from Hole 841A because it was difficult to propagate a signal through the coarse-grained sediments; therefore, the resolution in the upper part of the section using compressional wave velocity is poorer than with the index properties.

The compressional wave velocity data shows variations that correspond roughly with the trends suggested by the index properties. Compressional wave velocity increases in the upper 15 mbsf and decreases between 15 and 40 mbsf. Too few measurements are available to define absolute trends between 40 and 65 mbsf. Below 65 mbsf, the data are scattered but show little increase with depth to 200 mbsf.

P-wave logger compressional wave velocity data, measured within the upper 70 m, show an increase in the uppermost 2 m of sediment followed by a decrease in compressional wave velocity between 2 and 12 mbsf (Fig. 72). Compressional wave velocity increases between 12 mbsf and the last *P*-wave data near 80 mbsf. These trends are similar to those outlined by the discrete measurements of compressional wave velocity and index properties, although the depths are somewhat different.

Compressional wave velocity generally increases from around 200 to 390 mbsf, with a high-velocity region present between about 250 and 300 mbsf. Igneous Subunit 1D marks a major shift in velocity values. The three very high velocities measured between 390 and 395 mbsf are from this subunit, a basaltic andesite. From 395 mbsf to the fault at 600 mbsf, the data show a decrease in average compressional wave velocities. These sediments lie below the fault zone and the decreasing velocities may be the result of the higher pore pressures caused by the capping effect of the igneous unit. The values are scattered, reflecting the composition of the individual samples measured. This same scatter is also present in the index property data described above. Between 610 and 670 mbsf, compressional wave velocity decreases; this zone is immediately below a second fault that juxtaposes limestone against underlying rhyolitic lavas, breccias and tuffs. The measurements made on samples deeper than 690 mbsf from the rhyolitic material are all 4000 m/s or greater.

Undrained Vane Shear Strength

Values of undrained shear strength were obtained using the standard onboard miniature vane shear apparatus on unconsoli-

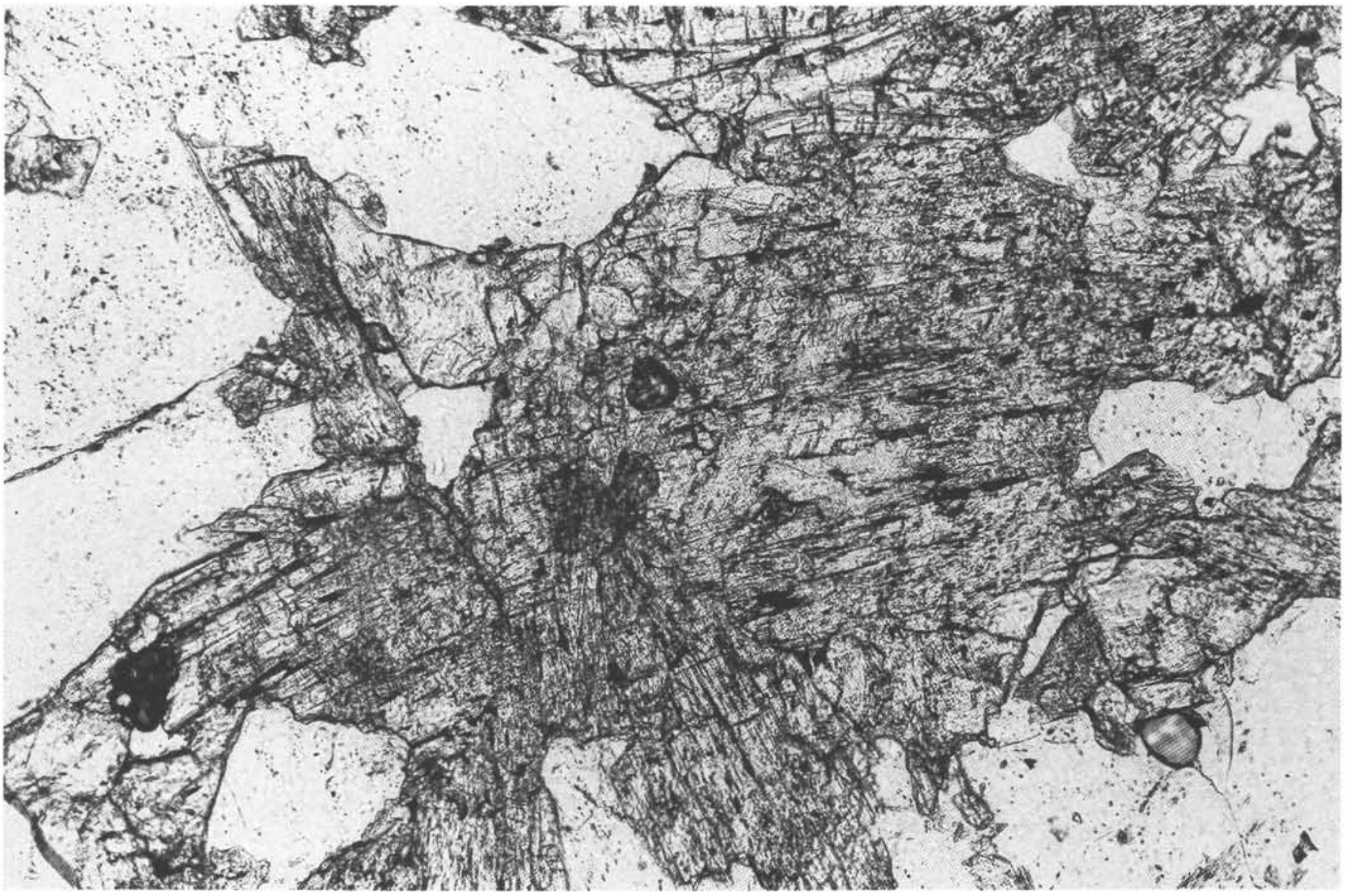

Figure 63. Transmitted light photomicrograph of epidote after plagioclase (?) in Sample 135-841B-34R-1, 2–4 cm, a tonalitic clast; field of view = 1.5 mm.

dated sediments in Hole 841A. The results are plotted in Figure 73 and reported in Table 16.

In general, measurements are made on representative sections of core, which means that the dominant lithology, generally the finer grained sediment, is sampled preferentially. Undrained shear strength increases downhole from less than 1 kPa at 1 mbsf to 176 kPa at 42 mbsf. Within these 42 m, the shear strength gradient is less in the upper 30 mbsf (the zone of increasing water content) than between 30 and 42 mbsf (the zone where water content decreases), although there is much scatter.

Thermal Conductivity

All thermal conductivity values in soft sediment cores were obtained using needle probes inserted through core liners into full core sections. For lithified sedimentary rocks and basalts, the thermal conductivity was measured on a split core face. Thermal conductivity measured at the top of the Hole 841A is 0.8847 W/(m · °K) and increases slightly downhole to 0.9317 W/(m · °K) (Fig. 74). In Hole 841B, thermal conductivity values increase between 173 and 440 mbsf and the fault, roughly down to the bottom of lithologic Unit III and the fault zone. The two high thermal conductivity values were measured on pieces of igneous Subunit 1D at 395 and 400 mbsf. Below 440 mbsf and the fault, thermal conductivity values drop to just over 1 W/(m · °K) and gradually increase through the remainder of the measured section. The thermal conductivity of the rhyolitic rocks was not measured because of the small size of the recovered pieces.

Temperature Measurements

The water sampler temperature probe (WSTP) was used to make temperature measurements at three depths in Hole 841A (Fig. 75). The temperature history in the sedimentary section should be such that after 5 min insertion in the sediment, the decay curve is approximated by:

$$T(t) = A/t + T_{eq},$$

where A is a constant determined experimentally, t is time, and T_{eq} is the equilibrium formation temperature (Hyndman et al., 1987). The temperature gradient defined by these measurements is about 2.84°C/100 m (Fig. 76), similar to the 2.93°C/100 m measured at Site 840 and the 3.2°C/100 m measured at a commercial well on Tongatapu (Maung et al., 1981). Thermal conductivity measurements were used to calculate thermal resistivity and integrated over depth. When the resulting thermal resistance is plotted against the temperature measurements from the WSTP (Fig. 77), the slope of the regression line indicates that the heat flow in the region is 29.5 mW/m².

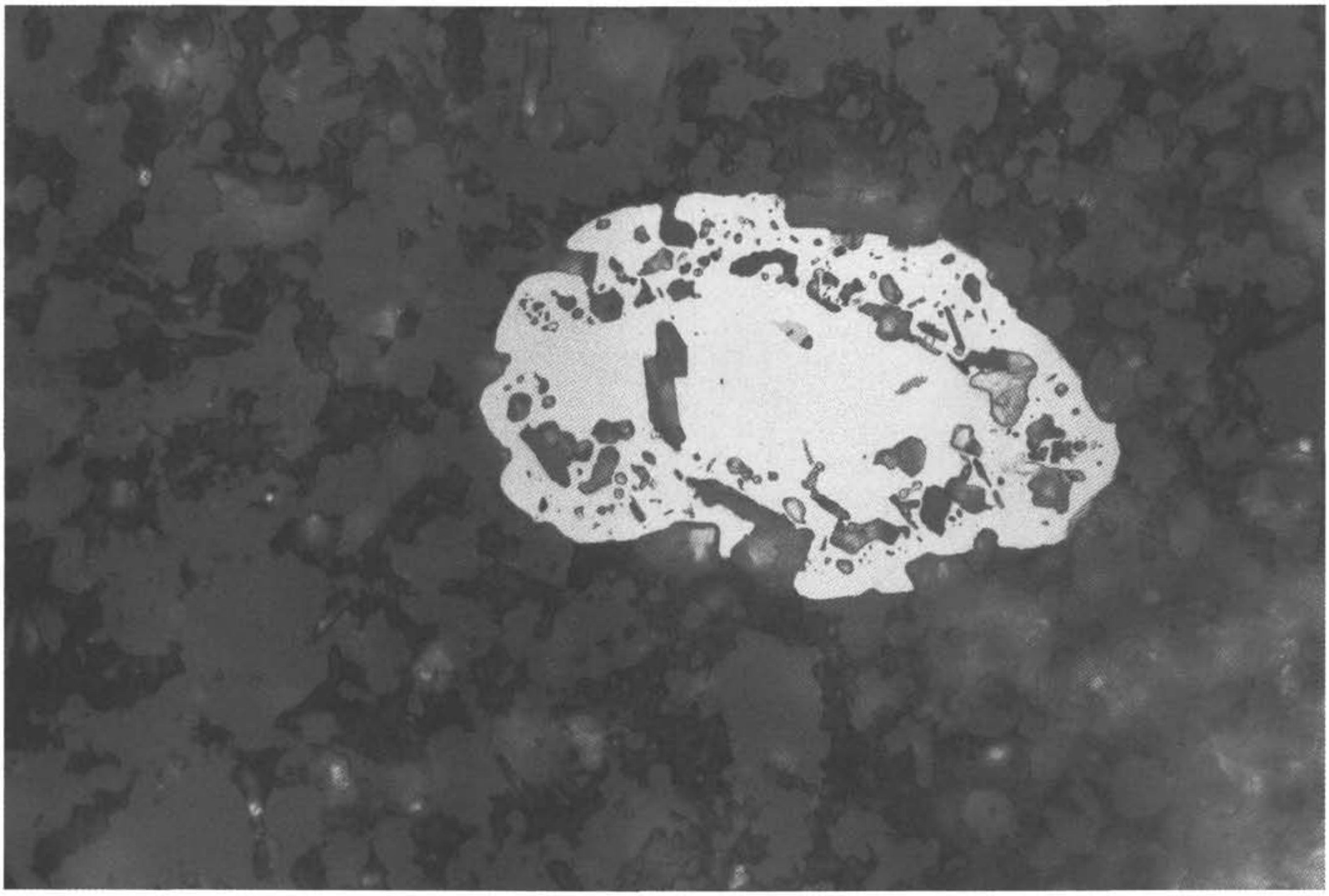

Figure 64. Pyrrhotite inclusion in rounded, highly porous pyrite; Sample 135-841B-55R-1, 1–3 cm; reflected light photomicrograph, 1 nicol; field of view = 0.3 mm.

Discussion

Physical properties reflect structural changes as well as lithologic changes within the sedimentary section. The igneous Subunit 1D at 390 to 400 mbsf apparently has a capping effect that prevents the sediment immediately beneath from consolidating normally. This is reflected in the increased water content and associated index properties below the unit. Faults also have an effect on physical properties. In Hole 841B, the values for density, compressional wave velocity, and thermal conductivity decreased and water content, porosity, and void ratio increased significantly at about 460 mbsf, the depth of an inferred fault. A similar drop in measured values occurred below 610 mbsf, the depth of an inferred second fault although "normal" consolidation occurred below this fault.

Thermal conductivity shows more variability at Site 841 than previous sites measured on Leg 135. Instead of a gradual increase in conductivity with depth, variations in conductivity reflect the various lithologies found downhole with the highest values being measured on samples from the basaltic andesites of Subunit 1D and the lowermost rhyolitic rocks. In addition, a sudden drop in thermal conductivity occurred below the inferred fault at 460 mbsf.

The temperature gradient and heat flow values are very consistent across the forearc. The temperature gradient from Site 841 is very similar to that measured at Site 840 and at well sites on Tongatapu. These gradients are higher than others measured in the Lau Basin, suggesting that there is less fluid circulation at Site 841 than at those backarc sites in the Lau Basin. This is supported by the pore-fluid geochemistry (see "Inorganic Geochemistry" section, this chapter), where significant variations in calcium, magnesium, and other elements indicate that the forearc sites have less exchange with surface water than the backarc sites.

DOWNHOLE MEASUREMENTS

Operations

Logging operations at Hole 841C began at 1815 UTC on 13 February 1991 and ended at 1600 UTC on 14 February. The driller's mudline was at 4821 mbrf, and the driller's total depth was 775 mbsf. During logging the end of the drill pipe was set at 78.14 mbsf, although some open-hole logs were obtained at shallower depths when it was safe for the driller to raise the pipe. Well-logging operations consisted of two logging runs using the formation microscanner (FMS) logging string and the quad tool combination.

Table 14. XRF analyses of representative samples from igneous units recovered in Hole 841B.

Core, section	18R-2	22R-1	23R-4	25R-1	26R-2	36R-1	41R-1	49R-1	56R-CC	62R-CC
Interval (cm)	28–32	138–142	8–12	105–109	88–91	84–86	136–140	10–13	2–8	11–15
Depth (mbsf)	325.28	362.78	375.05	391.45	402.45	497.64	546.36	622.00	689.75	749.97
Unit	1A	III	1B	1D	1E	1F	V	2B	3D	4
Major elements (wt%):										
SiO_2	54.13	57.18	52.59	52.58	51.85	54.64	58.12	78.46	80.50	75.94
TiO_2	1.01	0.95	1.06	1.05	1.08	1.03	0.76	0.25	0.28	0.23
Al_2O_3	16.04	15.99	16.83	16.62	16.46	15.64	12.89	12.35	11.56	10.83
Fe_2O_3	12.53	12.62	13.06	13.13	13.08	12.42	15.67	2.37	2.48	4.35
MnO	0.22	0.19	0.27	0.24	0.25	0.20	0.28	0.07	0.02	0.06
MgO	4.55	4.92	4.76	4.80	4.93	4.36	5.72	0.25	0.95	0.74
CaO	9.52	3.31	10.26	10.18	9.61	9.33	4.51	1.83	1.80	4.97
Na_2O	2.78	5.64	2.84	2.90	3.28	2.94	2.15	4.52	3.00	3.18
K_2O	0.16	1.16	0.20	0.09	0.45	0.26	1.62	1.46	0.38	1.39
P_2O_5	0.15	0.10	0.17	0.15	0.17	0.16	0.14	0.05	0.04	0.06
Total	101.09	102.06	102.04	101.74	101.16	100.98	101.86	101.61	101.01	101.75
LOI	1.29	5.77	1.01	0.72	1.55	0.87	8.06	5.42	2.59	5.17
Mg#	41.8	43.6	41.9	42.0	42.7	41.0	42.0			
Trace elements (ppm):										
Nb	1	1	1	1	1	2	1	2	2	2
Zr	71	56	73	74	76	74	40	175	184	137
Y	23	22	24	24	25	25	39	62	64	50
Sr	216	87	229	230	227	213	109	49	76	50
Rb	2	19	5	1	4	4	30	14	8	4
Zn	123	103	173	132	166	90	163	35	44	0
Cu	122	45	114	128	117	132	52	10	9	21
Ni	20	14	22	21	20	18	30	2	4	1
Cr	14	7	17	12	17	12	3	0	0	0
V	345	235	376	387	382	351	187	3	15	9
Ce	10	9	13	7	13	16	13	20	19	20
Ba	90	251	256	125	310	140	70	198	116	89
Ti/Zr	118	141	141	118	118	116	158	12	13	14
Ba/Zr	1.3	4.5	3.5	1.7	4.1	1.9	1.8	1.1	0.6	0.6
Y/Zr	0.32	0.39	0.33	0.32	0.33	0.34	0.98	0.35	0.35	0.36
Sr/Zr	2.8	1.6	3.1	3.1	3.0	2.9	2.7	0.3	0.4	0.4
Ti/V	18	24	17	16	17	18	24	500	112	153

Notes: Samples 135-841B-22R-1, 138–142 cm, and -41R-1m 136–140 cm, are volcanic clasts from sedimentary breccias. The analysis for Sample 135-841B-49R-1, 10–13 cm, is of a pitchstone glass separate from a crushed bulk-rock sample; the glass may contain up to about 4% plagioclase microlites. Mg# is 100 · Mg/(Mg + Fe^{2+}) where Fe^{3+}/Fe^{2+} is assumed to be 0.2. Mg# is not calculated for samples with SiO_2 > 65%. LOI = loss on ignition.

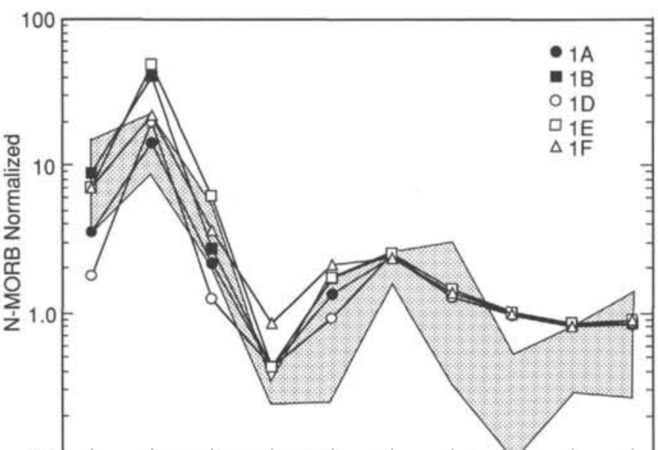

Figure 65. Trace elements normalized to N-MORB of samples from Subunits 1A to 1F from Hole 841B and compared to the range of abundances in the modern Tofua Arc (stippled field, data from Ewart et al., 1973; Ewart et al., 1977; Ewart and Hawkesworth, 1987). Normalizing values from Sun and McDonough (1989).

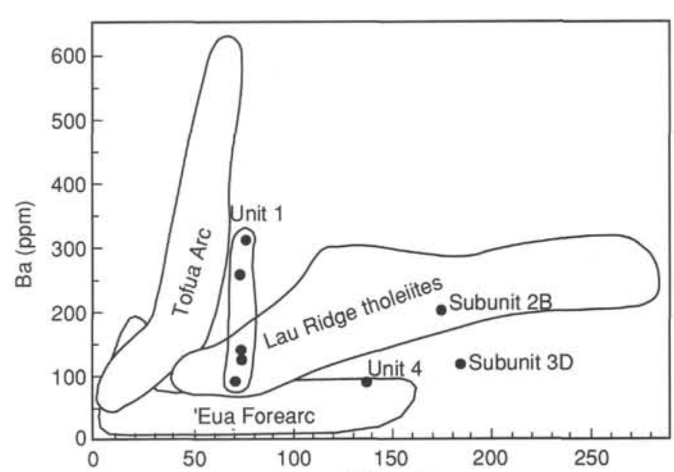

Figure 66. Comparison of Ba and Zr abundances in rocks from Units 1, 2B, 3D, and 4 from Hole 841B to fields for modern Tofua Arc (sources as in Fig. 66), Lau Ridge subalkaline volcanics (Cole et al., 1985), and the 'Eua forearc region (Ewart and Bryan, 1972; Hawkins and Falvey, 1985). Note the progressive increase in Ba from the older ('Eua) to the younger (Tofua) units.

Table 15. Comparison of analyses of basaltic andesites from Site 841 and average basaltic andesites from the Lau and Korobasaga volcanic groups on the Lau Ridge (Cole et al., 1985) and a comparison of high-silica volcanic rocks from Site 841, Site 840 tholeiitic and boninitic series dacites from the Mariana forearc (Bloomer, 1983), and dacitic rocks from the Bonin forearc (Fryer, Pearce, et al., 1990)

	Average basaltic andesite Site 841[a]	Tonga average excluding Ata	Lau Ridge		Sample 135-841B 49R-1, 10–13	Sample 135-841B 56R-CC, 2–8	Sample 135-841B 62R-CC, 11–15	Site 840[b] average pumices	Mariana forearc samples		Bonin forearc samples	
			Lau Group	Korobasaga Group					Tholeiite series MARA-D36	Boninite series MARA-D28	125-786B-61R-5, 56–58	125-786B-32R-2, 86–88
Depth (mbsf)	325.28				622.00	689.75	749.97					
Unit	1A				2B	3D	4					
SiO_2	53.16	53.21	55.16	55.76	78.46	80.50	75.94	71.28	68.09	67.85	72.30	71.04
TiO_2	1.05	0.74	1.14	0.73	0.25	0.28	0.23	0.71	0.58	0.19	0.24	0.23
Al_2O_3	16.32	17.09	18.08	18.58	12.35	11.56	10.83	14.17	14.10	14.17	13.12	12.85
Fe_2O_3*	12.84	10.94	9.42	7.48	2.37	2.48	4.35	4.60	5.72	4.90	3.26	3.85
MnO	0.24	0.18	0.17	0.15	0.07	0.02	0.06	0.15	0.13	0.07	0.05	0.02
MgO	4.68	5.37	3.62	4.41	0.24	0.95	0.74	1.01	1.45	2.81	ND	ND
CaO	9.78	11.15	8.54	8.81	1.83	1.80	4.97	3.58	5.56	4.05	2.49	2.88
Na_2O	2.95	1.57	3.30	2.99	4.52	3.00	3.18	4.41	3.98	3.95	3.35	3.35
K_2O	0.23	0.39	0.84	1.24	1.46	0.38	1.39	1.41	0.76	1.32	1.11	1.35
P_2O_5	0.16	0.07	0.25	0.29	0.05	0.04	0.06	0.17	0.18	0.06	ND	ND
Mg#	41.9	49.3	43.2	53.9								
Nb	1.2	0.6	2	2	2	2	2	2			1.4	1.4
Zr	74	18	97	66	175	184	137	147	86	72	72	74
Y	24	12	35	20	62	64	50	43	44	7	14	12
Sr	223	196	331	533	49	76	50	184	121	291	121	173
Rb	3	4	11.2	37	14	8	4	14	14	7	18	43
Zn	137	84	90	80	35	44	0	73				
Cu	123	—	45	47	10	9	21	12				
Ni	20	23	14	16	2	4	1	2	2	22	3	2
Cr	14	54	28	27	0	0	0	0	7	78	0	—
V	368	305	243	179	3	15	9	25	119	87	35	46
Ce	12	3.7	19	20	20	19	20	27				
Ba	184	88	138	309	198	116	89	246	26	46	91	77
Ti/Zr	118	246	70	66	12	13	14	29	40	16	20	19
Ba/Zr	1.3	4.9	1.4	4.7	1.1	0.6	0.6	1.7	0.3	0.6	0.5	1.0
Y/Zr	0.32	0.67	0.36	0.30	0.35	0.35	0.36	0.29	0.51	0.10	0.19	0.16
Sr/Zr	2.8	10.9	3.4	8.1	0.3	0.4	0.4	1.3	1.4	4.0	1.7	2.3

Note the generally low Ba abundances of the forearc volcanics, particularly in comparison to pumice clasts in Miocene sediments and the Lau Ridge volcanics. Mg# calculated as in Table 14.
[a] Average of five analyses.
[b] Average of three analyses of pumice clasts in Miocene sediments.

The first logging run was made with the FMS tool string. Pass 1 was recorded open hole from 611.1 to 70.7 mbsf and pass 2 was recorded from 603.8 to 70.7 mbsf open hole.

The second logging run was made with the quad-tool combination, which consists of the long-spaced sonic tool, the phasor dual induction tool, the high-temperature lithodensity tool, the compensated neutron porosity tool, and a natural gamma-ray tool. The logging sequence with the quad tool string consisted of a main uplog from 578.5 to 103.0 mbsf open hole, and another uplog from 177.0 to 103.0 mbsf open hole.

Onboard Processing

Data were processed as described in the "Explanatory Notes" chapter (this volume). Depths should be considered as uncorrected and preliminary, and may change by as much as 5 m during post-cruise processing.

The processed FMS images are on microfiche at the back of this volume. When the diameter of the hole is greater than 39.4 cm (15.5 in.), the FMS pads do not make sufficient contact with the borehole walls to produce images of satisfactory quality.

Results and Interpretation

The results of the logging in Hole 841C are shown in Figures 78 through 81. The Site 841 lithologic units that were logged are described in detail in the "Lithostratigraphy" section (this chapter).

Caliper Logs

The caliper logs record the diameter of the hole and are useful in evaluating whether information from the logs is valid. The lithodensity caliper logs indicate that most of the hole was within the 19-in. maximum for most of the logged interval. The only exception was the brief interval between 440 and 445 mbsf. In general, the hole was smaller than 15 in. in diameter except at 333 mbsf (the boundary between Units I and II), between 390 and 395 mbsf (the depth of a basaltic andesitic dike or sill), and between 445 and 460 mbsf, which includes a faulted region (see "Physical Properties" and "Structural Geology" sections, this chapter).

Density Log

The bulk density (RHOB on Fig. 78) in Hole 841C is relatively constant at 1.7 g/cm^{3}in the upper measured portion of the hole between 105 and 199 mbsf (Unit II). Bulk density increases to about 1.8 g/cm^3 by 199 mbsf and continues to increase to about 2 g/cm^3 by 332 mbsf. At 332 mbsf, a sharp, 2- to 3-m-wide density peak reaches 2.5 g/cm^3 and marks the top of Unit III. Density values immediately below this peak drop back to about 1.55 to 1.6 g/cm^3. At 394 mbsf and between 411 and 414 mbsf, density increases to 1.85 and 1.95 g/cm^3, respectively, and correlates with basaltic andesite igneous units (see "Igneous Petrology" section, this chapter). Several discrete bulk density measurements made within these intervals have similar values (see "Physical Proper-

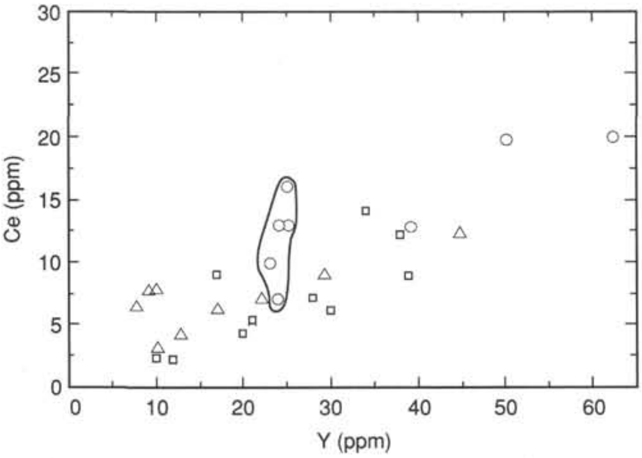

Figure 67. Ce vs. Y for lavas from the Tonga forearc. 'Eua data from Ewart and Bryan (1972); forearc data from northern end of platform from Falloon et al. (1987) and Falloon and Crawford (1991). Open circles = Site 841 data; open squares = 'Eua data, and open triangles = forearc data. Site 841 basaltic andesite is circled.

ties" section, this chapter). Between 452 and 465 mbsf, the bulk density increases sharply to 2.2 g/cm^3 before dropping back to between 1.9 and 2.09 g/cm^3 for the remainder of the measured hole (to 544 mbsf). This increase to 2.2 g/cm^3 occurs at the same stratigraphic level as a fault, and the drop in density measured immediately below correlates well with the discrete density measurements made gravimetrically at this same depth (see "Physical Properties" section, this chapter).

Neutron Porosity Log

In Hole 841C, the porosity at 105 mbsf (NPHI, Fig. 78) averages about 55% to 60% and remains constant throughout Unit II to 332 mbsf. At 333 mbsf, a sudden decrease in porosity to 35% for several meters marks the top of Unit III. At 394 mbsf and 411–415 mbsf, decreases in porosity to 38% mark basaltic andesite sills or dikes (see "Igneous Petrology" section, this chapter). Between these porosity excursions, porosity averages about 50%. Between 452 and 465 mbsf, the porosity drops to 20%, a value that may characterize the fault zone at this depth (see "Structural Geology" section, this chapter). The average porosity below this zone is about 50%.

Resistivity and Sonic Velocity Logs

The resistivity logs (ILM, ILD, and SFLU, Fig. 78) and the sonic velocity log (Fig. 78) are very similar in character. Both logs show relatively constant values to 245 mbsf, except between 117 and 128 mbsf, where both logs show increased values. At 245 mbsf, a gradual increase in values occurs at the same depth where discrete bulk density data suggest that sediment begins to consolidate normally (see "Physical Properties" section, this chapter). Resistivity and velocity peak at 332 mbsf at the top of Unit III. The depths where the igneous dikes intrude are marked by a significant resistivity and velocity increase. Velocity data below 422 mbsf needs further processing to eliminate cycle skipping, especially in the shear zone between 452 and 465 mbsf.

Gamma-ray Log

The gamma-ray log (SGR, Fig. 78) shows constant gamma radiation intensity throughout Unit II. Below 330 mbsf, and between 392 and 412 mbsf, gamma radiation decreases, and correlates with two basalt dikes located between these depths (see "Igneous Petrology" section, this chapter). The gamma radiation remains constant from 412 mbsf through the bottom of the measured section at 544 mbsf.

Formation Microscanner

Data were acquired by the FMS tool between 70 and 610 mbsf and plotted at a scale of 1:240 for preliminary shipboard interpretation. The FMS calipers (Fig. 79) indicate that the hole is elliptical to 200 mbsf, circular between 200 and 350 mbsf, and elliptical to 405 mbsf. At 405 mbsf, the caliper skidded, rotating 90°. From 445 to 480 mbsf, the hole became very narrow and jagged. Below 480 mbsf, the hole remained narrow, circular, and fairly smooth except for a couple of washouts at 515 and 545 mbsf.

Initial interpretation of the FMS resistivity image indicates the following: first, the FMS images of the upper portions of the hole can be described as regular bands of relatively low-resistive material, with few zones of more highly resistive beds as, for example, at 130 mbsf. Processed MSD dip data from this zone are generally toward the northeast. Second, the FMS image in the region between 445 and 485 mbsf is highly irregular, consisting of bands of high and low resistivity (Fig. 80). The dips are highly erratic. The actual fault trace within this zone cannot be picked definitively on the 1:240 plot (see "Igneous Petrology" section, this chapter) but is suggested by a white (highly resistive) band between 454 and 458 mbsf. This highly resistive band is at the same depth as the high-velocity, high-density, and low-porosity region identified above. The caliper logs indicate that the hole diameter is very irregular throughout this interval. Third, at a level of about 552 to 555 mbsf, the attitude of the bedding as deduced from the dipmeter data suddenly changes from a southeasterly direction above to an easterly direction below the middle Miocene (Fig. 81). This change in dip direction correlates with an unconformity between middle Miocene and lower Oligocene strata identified within the core at 549.1 mbsf (see "Lithostratigraphy" section, this chapter).

DISCUSSION

The objectives for Site 841 were addressed by drilling three holes that penetrated to 834.2 mbsf. The drilling program met the objectives for the site, which were to identify the basement material and its age, to determine the stratigraphy and lithologies of the sedimentary sequence, to investigate the structures of the forearc slope, and to sample and analyze fluids in the crust.

The major discovery was that the basement rocks under this part of the forearc comprise a low-K rhyolitic volcanic complex of uncertain age which is overlain, on a fault contact, by upper Eocene shallow-water carbonates. The rhyolitic assemblage is characterized by very high silica content (76%–80%) but very low potassium (0.4%–1.6% K_2O) for that level of silica. This is a common feature of silicic rocks of intraoceanic arc systems. The volcanic rock series includes rhyolite, rhyolitic tuffs, lapilli tuffs, flow breccias, and welded tuffs. The best estimate is that these formed subaerially or in a very shallow-water environment. The silicic rocks may represent an early stage in the evolution of the ancestral Melanesian proto-arc. A consideration of plate tectonic evolution of the southwestern Pacific since the late Mesozoic offers the interesting but highly speculative alternative possibility that these may have some petrologic relationship to rhyolitic rocks drilled on Lord Howe Rise at DSDP Site 207. Apart from the great distance of present separation, which is minimal once post-Eocene crust is accounted for, there is an apparent age gap. The Lord Howe Rise rocks have been radiometrically dated as 93.7 ± 1.2 Ma and are overlain by Maestrichtian sediments. There is no reliable age for the Site 841 rhyolites other than that a major low-angle fault zone separates them from upper Eocene rocks.

The rhyolitic complex was drilled at a depth of about 5400 mbsl, and all indications are that it formed very near or above sea

Table 16. Physical properties data, Holes 841A and 841B.

Core, section, interval (cm)	Depth (mbsf)	TC (W/[m · °K])	Su (kPa)	Bulk density (g/cm^3)	Grain density (g/cm^3)	Porosity (%)	Water content (%)	Void ratio	V_p (m/s)	V_p dir.
135-841A-										
1H-1, 88–90	0.88			1.51	2.69	80	117	3.9		
1H-2, 60–60	2.10	0.885								
1H-2, 82–83	2.32		10.0	1.48	2.88	77	115	3.3		
1H-3, 60–60	3.60	1.007								
1H-3, 79–81	3.79		15.4	1.57	5.74	75	96	3.0	1462	A
1H-4, 60–60	5.10	0.937								
1H-5, 77–79	6.77		19.9	1.64	2.70	71	79	2.4	1510	A
1H-6, 38–40	7.88		24.2	1.63	2.63	79	97	3.6		
1H-6, 60–60	8.10	0.938								
2H-1, 101–103	9.51		34.9	1.52	2.64	75	102	3.0	1513	A
2H-2, 60–60	10.60	0.855								
2H-3, 60–60	12.10	0.984								
2H-3, 63–65	12.13		39.7						1536	C
2H-3, 69–71	12.19	0.931		1.49	2.61	78	116	3.6		
2H-4, 60–60	13.60									
2H-5, 90–91	15.40			1.55	2.68	78	106	3.5		
2H-5, 95–97	15.45		48.7						1574	C
2H-6, 60–60	16.60	0.855								
2H-6, 72–73	16.72		122.5							
2H-6, 79–81	16.79								1620	C
2H-6, 124–126	17.24								1589	C
3H-1, 81–83	18.81		50.8	1.48	2.66	80	124	3.9		
3H-1, 83–85	18.83								1585	C
3H-2, 60–60	20.10	0.800								
3H-3, 60–60	21.60	0.955								
3H-3, 84–86	21.84		71.7	1.46	2.75	82	136	4.5		
3H-3, 87–89	21.87								1584	C
3H-3, 91–93	21.91								1559	C
3H-4, 60–60	23.10	0.920								
3H-5, 73–74	24.73		35.3	1.36	2.38	81	155	4.2		
3H-5, 75–77	24.75								1612	C
3H-6, 38–40	25.88		156.7	1.44	2.66	83	145	5.0		
3H-6, 60–60	26.10	0.891								
4H-1, 68–70	28.18			1.39	2.65	84	159	5.0	1495	C
4H-1, 74–75	28.24		41.9							
4H-2, 60–60	29.60	0.830								
4H-2, 118–120	30.18			1.50	2.76	78	114	3.6	1526	C
4H-3, 60–60	31.10	0.990								
4H-3, 74–75	31.24		82.8							
4H-3, 76–78	31.26		82.8	1.43	2.65	83	147	5.0		
4H-4, 60–60	32.60	0.983								
4H-4, 75–77	32.75								1570	C
4H-5, 92–94	34.42			1.46	2.69	82	135	4.5	1560	C
4H-5, 96–97	34.46		115.9							
4H-6, 60–60	35.20	0.944								
5H-2, 36–38	38.41			1.47	2.72	79	123	3.8	1495	A
5H-2, 60–60	39.10	0.727								
5H-2, 88–89	39.93		130.0							
5H-3, 64–66	40.19			1.52	2.64	76	105	3.2		
5H-3, 98–100	40.53			1.53	2.69	77	105	3.3		
5H-3, 60–60	40.60	0.940								
5H-3, 102–103	40.57		137.0							
5H-4, 98–100	42.03			1.49	2.57	79	117	3.6		
5H-4, 60–60	42.10	0.901								
5H-4, 100–101	42.05		176.0							
5H-5, 64–66	43.21			1.70	2.63	62	60	1.6		
5H-6, 82–84	44.85			1.53	2.76	78	109	3.5	1709	C
5H-6, 60–60	45.10	0.936								
6H-1, 25–27	46.75			1.52	2.75	76	105	3.2		
6H-1, 28–29	46.78			1.66	2.39	70	77	2.4	1521	A
6H-2, 60–60	48.60	0.868								
6H-3, 60–60	50.10	1.092								
6H-3, 78–80	50.28			1.6	2.77	73	88	2.7		
6H-4, 60–60	51.60	0.957								
6H-5, 38–40	52.88			1.58	2.75	75	94	3.0		
6H-5, 60–60	53.10	0.915								
7H-CC, 11–13	56.40			1.91	2.68	57	44	1.3	2086	A
8H-1, 45–45	65.95	0.756								
8H-1, 87–89	66.37			1.67	2.71	69	73	2.2	1778	A
8H-2, 35–36	67.35			1.75	2.80	66	63	1.9	1835	A
8H-2, 60–60	67.60	0.961								
8H-3, 60–60	69.10	0.911								

Notes: TC = thermal conductivity, Su = undrained vane shear strength, V_p = compressional (*P*-wave logger) velocity, and V_p dir. = velocity direction, where A is the vertical velocity along the core, B is the horizontal velocity parallel to the cut core face, and C is the horizontal velocity perpendicular to the core face. Table 16 appears in its entirety on the back-pocket microfiche.

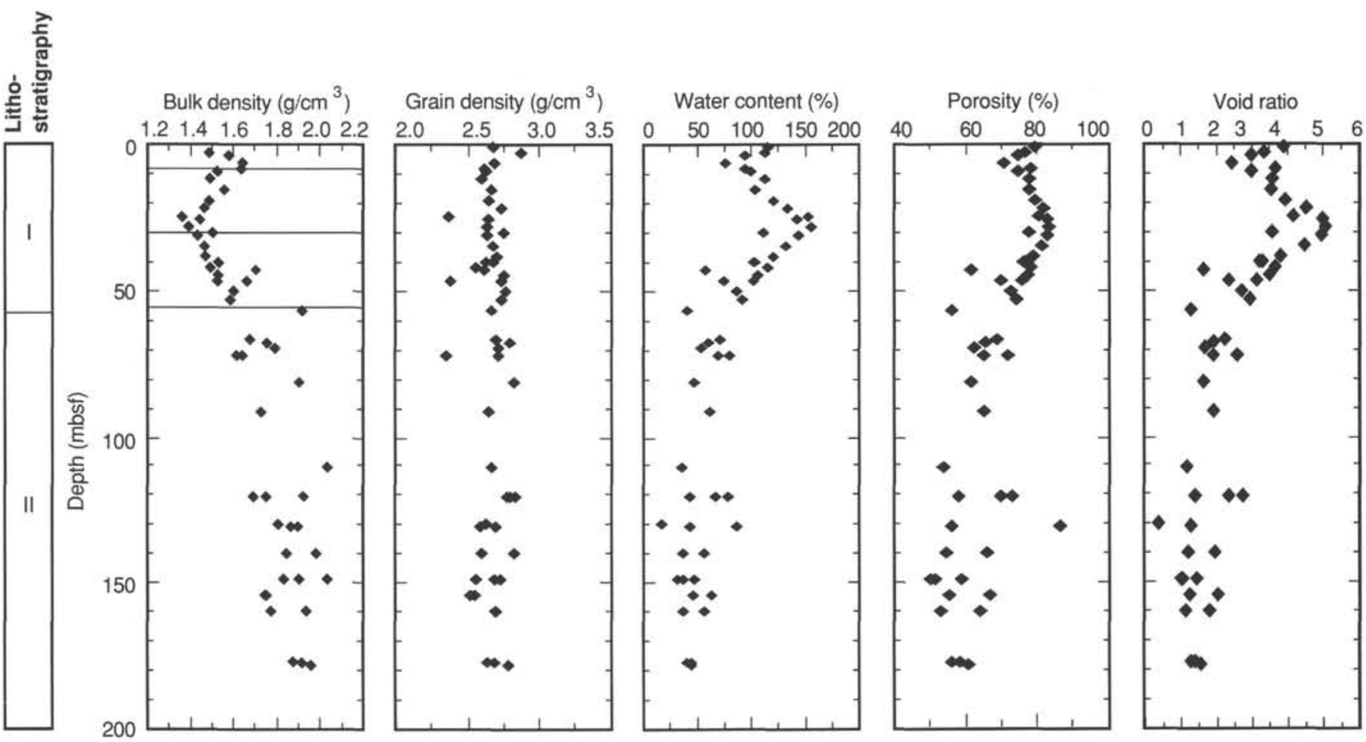

Figure 68. Plots of index properties data vs. depth for the sedimentary section from Hole 841A: bulk density, grain density, water content, porosity, and void ratio.

level. Therefore, there has been a remarkable foundering of the crust at this site since the latest Eocene. If this rhyolitic material initially formed as part of the present Tonga Ridge system, then there has been considerable tectonic erosion of the deep levels of the forearc crust during Cenozoic plate subduction into the Tonga Trench. If it is a far-traveled exotic terrane, then some of this subsidence may have been due to repeated rifting, rotation, and/or collapse.

The presence of intrusive material in forearc sedimentary accumulations is very unusual, although not without precedent, having been found in the Mariana forearc on Leg 125, Site 781, where a Pliocene or younger basalt flow or sill was encountered. Site 841 cored nine separate basaltic andesite to andesite units in the Miocene forearc sediments. An intrusive relationship was indicated by chilled margins, hyaloclastite breccias on the igneous rocks, and indurated sediments at the contact. These intrusive layers may have given rise to steepened thermal gradients that are expressed as a downward increase in low grade metamorphic mineral assemblages from clays, to zeolites, to prehnite followed downward by a sharp inversion to unmetamorphosed sediments.

Interstitial waters from the forearc sediments proved unusual in that beginning with the upper Miocene sediments at 171.3 mbsf there is an increase in calcium and chloride that is associated with a decrease in magnesium, potassium, and sodium. These variations are attributed to a zone of reaction between 250 and 640 mbsf below which these relative concentrations are reversed. These trends are opposite to what is usually observed in seawater/basalt interaction. In this reaction zone, the porewater chemistry is some of the most intensively modified pore water of seawater origin yet sampled by the DSDP/ODP drilling. Only three other sites with similar fluid chemistry have been found: Sites 792 and 793 in the Izu-Bonin forearc and Site 802 in the deep-sea Central Mariana Basin. At Site 841, the $CaCl_2$ brine probably is the result of the combined effects of high rates of sedimentation that causes diminished diffusive exchange with the overlying ocean water, and the chemical exchange with the abundant supply of volcanogenic material.

There was only minor evidence for sulfide mineralization at the other drill sites but Site 841 was distinctive in having several zones of sulfide minerals, mainly fine-grained pyrite but also minor pyrrhotite, chalcopyrite, and marcasite. These were commonly dispersed in zones of kaolinitic clay typically associated with brecciated rhyolitic rocks.

REFERENCES

Adams, C. G., 1970. A reconsideration of the East Indian Letter Classification of the Tertiary. *Bull. Br. Mus. (Nat. Hist.), Geol.*, 19:87–137.

Alexander, C., 1985. 2-D gravity and magnetic modeling of subsurface domical structure 11/14. *In* Scholl, D. W., and Vallier, T. L. (Eds.), *Geology and Offshore Resources of Pacific Island Arcs—Tonga Region.* Circum-Pac. Counc. Energy Miner. Resour., Earth Sci. Ser., 2:197–202.

Anderson, J. E., 1969. Development of snowflake texture in a welded tuff. *Geol. Soc. Am. Bull.*, 80:2075.

Bailey, R. A., Dalrymple, G. B., and Lamphere, M. A., 1976. Volcanism, structure and geochronology of Long Valley Caldera, Mono County, California. *J. Geophys. Res.*, 81:725–744.

Basaltic Volcanism Study Project, 1981. Island arc basalts. *In* Taylor, S. R., Arculus, R. J., Perfit, M. R., and Johnson, R. W. (Eds.), *Basaltic Volcanism on the Terrestrial Planets:* New York (Pergamon Press), 193–213.

Bentz, F. P., 1974. Marine geology of the southern Lord Howe Rise, southwest Pacific. *In* Burk, C. A., and Drake, C. L. (Eds.), *The Geology of Continental Margins:* New York (Springer-Verlag), 537–547.

Berggren, W. A., Kent, D. V., Flynn, J. J., and Van Couvering, J. A., 1985. Cenozoic geochronology. *Geol. Soc. Am. Bull.*, 96:1407–1418.

Berggren, W. A., and Miller, K. G., 1988. Paleogene tropical planktonic foraminiferal biostratigraphy and magnetobiochronology. *Micropaleontology*, 34:362–380.

Blanc, G., Boulegue, J., and Gieskes, J. R., 1991. Chemical evidence for advection of interstitial fluid in the sedimentary series of the Barbados accretionary complex (Leg 110). *Oceanol. Acta*, 14:1–18.

Bloomer, S. H., 1983. Distribution and origin of igneous rocks from the landward slopes of the Mariana Trench: implications for its structure and evolution. *J. Geophys. Res.*, 88:7411–7428.

Bloomer, S. H., and Fisher, R. L., 1987. Petrology and geochemistry of igneous rocks from the flanks of the Tonga Trench—a non-accreting plate boundary. *J. Geol.*, 95:469–495.

Bloomer, S. H., and Hawkins, J. W., 1983. Gabbroic and ultramafic rocks from the Mariana trench: an island arc ophiolite. *In* Hayes, D. E. (Ed.), *The Tectonic and Geologic Evolution of Southeast Asian Seas and Islands* (Pt. 2). Am. Geophys. Union, AGU Monogr. Ser., 23:294–317.

Blow, W. H., 1969. Late middle Eocene to Recent planktonic foraminiferal biostratigraphy. *In* Brönniman, P., and Renz, H. H. (Eds.), *Proc. First Int. Conf. Planktonic Microfossils*, Geneva, 1967. Leiden (E. J. Brill), 1:199–422.

Broecker, W. S., and Peng, T.-H., 1982. *Tracers in the Sea:* Palisades, NY (Eldigio Press).

Browne, P.R.L., 1978. Hydrothermal alteration in active geothermal fields. *Annu. Rev. Earth Planet. Sci.*, 6:229–250.

Buchbinder, B., and Halley, R. B., 1985. Source rock evaluation of outcrop and borehole samples from Tongatapu and 'Eua Islands, Tonga, and from Viti Levu and Vanua Levu Islands, Fiji. *In* Scholl, D. W., and Vallier, T. L. (Eds.), *Geology and Offshore Resources of Pacific Island Arcs—Tonga Region.* Circum-Pac. Counc. Energy Miner. Resour., Earth Sci. Ser., 2:335–349.

Bukry, D., 1973. Low-latitude coccolith biostratigraphic zonation. *In* Edgar, N. T., Saunders, J. B., et al., *Init. Repts. DSDP*, 15: Washington (U.S. Govt. Printing Office), 685–703.

Burns, R., and Andrews, J., 1973. Regional aspects of drilling in the southwest Pacific. *In* Burns, R. E., Andrews, J. E., et al., *Init. Repts. DSDP*, 21: Washington (U.S. Govt. Printing Office), 897–906.

Cawood, P., 1985. Petrography, phase chemistry and provenance of volcanogenic debris from the southern Tonga Ridge: implications for arc history and magmatism. *In* Scholl, D. W., and Vallier, T. L. (Eds.), *Geology and Offshore Resources of Pacific Island Arcs—Tonga Region.* Circum-Pac. Counc. Energy Miner. Resour., Earth Sci. Ser., 2:149–170.

Chaproniere, G.C.H., 1983. Tertiary larger foraminiferids from the northwestern margin of the Queensland Plateau, Australia. *Bull. Bur. Miner. Resour., Geol. Geophys. (Aust.)*, 217:31–57.

Church, B. N., and Johnson, W. M., 1980. Calculation of the refractive index of silicate glasses from chemical composition. *Geol. Soc. Am. Bull.*, 91:619–625.

Claypool, G. E., and Kvenvolden, K. A., 1983. Methane and other hydrocarbon gases in marine sediment. *Annu. Rev. Earth Planet. Sci.*, 11:299–327.

Cole, J. W., Gill, J. B., and Woodhall, D., 1985. Petrologic history of the Lau Ridge, Fiji. *In* Scholl, D. W., and Vallier, T. L. (Eds.), *Geology and Offshore Resources of Pacific Island Arcs—Tonga Region.* Circum-Pac. Counc. Energy Miner. Resour., Earth Sci. Ser., 2:379–414.

Cunningham, J. K., and Anscombe, K. J., 1985. Geology of 'Eua and other islands, Kingdom of Tonga. *In* Scholl, D. W., and Vallier, T. L. (Eds.), *Geology and Offshore Resources of Pacific Island Arcs—Tonga Region.* Circum-Pac. Counc. Energy Miner. Resour., Earth Sci. Ser., 2:221–258.

Duncan, R. A., Vallier, T., and Falvey, D. A., 1985. Volcanic episodes at 'Eua Tonga. *In* Scholl, D. W., and Vallier, T. L. (Eds.), *Geology and Offshore Resources of Pacific Island Arcs—Tonga Region.* Circum-Pac. Counc. Energy Miner. Resour., Earth Sci. Ser., 2:281–290.

Ekdale, A. A., Bromley, R. G., and Pemberton, S. G. (Eds.), 1984. *Ichnology: Trace Fossils in Sedimentology and Stratigraphy.* SEPM Short Course, No. 15.

Ellis, A. J., 1979. Explored geothermal systems. *In* Barnes, H. L. (Ed.), *Geochemistry of Hydrothermal Ore Deposits:* New York (Wiley), 632–683.

Emeis, K.-C., and Kvenvolden, K. A., 1986. Shipboard organic geochemistry on *JOIDES Resolution. ODP Tech. Note*, No. 7.

Espitalié, J., Laporte, J. L., Leplat, P., Madec, M., Marquis, F., Paulet, J., and Boutefeu, A., 1977. Méthode rapide de caractérisation des roches mères, de leur potentiel pétrolier et de leur degrée d'évolution. *Rev. Inst. Fr. Pet.*, 32:23–42.

Evarts, R. C., and Schiffmann, P., 1983. Submarine hydrothermal metamorphism of the Del Puerto ophiolite, California. *Am. J. Sci.*, 283:289–340.

Ewart, A., Brothers, R. N., and Mateen, A., 1977. An outline of the geology and geochemistry, and the possible petrogenetic evolution of the volcanic rocks of the Tonga-Kermadec-New Zealand island arc. *J. Volcanol. Geotherm. Res.*, 2:205–250.

Ewart, A., and Bryan, W., 1972. Petrography and geochemistry of the igneous rocks from 'Eua, Tonga Islands. *Geol. Soc. Am. Bull.*, 83:3281–3298.

Ewart, A., Bryan, W. B., and Gill, J., 1973. Mineralogy and geochemistry of the younger volcanic islands of Tonga, southwest Pacific. *J. Petrol.*, 14:429–465.

Ewart, A., and Hawkesworth, C. J. 1987. Pleistocene to Recent Tonga-Kermadec arc lavas: interpretation of new isotopic and rare earth data in terms of a depleted mantle source model. *J. Petrol.* 28:495–530.

Ewart, A. E., 1965. Mineralogy and petrology of the Whakamaru ignimbrite in the Maraetai area of the Taupo Volcanic Zone, New Zealand. *N. Z. J. Geol. Geophys.*, 8:611.

Exon, N. F., Herzer, R. H., and Cole, J., 1985. Mixed volcaniclastic and sedimentary rocks from the Cenozoic southern Tonga platform and their petroleum potential. *In* Scholl, D. W., and Vallier, T. L. (Eds.), *Geology and Offshore Resources of Pacific Island Arcs—Tonga Region.* Circum-Pac. Counc. Energy Miner. Resour., Earth Sci. Ser., 2:75–108.

Falloon, T. J., and Crawford, A. J., 1991. The petrogenesis of high-calcium boninite lavas dredged from the north Tonga Ridge. *Earth Planet. Sci. Lett.*, 102:375–394.

Falloon, T. J., Green, D. H., and Crawford, A. J., 1987. Dredged igneous rocks from the northern termination of the Tofua magmatic arc, Tonga and adjacent Lau Basin, *Aust. J. Earth Sci.*, 34:487–506.

Fisher, R. L., 1974. Pacific-type continental margins. *In* Burk, C. A., and Drake, C. L. (Eds.), *The Geology of Continental Margins:* New York (Springer-Verlag), 25–41.

Fisher, R. L., and Engel, C. G., 1969. Ultramafic and basaltic rocks dredged from the nearshore flank of the Tonga Trench. *Geol. Soc. Am. Bull.*, 80:1373–1378.

Fisher, R. V., and Schmincke, H.-U., 1984. *Pyroclastic Rocks:* New York (Springer-Verlag).

Gatliff, R. W., 1990. The petroleum prospects of the Kingdom of Tonga. Rep. published by South Pacific Applied Geoscience Commission (SOPAC) on behalf of the Aust. Int. Dev. Assoc. Bureau.

Gieskes, J. M., 1983. The chemistry of interstitial waters of deep-sea sediments: interpretation of Deep-Sea Drilling data. *In* Riley, J. P., and Chester, R. (Eds.), *Chemical Oceanography* (Vol. 8): London (Academic Press), 222–269.

Gieskes, J. M., Blanc, G., Vrolijk, P., Elderfield, H., and Barnes, R., 1990. Interstitial water chemistry—major constituents. *In* Moore, J. C., Mascle, A., et al., *Proc. ODP, Sci. Results*, 110: College Station, TX (Ocean Drilling Program), 155–178.

Gieskes, J. M., and Johnston, K., 1984. Interstitial water studies Leg 81. *In* Roberts, D. G., Schnitker, D., et al., *Init. Repts. DSDP*, 81: Washington (U.S. Govt. Printing Office), 829–836.

Hawkins, J. W., 1976. Petrology and geochemistry of basaltic rocks of the Lau Basin. *Earth Planet. Sci. Lett.*, 28:283–297.

_______, 1985. Low-K rhyolitic pumice from the Tonga ridge. *In* Scholl, D. W., and Vallier, T. L. (Eds.), *Geology and Offshore Resources of Pacific Island Arcs—Tonga Region.* Circum-Pac. Counc. Energy and Miner. Resour., Earth Sci. Ser., 2:171–178.

_______, 1989. Cruise Report—ROUNDABOUT Expedition, Legs 14, 15, R/V *Thomas Washington.* SIO Ref. Ser., No. 89-13.

Hawkins, J. W., Bloomer, S. H., Evans, C. A., and Melchior, J. T., 1979. Mariana arc-trench system, petrology of the inner trench wall. *Eos*, 60:968.

_______, 1984. Evolution of intra-oceanic arc-trench systems. *Tectonophysics*, 102:174–205.

Hawkins, J. W., and Falvey, D. A., 1985. Petrology of andesitic dikes and flows from 'Eua, Tonga. *In* Scholl, D. W., and Vallier, T. L. (Eds.), *Geology and Offshore Resources of Pacific Island Arcs—Tonga Region.* Circum-Pac. Counc. Energy Miner. Resour., Earth Sci. Ser., 2:269–280.

Hay, W. W., 1988. Paleoceanography: a review for the GSA Centennial. *Geol. Soc. Am. Bull.*, 100:1934–1956.

Healy, J., Vucetich, C. G., and Pullar, W. A., 1964. Stratigraphy and chronology of Late Quaternary volcanic ash in Tampo, Rotorna, and Gisborne Districts. *N. Z. Geol. Survey Bull.*, 73:7–88.

Herzer, R. H., and Exon, N., 1985. Structure and basin analysis of the southern Tonga forearc. *In* Scholl, D. W., and Vallier, T. L. (Eds.), *Geology and Offshore Resources of Pacific Island Arcs—Tonga Region*. Circum-Pac. Counc. Energy Miner. Resour., Earth Sci. Ser., 2:55–74.

Hoffmeister, J. E., 1932. Geology of 'Eua, Tonga. *Bull. B.P. Bishop Museum*, No. 96.

Hussong, D. M., and Fryer, P., 1985. Fore-arc tectonics in the northern Mariana Arc. *In* Nasu, N., Kobayashi, K., Uyeda, S., et al., (Eds.), *Formation of Active Ocean Margins:* Tokyo (Terra Scientific Publishing), 273–290.

Hyndman, R. D., Langseth, M. G., and Von Herzen, R. P., 1987. Deep Sea Drilling Project geothermal measurements: a review. *Rev. Geophys.*, 25:1563–1582.

Karig, D. E., 1970. Ridges and basins of the Tonga-Kermadec island arc system. *J. Geophys. Res.*, 75:239–254.

Kennett, J. P., and Srinivasan, M. S., 1983. *Neogene Planktonic Foraminifera: A Phylogenetic Atlas:* Stroudsburg, PA (Hutchinson Ross).

Kroenke, L., 1984. *Cenozoic Development of the Southwest Pacific*. Suva, CCOP/SOPAC, Tech. Bull.—U. N. Econ. Soc. Comm. Asia Pac.

Lancelot, Y., Larson, R., et al., 1990. *Proc. ODP, Init. Repts.*, 129: College Station, TX (Ocean Drilling Program).

Lonsdale, P., 1986. A multibeam reconnaissance of the Tonga Trench axis and its intersection with Louisville Guyot Chain. *Mar. Geophys. Res.*, 8:295–327.

Maung, T. U., Anscombe, K. J., and Tongilava, S. L., 1981. Assessment of petroleum potential of the southern and northern parts of the Tonga platform. Tech. Rep.—U. N. Econ. Soc. Comm. Asia Pac., CCOP/SOPAC, No. 18.

Meijer, A., 1983. The origin of low-K rhyolites from the Mariana frontal arc. *Contrib. Mineral. Petrol.*, 83:45–51.

Nilsson, K., Florendo, F. F., and Hawkins, J. W., et al., 1989. Petrology of a nascent triple junction, northeastern Lau Basin. *Eos*, 70:1389.

Okada, H., and Bukry, D., 1980. Supplementary modification and introduction of code numbers to the low-latitude coccolith biostratigraphic zonation (Bukry, 1973; 1975). *Mar. Micropaleontol.*, 5:321–325.

Packham, G. H., 1985. Vertical tectonics on the Tonga Ridge from the Tongatapu oil exploration wells. *In* Scholl, D. W., and Vallier, T. L. (Eds.), *Geology and Offshore Resources of Pacific Island Arcs—Tonga Region*. Circum-Pac. Counc. Energy Miner. Resour., Earth Sci. Ser., 2:301–316.

Paris, J. P., and Lille, R., 1977. New Caledonia: evolution from Permian to Miocene: mapping data and hypotheses about geotectonics. Int. Symp. of Geodynamics of the Southwest Pacific, New Caledonia, August-September, 1976. Paris (Ed. Technip.), 195–208.

Parson, L. M., et al., 1989. *RRS Charles Darwin* Cruise 33/88, 5 May–1 June 1988. Geophysical and geological investigations of the Lau back-arc basin, SW Pacific. Inst. Oceanogr. Sci. Deacon Lab. Cruise Report, No. 206.

Parson, L. M., Pearce, J. A., Murton, B. J., Hodkinson, R. A., Bloomer, S., Ernewein, M., Huggett, Q. J., Miller, S., Johnson, L., Rodda, P., and Helu, S., 1990. Role of ridge jumps and ridge propagation in the tectonic evolution of the Lau back-arc basin, southwest Pacific. *Geology*, 18:470–473.

Raitt, R. W., Fisher. R. L., and Mason, R. G., 1955. Tonga Trench. *In* Poldervaart, A. (Ed.), *Crust of the Earth*. Spec. Pap.—Geol. Soc. Am., 62:237–254.

Sandstrom, M. W., 1985. Organic chemistry of dredge samples and oil seeps from the southern Tonga platform. *In* Scholl, D. W., and Vallier, T. L. (Eds.), *Geology and Offshore Resources of Pacific Island Arcs—Tonga Region*. Circum-Pac. Counc. Energy and Miner. Resour., Earth Sci. Ser., 2:129–129.

Schmincke, H.-U., 1981. Ash from vitric muds in deep sea cores from the Mariana Trough and fore-arc regions (south Philippine Sea) (Sites 453, 454, 455, 458, 459). *In* Hussong, D. M., Uyeda, S., et al., *Init. Repts. DSDP*, 60: Washington (U.S. Govt. Printing Office), 473–481.

Scholl, D. W., and Vallier, T. L. (Eds.), 1985. *Geology and Offshore Resources of Pacific Island Arcs—Tonga Region*. Circum-Pac. Counc. Energy Miner. Resour., Earth Sci. Ser., No. 2.

Scholl, D. W., Vallier, T. L., and Packham, G. H., 1985. Framework geology and resource potential of the southern Tonga platform and adjacent terranes—a synthesis. *In* Scholl, D. W., and Vallier, T. L. (Eds.), *Geology and Offshore Resources of Pacific Island Arcs—Tonga Region*. Circum-Pac. Counc. Energy Miner. Resour., Earth Sci. Ser., 2:457–488.

Shipboard Scientific Party, 1973. Site 207. *In* Burns, R. E., Andrews, J. E., et al., *Init. Repts. DSDP*, 21: Washington (U.S. Govt. Printing Office), 197–269.

_______ 1990. Site 786. *In* Fryer, P., Pearce, J. A., et al., *Proc. ODP, Init. Repts.*, 125: College Station, TX (Ocean Drilling Program), 313–363.

Sun, S.-S., and McDonough, W. F., 1989. Chemical and isotopic systematics of oceanic basalts: implications for mantle composition and processes. *In* Saunders, A. D., and Norry, M. J. (Eds.), *Magmatism in the Ocean Basins*. Geol. Soc. Spec. Publ. London, 42:313–345.

Tappin, D. R., and Ballance, P. F., in press. Contributions to the sedimentary geology of 'Eua Island—Kingdom of Tonga: reworking in an oceanic forearc. *In* Stevenson, A., and Ballance, P. (Eds.), *Tonga Arc:* Berlin (Springer Verlag).

Tappin, D. R., Herzer, R. H., and Stevenson, A. J., in press. Structure and history of an oceanic forearc—the Tonga Ridge 22° to 26° South. *In* Stevenson, A., and Ballance, P. (Eds.), *Tonga Arc:* Berlin (Springer Verlag).

Taylor, B., Fujioka, K., et al., 1990. *Proc. ODP, Init. Repts.*, 126: College Station, TX (Ocean Drilling Program).

Vallier, T. L., O'Connor, R. M., Scholl, D. W., Stevenson, A. J., and Quinterno, P. J., 1985. Petrology of rocks dredged from the landward slope of the Tonga Trench: implications for middle Miocene volcanism and subsidence of the Tonga Ridge. *In* Scholl, D. W., and Vallier, T. L. (Eds.), *Geology and Offshore Resources of Pacific Island Arcs—Tonga Region*. Circum-Pac. Counc. Energy Miner. Resour., Earth Sci. Ser., 2:109–120.

van der Lingen, G., 1973. The Lord Howe rhyolites. *In* Burns, R. E., Andrews, J. E., et al., *Init. Repts. DSDP*, 21: Washington (U.S. Govt. Printing Office), 523–540.

von Stackelberg, U., 1990. R.V. *Sonne* Cruise SO48: summary of results testing a model of mineralization. *Mar. Min.*, 9:135–144.

Wilcox, J. B., Symonds, P. A., Hinz, K., Bennet, D., 1980. Lord Howe Rise, Tasman Sea—preliminary geophysical results and petroleum prospects. *BMR J. Aust. Geol. Geophys.*, 5:225–236.

Ms 135A-111

NOTE: All core description forms ("barrel sheets") and core photographs have been printed on coated paper and bound separately as Part 2 of this volume, beginning on page 681.

Formation microscanner images for this site are presented on microfiche in the back of Part 2.

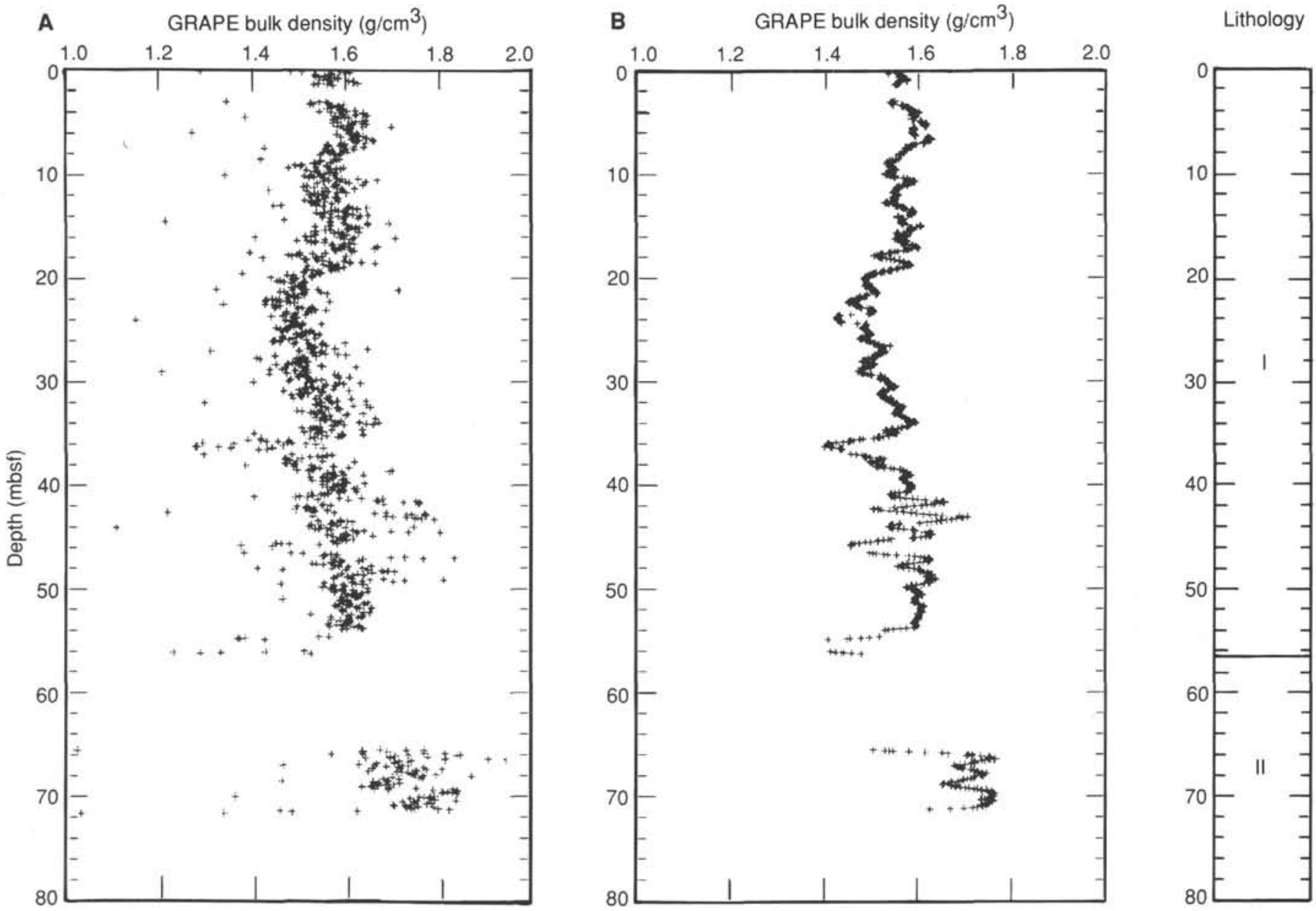

Figure 69. GRAPE bulk density vs. depth for Hole 841A at 5-cm intervals (**A**) and after 5-point running average has been applied (**B**). Corresponding lithologic column shown to the right of plots.

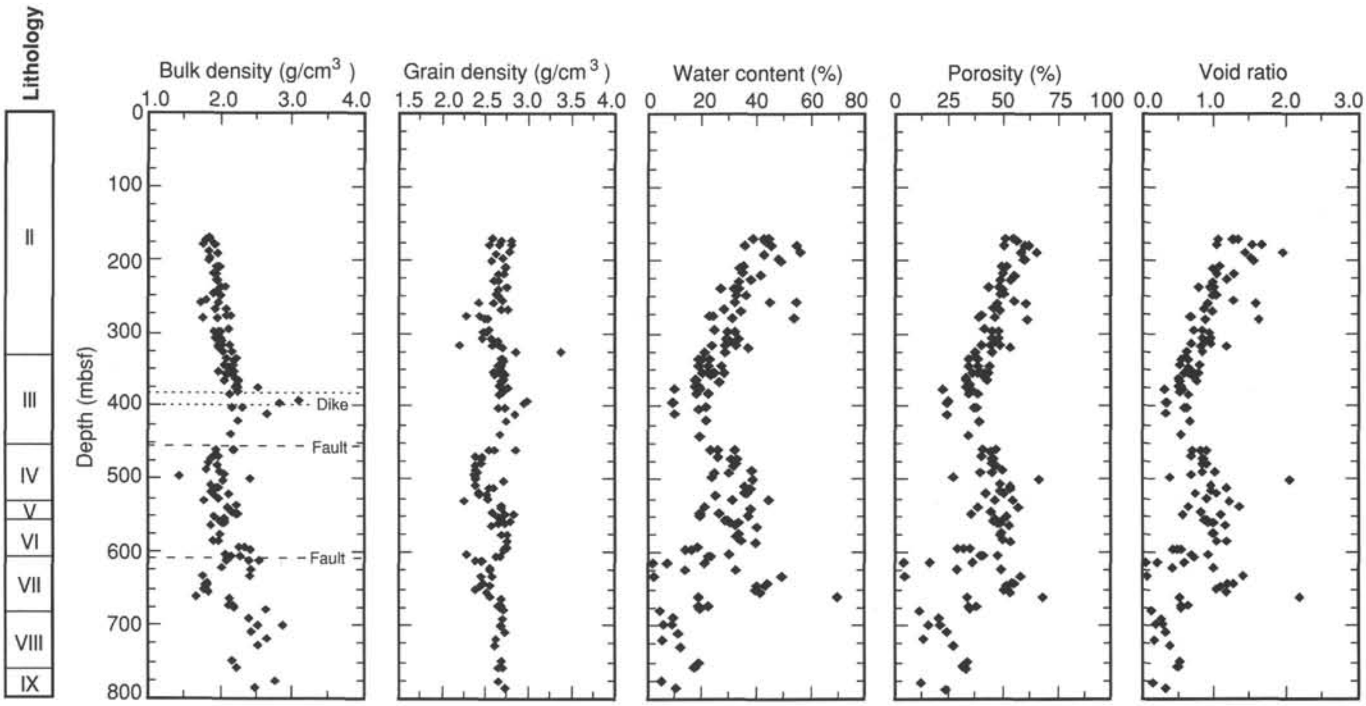

Figure 70. Index properties data vs. depth for sediments and rocks recovered from Hole 841B: bulk density, grain density, water content, porosity, and void ratio.

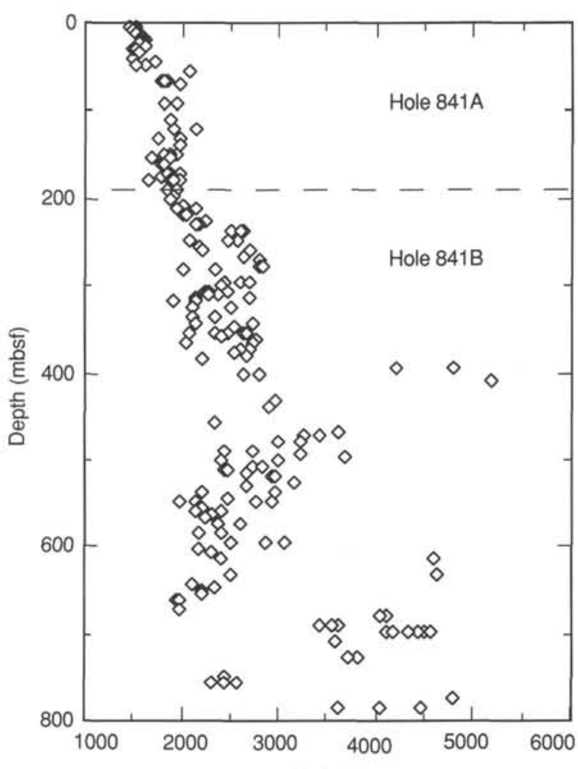

Figure 71. Compressional wave velocity vs. depth for samples from Site 841.

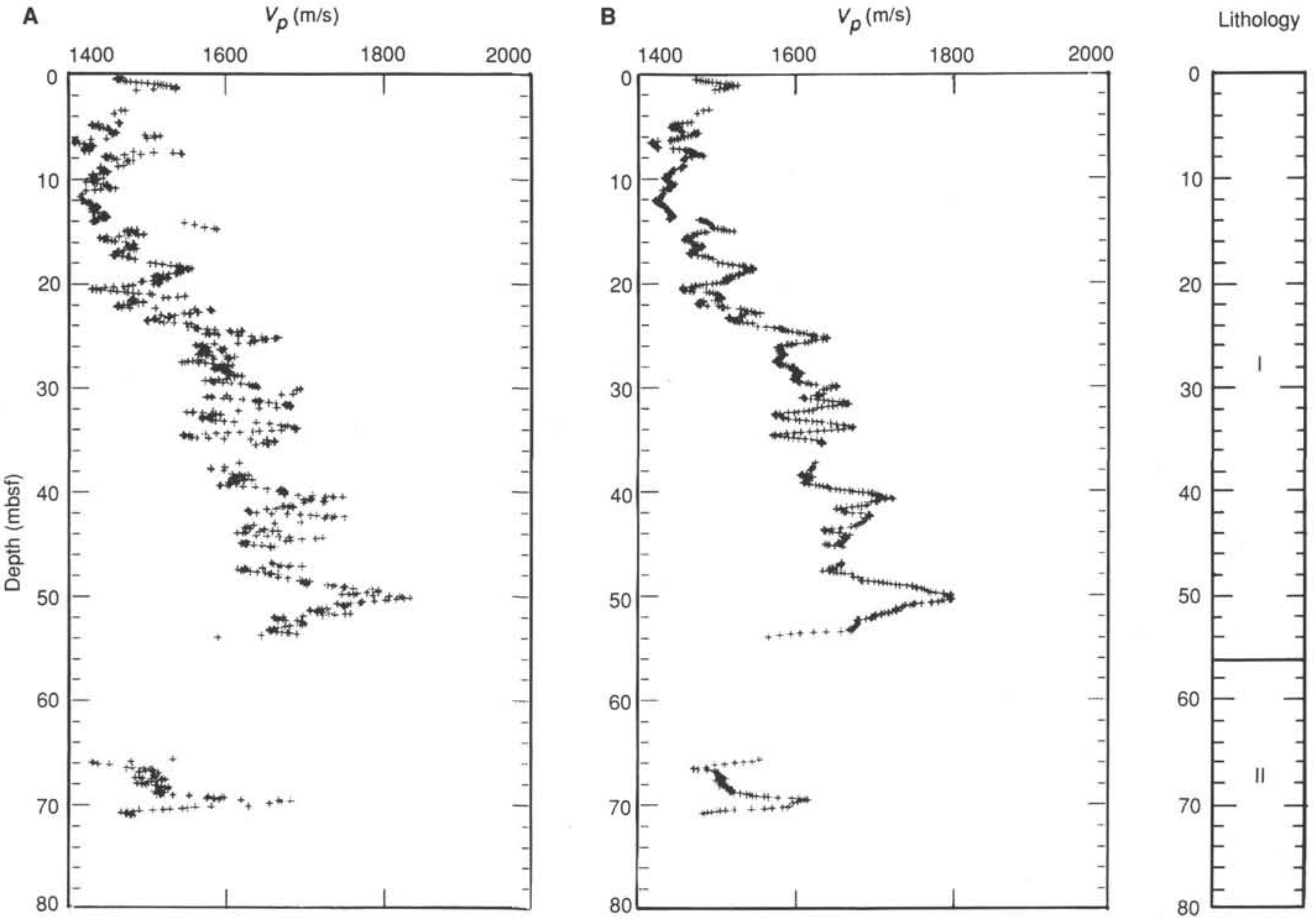

Figure 72. *P*-wave logger data vs. depth from Hole 841A after initial 5-cm averaging (**A**) and after applying a 5-point running average (**B**). Lithologic units shown to the right of plots.

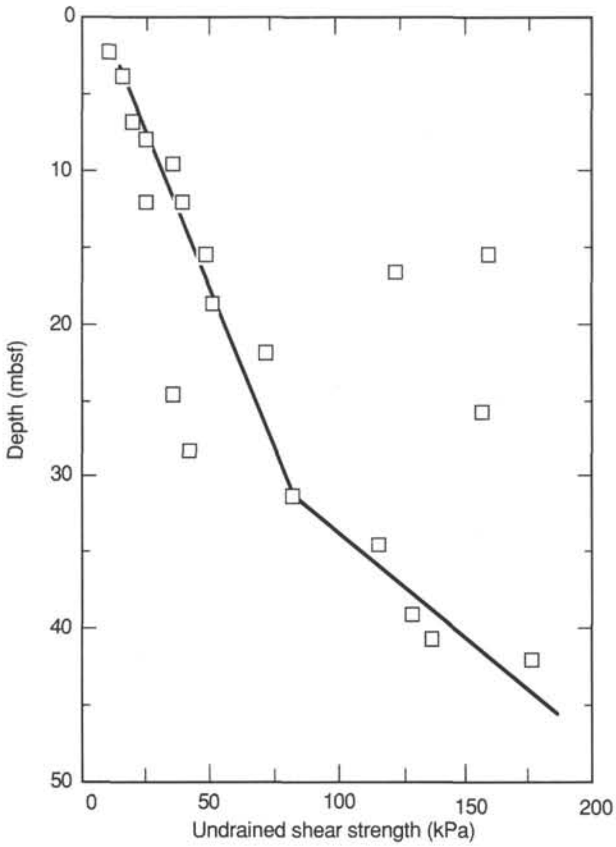

Figure 73. Undrained vane shear strength vs. depth for samples from Holes 841A and 841B. Gradients are inserted visually.

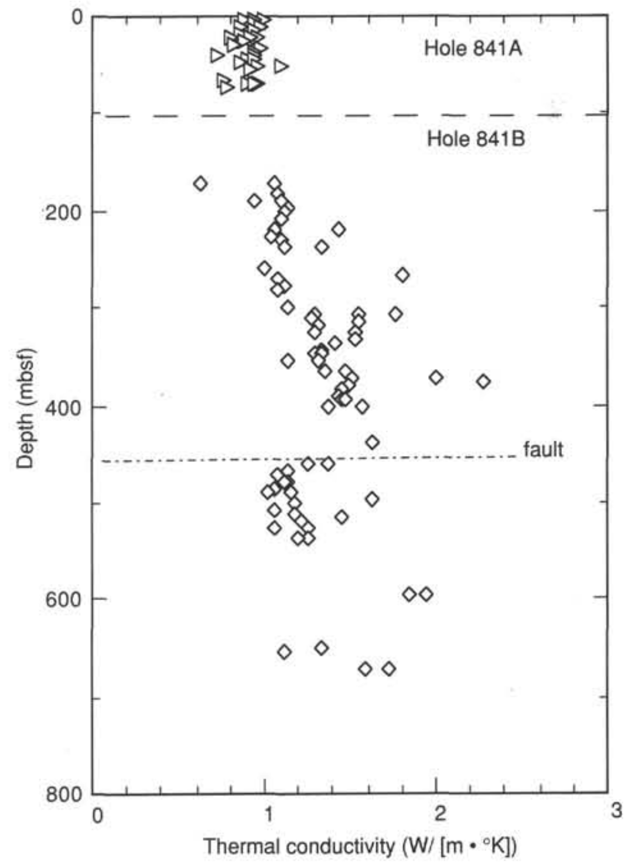

Figure 74. Thermal conductivity vs. depth for sediments from Hole 841A (triangles) and consolidated sediments and basalt samples from Hole 841B (diamonds).

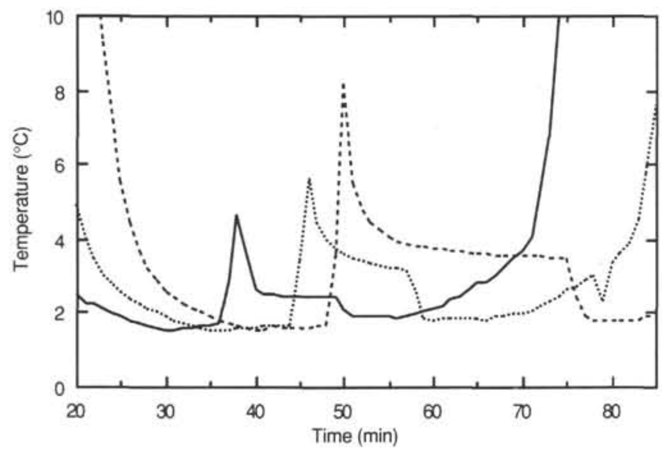

Figure 75. WSTP measurements from Holes 841A. Measurement depths were 27.5 mbsf (solid line), 56 mbsf (short dashes), and 65.5 mbsf (long dashes).

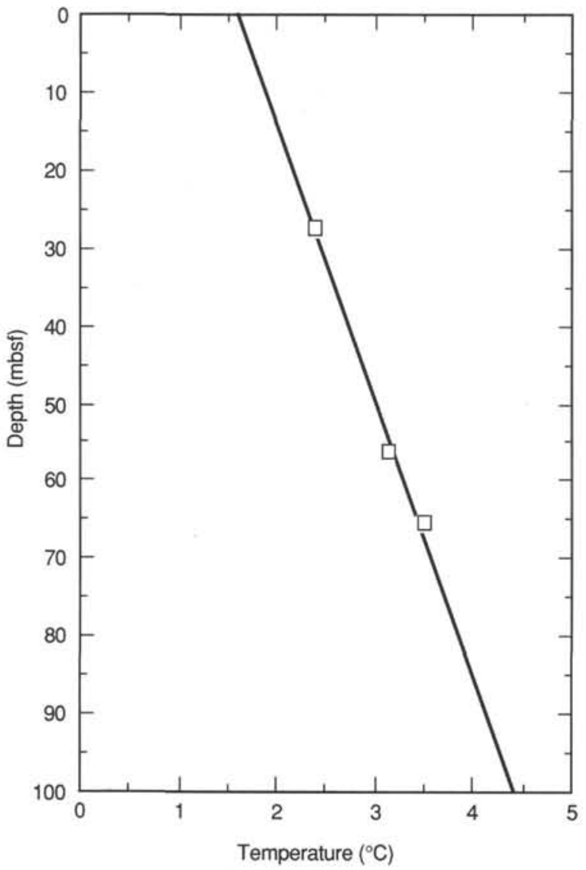

Figure 76. Temperature vs. depth for Site 841, with line showing geothermal gradient of 2.8°C/100 m.

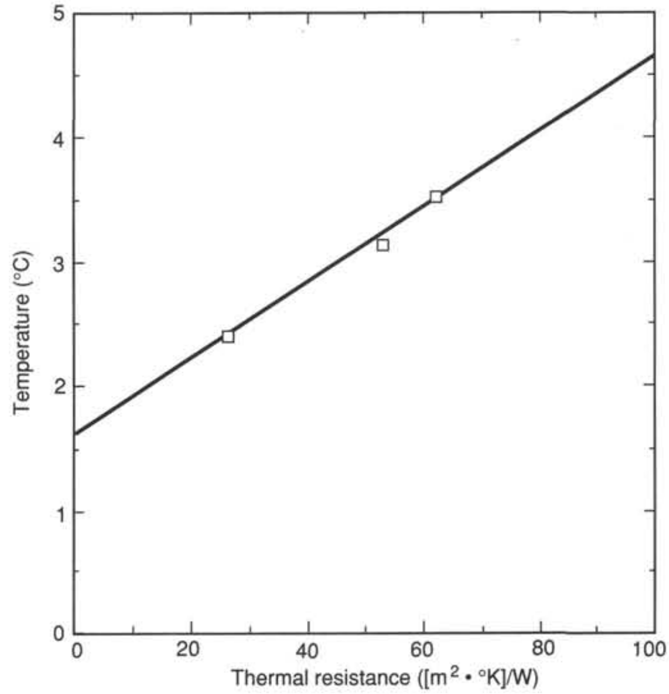

Figure 77. Thermal resistance vs. temperature at Site 841. The slope of the line indicates the magnitude of the heat flow for this site of 29.5 mW/m^2.

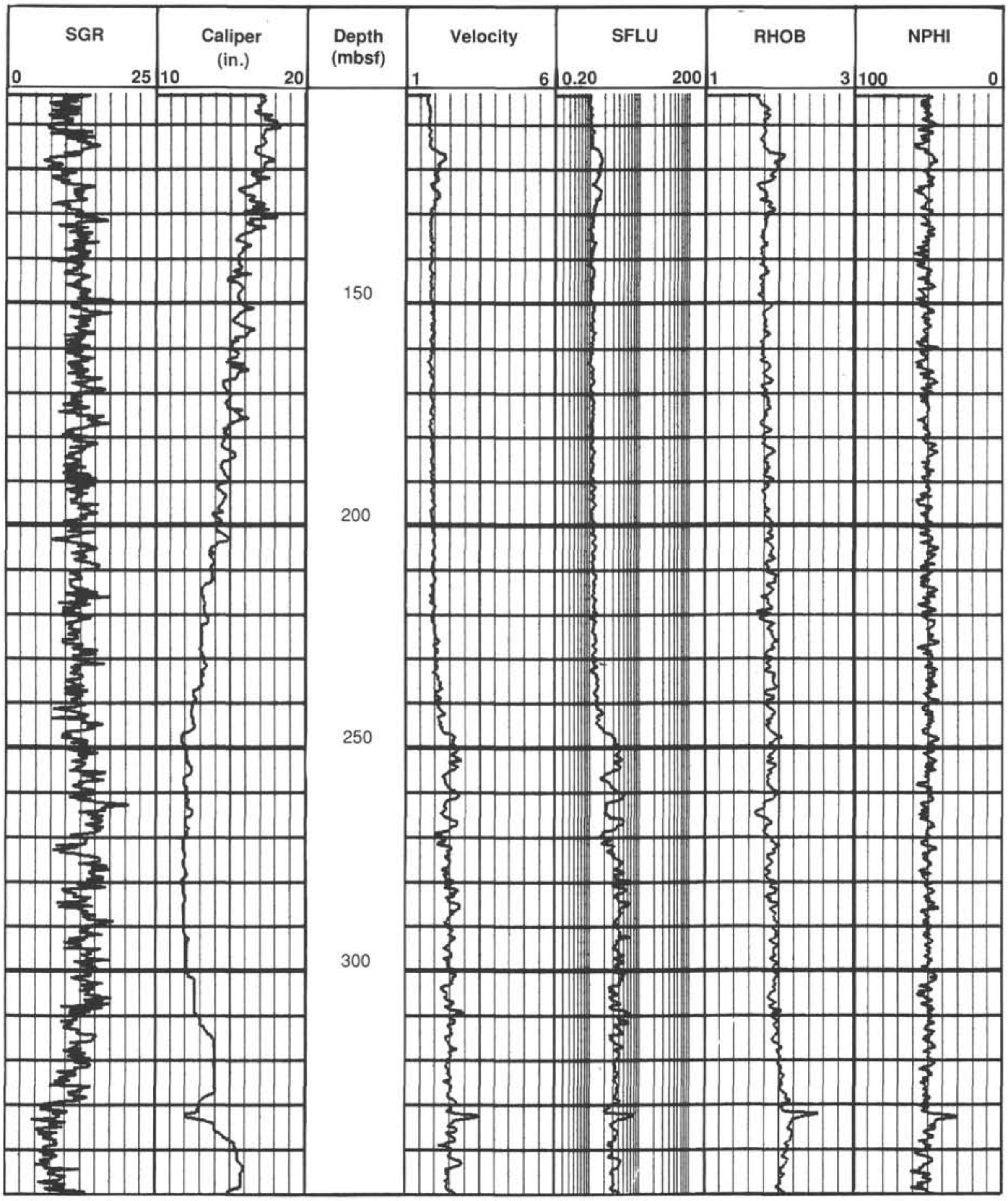

Figure 78. Quad-tool-string logs vs. depth (mbsf). Logs and scales are SGR = total gamma ray (in American Petroleum Institute [API] units), caliper, sonic velocity, spherically focused resistivity (logarithmic scale), RHOB = bulk density, and NPHI = neutron porosity.

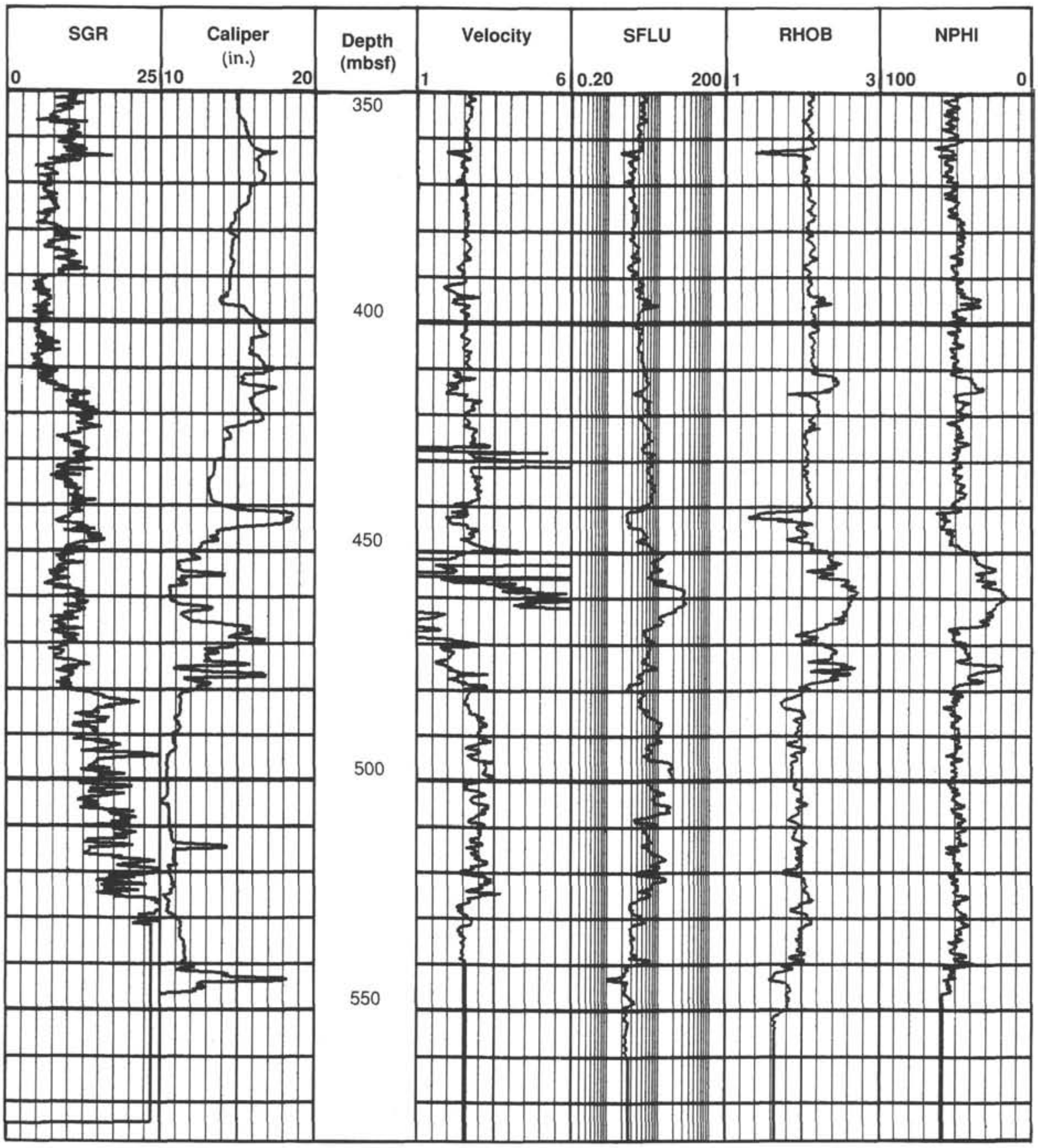

Figure 78 (continued).

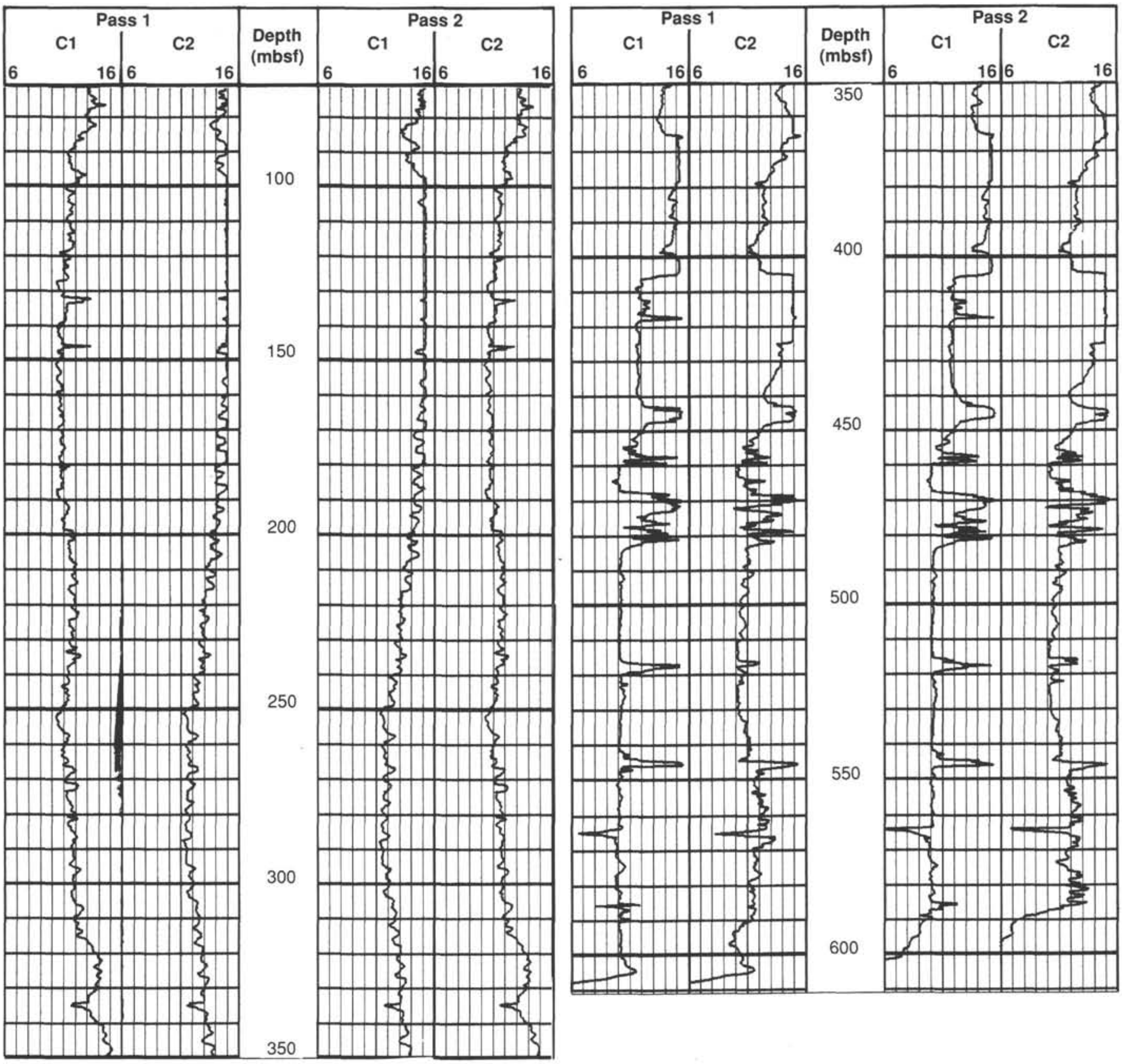

Figure 79. Calipers (diameter vs. depth in mbsf) obtained from both passes of the formation microscanner tool. C1 (caliper 1–3) and C2 (caliper 2–4) are plotted on a scale of 6 to 16 in.

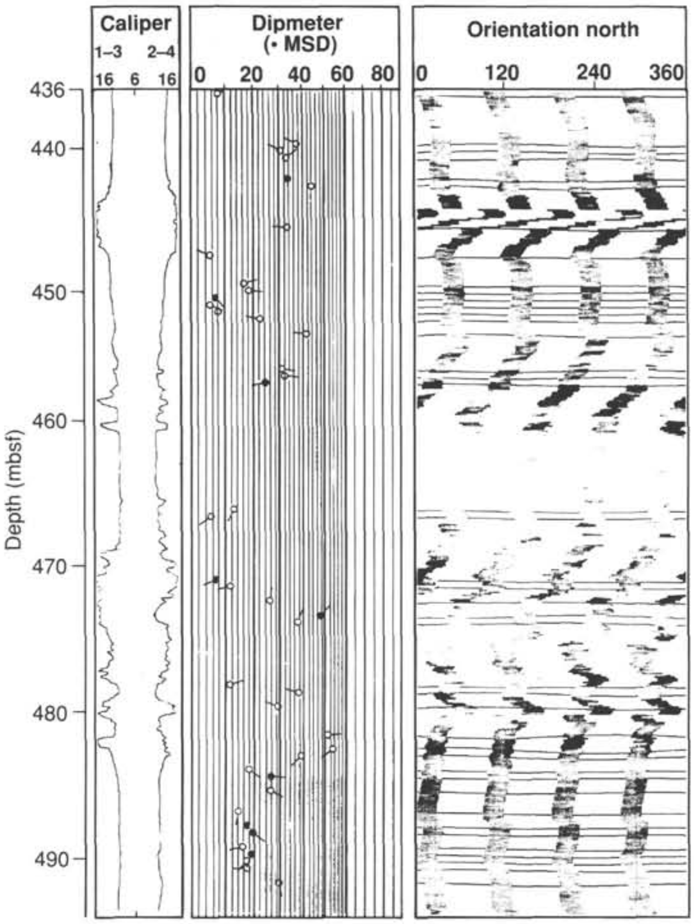

Figure 80. Formation microscanner logging data. Caliper log at left, dipmeter plot at center, and FMS images at right. The horizontal to vertical ratio of the FMS images is 1:1. FMS images are across a zone of faulting at about 454–458 mbsf. Jagged data are caused by skidding or turning of the FMS tool in the hole, and is commonly caused by hole rugosity.

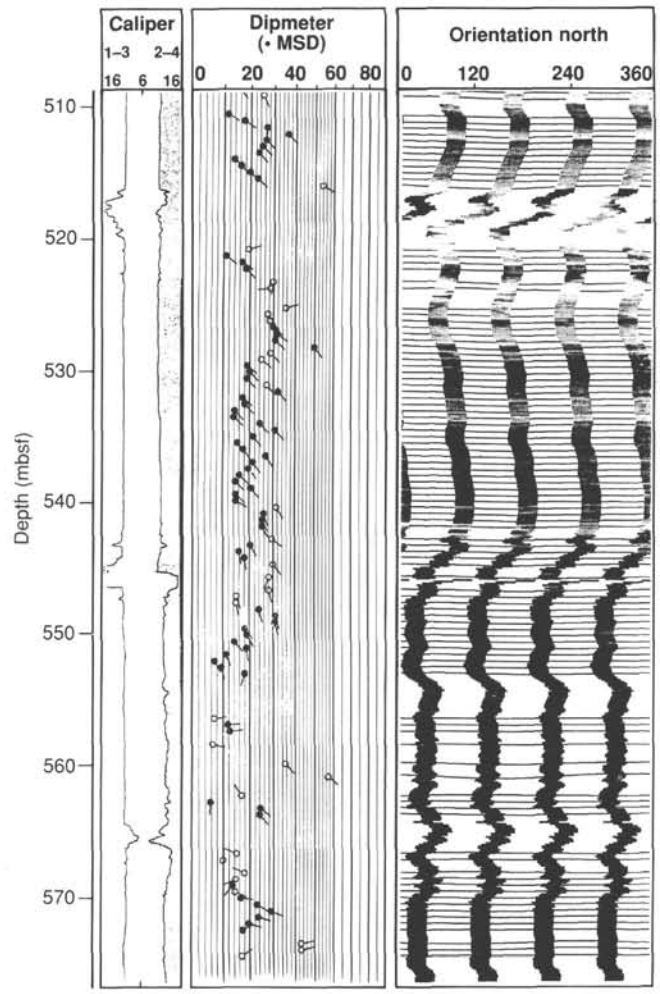

Figure 81. Formation microscanner logging images, 508–575 mbsf. Caliper log at left, dipmeter plot at center, and FMS images at right. Note the change in dip direction at approximately 552–555 mbsf that corresponds to the unconformity identified in the core, between middle Miocene and lower Oligocene strata, at 549.1 mbsf.

Hole 841C: Resistivity-Sonic-Natural Gamma Ray Log Summary

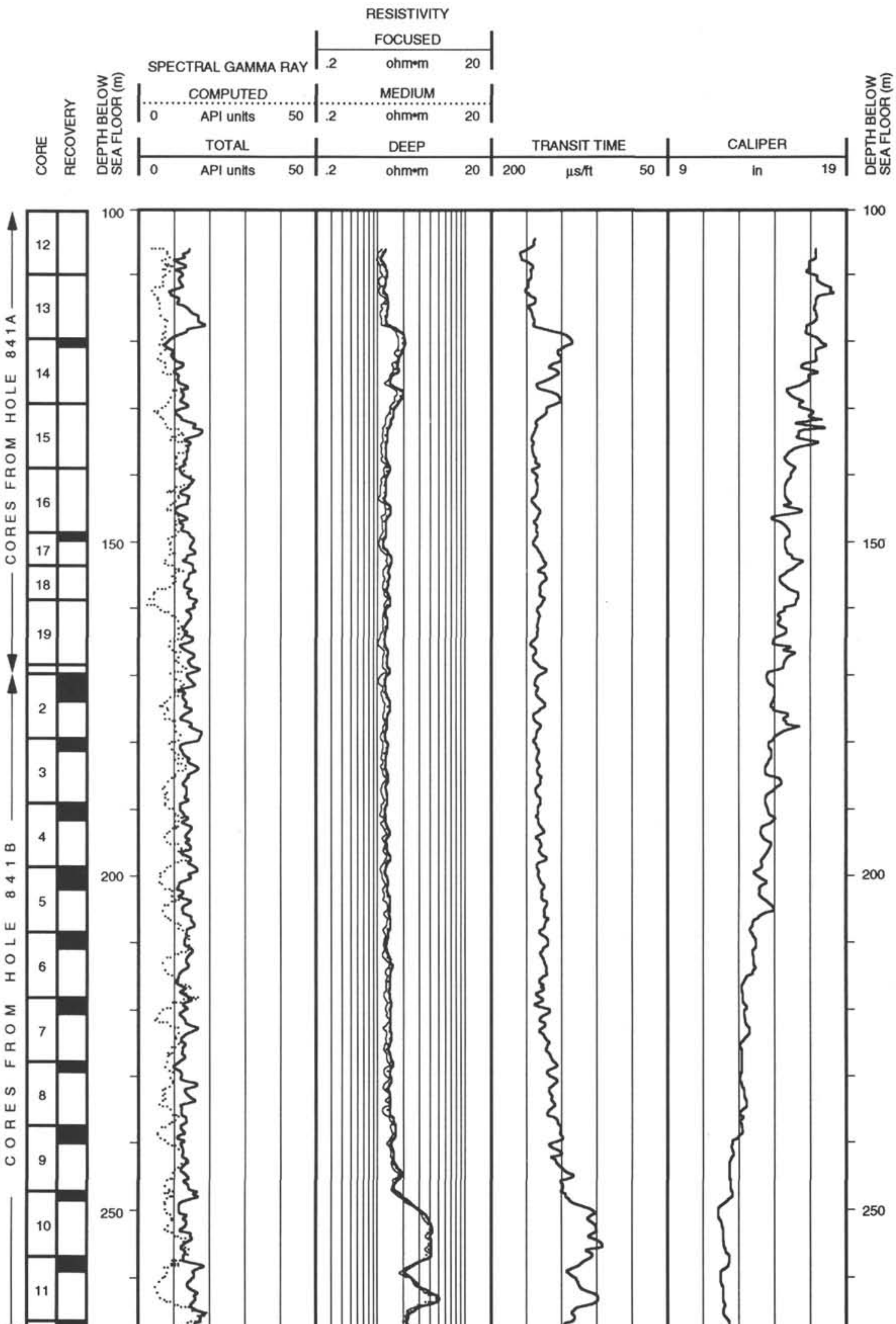

Hole 841C: Resistivity-Sonic-Natural Gamma Ray Log Summary (continued)

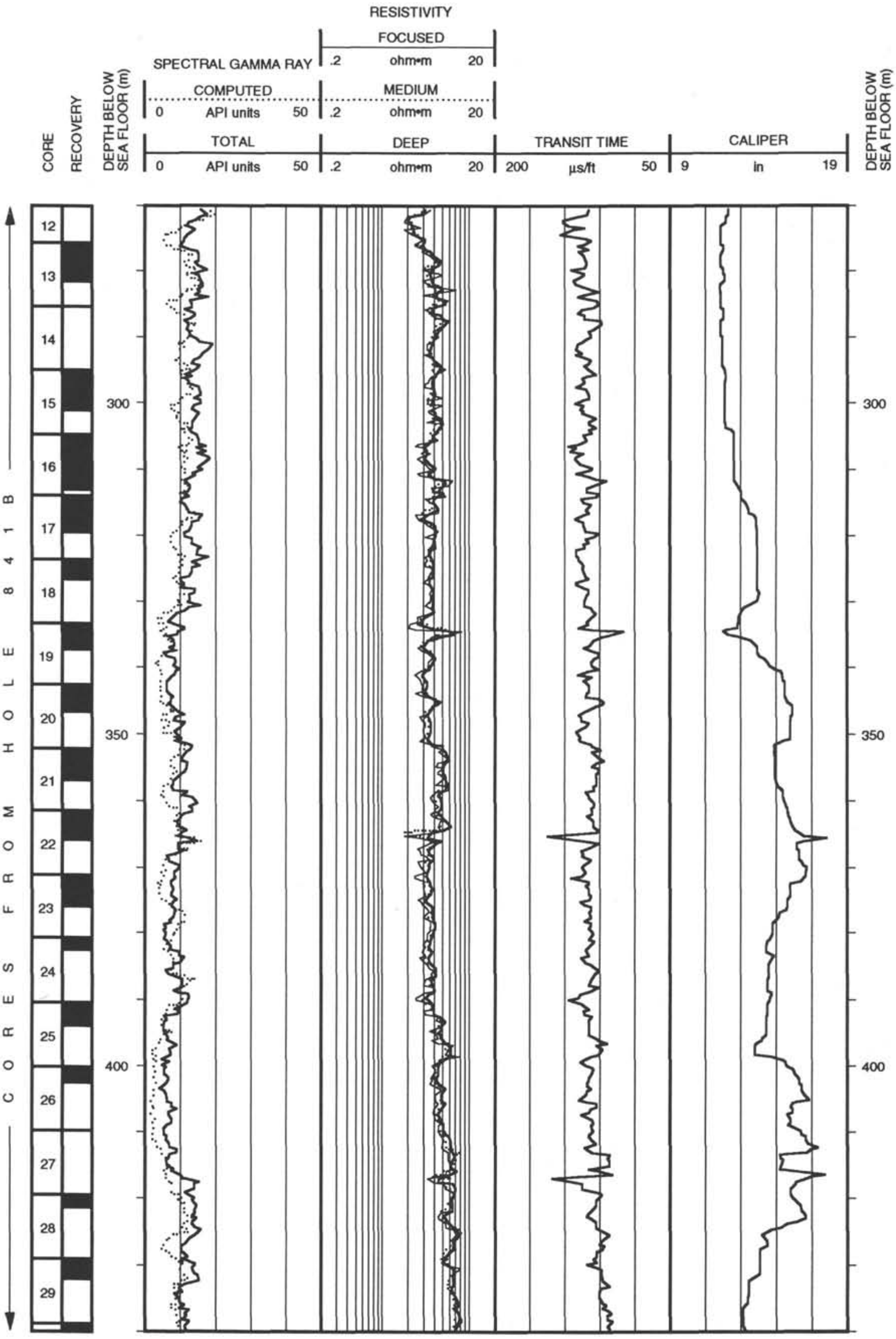

Hole 841C: Resistivity-Sonic-Natural Gamma Ray Log Summary (continued)

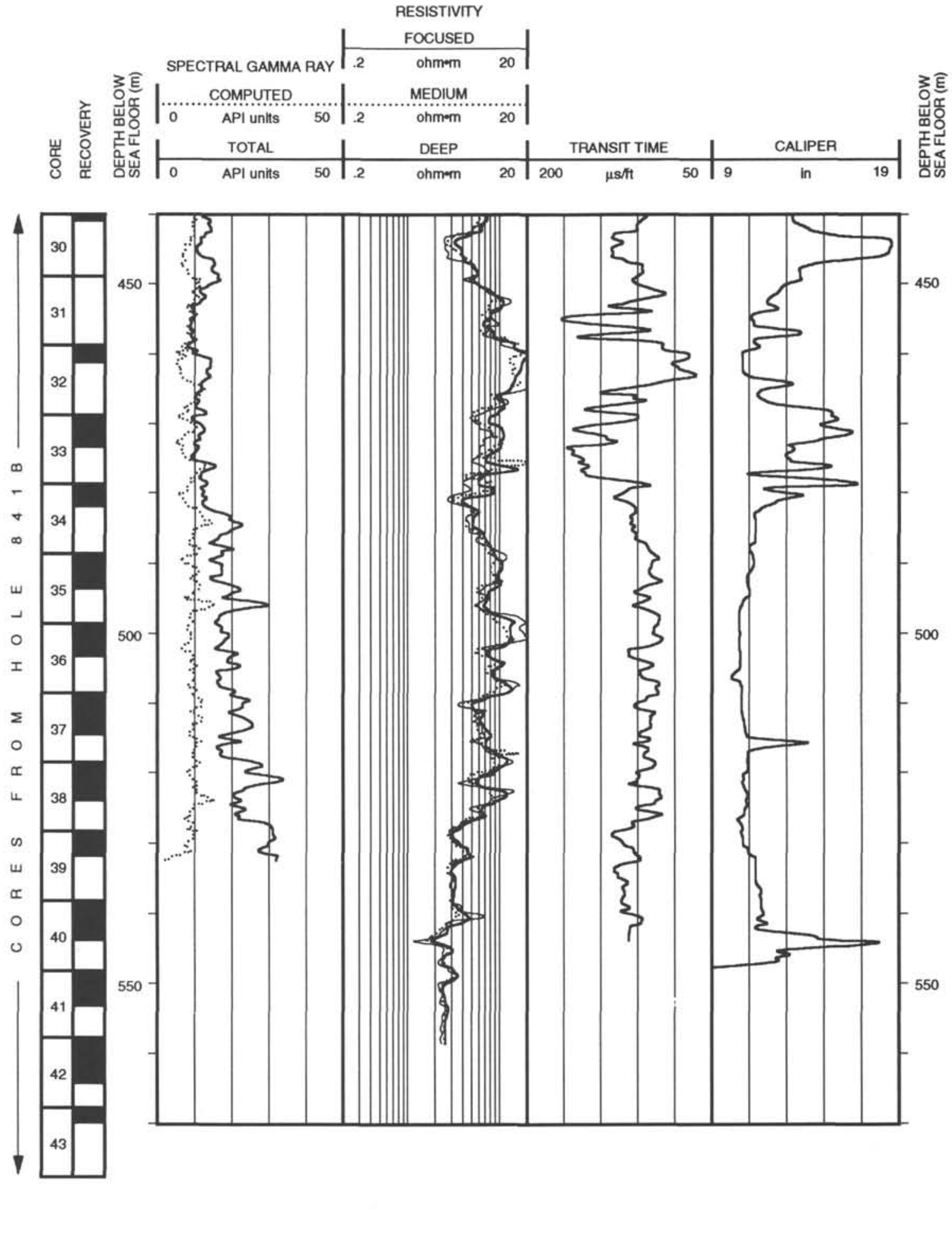

Hole 841C: Density-Natural Gamma Ray Log Summary

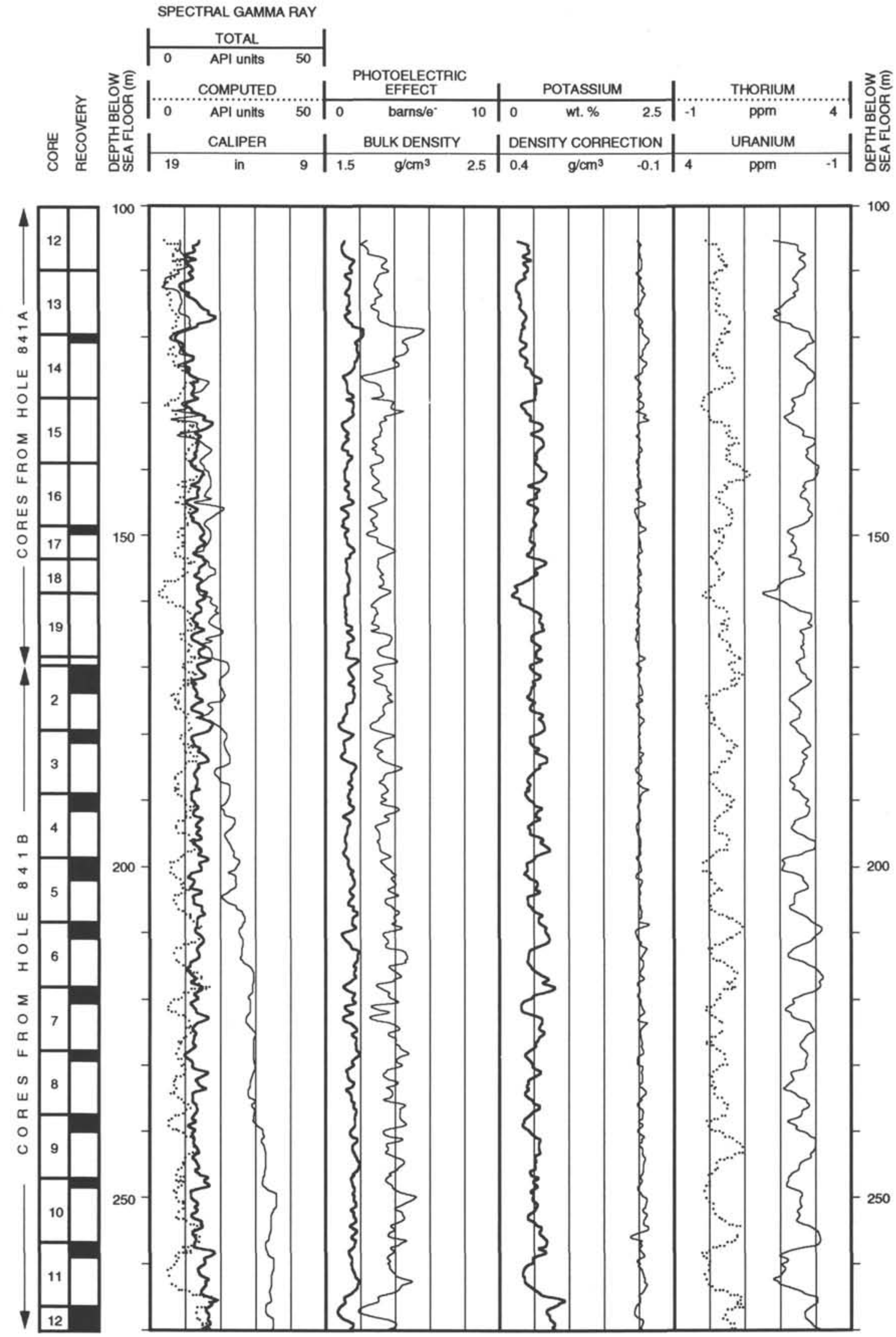

Hole 841C: Density-Natural Gamma Ray Log Summary (continued)

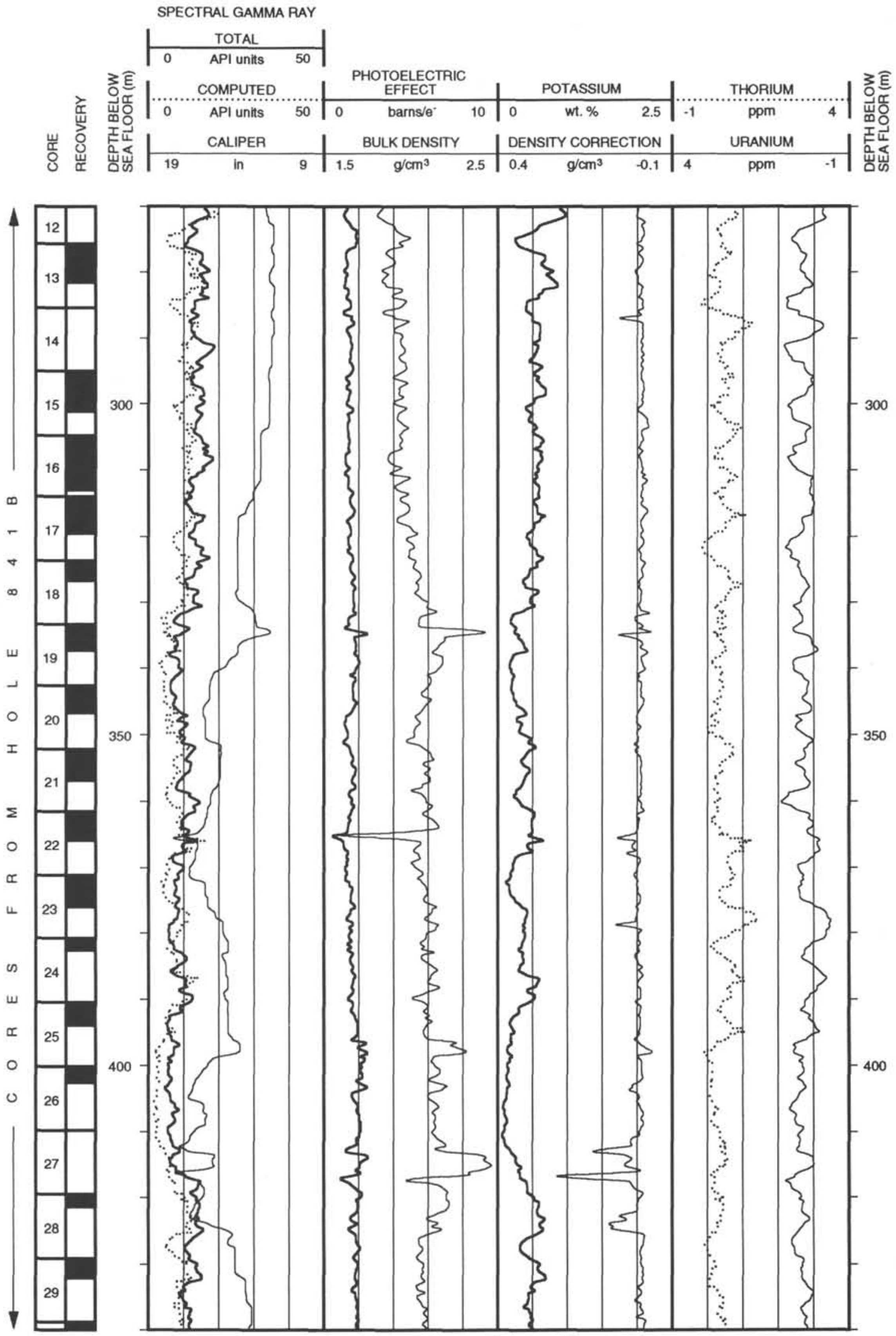

Hole 841C: Density-Natural Gamma Ray Log Summary (continued)